



# New numerical approaches for micromagnetism and Current-induced domain wall motion

Helga Szambolics

## ► To cite this version:

Helga Szambolics. New numerical approaches for micromagnetism and Current-induced domain wall motion. Condensed Matter [cond-mat]. Institut National Polytechnique de Grenoble - INPG, 2008. English. NNT : . tel-00382710

**HAL Id: tel-00382710**

**<https://theses.hal.science/tel-00382710>**

Submitted on 11 May 2009

**HAL** is a multi-disciplinary open access archive for the deposit and dissemination of scientific research documents, whether they are published or not. The documents may come from teaching and research institutions in France or abroad, or from public or private research centers.

L'archive ouverte pluridisciplinaire **HAL**, est destinée au dépôt et à la diffusion de documents scientifiques de niveau recherche, publiés ou non, émanant des établissements d'enseignement et de recherche français ou étrangers, des laboratoires publics ou privés.

INSTITUT POLYTECHNIQUE DE GRENOBLE

N° attribué par la bibliothèque

THESE

pour obtenir le grade de  
DOCTEUR DE L'Institut Polytechnique de Grenoble  
*Spécialité: Physique*

préparée à l'INSTITUT NEEL  
dans le cadre de l'Ecole Doctorale de Physique

présentée et soutenue publiquement

par

Helga SZAMBOLICS

le 05 décembre 2008

Nouvelles formulations éléments finis pour le micromagnétisme  
et  
Déplacement de parois par courant polarisé en spin

DIRECTEUR DE THESE: Jean-Christophe TOUSSAINT  
CO-DIRECTEUR DE THESE: Liliana BUDA-PREJBEANU

JURY

M. Jean-Marc DEDULLE	Président
M. François ALOUGES	Rapporteur
M. Dafiné RAVELOSONA	Rapporteur
M. Jean-Christophe TOUSSAINT	Directeur de thèse
Mme. Liliana BUDA-PREJBEANU	Co-directeur de thèse
M. Nicolas VUKADINOVIC	Examineur









## Remerciements

Pendant ces trois ans de thèse, j'ai eu la chance de découvrir le monde de la recherche. Je tiens tout d'abord à remercier ceux qui ont orienté mes premiers pas sur ce terrain inconnu, mes directeurs de thèse Mme Liliana Buda-Prejbeanu et M. Jean-Christophe Toussaint. Merci pour m'avoir accueillie avec tant de chaleur, pour m'avoir guidée, encouragée, conseillée pendant ces années, tout en me laissant une grande liberté. Merci pour tous ce qu'ils m'ont appris sur le plan scientifique et humain !

Mes remerciements vont aussi envers mes collègues de l'Institut Néel et du laboratoire Spintec, pour leur sympathie et leur amitié, pour les discussions intéressantes et pour la très bonne ambiance qu'ils ont su créer au sein du laboratoire.

Je voudrais remercier les membres du jury de thèse: M. François Alouges et M. Dafiné Ravelosona pour avoir accepté la responsabilité de juger mon travail de thèse en tant que rapporteurs, M. Jean-Marc Dedulle pour avoir présidé le jury de thèse et M. Nicolas Vukadinovic pour l'intérêt qu'il a porté à mon travail.

J'exprime ma gratitude envers M. Emil Burzo, Professeur à l'Université Babeş-Bolyai de Cluj-Napoca, car ma rencontre avec le micromagnétisme a été possible grâce à la collaboration franco-roumaine qu'il a initiée.

En dehors de la découverte du monde du micromagnétisme, cette expérience m'a permis de rencontrer des personnes tout à fait extraordinaires. Certains d'entre eux m'ont accompagnée pendant ces trois ans et sont devenus mes amis. Je voudrais les remercier pour m'avoir remonté le moral et pour avoir su rompre la routine des jours de travail avec les discussions partagées lors des repas ou des pauses café.

Pour leurs encouragements, leur confiance et leur soutien constants pendant mes études en France, je remercie chaudement les membres de ma famille.

Finalement, mes remerciements s'adressent plus particulièrement à mon compagnon et collègue de laboratoire Mihai Miron. Je le remercie pour sa patience et pour avoir consacré tant de temps pour faire de moi une personne beaucoup plus confiante et sûre d'elle même.

Le support financier de cette thèse a été offert par le cluster de recherche « Microélectronique, Nanosciences et Nanotechnologies » de la région Rhône-Alpes. Dans ce cadre, je voudrais remercier M. Jean-Pierre Nozières, ancien directeur du Laboratoire Spintec qui, en accordant sa confiance à notre équipe et à notre projet, s'est battu pour obtenir ce financement.

## Contents

Introduction.....	1
I. Micromagnetic theory.....	5
I.1. Energy functional .....	7
I.2. Equilibrium state .....	14
I.3. The Landau-Lifshitz-Gilbert equation .....	17
I.4. Towards numerical micromagnetism.....	20
References.....	22
II. Numerical micromagnetism .....	25
II.1. The finite difference method.....	27
II.2. The finite element method .....	34
II.2.1. Magnetostatic problem .....	37
II.2.1.1. Condition at infinity .....	40
II.2.2. Classical finite element approach for the Landau-Lifshitz-Gilbert equation – WF1 .....	46
II.2.2.1. Integration scheme and constraint handling.....	48
II.2.3. Applications WF1 .....	57
II.2.3.1. Stripe domains.....	57
II.2.3.2. Exchange coupled magnetic moments in an infinite prism with square cross- section .....	66
II.2.4. The finite element approach – WF2 .....	69
II.2.4.1. $\theta$ integration scheme for the exchange term .....	71
II.2.4.2. First order integration scheme including all the field terms .....	73
II.2.4.3. Second order integration scheme for the exchange field .....	76
II.2.4.4. Second order integration scheme for all the field terms .....	77
II.2.5. Applications WF2.....	79
II.2.5.1. Infinite prism.....	79
II.2.5.2. Stripe domains structure.....	80
II.2.5.3. Stripe domains structure with moderate magnetocrystalline anisotropy .....	85

II.2.5.4. Constricted stripe domains.....	88
II.2.5.5. Numerical ferromagnetic resonance .....	92
References.....	101
III. Domain wall motion .....	107
III.1. State of the art.....	110
III.1.1. Theory .....	110
III.1.1.1. Theory of field-driven domain wall motion .....	110
III.1.1.2. Theory of domain wall motion under spin-polarized current.....	111
III.1.2. Experiments.....	115
III.1.2.1. Field induced motion .....	115
III.1.2.2. Current driven domain wall motion.....	116
III.2. Numerical approaches .....	120
III.2.1. State of the art .....	120
III.2.2. Domain wall dynamics under spin-polarized current as proposed by Thiaville et al. ....	123
III.2.3. The WALL_ST micromagnetic tool .....	130
III.3. Results .....	136
III.3.1. Bulk system.....	136
III.3.1.1. Domain wall motion under applied field in a bulk system.....	137
III.3.1.2. Domain wall motion under spin-polarized current in a bulk system.....	142
III.3.2. Size effects .....	145
III.3.2.1. Size effects in the framework of quasi-1D simulations.....	145
III.3.2.2. Size effects revisited: framework of 3D simulations.....	147
III.3.3. The role of disorder in the displacement of Bloch walls .....	154
III.3.3.1. Effect of anisotropy distribution .....	155
III.3.4. Depinning from geometrical or anisotropy defects.....	161
III.3.4.1. Geometrical constrictions .....	161
III.3.4.2. Crystalline defects .....	166
III.3.5. Current pulses and Bloch wall displacement .....	171
References.....	176
Conclusions.....	182

## Introduction

Thanks to high-resolution fabrication and measurement techniques, one succeeds in deciphering more and more of the secrets hidden by the word “nano”. Submicron magnetic systems are now routinely fabricated based on different materials and with precisely controlled sizes and shapes [Li 2001, Jubert 2001]. Techniques like scanning tunneling microscopy and atomic (magnetic) force microscopy [Binnig 1986] give access to their structural and magnetic properties. Nonetheless, even with the high performance of the available experimental techniques, certain details of the magnetization dynamics in such magnetic bodies are accessible only through micromagnetic modeling.

When it comes to magnetization dynamics, one of the topics of most interest in magnetism nowadays is the spin transfer [Slonczewski 1996]. The theoretical approaches dealing with this topic, translated the complex physical phenomenon in new terms that must be included in the dynamic Landau-Lifshitz-Gilbert equation. In this light, the purpose of the work presented here was to develop an up-to-date micromagnetic simulation tool that would make possible the treatment of systems with irregular shape, meeting certain accuracy and rapidity requirements. In other words, our goal is to find solutions of the Landau-Lifshitz-Gilbert equation, which includes the spin torque terms specific for domain wall motion, by means of micromagnetic simulations.

There are two numerical approaches widely used in numerical micromagnetism: the finite difference and the finite element approximation [Fidler 2000].

The first method is interesting because of the straightforwardness of its implementation and its rapidity, both of these qualities arising from a regular space

---

[Li 2001] S. Li, D. Peyrade, M. Natali, A. Lebib, Y. Chen, U. Ebels, L. D. Buda, K. Ounadjela, “Flux closure structures in Co rings”, *Phys. Rev. Lett.* 86, 1102 (2001).

[Jubert 2001] P. O. Jubert, O. Fruchart, C. Meyer, “Self-assembled growth of faceted epitaxial Fe(110) islands on Mo(110)/Al<sub>2</sub>O<sub>3</sub>”, *Phys. Rev. B* 64, 115419 (2001).

[Binnig 1986] G. Binnig, H. Rohrer “Scanning tunneling microscopy” *IBM J. Res. and Dev.* 30,4 (1986).

[Fidler 2000] J. Fidler, T. Schrefl, “Micromagnetic modeling - the current state of the art”, *J. Phys. D: Appl. Phys.* 33, 135 (2000).

[Slonczewski 1996] J. C. Slonczewski, “Current-driven excitation of magnetic multilayers”, *J. Magn. Magn. Mat.* 159, L1 (1996).

discretization of the magnetic body. The shortcoming of this numerical approach is that, unfortunately, any finite differences-based algorithm is intrinsically affected by the roughness of the grid at surfaces [García-Cervera 2003]. A reliable computation can be assured only for systems bounded by planar surfaces parallel to some axes of the discretization grid.

One of the solutions that would make possible to take advantage, to a certain extent, of the positive features of the finite difference approximation, while reducing its negative effects, is to correct the evaluation of the fields in the border cells. However the implementation of such corrections is not straightforward, their accuracy is not entirely guaranteed and their use can significantly increase the computation time.

Another solution, adopted by us, consists in treating the micromagnetic problem by applying the finite element approach [Braess 2001], well known for its applications to engineering problems with complex shapes. The advantage of geometry independence comes at the cost of a relatively complex mathematical apparatus. The implementation of a finite element approach is not as clear-cut as the finite difference one. Before even starting the development of a finite element software, one has to rewrite the problem to be solved (the initial partial differential equation together with the boundary conditions) under an integral form, the so-called *weak formulation*. One of the main issues is that this integral form is not unique.

In the present manuscript, two integral formulations for the Landau-Lifshitz-Gilbert equation were derived and implemented. The importance of choosing a correct integral form was proved based on the results obtained for several 2D test cases.

After the numerous difficulties encountered while deriving the integral form for the classical Landau-Lifshitz-Gilbert equation and implementing it, it was clear that the inclusion of the additional spin torque terms would require a large amount of time. Firstly, one has to establish a proper integral form and, secondly, this has to be implemented. Unfortunately, the first step is already a problematical task, as there is no clear criterion saying what integral form can or cannot be used. However, the aim of this work was the

---

[García-Cervera 2003] C. J. García-Cervera, Z. Gimbutas, E. Weinan, "Accurate numerical methods for micromagnetics simulations with general geometries", J. Comput. Phys. 184, 37 (2003).

[Braess 2001] D. Braess, "Finite elements", 2<sup>nd</sup> ed., Cambridge University Press, Cambridge, 2001.

development of up-to-date micromagnetic tools. To continue this work, we turned our attention to the finite difference software called GL\_FFT, earlier developed in our group by Brandusa Kevorkian [Kevorkian 1998]. In this numerical tool the classical Landau-Lifshitz-Gilbert equation is integrated. This software was tested with several occasions on various systems and with various purposes. Its accuracy and performance is therefore well established.

As mentioned previously, GL\_FFT served firstly as a reference, as the results obtained with the finite element implementations had to be compared to results issued by a numerical tool that was known to be accurate. Secondly, encouraged by the growing interest in the spin torque phenomenon, we considered interesting and important to include in this software the spin torque terms, making possible the numerical study of spin-polarized current driven domain wall displacement. The so-obtained software was named WALL\_ST.

One of the boiling points of this domain wall motion topic is: what kinds of materials are better suited for spintronic applications, those in which the magnetization lays in-plane or those in which an out-of-plane orientation is adopted? Before studying this question, the WALL\_ST software was obviously benchmarked against analytical results (concerning out-of-plane magnetized systems) and numerical results (for the in-plane magnetized scenario). As the results were encouraging, WALL\_ST was employed in studying the domain wall propagation in systems with perpendicular magnetization.

This manuscript is organized as follows:

The first chapter contains a short description of the basic notions used in micromagnetism. The main interactions occurring in a micromagnetic system are presented, together with the corresponding energy terms. Based on these the equilibrium state is defined. The chapter ends with the description of the dynamic Landau-Lifshitz-Gilbert equation.

The second chapter presents in detail the two numerical approaches used for solving the micromagnetic problem: the finite difference and the finite element method. In

---

[Kevorkian 1998] B. M. Kevorkian, "Contribution à la modélisation du retournement d'aimantation. Application a des systèmes magnétiques nanostructurés ou de dimensions réduites", Ph.D. dissertation, Université Joseph Fourier, Grenoble, 1998.



the description of finite difference-based GL\_FFT software, topics like the space discretization, integration scheme and the solving process of the Landau-Lifshitz-Gilbert equation are treated. In the next paragraph, first a general introduction in the finite element approximation is given. Then we derive two integral formulations for the dynamic equation. After testing the first of them on two 2D test cases, we will see what details should be modified in order to get an improved description of the magnetization dynamics. The resulting second integral formulation is benchmarked against the GL\_FFT simulation tool. Finally, after determining the equilibrium configuration of a FePd thin film, small excitations are introduced in the system and the ferromagnetic resonance spectrum is determined. The results are compared to experimental data.

The last chapter concerns the magnetic domain wall dynamics in systems with perpendicular anisotropy. The chapter starts with a list of the main theoretical and experimental results concerning this topic. As our micromagnetic simulation tool adapted for the study of domain wall dynamics is derived from the GL\_FFT software, in the next paragraph of this chapter only the features that had to be added or modified in order to take into account the effect of a spin-polarized current are presented. Next WALL\_ST is benchmarked against other numerical approaches and analytical treatments. Then follow the results, first on ideal systems and in the last part of the chapter, trying to approach reality, several kinds of defects were introduced in the magnetic system.

The conclusions and the prospective close the manuscript.

## I. Micromagnetic theory

A ferromagnetic body is rarely uniformly magnetized. In most of the cases, it consists of small regions with constant magnetization vector  $\mathbf{M}$ , called magnetic domains, separated by so-called domain walls, where the orientation of the magnetization changes rapidly with the position. A relatively complete understanding of such magnetic entities can be obtained using the micromagnetic theory. William F. Brown put together the concepts previously developed by Weiss [Weiss 1907], Landau and Lifshitz [Landau-Lifshitz 1935], and created a unitary continuous theory for ferro- and ferrimagnetic systems that he named *micromagnetism* [Brown 1963]. Micromagnetics addresses magnetic bodies on a length scale situated between that employed by atomistic approaches and the one used in domain/magnetic microstructure analysis.

The ferro- and ferrimagnetic systems are characterized by a *spontaneous magnetization*  $M_S$  - a net magnetic moment per unit volume, resulting from a magnetic order even in the absence of an externally applied field. Weiss explained this collective behavior of the individual moments by the “molecular field”, whose origin, as shown by Heisenberg, lies in the exchange coupling. Due to this interaction, the magnetic moments tend to be aligned parallel to each other, and therefore the amplitude of the magnetization vector must be  $M_S$ . Introducing  $\mathbf{m}(\mathbf{r}, t)$ , the normalized magnetization vector, the first hypothesis of the micromagnetic theory becomes:

$$\begin{cases} \mathbf{M}(\mathbf{r}, t) = M_S \mathbf{m}(\mathbf{r}, t) \\ |\mathbf{m}(\mathbf{r}, t)| = 1 \end{cases} \quad (\text{I.1})$$

The modulus of the magnetization is then known; its orientation however, cannot be specified based on the exchange coupling. Indeed, the sources of non-uniform magnetization distribution are forces due to coupling with the crystalline structure or due to magnetostriction, dipolar forces arising from the magnetic “charges” and due to the

presence of an external magnetic field. One can consider these forces as secondary, their effect being as a perturbation of the parallel alignment imposed by the exchange coupling, which leads to small variations of the orientation of the magnetization vector. This is the second hypothesis of the micromagnetic theory. It makes possible the substitution of the atomic moments by a continuous magnetization distribution, and all the quantities that depend on the magnetization will also be continuous functions of position and time.

Depending on the forces, external and internal, acting upon a magnetic system, different equilibrium magnetization configurations are foreseeable. The micromagnetic theory is based on the principle that a magnetic equilibrium state is reached when the total energy of the system becomes minimal. In order to have a constant  $M_S$  one has to assume conditions of constant temperature. In isothermal processes, the appropriate energy functional is the *Gibbs free energy*. This energy functional comports several contributions. The constituting energy terms, will be defined in the following together with the equilibrium equations. In the last part of the chapter, the equation describing the magnetization dynamics, called the Landau-Lifshitz-Gilbert equation, is introduced.

### 1.1. Energy functional

The free energy of a ferromagnetic system of volume  $V_m$  and under the influence of an external magnetic field contains four fundamental terms [Brown 1963]: the exchange, the magnetocrystalline anisotropy, the demagnetizing and the applied field energy:

$$E_{tot} = E_{ex} + E_{anis} + E_{dem} + E_{app} \quad (I.2)$$

#### *Exchange energy*

This contribution arises from the short-range interaction called *exchange coupling*, inducing the parallel alignment of the magnetic moments. Determined by Heisenberg, the exchange interaction is the strongest coupling occurring between two neighboring spins. The most common form of the exchange Hamiltonian [Buschow 2003] is:

$$H_{ex} = -2 \sum_{i,j=1}^{nn} J_{ij} \mathbf{S}_i \cdot \mathbf{S}_j \quad (I.3)$$

where  $nn$  stands for the nearest neighbors. The exchange integral  $J_{ij}$  depends on the distance between the interacting spins, its sign determining a parallel (ferromagnetic) or anti-parallel (antiferromagnetic) ordering.  $J_{ij}$  is related to the overlap of the magnetic orbitals of adjacent atoms and to the Pauli exclusion principle. The scalar product  $\mathbf{S}_i \cdot \mathbf{S}_j$  can be easily transformed making a few basic assumptions:

One can suppose that the amplitude of the spins is constant,

$|\mathbf{S}_i| = |\mathbf{S}_j| = S$ . Moreover, working in the framework of small deviations from the parallel alignment of the atomic moments, the direction vectors  $\mathbf{m}_i$ ,  $i \in \{1, N\}$ , of the spin system can be replaced by a continuous function  $\mathbf{m} = \mathbf{m}(\mathbf{r})$  with amplitude equal to 1. Taking into account these,  $\mathbf{S}_i \cdot \mathbf{S}_j$  reads as:

$$\mathbf{S}_i \cdot \mathbf{S}_j = S^2 \left( 1 - \frac{1}{2} \left[ (\mathbf{r}_i - \mathbf{r}_j) \cdot \nabla \mathbf{m}(\mathbf{r}_i) \right]^2 \right) \quad (I.4)$$

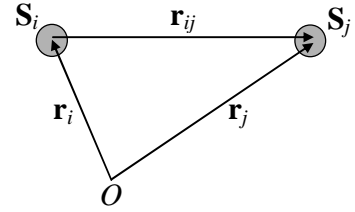


Figure I.1: Schematic representation of the interaction between two adjacent spins  $\mathbf{S}_i$  and  $\mathbf{S}_j$ .

with  $\mathbf{r}_i$  the position of the spin  $\mathbf{S}_i$  (Figure I.1). Substituting (I.4) in (I.3) and considering an isotropic exchange interaction ( $J_{ij}=J$ ), like for example in a simple cubic crystal, a simplified form is obtained:

$$H_{ex} = -2JS^2 + JS^2 \sum_{i,j=1}^N \left[ (\mathbf{r}_i - \mathbf{r}_j) \cdot \nabla \mathbf{m}(\mathbf{r}_i) \right]^2 \quad (\text{I.5})$$

Based on (I.5) and on the continuity hypothesis of the micromagnetic theory, any excess resulting from the deviation from the perfectly aligned state is quantified by:

$$E_{ex} = \int_{V_m} A_{ex} \left[ (\nabla m_x(\mathbf{r}))^2 + (\nabla m_y(\mathbf{r}))^2 + (\nabla m_z(\mathbf{r}))^2 \right] dV \quad (\text{I.6})$$

The parameter  $A_{ex}$  (J/m) is called the *exchange constant*. In the simple case of a cubic crystal,  $A_{ex}$  is  $JS^2/a$ , with  $a$  the crystalline lattice constant. Through its dependence on the lattice constant, the exchange constant is also temperature dependent. A perfect alignment of the magnetic moments corresponds to a minimum of the exchange energy ( $E_{ex}=0$  J/m<sup>3</sup>).

#### *Magnetocrystalline anisotropy energy*

So far it has been established that the isotropic exchange interaction is responsible for the magnitude of the magnetization vector but gives no information about its orientation. One of the factors that can impose a certain direction of  $\mathbf{M}$  is the electrostatic interaction between the orbitals of the electrons determining the magnetic properties and the charge distribution of the ions forming the crystal lattice. This interaction is quantified by the *magnetocrystalline anisotropy energy*. The name “magnetocrystalline anisotropy” already suggests the basic idea behind this concept: with respect to the arrangement of the ions in the crystal structure, certain orientations of the magnetic moments are more favorable energetically than others. These axes along which it is preferable for the magnetization to lay are called easy axes.

The magnetocrystalline energy is usually small compared to the exchange energy. Its definition depends on the symmetry of the crystalline structure [Hubert 1998]. For instance, one can define uniaxial or hexagonal magnetocrystalline anisotropy. For the simplest case of uniaxial anisotropy, the corresponding anisotropy energy has the expression:

$$E_{anis} = \int_{V_m} K_{anis} \left[ 1 - (\mathbf{u}_K \cdot \mathbf{m}(\mathbf{r}))^2 \right] dV \quad (I.7)$$

Where  $\mathbf{u}_K$  is the direction of the easy axis and  $K_{anis}$  is the temperature dependent *anisotropy constant*, expressed in J/m<sup>3</sup>.

In ultrathin layers other types of anisotropy terms (surface, interface and exchange) can also occur, and these contributions might be as important as the magnetocrystalline one.

#### *Applied field energy*

If an external field  $\mathbf{H}_{app}$  is applied, the magnetization  $\mathbf{M}$  is submitted to a torque which tends to align it parallel to the field direction. Due to the misalignment between  $\mathbf{H}_{app}$  and  $\mathbf{M}$ , a supplementary contribution has to be included in the total energy:

$$E_{app} = -\mu_0 \int_{V_m} M_s [\mathbf{m}(\mathbf{r}) \cdot \mathbf{H}_{app}(\mathbf{r})] dV \quad (I.8)$$

where  $\mu_0 = 4\pi \cdot 10^{-7}$  H/m is the permeability of the vacuum.

#### *Demagnetizing energy*

To minimize the last two terms the orientation of the magnetization vector is varied. However none of these contributions can be held responsible for the formation of the magnetic domains. The magnetic domain structure is organized so to avoid the formation of magnetic charges, by closing in the magnetic flux (flux-closure type domains). It is the magnetization itself that gives rise to the field imposing such a behavior. The contribution inside the magnetic material is called *demagnetizing field*, and the corresponding energy is named the demagnetizing energy.

Similarly with electrostatics, the sources of the demagnetizing field are the volume or the surface magnetic charges associated to the magnetization distribution inside a magnet. The magnetic charges are analogous to the electric ones, with the difference that they always appear in pairs, a magnetic charge being always balanced by one having the opposite sign.

From a magnetostatic point of view, there are three important equations connecting magnetization  $\mathbf{M}$ , applied current density  $\mathbf{j}_0$ , magnetic induction  $\mathbf{B}$  and magnetic field  $\mathbf{H}$  [Jackson 1999]:

$$\mathbf{B} = \mu_0 (\mathbf{H} + \mathbf{M}) \quad (\text{I.9})$$

and two of Maxwell's equations:

$$\nabla \cdot \mathbf{B} = 0 \quad (\text{I.10})$$

$$\nabla \times \mathbf{H} = \mathbf{j}_0 \quad (\text{I.11})$$

The magnetic field  $\mathbf{H}$  can be decomposed in two contributions: the applied field  $\mathbf{H}_{\text{app}}$  generated by the current  $\mathbf{j}_0$  and satisfying the relations:

$$\begin{cases} \nabla \times \mathbf{H}_{\text{app}} = \mathbf{j}_0 \\ \nabla \cdot \mathbf{H}_{\text{app}} = 0 \end{cases} \quad (\text{I.12})$$

and the demagnetizing field  $\mathbf{H}_{\text{dem}}$  that fulfils the following conditions:

$$\begin{cases} \nabla \times \mathbf{H}_{\text{dem}} = 0 \\ \nabla \cdot \mathbf{H}_{\text{dem}} = -\nabla \cdot \mathbf{M} \end{cases} \quad (\text{I.13})$$

Together with the differential equations (I.10) and (I.13), boundary conditions are also imposed on the magnetic induction and the demagnetizing field:

$$\begin{aligned} \mathbf{n} \cdot (\mathbf{B}_{\text{int}} - \mathbf{B}_{\text{ext}}) &= 0 \\ \mathbf{n} \times (\mathbf{H}_{\text{dem\_int}} - \mathbf{H}_{\text{dem\_ext}}) &= 0 \end{aligned} \quad (\text{I.14})$$

where  $\mathbf{n}$  is the normal vector pointing always outwards, the subscript “int” corresponds to the magnetic material and “ext” to the surrounding medium. Furthermore,  $\mathbf{B}$  is supposed to cancel at infinity. Based on the equations presented above, the demagnetizing field can be determined in two ways: using either the magnetic scalar potential approach or the magnetic vector potential approach. As from a numerical point of view it is more advantageous to use the magnetic scalar potential approach (only one unknown has to be determined, whereas for the vector potential three components are required), in the following part this method is shortly presented.

### Magnetic scalar potential approach

The magnetic scalar potential approach is based on the irrotational property of the demagnetizing field. By analogy with electrostatics, it follows that this field is derived from a magnetic scalar potential  $\Phi$ :

$$\mathbf{H}_{\text{dem}} = -\nabla\Phi \quad (\text{I.15})$$

determined by Poisson's equation inside the magnetic system (Figure I.2):

$$\Delta\Phi_{\text{int}} = -\rho_m \quad (\text{I.16})$$

$\rho_m = -\nabla \cdot \mathbf{M}$  being the volume density of magnetic charges

(Figure I.2). In the surrounding region,  $\Phi$  is governed by the Laplace equation:

$$\Delta\Phi_{\text{ext}} = 0 \quad (\text{I.17})$$

The continuity conditions (I.14) can be turned into passage conditions for  $\Phi$ :

$$\begin{cases} \Phi_{\text{int}}(\mathbf{r}) = \Phi_{\text{ext}}(\mathbf{r}), & \mathbf{r} \in S_m \\ \frac{\partial \Phi_{\text{int}}}{\partial \mathbf{n}}(\mathbf{r}) - \frac{\partial \Phi_{\text{ext}}}{\partial \mathbf{n}}(\mathbf{r}) = -\sigma_m(\mathbf{r}), & \mathbf{r} \in S_m \end{cases} \quad (\text{I.18})$$

$\sigma_m = \mathbf{M} \cdot \mathbf{n}$  being the surface density of the magnetic charges (Figure I.2) and  $S_m$  represents the magnetic surface. Finally a condition requiring the cancellation of the scalar potential at infinity is applied [Brown 1963, Jackson 1999].

The Green function formalism can be applied to determine the potential  $\Phi$ . The Green functions associated with Poisson's equation for the 2D and 3D case are:

$$\begin{aligned} \text{2D:} \quad G_2(\mathbf{r}, \mathbf{r}') &= -\frac{1}{2\pi} \ln|\mathbf{r} - \mathbf{r}'| \\ \text{3D:} \quad G_3(\mathbf{r}, \mathbf{r}') &= \frac{1}{4\pi|\mathbf{r} - \mathbf{r}'|} \end{aligned} \quad (\text{I.19})$$

The potential  $\Phi$  is then given the following integral formulas:

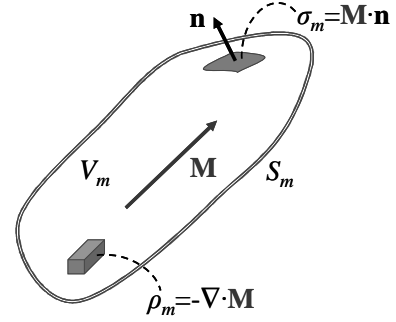


Figure I.2: Magnetic surface and volume charges.



$$\begin{aligned}
2D: \quad \Phi(\mathbf{r}) &= -\frac{1}{2\pi} \int_{S_m} \rho_m(\mathbf{r}') \ln|\mathbf{r}-\mathbf{r}'| dS' - \frac{1}{2\pi} \int_{\Gamma_m} \sigma_m(\mathbf{r}') \ln|\mathbf{r}-\mathbf{r}'| dl' \\
3D: \quad \Phi(\mathbf{r}) &= \frac{1}{4\pi} \int_{V_m} \frac{\rho_m(\mathbf{r}')}{|\mathbf{r}-\mathbf{r}'|} dV' + \frac{1}{4\pi} \int_{S_m} \frac{\sigma_m(\mathbf{r}')}{|\mathbf{r}-\mathbf{r}'|} dS'
\end{aligned} \tag{I.20}$$

Equations (I.20) can be rewritten in a more compact form:

$$\begin{aligned}
\Phi(\mathbf{r}) &= \int_{V_m} G(\mathbf{r}-\mathbf{r}') \rho_m(\mathbf{r}') dV' + \int_{S_m} G(\mathbf{r}-\mathbf{r}') \sigma_m(\mathbf{r}') dS' \\
&= [G * \rho_m](\mathbf{r}) + [G * \sigma_m](\mathbf{r})
\end{aligned} \tag{I.21}$$

Here  $G * \rho_m$  and  $G * \sigma_m$  are the convolution products between the Green function and the volume and surface density of the magnetic charges. Knowing the scalar potential, its gradient - the demagnetizing field - is easily determined:

$$\begin{aligned}
\mathbf{H}_{\text{dem}}(\mathbf{r}) &= -\int_{V_m} \nabla G(\mathbf{r}-\mathbf{r}') \rho_m(\mathbf{r}') dV' - \int_{S_m} \nabla G(\mathbf{r}-\mathbf{r}') \sigma_m(\mathbf{r}') dS' \\
&= -[\nabla G * \rho_m](\mathbf{r}) - [\nabla G * \sigma_m](\mathbf{r})
\end{aligned} \tag{I.22}$$

Before continuing, it is important to note that the first three interactions: exchange, magnetocrystalline anisotropy and Zeeman coupling are acting on a short range. The demagnetizing field depends on the magnetization distribution in the whole volume of the sample. In computational micromagnetics the calculation of this field is the most problematic one, especially its cancellation at infinity posing many difficulties.

Once the demagnetizing field calculated, the resulting energy  $E_{\text{dem}}$  is defined in a similar way with the applied energy:

$$E_{\text{dem}} = -\frac{1}{2} \mu_0 M_s \int_{V_m} \mathbf{m}(\mathbf{r}) \cdot \mathbf{H}_{\text{dem}}(\mathbf{r}) dV \tag{I.23}$$

This energy is minimal if the density of magnetic charges is the smallest possible. For example, the demagnetizing energy of a uniformly magnetized parallelepiped sample (shown in Figure I.3 a) can be reduced dividing the magnetic body into anti-parallel magnetized domains (Figure I.3 b and c). However, even though the domain formation is benefic from magnetostatic point of view, it is in conflict with the exchange interaction, as in the walls separating the domains the magnetization orientation varies rapidly. A stable

domain structure is therefore based on the equilibrium between the energy contributions present in the magnetic system.

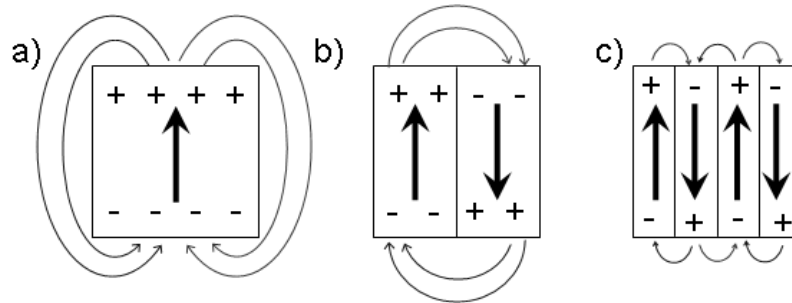


*Figure 1.3: The magnetization and the magnetic poles in a rectangular body. a) corresponds to uniform magnetization, while b), c) depict domain structures.*

## 1.2. Equilibrium state

Assembling the energy terms derived previously, the total energy in reduced units ( $\mathbf{m}=\mathbf{M}(\mathbf{r})/M_s$ ) is:

$$E_{tot}(\mathbf{m}) = \int_{V_m} A_{ex} [\nabla \mathbf{m}(\mathbf{r})]^2 dV + \int_{V_m} K_{anis} \left[ 1 - (\mathbf{u}_K \cdot \mathbf{m}(\mathbf{r}))^2 \right] dV \\ - \int_{V_m} \mu_0 M_s [\mathbf{m}(\mathbf{r}) \cdot \mathbf{H}_{app}(\mathbf{r})] dV - \int_{V_m} \frac{1}{2} \mu_0 M_s [\mathbf{m}(\mathbf{r}) \cdot \mathbf{H}_{dem}(\mathbf{m}(\mathbf{r}))] dV \quad (\text{I.24})$$

for the simplest case of a uniaxial material. The terms presented here are the basic ones. Eventually, supplementary contributions arising from magnetostriction, surface and shape anisotropies, RKKY coupling have to be added.

The aim of micromagnetism is to find a distribution of magnetic moments:

$$\mathbf{m} = \{ \mathbf{m}(\mathbf{r}) \mid \mathbf{r} \in V_m, |\mathbf{m}| = 1 \} \quad (\text{I.25})$$

that minimizes the free energy functional (I.24). Such an equilibrium magnetization distribution satisfies two equilibrium conditions:

$$\begin{cases} \delta E_{tot}(\mathbf{m}) = 0 \\ \delta^2 E_{tot}(\mathbf{m}) > 0 \end{cases} \quad (\text{I.26})$$

derived from variational principles [Brown 1963, Miltat 1994]. The minimization process has to take into account the constraint of constant magnetization magnitude.

Supposing that the magnetization  $\mathbf{m}$  is varied by a small amount:  $\mathbf{m} \rightarrow \mathbf{m} + \delta \mathbf{m}$ . The change in the total energy is then  $\delta E_{tot} = E_{tot}(\mathbf{m} + \delta \mathbf{m}) - E_{tot}(\mathbf{m})$ .

The variation of the exchange energy term can be determined knowing that, for a scalar  $\lambda$  and a vector  $\mathbf{v}$  one has  $\delta(\nabla \lambda)^2 = 2 \nabla \lambda \cdot \nabla(\delta \lambda)$  and  $\nabla \cdot (\lambda \mathbf{v}) = \nabla \lambda \cdot \mathbf{v} + \lambda \nabla \cdot \mathbf{v}$ , and therefore  $\delta E_{ex}$  is:

$$\delta E_{ex} = \int_{V_m} 2 A_{ex} [\nabla m_x \cdot \nabla \delta m_x + \nabla m_y \cdot \nabla \delta m_y + \nabla m_z \cdot \nabla \delta m_z] dV \quad (\text{I.27})$$

Then replacing

$$\nabla m_x \cdot \nabla \delta m_x = \nabla \cdot (\delta m_x \nabla m_x) - \delta m_x \Delta m_x \quad (\text{I.28})$$

and using the Gauss (divergence) theorem the exchange term is transformed into the sum of two integrals: one covering the magnetic volume and the second over the surface delimiting it:

$$\int_{V_m} 2A_{ex} \nabla m_x \cdot \nabla \delta m_x dV = \int_{S_m} 2A_{ex} \delta m_x (\nabla m_x \cdot \mathbf{n}) dS - \int_{V_m} 2A_{ex} \delta m_x \Delta m_x dV \quad (\text{I.29})$$

Finally  $\delta E_{ex}$  reads as:

$$\delta E_{ex} = \int_{S_m} 2A_{ex} \delta \mathbf{m} \cdot (\nabla \mathbf{m} \cdot \mathbf{n}) dS - \int_{V_m} 2A_{ex} \delta \mathbf{m} \cdot \Delta \mathbf{m} dV \quad (\text{I.30})$$

The variation of the next two terms poses no problems:

$$\delta E_{anis} = - \int_{V_m} 2K_{anis} (\mathbf{u}_K \cdot \mathbf{m}) (\mathbf{u}_K \cdot \delta \mathbf{m}) dV \quad (\text{I.31})$$

$$\delta E_{app} = - \int_{V_m} \mu_0 M_s \delta \mathbf{m} \cdot \mathbf{H}_{app} dV \quad (\text{I.32})$$

Finally keeping in mind that:  $\int_{V_m} \delta \mathbf{m} \cdot \mathbf{H}_{dem} dV = \int_{V_m} \mathbf{m} \cdot \delta \mathbf{H}_{dem} dV$ , the demagnetizing term is easily derived:

$$\delta E_{dem} = - \int_{V_m} \mu_0 M_s \delta \mathbf{m} \cdot \mathbf{H}_{dem}(\mathbf{m}) dV \quad (\text{I.33})$$

Putting together the components, the first variation of the total energy  $\delta E_{tot}$  reads as:

$$\begin{aligned} \delta E_{tot} = & \int_{S_m} 2A_{ex} \delta \mathbf{m} \cdot \frac{\partial \mathbf{m}}{\partial \mathbf{n}} dS \\ & - \int_{V_m} \mu_0 M_s \delta \mathbf{m} \cdot \left[ -\frac{2A_{ex}}{\mu_0 M_s} \Delta \mathbf{m} + \frac{2K_{anis}}{\mu_0 M_s} (\mathbf{u}_K \cdot \mathbf{m}) \mathbf{u}_K + \mathbf{H}_{app} + \mathbf{H}_{dem}(\mathbf{m}) \right] dV \end{aligned} \quad (\text{I.34})$$

To obtain the equilibrium condition, both the surface and volume integrals are set to 0. Using the constraint on the magnetization  $|\mathbf{m}|^2=1$ ,  $\delta \mathbf{m}$  is  $\delta \mathbf{m} = \delta \boldsymbol{\theta} \times \mathbf{m}$ , with  $\delta \boldsymbol{\theta}$  an infinitesimal rotation of the magnetization. The scalar product in the surface integral becomes then:

$$\int_{S_m} 2A_{ex} \delta \mathbf{m} \cdot \frac{\partial \mathbf{m}}{\partial \mathbf{n}} dS = \int_{S_m} 2A_{ex} \left( \mathbf{m} \times \frac{\partial \mathbf{m}}{\partial \mathbf{n}} \right) \cdot \delta \boldsymbol{\theta} dS \quad (\text{I.35})$$

and the resulting equilibrium condition is:

$$\frac{\partial \mathbf{m}}{\partial \mathbf{n}} = 0 \quad (\text{I.36})$$

valid on the magnetic surface  $S_m$ . In the volume integral, noting:

$$\mathbf{H}_{\text{eff}} = -\frac{2A_{ex}}{\mu_0 M_s} \Delta \mathbf{m} + \frac{2K_{anis}}{\mu_0 M_s} (\mathbf{u}_K \cdot \mathbf{m}) \mathbf{u}_K + \mathbf{H}_{\text{app}} + \mathbf{H}_{\text{dem}}(\mathbf{m}) \quad (\text{I.37})$$

the effective field, the second equilibrium condition - *the torque condition* - is obtained:

$$\mathbf{m} \times \mathbf{H}_{\text{eff}} = 0 \quad (\text{I.38})$$

The effective field is proportional to the variational derivative of the total energy density:

$$\mathbf{H}_{\text{eff}} = -\frac{1}{\mu_0 M_s} \frac{\delta \mathcal{E}_{\text{tot}}}{\delta \mathbf{m}} \quad (\text{I.39})$$

Because of the constraint on the magnetization amplitude (I.1) the field component along  $\mathbf{m}$  plays no role.

Conditions (I.36) and (I.38) were deduced by Brown [Brown 1963], and therefore are called the *Brown equations*. Their solution specifies the equilibrium state. The first one is a Neumann boundary condition, which forces the magnetization to be stationary near the free surface  $S_m$ . The second equation states that for a magnetization distribution to be at equilibrium, the torque from the effective field acting on  $\mathbf{m}$  must be nil everywhere.

### 1.3. The Landau-Lifshitz-Gilbert equation

The Brown equations (I.36) and (I.38) are enough to define the equilibrium state of a magnetic system, but they do not specify how the system reaches this state. The magnetization dynamics can be accessed through the *Landau-Lifshitz-Gilbert equation*. The starting point in deducing this equation is:

$$\frac{\partial \mathbf{M}}{\partial t} = -\gamma \mathbf{M} \times \mu_0 \mathbf{H}_{\text{eff}} \quad (\text{I.40})$$

describing the magnetization's gyrotropic reaction in the presence of the field  $\mathbf{H}_{\text{eff}}$ .  $\gamma$  is the gyromagnetic ratio of the free electron ( $1.7608592 \cdot 10^{11} \text{ s}^{-1} \text{ T}^{-1}$ ). From (I.40) the torque from the field  $\mathbf{H}_{\text{eff}}$  induces a rotation of  $\mathbf{M}$ , with an angular velocity  $\omega = \gamma \mu_0 \mathbf{H}_{\text{eff}}$ . In this precessional motion, the modulus and the component of  $\mathbf{M}$  along the field  $\mathbf{H}_{\text{eff}}$  do not change. Consequently the energy of the system is constant.

The second Brown condition imposes zero torque from the effective field on  $\mathbf{M}$  at equilibrium. Equation (I.40) in its present form cannot describe the dissipation process resulting in a parallel alignment of  $\mathbf{H}_{\text{eff}}$  and  $\mathbf{M}$ . To include the relaxation of  $\mathbf{M}$  towards the equilibrium state, Gilbert added to the effective field a supplementary contribution,  $-\frac{\alpha}{\gamma \mu_0 M_s} \frac{\partial \mathbf{M}}{\partial t}$ , derived based on a Rayleigh dissipation functional approach [Gilbert 2004].

The resulting dynamic equation read as:

$$\frac{\partial \mathbf{M}}{\partial t} = -\gamma \mu_0 (\mathbf{M} \times \mathbf{H}_{\text{eff}}) + \frac{\alpha}{M_s} \left( \mathbf{M} \times \frac{\partial \mathbf{M}}{\partial t} \right) \quad (\text{I.41})$$

This equation is called the Gilbert or Landau-Lifshitz-Gilbert (LLG hereafter) equation and  $\alpha$  is the dimensionless damping parameter. According to this equation, the magnetization turns around the effective field having a damped movement (Figure I.4 b). Without damping the precession of the magnetization would go on endlessly (Figure I.4 a). The damping term controls the extent of this precession: the smaller the value of  $\alpha$  - the longer it takes for the system to arrive at equilibrium. The Gilbert form of the dynamic equation can be easily transformed [Mallinson 1987] into the previously determined Landau-Lifshitz form [Landau-Lifshitz 1935]:

$$(1 + \alpha^2) \frac{\partial \mathbf{M}}{\partial t} = -\gamma (\mathbf{M} \times \mu_0 \mathbf{H}_{\text{eff}}) - \frac{\alpha \gamma}{M_s} [\mathbf{M} \times (\mathbf{M} \times \mu_0 \mathbf{H}_{\text{eff}})] \quad (\text{I.42})$$

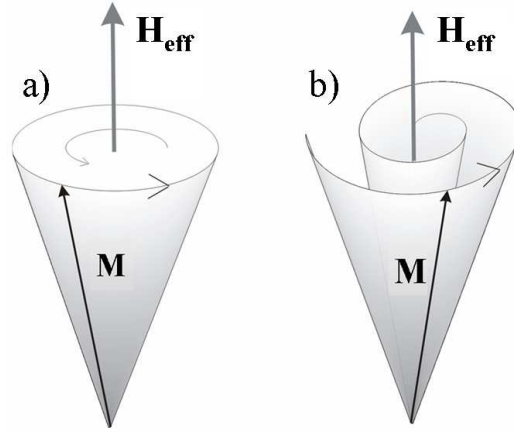


Figure I.4: a) Precession of the magnetization vector  $\mathbf{M}$  around the field  $\mathbf{H}_{\text{eff}}$  without damping ( $\alpha=0$ ) and damped motion ( $\alpha>0$ ).

In a relaxation process, in the presence of a constant applied field, the total energy of a magnetic system can only decrease, the energy dissipation rate being:

$$\frac{dE_{\text{tot}}}{dt} = -\mu_0 \int_{V_m} \mathbf{H}_{\text{eff}} \cdot \frac{\partial \mathbf{M}}{\partial t} dV. \quad (\text{I.43})$$

Multiplying the LLG equation, by  $\mathbf{H}_{\text{eff}}$  and, respectively by  $\partial \mathbf{M} / \partial t$  results in:

$$\mathbf{H}_{\text{eff}} \cdot \frac{\partial \mathbf{M}}{\partial t} = -\frac{\alpha}{M_s} \frac{\partial \mathbf{M}}{\partial t} \cdot (\mathbf{M} \times \mathbf{H}_{\text{eff}}) \quad \text{and} \quad \frac{\partial \mathbf{M}}{\partial t} \cdot (\mathbf{M} \times \mathbf{H}_{\text{eff}}) = -\frac{1}{\gamma \mu_0} \left( \frac{\partial \mathbf{M}}{\partial t} \right)^2 \quad (\text{I.44})$$

Combining these relationships and then introducing the result in (I.43), the rate of change of the system's total energy is:

$$\frac{dE_{\text{tot}}}{dt} = -\frac{\alpha}{\gamma M_s} \int_{V_m} \left( \frac{\partial \mathbf{M}}{\partial t} \right)^2 dV \quad (\text{I.45})$$

This is a very important property of the LLG equation as it guarantees a proper evolution towards the equilibrium state corresponding to the minimum of the total energy. Setting the damping parameter to 0, the energy of the system is preserved just as expected in the case of a Larmor precession of the magnetization around the effective field.

The form (I.41) of the dynamic equation is suitable for describing the evolution of a micromagnetic system when being under the influence of an external field. However, since the first evidence of the effect of an electric current on the magnetization, this phenomenon attracted more and more interest. In order to describe this new kind of interaction, the LLG

equation has to be adapted. The numerous theoretical showed that introducing in LLG two new torques an appropriate description of this phenomenon is obtained. Obviously, the list of physical phenomena that can be coupled with micromagnetic studies does not stop here. For example, a very interesting and absolutely necessary step in understanding the behavior of a magnetic body is the study of thermal effects.



#### 1.4. Towards numerical micromagnetism

The above presented micromagnetic equations (the Brown and the LLG equations) are nonlinear and non-local equations. Nonlinearities arise because of the constraint  $|\mathbf{m}|^2=1$  and also if higher order components of the magnetocrystalline anisotropy energy are taken into account. The non-local character has its source in the definition of the demagnetizing field. All these make the micromagnetic equations difficult to solve. Analytical solutions are known for only a few simple cases, none of them including non-uniform magnetization distributions. For example, nucleation processes have been described in [Brown 1957, Frei 1957, Aharoni 1963, Eisenstein 1976, Ramesh 1988], whereas in [Stoner-Wohlfarth 1948, Kikuchi 1956, Albuquerque 2001] the *macrospin* approximation was employed. In most of the cases solutions are sought numerically.

From a numerical point of view, if one is interested in determining only the equilibrium state of a certain magnetic body, putting aside its dynamic behavior, one proceeds to the minimization of the total energy. For example, in [LaBonte 1969, Jakubovics 1991, Trouilloud 1987] iterative methods are used. Another possibility - giving information also about the relaxation process - consists in solving the LLG equations. It is important to note that in theoretical and numerical calculations the Gilbert damping parameter is considered to have a constant value over the sample, although there are no experimental proofs for this assumption. It is almost certain that  $\alpha$  depends in an undetermined (and most likely non-linear) fashion on the magnetization distribution. From ferromagnetic resonance experiences and domain wall velocity measurements it has been determined that  $\alpha$  takes values in the interval  $[10^{-4}, 10^{-1}]$ . For dynamic simulations, realistic values for the damping parameter have to be used, whereas to get the same outcome as from energy minimization, one can solve the LLG equations using high values of the damping parameter (over-damped regime), for example 1 or even higher.

An important remark has to be made concerning numerical techniques. These methods are based on splitting up the magnetic system into small discretization cells, the micromagnetic equations being solved for each of these discretization elements. The choice discretization elements' size is very important, as it influences very much the accuracy of the result. The correct value is selected based on a physical criterion. This

selection rule was established based on the hypothesis that, in micromagnetism the exchange interaction is considered to be the leading one, the other interactions being viewed as perturbations. Therefore, when choosing the space step one has to take into account the extent over which the second order interactions perturb the equilibrium that would be imposed by the exchange field. There are two characteristic lengths that serve as reference [Hubert 1998]: the *exchange length* ( $l_{ex}$ ) - quantifying the competition between the exchange and magnetostatic interaction - and the *Bloch length* ( $l_B$ ) - the measure of the competition between exchange and magnetocrystalline interaction:

$$l_{ex} = \sqrt{\frac{2A_{ex}}{\mu_0 M_s^2}} \quad \text{and} \quad l_B = \sqrt{\frac{A_{ex}}{K_{anis}}} \quad (\text{I.46})$$

Making use of these two quantities, a rule of thumb was established: in micromagnetic simulations the maximum discretization element must be smaller than the minimum of these two characteristic lengths.

## References

- [**Aharoni 1963**] A. Aharoni, “Complete eigenvalue spectrum for the nucleation in a ferromagnetic prolate spheroid”, *Phys. Rev.* 131, 1478 (1963).
- [**Albuquerque 2001**] G. Albuquerque, J. Miltat, A. Thiaville, “Self-consistency based control scheme for magnetization dynamics”, *J. Appl. Phys.* 89, 6791 (2001).
- [**Brown 1963**] W. F. Brown, Jr., “Micromagnetics”, Interscience Publishers, J. Wiley and Sons, New York, 1963.
- [**Brown 1957**] W. F. Brown, Jr., “Criterion for uniform micromagnetization”, *Phys. Rev.* 105, 1479 (1957).
- [**Buschow 2003**] K. H. J. Buschow, F. R. de Boer, “Physics of magnetism and magnetic materials”, Kluwer Academic/Plenum Publishers, New York, 2003.
- [**Gilbert 2004**] T. L. Gilbert, Armour Research Report (1956). T. L. Gilbert, “A phenomenological theory of damping in ferromagnetic materials”, *IEEE Trans. Magn.* 40, 3443 (2004).
- [**Hubert 1998**] A. Hubert, R. Schafer, “Magnetic domains”, Springer, New York, 1998.
- [**Jackson 1999**] J. D. Jackson, “Classical electrodynamics”, 3rd ed., Wiley, New York, 1999.
- [**Jakubovics 1991**] J. P. Jakubovics, “Interaction of Bloch-wall pairs in thin ferromagnetic films”, *J. Appl. Phys.* 69, 4029 (1991).
- [**Eisenstein 1976**] I. Eisenstein, A. Aharoni, “Magnetization curling in a sphere”, *J. Appl. Phys.* 47, 321 (1976).
- [**Frei 1957**] E. H. Frei, S. Shtrikman, D. Treves, “Critical size and nucleation field of ideal ferromagnetic particles”, *Phys. Rev.* 106, 446 (1957).
- [**Kikuchi 1956**] R. Kikuchi, “On the minimum of magnetization reversal time”, *J. Appl. Phys.* 27, 1352 (1956).

[**LaBonte 1969**] A. E. LaBonte, “Two-dimensional Bloch-type domain walls in ferromagnetic films”, J. Appl. Phys. 40, 2450 (1969).

[**Landau-Lifshitz 1935**] L. D. Landau, E. M. Lifshitz, “On the theory of the dispersion of magnetic permeability in ferromagnetic bodies”, Phys. Z. Sowjet. 8, 153 (1935).

[**Mallinson 1987**] J. Mallinson, “On the damped gyromagnetic precession”, IEEE Trans. Magn. 23, 2003 (1987).

[**Miltat 1994**] J. Miltat, “Domains and domains walls in soft magnetic materials, mostly”, in Applied Magnetism, NATO ASI Series, Dordrecht: Kluwer, 221, 1994.

[**Ramesh 1988**] M. Ramesh, P. E. Wigen, “Ferromagnetic resonance of parallel stripe domains-domain walls system”, J. Magn. Magn. Mat. 74, 123 (1988).

[**Stoner-Wohlfarth**] E. C. Stoner, E. P. Wohlfahrt, “A mechanism of magnetic hysteresis in heterogeneous alloys”, Phil. Trans. Roy. Soc. A240, 599 (1948).

[**Trouilloud 1987**] P. Trouilloud, J. Miltat, “Néel lines in ferrimagnetic garnet epilayers with orthorhombic anisotropy and canted magnetization”, J. Magn. Magn. Mat. 66, 194 (1987).

[**Weiss 1907**] P. Weiss, “L’hypothèse du champ moléculaire et la propriété ferromagnétique”, J. Phys. 6, 401 (1907).



## II. Numerical micromagnetism

In the present work we are interested in solving the Landau-Lifshitz-Gilbert (LLG) partial differential equation (PDE) describing magnetization dynamics. The complexity of the LLG equation limited the number of analytical solutions, the tendency being to use numerical methods to determine approximate solutions.

There are two widely used methods: the *finite difference* (FD) approximation and the *finite element* (FE) approximation [Fidler 2000]. The FD approximation is widespread because it is easy to implement and fast [Schabes 1988, Nakatani 1989, Zhu 1989, Scheinfein 1991, Berkov 1993, Kevorkian 1998, Buda 2001, OOMMF-site] due to the possibility of computing the demagnetizing field using the Fast Fourier transforms [Masuripur 1988, FFTW-site]. The FE method is a very effective numerical tool, especially in engineering problems involving complex geometries. In micromagnetism it is less used [Fredkin 1987, Bagnères 1991, Schrefl 1999, Fidler 2000] than the FD method, mostly because of the complex mathematical apparatus [Braess 2001] that it is founded on.

The FD method solves a discrete form of the LLG equation, while in the case of the FE approximation an integral formulation is associated problem. In the first method the system is space-discretized by repetition of some regular-shaped mesh cell. The periodic discretization makes possible the replacement of the derivatives occurring in the LLG equation with expressions derived from a Taylor expansion. The method is therefore very easy to implement, but the accuracy of the solution can be affected if complex boundaries delimitate the domain [García-Cervera 2003]. The FE approximation uses an irregular discretization. Due to this, the theory behind the FE is much more complicated than the basis of the FD approximation, but the method is not restricted with respect to the geometry shape.

The present chapter is dedicated to the presentation of the two numerical methods:

1. The FD-based GL\_FFT micromagnetic code, developed by Brandusa Kevorkian at the Néel Institute in 1998 under the supervision of JC Toussaint [Kevorkian 1998], is shortly presented in the first part.
2. Then a description of the FE method is given, followed by a first FE approach developed for the LLG equation, presented together with the results obtained for two test cases. The FE results are always compared with those obtained by the GL\_FFT software. In the last part of the chapter, the details and results obtained with a second FE approach are presented.

### II.1. The finite difference method

In this part, the space discretization and the relationships that determine the effective field in the FD-based GL\_FFT micromagnetic software are given.

The first step in numerical calculations is to divide the magnetic system in small cells, procedure called *space-discretization* or *meshing*. The type of cells used is very important as it has great influence on the manner in which the equation is solved. In the case of the FD approach, the simulated systems are divided into regular discretization units (cubic, hexagonal, orthorhombic).

The space discretization in a bi-dimensional system contains  $N_x$  cells along the Ox direction and  $N_y$  cells along the Oy direction. The mesh cells are prisms with rectangular cross section, covering the surface  $\delta_x\delta_y$  (infinite along the Oz direction). For the 3D systems, the mesh consists of  $N_x \times N_y \times N_z$  orthorhombic cells having each the volume  $\delta_x\delta_y\delta_z$ . A 2D and a 3D example of meshing is shown in Figure II.1:

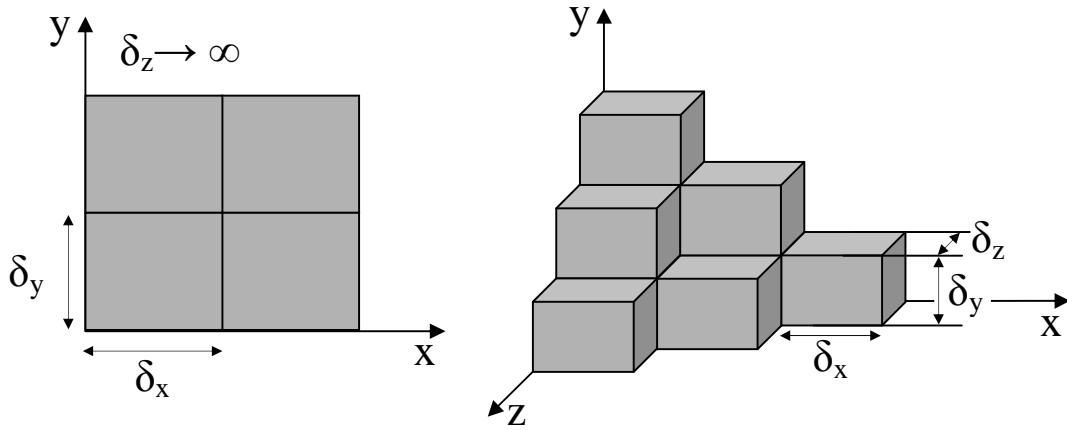


Figure II.1: 2D and 3D finite difference discretization

The evaluation of the magnetization is done in the centre of each cell:

$$x_i = \left(i - \frac{1}{2}\right)\delta_x \quad y_j = \left(j - \frac{1}{2}\right)\delta_y \quad z_k = \left(k - \frac{1}{2}\right)\delta_z \quad (\text{II.1})$$



where  $i \in \{1, \dots, N_x\}$ ,  $j \in \{1, \dots, N_y\}$  and  $k \in \{1, \dots, N_z\}$ . Based on this space-discretization, the vector field  $\mathbf{m}(\mathbf{r})$ ,  $\mathbf{r} \in V_m$ , solution of the LLG equation is in fact the magnetization distribution  $\{\mathbf{m}(i,j,k)\}$  satisfying in each mesh node  $|\mathbf{m}(i,j,k)|^2=1$ .

To find the magnetic equilibrium state, one has to evaluate the field and energy terms. The estimation of the magnetocrystalline anisotropy and the applied field energy, which are simple, local terms, is straightforward. On the other hand, the exchange field requires the estimation of the second-order derivatives of the magnetization and the demagnetizing field is also requires a special treatment.

To calculate the first and second order magnetization derivatives the GL\_FFT software uses the *centered differences approximation*, derived based on the Taylor expansion of the magnetization. For example, in a 2D case, using the grid in Figure II.2, the Taylor expansion of the magnetization gives:

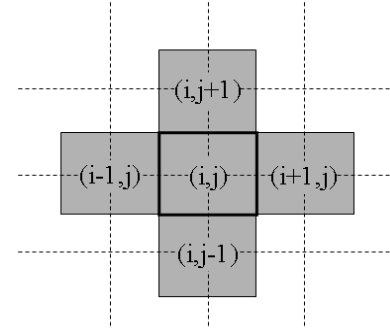


Figure II.2: Regular 2D grid

$$\begin{aligned} \mathbf{m}(i+1, j) &= \mathbf{m}(i, j) + \delta_x \frac{\partial \mathbf{m}}{\partial x}(i, j) + \frac{1}{2} \delta_x^2 \frac{\partial^2 \mathbf{m}}{\partial x^2}(i, j) + O(\delta_x^3) \\ \mathbf{m}(i-1, j) &= \mathbf{m}(i, j) - \delta_x \frac{\partial \mathbf{m}}{\partial x}(i, j) + \frac{1}{2} \delta_x^2 \frac{\partial^2 \mathbf{m}}{\partial x^2}(i, j) + O(\delta_x^3) \end{aligned} \quad (\text{II.2})$$

The first and second order derivatives, and also the Laplacian of the magnetization can now be evaluated:

$$\begin{aligned} \frac{\partial \mathbf{m}}{\partial x}(i, j) &\cong \frac{\mathbf{m}(i+1, j) - \mathbf{m}(i-1, j)}{2\delta_x} \\ \frac{\partial^2 \mathbf{m}}{\partial x^2}(i, j) &\cong \frac{\mathbf{m}(i+1, j) - 2\mathbf{m}(i, j) + \mathbf{m}(i-1, j)}{\delta_x^2} \\ \Delta \mathbf{m} &\cong \frac{\mathbf{m}(i+1, j) - 2\mathbf{m}(i, j) + \mathbf{m}(i-1, j)}{\delta_x^2} + \frac{\mathbf{m}(i, j+1) - 2\mathbf{m}(i, j) + \mathbf{m}(i, j-1)}{\delta_y^2} \end{aligned} \quad (\text{II.3})$$

These relationships are applicable to the nodes situated inside the magnetic volume. For the points situated on the surface one has to make sure that the first Brown equation (see equation (I.36)), assuring the stationarity of the magnetization is respected.

Bearing these in mind, we proceed to the definition of each discrete energy and field for a bi-dimensional case.

#### *The exchange energy*

Replacing the Laplacian of the magnetization with the formula derived from the Taylor expansion the exchange field is:

$$\mathbf{H}_{\text{ex}}(i, j) = \frac{2A_{\text{ex}}}{\mu_0 M_s} \left[ \frac{\mathbf{m}(i+1, j) - 2\mathbf{m}(i, j) + \mathbf{m}(i-1, j)}{\delta_x^2} + \frac{\mathbf{m}(i, j+1) - 2\mathbf{m}(i, j) + \mathbf{m}(i, j-1)}{\delta_y^2} \right] \quad (\text{II.4})$$

In addition, the exchange energy is:

$$E_{\text{ex}} = \frac{A_{\text{ex}} \delta_x \delta_y}{4} \sum_{i,j} \sum_{l=x,y,z} \frac{1}{\delta_x^2} [m_l(i+1, j) - m_l(i-1, j)]^2 + \frac{1}{\delta_y^2} [m_l(i, j+1) - m_l(i, j-1)]^2 \quad (\text{II.5})$$

with  $i \in \{1, \dots, N_x\}, j \in \{1, \dots, N_y\}$ .

#### *The magnetocrystalline anisotropy contribution*

In the case of uniaxial symmetry, the anisotropy field and the anisotropy energy can be written as:

$$\mathbf{H}_{\text{anis}}(i, j) = \frac{2K_{\text{anis}}}{\mu_0 M_s} [\mathbf{m}(i, j) \cdot \mathbf{u}_{\mathbf{K}}(i, j)]_{ij} \mathbf{u}_{\mathbf{K}}(i, j) \quad (\text{II.6})$$

$$E_{\text{anis}} = \sum_{i,j} K_{\text{anis}} \left\{ 1 - [\mathbf{m}(i, j) \cdot \mathbf{u}_{\mathbf{K}}(i, j)]^2 \right\} (\delta_x \delta_y) \quad (\text{II.7})$$

with  $i \in \{1, \dots, N_x\}$  and  $j \in \{1, \dots, N_y\}$ .

#### *The applied field energy*

After the discretization of the simulated system, the applied field energy takes the discrete form:

$$E_{\text{app}} = -\mu_0 M_s \sum_{i,j} [\mathbf{m}(i, j) \cdot \mathbf{H}_{\text{app}}(i, j)] (\delta_x \delta_y) \quad (\text{II.8})$$

where  $i \in \{1, \dots, N_x\}, j \in \{1, \dots, N_y\}$ .

### The demagnetizing term

The long-range character of the magnetostatic interaction makes the evaluation of the associated field the most complicated and time consuming one. However, quite unexpectedly, using the FD approach, this issue can be solved quite easily, namely via the *Fast Fourier transforms*.

The demagnetizing field is the convolution product of the magnetic charge density functions and the gradient of the Green function (see equation (I.22)). The theorem of the convolution gives a helping hand: according to this theorem, the Fourier transform (FT) of the convolution product between two functions,  $f$  and  $g$ , is equal to the ordinary product between their individual FTs:

$$FT(f \otimes g) = FT(f) FT(g) \quad (\text{II.9})$$

Using this property, the demagnetizing field evaluation may be optimized by using the following steps:

1. The FT of  $\nabla G$  is calculated.
2. The magnetic charge distributions are estimated from the magnetization distribution using (II.10), and then, their FTs are calculated.

$$\begin{aligned} \rho_m(i, j) &= - \left( \frac{\partial m_x}{\partial x}(i, j) + \frac{\partial m_y}{\partial y}(i, j) \right) \\ &\equiv - \frac{m_x(i+1, j) - m_x(i-1, j)}{2\delta_x} - \frac{m_y(i, j+1) - m_y(i, j-1)}{2\delta_y} \end{aligned} \quad (\text{II.10})$$

$$\sigma_m(i, j) = \mathbf{m}_{surf}(i, j) \cdot \mathbf{n}$$

3. Some ordinary operations are done in the inverse space and finally, the demagnetizing field is estimated by applying the inverse Fourier transform ( $FT^{-1}$ ):

$$\mathbf{H}_{dem} = FT^{-1} \left[ FT(\nabla G) FT(\rho_m) + FT(\nabla G) FT(\sigma_m) \right] \quad (\text{II.11})$$

As the FD method solves a discrete form of the LLG equation, further optimization can be achieved passing from the *continuous* FT to its *discrete* form. The discrete form of the algorithm is called Fast Fourier transform (FFT) and has the advantage that it reduces

the number of operations [FFTW-site]. Another advantage of this method is that the FT of the  $\nabla G$  is computed only one time at the beginning of the simulation [Kevorkian 1998].

Introducing these in the formula for the demagnetizing energy density one finds:

$$E_{dem} = -\frac{1}{2}\mu_0 M_s \sum_{i,j} [\mathbf{m}(i,j) \cdot \mathbf{H}_{dem}(i,j)] (\delta_x \delta_y) \quad (\text{II.12})$$

### *The Landau-Lifshitz-Gilbert equation*

The GL\_FFT software solves the non-linear LLG equation (I.42). The time integration schemes used for this equation are various: from forward and backward Euler [Nakatani 1989], to Crank-Nicholson [Albuquerque 2001] and to fourth order Runge-Kutta schemes [Ferre 1995, Lopez 1999].

The scheme of integration used in the present FD approach is an explicit method, preserving unconditionally constant the amplitude of the magnetization vector. This scheme was derived replacing  $t$  with  $\tau = \frac{\mu_0 \gamma t}{1 + \alpha^2}$  and noting  $\mathbf{H}(\tau) = \mathbf{H}_{eff}(\tau) + \alpha \mathbf{m}(\tau) \times \mathbf{H}_{eff}(\tau)$ .

The dynamic equation becomes then:

$$\frac{\partial \mathbf{m}}{\partial \tau} = -\mathbf{m}(\tau) \times \mathbf{H}(\tau) \quad (\text{II.13})$$

For sufficiently small time steps, the variation of  $\mathbf{H}$  is also very small, so that  $\mathbf{H}$  can be considered constant. Then, an exact solution of (II.13) can be found, that is in reality the analytical solution of the equation (I.42) without damping.

The series expansion of the magnetization  $\mathbf{m}(t+\delta t)$  as a function of  $\mathbf{m}(t)$  is first written:

$$\begin{aligned} \mathbf{m}(t + \delta t) &= \mathbf{m}(t) + \sum_{n=1}^{\infty} \frac{(\delta t)^n}{n!} \frac{d^n \mathbf{m}}{dt^n} = \\ &= \mathbf{m}(t) + \sum_{p=0}^{\infty} \frac{(\delta t)^{2p+1}}{(2p+1)!} \frac{d^{2p+1} \mathbf{m}}{dt^{2p+1}} + \sum_{p=1}^{\infty} \frac{(\delta t)^{2p}}{(2p)!} \frac{d^{2p} \mathbf{m}}{dt^{2p}} \end{aligned} \quad (\text{II.14})$$

The time derivatives of  $\mathbf{m}(t)$  can be replaced by:

$$\begin{aligned}\frac{d^{2n}\mathbf{m}}{dt^{2n}} &= (-H^2)^{n-1} \frac{d^2\mathbf{m}}{dt^2} = (-H^2)^{n-1} \mathbf{H} \times \frac{d\mathbf{m}}{dt} \\ \frac{d^{2n+1}\mathbf{m}}{dt^{2n+1}} &= (-H^2)^n \frac{d\mathbf{m}}{dt}\end{aligned}\quad (\text{II.15})$$

and the Taylor expansion of the magnetization  $\mathbf{m}(t+\delta t)$  takes the form:

$$\mathbf{m}(t+\delta t) = \mathbf{m}(t) + \sum_{p=0}^{\infty} \frac{(\delta t)^{2p+1}}{(2p+1)!} (-1)^p H^{2p} \frac{d\mathbf{m}}{dt} + \sum_{p=1}^{\infty} \frac{(\delta t)^{2p}}{(2p)!} (-1)^{p-1} H^{2p-2} \mathbf{H} \times \frac{d\mathbf{m}}{dt} \quad (\text{II.16})$$

Finally the following explicit integration scheme is obtained:

$$\begin{aligned}\mathbf{m}(t+\delta t) &= \mathbf{m}(t) \cos(H\delta t) + \frac{\sin(H\delta t)}{H} (\mathbf{H} \times \mathbf{m}(t)) + \\ &+ (1 - \cos(H\delta t)) \frac{\mathbf{m}(t) \cdot \mathbf{H}}{H^2} \mathbf{H}\end{aligned}\quad (\text{II.17})$$

In the case of a constant field, the time integration using this scheme is exact [Kevorkian 1998].

The stability analysis permitted to establish a critical time step related to the space discretization (valid for 2D simulations):

$$\delta\tau = \frac{\mu_0 M_S}{8A_{ex}} \left( \frac{1}{\delta_x^2} + \frac{1}{\delta_y^2} \right)^{-1} \frac{2\alpha}{\alpha^2 + 1} \quad (\text{II.18})$$

At equilibrium the torque on the magnetization should be 0 in each discretization cell. From a numerical point of view, the 0-torque requirement is replaced by a more suitable one, namely the equilibrium state is considered to be reached, when the maximum of  $(\mathbf{m} \times \mathbf{H}_{\text{eff}})/M_S$  is smaller than  $10^{-6}$  rad [Kevorkian 1998].

To synthesize this paragraph, the flowchart of the GL\_FFT software is presented in Figure II.3. The first step is the initialization where the geometrical and the material parameters are given, together with the initial magnetization distribution. Then the energy terms and the surface and volume charges are calculated, and finally the effective field is obtained. This is then introduced in the LLG equation. After solving it, the criterion of  $(\mathbf{m} \times \mathbf{H}_{\text{eff}})/M_S < 10^{-6}$  rad is verified. If fulfilled, the equilibrium state is determined and the simulation stops. Otherwise, the simulation advances to the next time step.

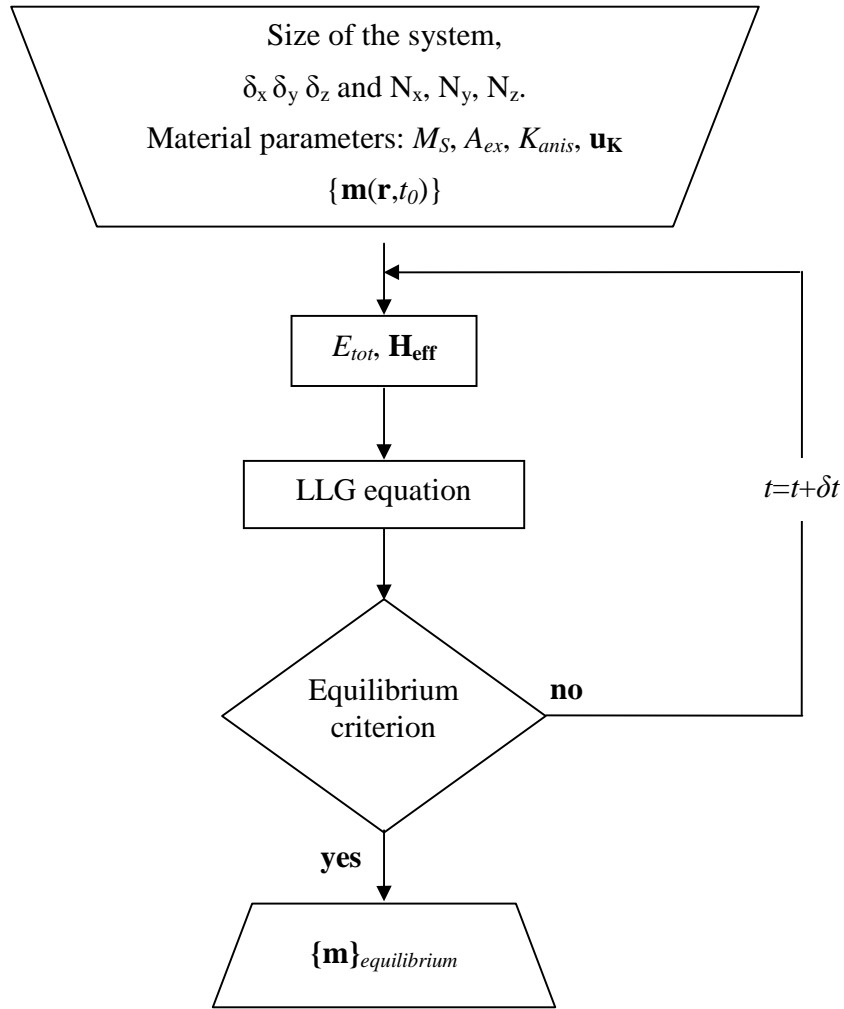


Figure II.3: Flowchart of the GL\_FFT software.

## II.2. The finite element method

The origins of the FE method lay in the need of solving complex engineering problems. To its development contributed mathematicians, physicists and engineers. In 1943 Courant [Courant 1943] published the first example of a FE approach based on piecewise continuous functions defined on triangular domains. Although his work differs very much from the FE method use nowadays, it is considered to be revolutionary, as it constitutes to the base of the modern FE approach, developed by scientists as Rayleigh, Ritz and Galerkin.

Nowadays the FE method has become a well established method, used fruitfully in elastic and thermal problems, in hydrodynamics, electromagnetics, etc. The FE method uses an integral formulation of the PDE [Braess 2001, Vermolen 2008, Mish 2000]. To obtain such a formulation two possible paths can be followed. Let us exemplify on a simple 1D pedagogical problem. The solution  $u$  of the following PDE is sought:

$$\frac{d^2u}{dx^2} = f(x) \quad (\text{II.19})$$

defined on an interval  $[a, b]$ , where  $u$  has two continuous derivatives ( $u \in C^2[a, b]$ ) and  $f(x)$  is a given continuous function. Equation (II.19) together with the boundary condition  $u(a)=u(b)=0$  forms the so-called *strong form* of the problem, the corresponding solution being called *strong solution*. In the first formalism proposed by Ritz and Rayleigh [Mish 2000], a functional is defined, that is in fact the integral of the PDE itself. For the PDE given in (II.19), this functional reads as:

$$\Pi(u) = \frac{1}{2} \int_a^b \left( \frac{du}{dx} \right)^2 dx + \int_a^b f u dx \quad (\text{II.20})$$

The solution of (II.19) is the function  $u(x)$  that minimizes (II.20).

The second way of determining the solution of a PDE is to seek for the solution of the following integral form:

$$\int_a^b \left( \frac{du}{dx} \frac{dw}{dx} + f w \right) dx = 0 \quad (\text{II.21})$$

This form was obtained by multiplying the initial PDE by so-called *test functions*,  $w$  (with  $w(a)=w(b)=0$ ), and then integrating over the corresponding domain [Braess 2001, Vermolen 2008]. Equations like (II.21) are called *weak formulations*. The nomenclature can be easily explained: using the integral form of the PDE, certain smoothness requirements on the solution are weakened, and consequently a *weak solution* is found. In the simple example presented above, the strong solution  $u$  is a  $C^2$  function, whereas the solution of (II.21) has to be square integrable, to assure the existence of the integral (the same is true for the test function  $w$ ). The main advantage of the weak form is that it can easily provide solutions for real world problems, even in cases when a strong solution cannot be defined in a classical (non-distributional) framework, leaving the integral form as the only possible way of solving the problem. Moreover, knowing that the weak form is solved by numerical means; a second advantage arises since the integral forms are better-conditioned numerical operations than differential ones.

This second approach, called *Galerkin method*, is more general than the first one, as a weak formulation can always be written, whereas to define a functional, the operators occurring in the PDE have to meet certain mathematical symmetry conditions, e.g. they have to be positive definite and self-adjoint [Vermolen 2008], to assure the equivalence between the integral and differential form. However when both integral forms are foreseeable their discrete solutions will be the same.

Once the wanted integral formulation is determined, in both methods (the Ritz-Rayleigh and the Galerkin method) the same steps are followed. The integral equation has to be transformed into a discrete one. This is carried out by approximating the solution, in the present example  $u$ , using approximation functions that are related to the spatial discretization of the domain of solution. An equation is obtained for every mesh element. Assembling these results in a matrix equation, that provides the solution of the PDE on the domain of definition.

In the following we present in detail the Galerkin method. The solving process can be divided into three steps:



1. First the weak form of the equation is established.
2. The domain  $\Omega$  on which the problem is defined is discretized into a number  $N_e$  of small elements, the so-called finite elements. The integral over  $\Omega$  can then be written as the sum of the integrals over each finite element. Moreover, due to the discretization the solution in each element is interpolated.
3. Next, the system obtained by putting together all the element-equations is solved. In the assembling process one takes into account the connections (common nodes) between the elements. The solution for the initial PDE is therefore determined.

The purpose of this work is to apply the FE method to solve the LLG equation numerically. This equation plays a very important role as it describes the damped motion of the magnetization around the effective field that acts on it. Because of the special treatment required by the demagnetizing field, the solving procedure is divided in two parts at each time step:

1. First the magnetostatic part is solved.
2. The LLG equation is then integrated.

Following the steps in the resolution of the LLG equation, we apply in the first part the FE method to the demagnetizing problem, and then to the LLG equation itself.

### II.2.1. Magnetostatic problem

As described in the paragraph I.2, the demagnetizing field can be determined using either a magnetic scalar potential or a magnetic vector potential approach. When the former approach is used the demagnetizing field is the gradient of the scalar potential  $\Phi$  (see equation (I.15)), the latter one being the solution of the Poisson equation (see equation (I.16)).

#### *Weak formulation*

In the magnetic scalar potential approach, the magnetic induction  $\mathbf{B}$  is expressed as:

$$\mathbf{B} = \mu_0 (-\nabla\Phi + \mathbf{M}) \quad (\text{II.22})$$

The FE approach will be applied to:

$$\nabla \cdot \mathbf{B} = \nabla \cdot (-\nabla\Phi + \mathbf{M}) = 0 \quad (\text{II.23})$$

The weak form of (II.23) is derived by multiplying it by a scalar test function  $\omega$  and integrating the obtained equation over  $V$ , where  $V$  is the domain made up from the magnetic volume  $V_m$  and the surrounding vacuum:

$$\int_V \omega \nabla \cdot (-\nabla\Phi + \mathbf{M}) dV = 0 \quad (\text{II.24})$$

This term can be rewritten as:

$$\int_V \omega \nabla \cdot (-\nabla\Phi + \mathbf{M}) dV = \int_V \nabla \cdot [\omega(-\nabla\Phi + \mathbf{M})] dV - \int_V \nabla \omega \cdot (-\nabla\Phi + \mathbf{M}) dV \quad (\text{II.25})$$

The first volume integral in the right-hand side can be transformed into a surface integral, using the Gauss theorem:

$$\int_V \nabla \cdot [\omega(-\nabla\Phi + \mathbf{M})] dV = \int_S \omega [(-\nabla\Phi + \mathbf{M}) \cdot \mathbf{n}] dS \quad (\text{II.26})$$

By using the continuity conditions of the normal component of the induction at the interfaces and surfaces (see equations (I.14)), this term is eliminated:

$$\int_{\{S\}} \omega [(-\nabla\Phi + \mathbf{M}) \cdot \mathbf{n}] dS = \int_{\{S\}} \omega \mathbf{B} \cdot \mathbf{n} dS = \int_S \omega (\mathbf{B}_{\text{int}} - \mathbf{B}_{\text{ext}}) \cdot \mathbf{n} dS = 0 \quad (\text{II.27})$$

The weak form of the demagnetizing problem is then simplified:

$$\int_V \nabla \omega \cdot \nabla \Phi \, dV = \int_V \nabla \omega \cdot \mathbf{M} \, dV \quad (\text{II.28})$$

Comparing (II.23) and (II.28), a first advantage of writing a weak formulation is revealed. In the first case, the solution of must be in  $C^2(V)$ , as  $\Delta\Phi = \nabla \cdot \nabla\Phi$ . The use of the weak form relaxed this condition, as only the integrability of the first derivative is required. Therefore  $\Phi$  is sought in the Hilbert space  $H^1(V)$  of square-integrable functions defined on the  $V$  domain and whose first derivatives are also square-integrable. The solution space for  $\Phi$  is then  $\{\Phi \in H^1(V): \Phi(\mathbf{r} \rightarrow \infty) \rightarrow 0\}$ , while  $\omega$  is chosen from  $\{\omega \in H^1(V): \omega = 0 \text{ on } \partial V\}$ . These conditions assure the existence of the integral on the left side.

#### *Discretization and resolution*

In the FE procedure we arrived now to the second step: discretization. The integration domain is divided into a set of  $N_e$  elements, characterized by a certain space step. In 2D simulations, the most currently used elements are triangles with either three or six nodes. Based on the  $N$  nodes of the discretization, a set of  $N$  basis (interpolation) functions  $\beta_i$  is selected, that generates a finite subspace of the initial solution space. A discrete form of the weak formulation is then written, by expressing the test function and the solution as:

$$\begin{aligned} \omega &= \beta_i(\mathbf{r}) \\ \Phi &= \sum_{j=1}^N \phi_j \beta_j(\mathbf{r}) \end{aligned} \quad (\text{II.29})$$

where  $\phi_j = \phi(\mathbf{r}_j)$ ,  $j \in \{1, \dots, N\}$ .

The next step is to write for each mesh element a local weak form, meaning that all the integrals over the domain  $V$  are transformed into sums of  $N_e$  integrals. Each of the  $N_e$  “small” integrals is exactly determined in the corresponding mesh elements using the

Gaussian integration method. By putting these integrals together a matrix equation is obtained.

In the present case, rewriting the weak formulation (II.28) by taking (II.29) into account, the following equation is obtained:

$$\int_V \nabla \beta_i \phi_j \nabla \beta_j dV = \int_V \nabla \beta_i \cdot \mathbf{m} dV \quad (\text{II.30})$$

with  $i \in \{1, \dots, N\}$ . As one can choose the basis functions and  $\mathbf{m}$  is a given magnetization distribution, the unknowns of (II.30) are the  $\phi_i$  values, representing the nodal values of the scalar potential. Assembling these integrals (by taking into account the eventual common nodes) the following matrix equation is obtained  $A_{ij}\phi_j = b_i$ , with  $A_{ij} = \int_V \nabla \beta_i \cdot \nabla \beta_j dV$  and

$b_i = \int_V \nabla \beta_i \cdot \mathbf{m} dV$ .  $A_{ij}$  is called the *stiffness matrix* and plays a very important role as it can

give a criterion for the choice of the basis functions. In fact  $A_{ij}$  should be as sparse as possible as this would increase the efficiency of the method. To obtain such matrices one can choose basis functions that satisfy:

$$\beta_i(\mathbf{r}_j) = \begin{cases} 1, & i = j \\ 0, & i \neq j \end{cases} \quad (\text{II.31})$$

Figure II.4 shows a schematic representation of such 1D and 2D test functions:

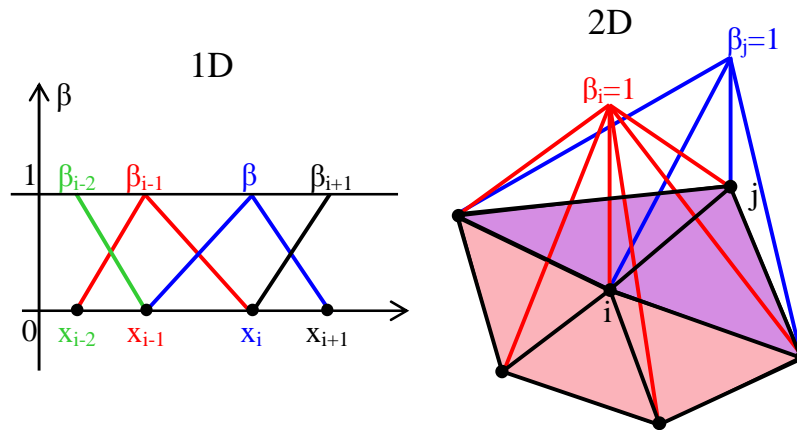
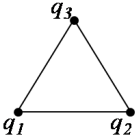
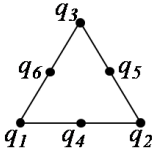


Figure II.4: Schematic representation of 1D and 2D piecewise linear test functions.

In the 2D case, for a mesh consisting of 3-noded triangles our choice for the basis functions were the first order ( $P_1$ ) Lagrange polynomials, whereas for 6-noded triangles second order ( $P_2$ ) Lagrange polynomials were chosen [Braess 2001, Vermolen 2008]. The basis functions and the corresponding mesh elements are listed in the Table II.1. These functions satisfy the above condition (II.31).

Table II.1: First and second order Lagrange basis functions.

type	Number of nodes	The basis function	Element
$P_1$	3	$\beta_j(x,y)=a_j+b_jx+c_jy$ , for $(x,y)\in e$	
$P_2$	6	$\beta_j(x,y)=a_j+b_jx+c_jy+d_jx^2+e_jxy+f_jy^2$ for $(x,y)\in e$	

In the last part of the FE procedure, after the choice of the basis functions has been made, a matrix equation is obtained. To solve it, iterative algorithms are employed, for example the conjugate gradient technique. Thus the magnetic scalar potential, and from it, the demagnetizing field is determined.

#### II.2.1.1. Condition at infinity

In the FE approximation to calculate the demagnetizing field one uses a potential approach. Based on Maxwell's equations, is possible to define both a scalar and a vector potential. The demagnetizing field can be calculated from these quantities through simple derivation. However, one issue comes up, as the problem domain extends to infinity, where the regularity of the potentials is required. It is not clear how one should treat an infinite system using the FE method, as one cannot mesh infinitely. Fortunately, several methods [Bettes 1988, Emson 1988] were proposed to make possible the transformation of such *open boundary problems* into *closed boundary problems*: the truncation method,

ballooning, “infinite” or “mapped” elements, spatial transformations and hybrid methods that couple the FE method with integral methods. In micromagnetism, the truncation method [Chen 1997], spatial transformations [Brunotte 1991, Hertel 2002] and Fredkin and Kohler’s FEM-BEM method [Fredkin 1990, Koehler 1997] are the most widely spread [Scholz 1999, Fidler 2000, Süss 2002, Hertel 2004].

We implemented the truncation method and special spatial transformations to determine the demagnetizing field. Both methods are shortly presented in the following.

#### *The truncation method*

The truncation method consists in moving the boundary of the system at distance that is far enough from the magnetic system. The Dirichlet or Neumann boundary conditions are applied then on this boundary. This is the most basic method that can be used. Unfortunately, there are no rules that can help establishing this distance - “far enough”. Additionally, because of the outside region is several times larger than the magnetic region, the efficiency of the method can be quite reduced. As the limitation on the mesh size is valid only in the magnetic region, the method can be optimized using a coarse mesh in the outside region.

#### *Spatial transformations*

Through spatial transformations the open boundaries are transformed into closed ones. The first such transformations were conformal, limited to 2D Cartesian coordinates and to the Laplace equation. It has been shown [Imhoff 1990a, Imhoff 1990b] that it is not necessary for the transformations to be conformal, and therefore the method can be applied to various geometries and equations. An important feature of the method is that it does not alter the solving procedure imposed by the use of the FE method.

The transformation to use depends very much on the shape of the magnetic system. For simple geometries the *spherical* or the *elliptical shell transformation* is used [Brunotte 1991]. The FE approaches we will describe later are tested on periodic systems and, consequently, one has to use transformations that take into account this feature of the

geometry. That is why in the following part a new type of transformation is developed, adapted specially for the periodic systems studied later.

Consider a film having the thickness  $2h$ , with the magnetization varying as shown in Figure II.5. The magnetic domains have a width of  $d=2a$ . Noting  $T (=2d)$  - the period of the structure, the magnetization distribution can be expanded in Fourier series. If  $O$  is the origin than  $M_y$  is the linear combination of sinusoidal functions:

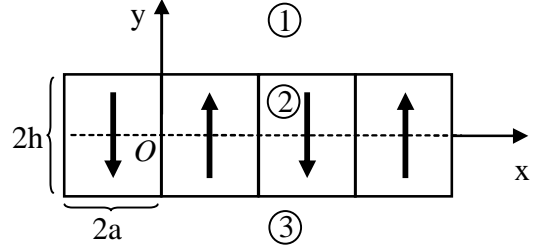


Figure II.5: Schematic representation of a magnetic thin film consisting of periodic "up" and "down" domains.

$$M_y(x) = M_s \sum_{n=0}^{\infty} \frac{4}{\pi} \frac{-1}{2n+1} \sin(k_n x) \quad (\text{II.32})$$

where  $k_n = \frac{2\pi}{T}(2n+1)$ . For a mode  $k$ , with  $M_y(x) = M_k \sin(kx)$ , the generated demagnetizing

field is calculated using the scalar potential  $\Phi(x,y)$ . The boundary conditions for  $\Phi$  are:

1.  $\Phi$  is nil at infinity
2. The continuity conditions (I.18) are adapted for this particular case: if  $y=h$ , at the transition between the regions 1 and 2 one has:

$$\begin{cases} \Phi_1(x, h) = \Phi_2(x, h) \\ \partial_y \Phi_1(x, h) - \partial_y \Phi_2(x, h) = -M_y(x) \end{cases} \quad (\text{II.33})$$

Similar relationships are obtained for the transition from region 2 to 3.

The general solutions of the Laplace equation for a 2D Cartesian problem are well known:

$$\Phi(x, y) = f(y) \cos(kx) + g(y) \sin(kx) \quad (\text{II.34})$$

with  $f$  and  $g$  functions depending on  $y$ . Considering the magnetic charge distribution, several symmetry conditions can be produced:  $\Phi(-x, y) = -\Phi(x, y)$  and  $\Phi(x, -y) = -\Phi(x, y)$ , simplifying the general solution:

$$\Phi(x, y) = g(y) \sin(kx) \quad (\text{II.35})$$

with  $g$  an odd function of  $y$ . Therefore solving the Laplace equation is equivalent to finding  $g(y)$  so that  $\partial_y^2 g(y) - k^2 g(y) = 0$ . In the different regions the solutions of this equation are:

- in region 1:  $g_1(y) = a_1 e^{-ky}$
- in region 2:  $g_2(y) = a_2 \text{sh}(ky)$
- in region 3:  $g_3(y) = -a_1 e^{ky}$

The coefficients  $a_1$  and  $a_2$  are calculated from the continuity conditions for  $y=h$ , and they read as:  $a_1 = \frac{M_k}{k} \text{sh}(kh)$  and  $a_2 = \frac{M_k}{k} e^{-kh}$ .

The scalar potential in the magnetic system is in fact the sum of all the contributions, taken for all the modes  $k$ :

$$\Phi_2(x, y) = \sum_k \frac{M_k}{k} e^{-kh} \text{sh}(ky) \sin(kx) \quad (\text{II.36})$$

The demagnetizing field,  $H_{\text{dem}}$ , is then:

$$\begin{aligned} H_{\text{dem}}(x, y) &= \sum_k -M_k e^{-kh} \begin{cases} \text{sh}(ky) \cos(kx) \\ \text{ch}(ky) \sin(kx) \end{cases} \\ &= M_s \frac{4}{\pi} \sum_{n=0}^{\infty} \frac{-1}{2n+1} e^{-k_n h} \begin{cases} \text{sh}(k_n y) \cos(k_n x) \\ \text{ch}(k_n y) \sin(k_n x) \end{cases} \end{aligned} \quad (\text{II.37})$$

Based on the exponential variation, the space transformation that will cope with the cancellation of  $\Phi$  at infinity can be simply derived. Two rectangular regions are attached on the upper and lower side of the magnetic system. In the upper region the transformation is:

$$y = T(Y) = Y_0 - \frac{1}{k_0} \text{Log} \left| \frac{Y_{\infty} - Y}{Y_{\infty} - Y_0} \right| \quad (\text{II.38})$$

whereas for the lower region one must use:



$$y = T(Y) = -Y_0 - \frac{1}{k_0} \text{Log} \left| \frac{Y_\infty + Y}{Y_\infty - Y_0} \right| \quad (\text{II.39})$$

The general form of the equation is:

$$y = T(Y) = \text{sgn}(Y) \cdot \left( Y_0 - \frac{1}{k_0} \text{Log} \left| \frac{Y_\infty - |Y|}{Y_\infty - Y_0} \right| \right) \quad (\text{II.40})$$

The transformations are employed only in the light gray regions (Figure II.6), the superior one is bounded by the lines with constant  $y=Y_0$  and

$y=Y_\infty$ , the inferior one situated between  $y=-Y_0$  and  $y=-Y_\infty$ . It is easy to see that for  $Y=Y_0$ ,  $y$  is also  $Y_0$ , while if  $Y=Y_\infty$  then the outer boundary is projected towards infinity and  $y=\infty$ .

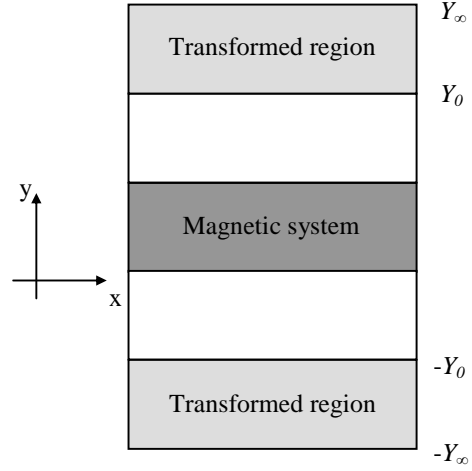


Figure II.6: The magnetic system together with the regions where the space transformations are applied.

But how do these transformations intervene in the resolution of the magnetostatic problem? In the outside region,  $\Phi$  is given by the Laplace equation. The weak formulation is in this case:

$$\int_V \mathbf{grad}(\omega) \cdot \mathbf{grad}(\Phi) dV = 0 \quad (\text{II.41})$$

If one changes  $y$  into  $Y$  the related differential operators are also modified, so that  $\mathbf{grad}$  becomes  $\mathbf{GRAD}$ . The Jacobian matrix of the transformation is:

$$\begin{pmatrix} \frac{\partial}{\partial X} \\ \frac{\partial}{\partial Y} \\ \frac{\partial}{\partial Z} \end{pmatrix} = \begin{pmatrix} \frac{\partial x}{\partial X} & \frac{\partial y}{\partial X} & \frac{\partial z}{\partial X} \\ \frac{\partial x}{\partial Y} & \frac{\partial y}{\partial Y} & \frac{\partial z}{\partial Y} \\ \frac{\partial x}{\partial Z} & \frac{\partial y}{\partial Z} & \frac{\partial z}{\partial Z} \end{pmatrix} \begin{pmatrix} \frac{\partial}{\partial x} \\ \frac{\partial}{\partial y} \\ \frac{\partial}{\partial z} \end{pmatrix} \quad (\text{II.42})$$

Then  $\mathbf{grad} = J^{-1} \mathbf{GRAD}$ , and the weak formulation for the magnetostatic problem in the “transformed” regions is:

$$\int_{V_{transf}} \mathbf{GRAD}(\beta_i) \mathbf{GRAD}(\Phi) (J^{-1})^T J^{-1} \det(J) d^3 R = 0 \quad (\text{II.43})$$

The size of the regions where the spatial transformations are applied is much smaller than the two regions that have to be connected to the magnetic region if the truncation method is applied. Such an approach is therefore more efficient.

### II.2.2. Classical finite element approach for the Landau-Lifshitz-Gilbert equation – WF1

The FE method in micromagnetism was used both for static computations in which the Gibbs energy minimum is sought [Fredkin 1987, Fredkin 1988] and dynamic calculations, based on the integration of the LLG equation [Yang 1996, Yang 1998, Schrefl 1999, Fidler 2000, Scholtz 2002, Hertel 2002, Hertel 2004, Bottauscio 2008].

The FE schemes coping with the LLG equation developed in the group from Vienna [Schrefl 1999, Scholtz 1999, Süß 2002] start from the FE discretization of the total energy. The effective field is then evaluated using the *box method* so that each node has its magnetic moment and its own effective field. The obtained expressions are directly introduced in the LLG equation and solved using an appropriate integration scheme. In the approach proposed by the group of the [Bottauscio 2008] the Landau-Lifshitz equation is integrated with the midpoint rule proposed earlier by D’Aquino et al. in [d’Aquino 2005].

A *classical* weak formulation for the LLG equation was proposed by Fredkin in [Yang 1996]. In the following, a similar formulation is presented. The difference between the two methods is the manner in which the constraint on the magnetization is handled: in Fredkin’s paper, the constraint is imposed by normalization after each time step, whereas in our approach, a constraint handling method was implemented.

Lately, the LLG equation gains more and more attention from the part of mathematicians. Methods based on *geometric integrators* have been proposed [Lewis 2003], interesting as through their use one can avoid the renormalization of the magnetization, apparently a not very “benefic” procedure. More than this, in [Bartels 2005, Alouges 2006, Alouges 2008] interesting FE formulations and integration schemes were proposed. The weak form proposed by Alouges [Alouges 2006] will be presented later in this chapter.

In this paragraph we will focus on writing down a first Galerkin-type weak formulation for the LLG equations, called WF1 from now on. To treat the constraint a special method was developed. The accuracy of the method was tested on two test cases.

The strong form is made up from the LLG equation together with the Brown boundary condition:

$$\begin{cases} \mathbf{v} - \alpha(\mathbf{m} \times \mathbf{v}) = -\mu_0 \gamma (\mathbf{m} \times \mathbf{H}_{\text{eff}}) & \text{on } V_m \\ \frac{\partial \mathbf{m}}{\partial \mathbf{n}} = 0, & \text{on } S_m \end{cases} \quad (\text{II.44})$$

and the constraint on the magnetization amplitude:

$$g(\mathbf{m}) = 1 - \mathbf{m}^2 = 0 \quad \text{on } V_m \quad (\text{II.45})$$

where  $\mathbf{v} = \partial \mathbf{m} / \partial t$ . As a part of the input, an initial magnetization distribution that respects the constraint is chosen.

Before writing down the weak form the solution space should be defined.  $\mathbf{v}$  is sought in the  $H^1(V_m)^3$  space, with  $V_m$  the volume occupied by the magnetic body and its surface  $S_m$ . By multiplication of the LLG equation with a vector test function  $\mathbf{w}$ ,  $\mathbf{w} \in H^1(V_m)^3$ , and then integration over  $V_m$ , WF1 is obtained:

$$\int_{V_m} \mathbf{w} \cdot [\mathbf{v} - \alpha(\mathbf{m} \times \mathbf{v})] dV = - \int_{V_m} \mu_0 \gamma \mathbf{w} \cdot [\mathbf{m} \times (\mathbf{H}_{\text{ex}} + \mathbf{H}_{\text{anis}} + \mathbf{H}_{\text{dem}} + \mathbf{H}_{\text{app}})] dV \quad (\text{II.46})$$

Generally speaking, for a PDE several weak forms can be derived, but as a rule of thumb the optimal one is the one in which the derivation order is reduced as much as possible. The exchange term:

$$- \int_{V_m} \mu_0 \gamma \mathbf{w} \cdot (\mathbf{m} \times \mathbf{H}_{\text{ex}}) dV = - \int_{V_m} \gamma \frac{2A_{\text{ex}}}{M_S} \mathbf{w} \cdot (\mathbf{m} \times \Delta \mathbf{m}) dV \quad (\text{II.47})$$

includes the test function  $\mathbf{w}$  and the second order derivative of  $\mathbf{m}$ . For this case the equilibration of the derivation order of the magnetization and of the test function is advised. Using integration by parts the integrand can be transformed as follows:

$$\frac{2A_{\text{ex}}}{\mu_0 M_S} (\mathbf{m} \times \Delta \mathbf{m}) \cdot \mathbf{w} = \frac{2A_{\text{ex}}}{\mu_0 M_S} \sum_l [\mathbf{m} \times (\Delta m_l \mathbf{e}_l)] \cdot \mathbf{w} = \frac{2A_{\text{ex}}}{\mu_0 M_S} \sum_l \Delta m_l [(\mathbf{m} \times \mathbf{e}_l) \cdot \mathbf{w}] \quad (\text{II.48})$$

where  $\mathbf{e}_l$  are unit vectors directed along the axes of the coordinate system,  $l \in \{x, y, z\}$ . (II.48) can be modified using the divergence theorem:

$$\Delta m_l (\mathbf{m} \times \mathbf{e}_l) \cdot \mathbf{w} = \text{div} [\nabla m_l \cdot (\mathbf{m} \times \mathbf{e}_l) \cdot \mathbf{w}] - \nabla m_l \cdot \nabla [(\mathbf{m} \times \mathbf{e}_l) \cdot \mathbf{w}], \quad i = \overline{1, N} \quad (\text{II.49})$$

and then integration leads to:

$$\int_{V_m} (\mathbf{m} \times \Delta \mathbf{m}) \cdot \mathbf{w} dV = \iint_{S_m} (\nabla m_l \cdot \mathbf{n}) (\mathbf{m} \times \mathbf{e}_l \cdot \mathbf{w}) dS - \int_{V_m} \nabla m_l \cdot \nabla [(\mathbf{m} \times \mathbf{e}_l) \cdot \mathbf{w}] dV \quad (\text{II.50})$$

The final form of the exchange term is obtained using the Gauss theorem and the Brown boundary condition:

$$\int_{V_m} (\mathbf{m} \times \Delta \mathbf{m}) \cdot \mathbf{w} dV = - \sum_l \int_{V_m} \left( \mathbf{m} \times \frac{\partial \mathbf{m}}{\partial x_l} \right) \cdot \frac{\partial \mathbf{w}}{\partial x_l} dV \quad (\text{II.51})$$

The other field terms in (II.46) remain unchanged and in conclusion the weak form of the LLG equation reads as:

$$\int_{V_m} \mathbf{w} \cdot [\mathbf{v} - \alpha (\mathbf{m} \times \mathbf{v})] dV = \sum_l \int_{V_m} \gamma \frac{2A_{ex}}{M_s} \left( \mathbf{m} \times \frac{\partial \mathbf{m}}{\partial x_l} \right) \cdot \frac{\partial \mathbf{w}}{\partial x_l} dV - \int_{V_m} \gamma \mu_0 \mathbf{w} \cdot (\mathbf{m} \times \mathbf{H}_r) dV \quad (\text{II.52})$$

Here  $\mathbf{H}_r$  stands for the sum  $\mathbf{H}_{anis} + \mathbf{H}_{dem} + \mathbf{H}_{app}$ .

### II.2.2.1. Integration scheme and constraint handling

The integration of the dynamic LLG equation consists in dividing the time interval into small time steps. To evolve from one time step to another, the linear equation (II.52) is solved, obtaining this way  $\mathbf{v}$ , and then the magnetization vector at each mesh node is updated using:

$$\mathbf{m}^{n+1} = \frac{\mathbf{m}^n + \delta t \mathbf{v}}{|\mathbf{m}^n + \delta t \mathbf{v}|} \quad (\text{II.53})$$

where  $\mathbf{m}^n$  is the magnetization determined at time step  $n$ . The normalization allows to respect the constraint (II.45), that forces the magnetization to remain on a sphere. This constraint affects also the time derivative  $\mathbf{v}$  of the magnetization, as this must always be in the tangent plane to  $\mathbf{m}$ ,  $\text{Tg}(\mathbf{m}) = \{\mathbf{v} \in H^1(V_m), \mathbf{m} \cdot \mathbf{v} = 0\}$ . To obtain a general time integration procedure, that assures such a behavior, a  $\theta$ -scheme [Lucquin 1995] has been

implemented. This scheme passes through an intermediate state  $\mathbf{m}^*$  defined as  $\mathbf{m}^n + \theta \delta \mathbf{v}$  (Figure II.7), with the requirement that  $\mathbf{m}^* \cdot \mathbf{v} = 0$ .  $\theta$  takes a fixed value in the range  $[0, 1]$ .

From (II.53) and the supposition that  $|\mathbf{m}^{n+1}|=1$  the following condition can be deduced:

$$\left( \mathbf{m}^n + \frac{1}{2} \delta t \mathbf{v} \right) \cdot \delta t \mathbf{v} = 0 \quad (\text{II.54})$$

Taking  $\theta=1/2$  in the  $\mathbf{m}^n + \theta \delta \mathbf{v}$ , one retrieves exactly the quantity in the parenthesis, with  $\mathbf{m}^* \cdot \mathbf{v} = 0$  automatically satisfied. In conclusion,  $1/2$  seems to be the best choice for  $\theta$ .

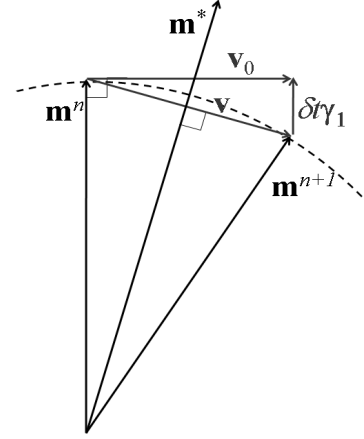


Figure II.7: The intermediate magnetization  $\mathbf{m}^*$  and the decomposition of  $\mathbf{v}$  into  $\mathbf{v}_0$  and the correction  $\delta \gamma_1$ .

More than this well-designed way of handling the constraint, the  $\theta$ -scheme offers a second advantage. For an explicit Euler scheme to be stable, very small time steps are required [Kevorkian 1998]. In a FE approach, the non-homogeneity of the spatial discretization makes that the time step is bounded by the square of the size of the smallest mesh element. This leads to its dramatic reduction, and accordingly, to the decreasing of the method's efficiency. Adopting the above described  $\theta$ -scheme the loss of efficiency is avoided.

Making use of the intermediate magnetization  $\mathbf{m}^*$ , the vector  $\mathbf{v}$  can be decomposed in two parts (Figure II.7):  $\mathbf{v}_0$  belonging to  $\text{Tg}(\mathbf{m}^n)$  and a correction that will place  $\mathbf{v}$  into  $\text{Tg}(\mathbf{m}^*)$ :

$$\mathbf{v} = \mathbf{v}_0 + \delta \gamma_1 \quad (\text{II.55})$$

Rewriting  $\mathbf{m}^*$  by taking into account this, one obtains:

$$\mathbf{m}^* = \mathbf{m}^n + \frac{\delta t}{2} \mathbf{v}_0 + \frac{\delta t^2}{2} \gamma_1 \quad (\text{II.56})$$

Therefore the condition  $\mathbf{m}^* \cdot \mathbf{v} = 0$  gains a new form:

$$\mathbf{m}^n \cdot \mathbf{v} = -\frac{1}{2} \delta t \mathbf{v}_0^2 \quad (\text{II.57})$$

In the above given formula the terms in  $\delta t^2$  and higher were neglected.

Introducing an intermediate magnetization state  $\mathbf{m}^*$  the vector  $\mathbf{v}$  was transformed into a sum of two contributions and a new form for the condition  $\mathbf{m} \cdot \mathbf{v}$  has been obtained. The next step is to rewrite the weak form by taking into account these new elements. The substitution of  $\mathbf{m}$  by  $\mathbf{m}^*$  is done only for the exchange term. In the other field terms  $\mathbf{m}$  is replaced by  $\mathbf{m}^n$ . After a proper rearrangement of the separate contributions, WF1 turns into:

$$\left\{ \begin{aligned} & \int_{V_m} \mathbf{w} \cdot \left( \mathbf{v} - \alpha (\mathbf{m}^n \times \mathbf{v}) \right) dV = \\ & \sum_l \int_{V_m} \gamma \frac{2A_{ex}}{M_s} \left[ \left( \mathbf{m}^n + \frac{1}{2} \delta t \mathbf{v}_0 \right) \times \frac{\partial \left( \mathbf{m}^n + \frac{1}{2} \delta t \mathbf{v}_0 \right)}{\partial x_l} \right] \cdot \frac{\partial \mathbf{w}}{\partial x_l} dV - \int_{V_m} \gamma \mu_0 \mathbf{w} \cdot \left( \mathbf{m}^n \times \mathbf{H}_r(\mathbf{m}^n) \right) dV \\ & \mathbf{m}^n \cdot \mathbf{v} = -\frac{1}{2} \delta t \mathbf{v}_0^2 \end{aligned} \right. \quad (\text{II.58})$$

Looking carefully to the above given weak form, one notices that  $\mathbf{v}_0$  intervenes in both the weak form and the constraint on  $\mathbf{v}$ . Therefore a two-step procedure is required: first  $\mathbf{v}_0$  is determined, and then reintroduced in (II.58) to get  $\mathbf{v}$ .

#### *Determining $\mathbf{v}_0$*

To calculate  $\mathbf{v}_0$ , only the equation containing the terms of order 0 in  $\delta t$  are solved. The corresponding weak form reads as:

$$\int_{V_m} \mathbf{w} \cdot \left[ \mathbf{v}_0 - \alpha (\mathbf{m}^n \times \mathbf{v}_0) \right] dV = \sum_l \int_{V_m} \gamma \frac{2A_{ex}}{M_s} \left( \mathbf{m}^n \times \frac{\partial \mathbf{m}^n}{\partial x_l} \right) \cdot \frac{\partial \mathbf{w}}{\partial x_l} dV - \int_{V_m} \gamma \mu_0 \mathbf{w} \cdot \left( \mathbf{m}^n \times \mathbf{H}_r(\mathbf{m}^n) \right) dV \quad (\text{II.59})$$

with the constraint  $\mathbf{m}^n \cdot \mathbf{v}_0 = 0$ .

Obviously, one searches for the solution of a discrete form of equation (II.59). To obtain it, the domain  $V_m$  is discretized and the magnetization components and the test functions  $\mathbf{w}$  are interpolated:

$$\begin{aligned}\mathbf{w} &= \beta_i(\mathbf{r}) \mathbf{e}_p \\ \mathbf{v}_0 &= \sum_{j=1}^N \beta_j(\mathbf{r}) \mathbf{v}_0(\mathbf{r}_j) = \sum_{j=1}^N \beta_j(\mathbf{r}) \sum_q \mathbf{v}_{j,q}^0 \mathbf{e}_q\end{aligned}\quad (\text{II.60})$$

where  $N$  is the number of nodes and  $p, q \in \{x, y, z\}$ . The magnetization can also be interpolated using the same interpolation functions. Again, first or second order Lagrange polynomials were employed. Introducing these interpolated quantities in the weak form (II.59), the following matrix equation is obtained:

$$(M + D) \mathbf{v}_0 = L \quad (\text{II.61})$$

with  $M$  (mass matrix),  $D$  (damping matrix) and  $L$  (load matrix) defined as:

$$\begin{aligned}M &= \int_{V_m} \beta_i \beta_j \delta_{pq} dV \\ D &= \alpha \int_{V_m} \beta_i \beta_j \mathbf{e}_p \cdot (\mathbf{m}^n \times \mathbf{e}_q) dV \\ L &= \sum_{l=x,y,z} \int_{V_m} \gamma \frac{2A_{ex}}{M_s} \frac{\partial \beta_i}{\partial x_l} \mathbf{e}_p \cdot \left( \mathbf{m}^n \times \frac{\partial \mathbf{m}^n}{\partial x_l} \right) dV + \int_{V_m} \beta_i \mathbf{e}_p \cdot (\mathbf{m}^n \times \mathbf{H}_r(\mathbf{m}^n)) dV\end{aligned}\quad (\text{II.62})$$

$M$  and  $D$  are  $3N \times 3N$  matrices and  $L$  is a vector of size  $3N$ , exactly like the solution  $\mathbf{v}_0$ .

To treat the constraint  $\mathbf{m}^n \cdot \mathbf{v}_0 = 0$  a Lagrange multiplier approach is used. Assembling (II.61) and the matrix equation for the constraint on  $\mathbf{m}^n$ , the following system is obtained, with the unknowns  $\mathbf{v}_0$  and the Lagrange multiplier  $\lambda$ :

$$\begin{cases} (M + D) \mathbf{v}_0 + H^T \lambda = L \\ H \mathbf{v}_0 = 0 \end{cases} \quad (\text{II.63})$$

where  $H$  is the  $N \times 3N$  matrix made up from the components of  $\mathbf{m}^n$  in each mesh node:



$$H = \begin{pmatrix} m_1^x & m_1^y & m_1^z & 0 & 0 & 0 & 0 & 0 & 0 \\ 0 & 0 & 0 & 0 & 0 & 0 & 0 & 0 & 0 \\ 0 & 0 & 0 & m_i^x & m_i^y & m_i^z & 0 & 0 & 0 \\ 0 & 0 & 0 & 0 & 0 & 0 & 0 & 0 & 0 \\ 0 & 0 & 0 & 0 & 0 & 0 & m_N^x & m_N^y & m_N^z \end{pmatrix} \quad (\text{II.64})$$

In the first time, the  $3N \times 2N$  *Null* matrix collecting all the vectors of  $\text{Ker}(H)$  is computed. As  $H \text{ Null} = 0$ , the elements of *Null* are in reality the vectors of  $\text{Tg}(\mathbf{m})$ . A schematic representation is given in Figure II.8:

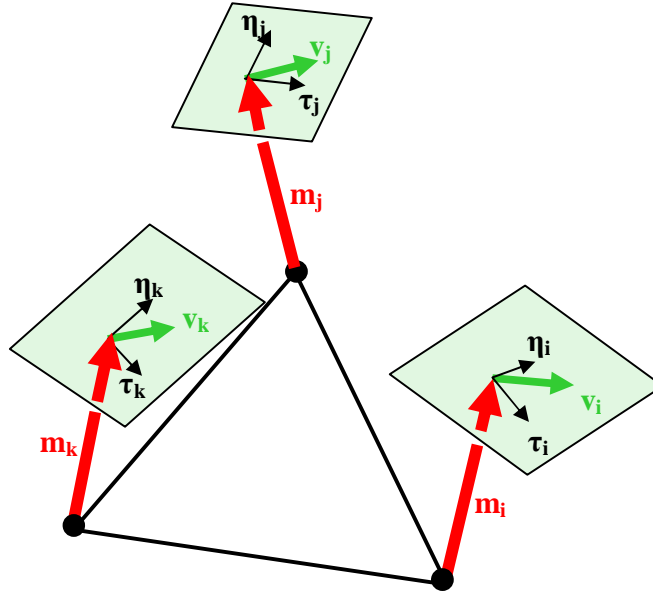


Figure II.8: The magnetization in three different mesh nodes, with the corresponding tangent space and the vectors  $\boldsymbol{\tau}$  and  $\boldsymbol{\eta}$  that generate it.

As the constraint asks that  $H \mathbf{v}_0 = 0$ ,  $\mathbf{v}_0$  can be written as  $\text{Null} \hat{\mathbf{v}}_0$ , where  $\hat{\mathbf{v}}_0$  is a vector to be determined. Schematically *Null* and  $\hat{\mathbf{v}}_0$  can be written as:

$$Null = \begin{pmatrix} \eta_1^x & \tau_1^x & 0 & 0 & 0 & 0 & 0 & 0 \\ \eta_1^y & \tau_1^y & 0 & 0 & 0 & 0 & 0 & 0 \\ \eta_1^z & \tau_1^z & 0 & 0 & 0 & 0 & 0 & 0 \\ 0 & 0 & 0 & 0 & 0 & 0 & 0 & 0 \\ 0 & 0 & 0 & \eta_i^x & \tau_i^x & 0 & 0 & 0 \\ 0 & 0 & 0 & \eta_i^y & \tau_i^y & 0 & 0 & 0 \\ 0 & 0 & 0 & \eta_i^z & \tau_i^z & 0 & 0 & 0 \\ 0 & 0 & 0 & 0 & 0 & 0 & 0 & 0 \\ 0 & 0 & 0 & 0 & 0 & 0 & \eta_N^x & \tau_N^x \\ 0 & 0 & 0 & 0 & 0 & 0 & \eta_N^y & \tau_N^y \\ 0 & 0 & 0 & 0 & 0 & 0 & \eta_N^z & \tau_N^z \end{pmatrix} \quad (II.65)$$

and  $\hat{\mathbf{v}}_0^T = \left( (\hat{v}_0^\eta)_1 \quad (\hat{v}_0^\tau)_1 \quad 0 \quad (\hat{v}_0^\eta)_i \quad (\hat{v}_0^\tau)_i \quad 0 \quad (\hat{v}_0^\eta)_N \quad (\hat{v}_0^\tau)_N \right)$ . The *Null* matrix can be viewed (Figure II.8) as a tool that transforms the vector  $\hat{\mathbf{v}}_0$  into its  $\mathbb{R}^3$  correspondent. Introducing *Null*  $\hat{\mathbf{v}}_0$  in the first matrix equation we get:

$$(M + D) Null \hat{\mathbf{v}}_0 + H^T \lambda = L \quad (II.66)$$

By multiplying the equation by  $Null^T$ , the Lagrange multiplier  $\lambda$  is eliminated and the vector  $\hat{\mathbf{v}}_0$  is then obtained:

$$\hat{\mathbf{v}}_0 = K_{eff}^{-1} Null^T L \quad (II.67)$$

where  $K_{eff} = Null^T (M + D) Null$ . Now  $\mathbf{v}_0$  can be easily reconstructed:

$$\mathbf{v}_0 = Null \hat{\mathbf{v}}_0 \quad (II.68)$$

and the resolution of the weak form (II.58) can be carried out.

### Determining $\mathbf{v}$

Now  $\mathbf{v}$  is the one expressed as:

$$\mathbf{v} = \sum_{j=1}^N \beta_j(\mathbf{r}) \mathbf{v}(\mathbf{r}_j) = \sum_{j=1}^N \beta_j(\mathbf{r}) \sum_q \mathbf{v}_{j,q} \mathbf{e}_q \quad (II.69)$$

with  $q \in \{x, y, z\}$ . Again a matrix equation is obtained, having similar form as (II.63):

$$\begin{cases} (M + D) \mathbf{v} + H^T \Lambda = L \\ H \mathbf{v} = G(\mathbf{v}_0) \end{cases} \quad (\text{II.70})$$

but with a modified  $L$  matrix:

$$L = \gamma \frac{A_{ex}}{M_S} \sum_{l=x,y,z} \int_{\Omega_m} \delta t \frac{\partial \beta_i}{\partial x_l} \mathbf{e}_p \cdot \left[ \left( \mathbf{m}^n \times \frac{\partial \mathbf{v}_0}{\partial x_l} \right) + \left( \mathbf{v}_0 \times \frac{\partial \mathbf{m}^n}{\partial x_l} \right) \right] d\Omega + \int_{\Omega_m} \beta_i \mathbf{e}_p \left( \mathbf{m}^n \times \mathbf{H}_r(\mathbf{m}^n) \right) d\Omega \quad (\text{II.71})$$

In the constraint equation, the second in (II.70), the matrix  $H$  is the same as before, and  $G$  is given by the values of  $-1/2 \delta t \mathbf{v}_0^2$ . As the matrix  $G$  is not zero (contrarily to the constraint corresponding to  $\mathbf{v}_0$ ), the general solution of (II.70) is expressed as:

$$\mathbf{v} = \text{Null} \cdot \hat{\mathbf{v}} + \mathbf{v}_d \quad (\text{II.72})$$

with  $\text{Null}$  given (II.65). To be able to find the solution  $\mathbf{v}$  the Lagrange multiplier  $\Lambda$  is eliminated, exactly as in the previous case, by multiplying the first equation with  $\text{Null}^T$ :

$$\begin{cases} \text{Null}^T (M + D) (\text{Null} \cdot \hat{\mathbf{v}} + \mathbf{v}_d) = \text{Null}^T L \\ H \mathbf{v}_d = -\frac{1}{2} \delta t \mathbf{v}_0^2 \end{cases} \quad (\text{II.73})$$

As from the second equation is clear that  $\mathbf{v}_d$  is not in  $\text{Tg}(\mathbf{m})$ , one can assume that it has a component along  $\mathbf{m}$ . Therefore in the node  $i$ ,  $\mathbf{v}_d$  reads as:

$$(\mathbf{v}_d)_i = -\frac{1}{2} \delta t (\mathbf{v}_0)_i^2 \mathbf{m}_i^n \quad (\text{II.74})$$

and then inserting it in the first equation of (II.73) the vector  $\hat{\mathbf{v}}$  is retrieved, and:

$$\hat{\mathbf{v}} = K_{eff}^{-1} L_{eff} \quad (\text{II.75})$$

with  $K_{eff}$  defined above and  $L_{eff}$  equal to:

$$L_{eff} = \text{Null}^T [L - (M + D) \mathbf{v}_d] \quad (\text{II.76})$$

Now  $\mathbf{v}$  can be assembled:

$$\mathbf{v} = \text{Null} \cdot K_{eff}^{-1} L_{eff} + \mathbf{v}_d \quad (\text{II.77})$$

The weak formulations for the magnetostatic equation and the LLG equation were directly implemented in the Comsol software [Comsol site], provided by Comsol Multiphysics. The flowchart of the solving process by Comsol is presented in Figure II.9. After defining the inputs of the problem, for each time step the solution of the micromagnetic problem is determined in two steps. First the magnetostatic part is solved using a linear solver. Then  $\mathbf{H}_{\text{dem}}$  is determined at each Gauss integration point and introduced into the LLG equation. The so-obtained linear system in  $\mathbf{v}$  is solved using a Comsol solver [Comsol site].

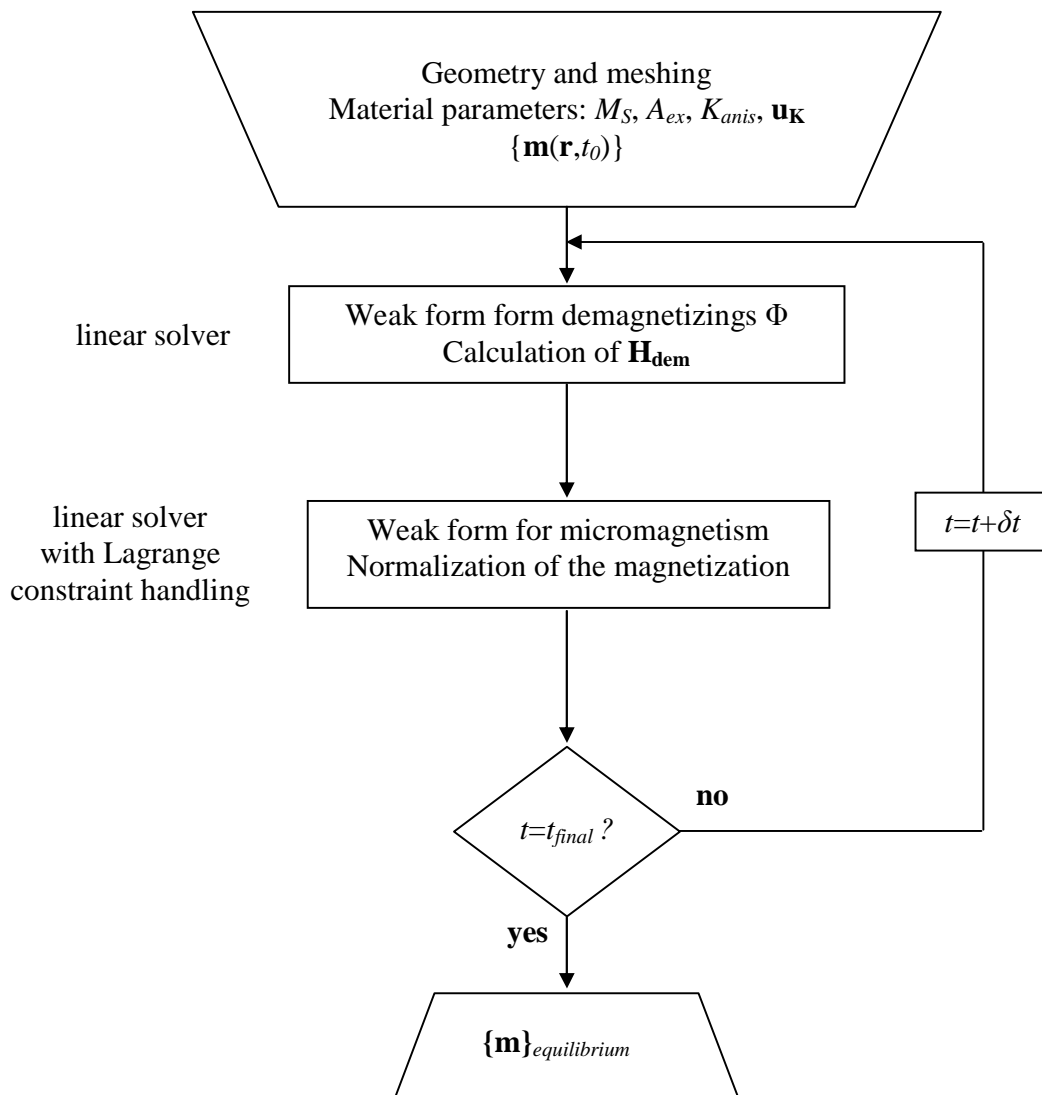


Figure II.9: Flowchart for the WF1 implementation under Comsol environment.

Now that the numerical means for solving the LLG equation were described, the WF1 formulation can be tested. Two test cases were chosen: a periodic system, the so-called stripe structure, and an infinite prism. Both model systems are presented in the following, together with results issues by static and dynamic computations.

### II.2.3. Applications WF1

#### II.2.3.1. *Stripe domains*

Weiss [Weiss 1907] was the first one to conclude the possibility of non-uniformly magnetized bodies, and therefore the presence of magnetic domains. The domain structure formation is the result of energy minimization. In the absence of an external magnetic field, the system's energy is made up from the exchange, the magnetocrystalline anisotropy and the magnetostatic terms, and therefore the equilibrium configuration will reflect the equilibrium between these contributions.

Although domain walls were considered less interesting objects, simple interfaces between the magnetic domains, they proved to be just as remarkable as the magnetic domains themselves. It seems that, several interesting phenomena originate from these magnetic objects, one of the most important being the electron scattering due to the presence of the domain wall, predicted theoretically by Cabrera [Cabrera 1974] and Berger [Berger 1978] and observed experimentally in systems with uniaxial magnetocrystalline anisotropy [Gregg 1996]. Such magnetic thin films are a very exciting topic. The applications based on such materials are various (information storage media, sensors), and even though the domain structure appears to be rather simple, the fundamental physics behind it is quite complex. Numerous equilibrium configurations are possible, depending on the orientation of the easy axis with respect to the film plane, on the thickness of the film, on the growth conditions and on the magnetic history of the sample [Hubert 1998].

In the following only systems with perpendicular anisotropy will be considered. To this category of thin films belong FePd alloys, Co/Pt multilayers and Co films. The equilibrium configuration consists of domains, resulting from a periodic modulation of the out-of-plane magnetization component, and regular Bloch walls. This formation is named stripe domains structure, an example being shown in Figure II.10. Stripe domains were

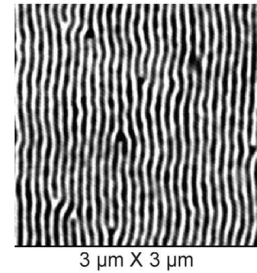


*Figure II.10: MFM image of a 50nm thick Co film, with the easy axis perpendicular to the film plane*

first discussed by Landau-Lifshitz. Then in a relatively short interval (1961-1968) several theoretical and experimental observations were published [Muller 1961, Spain 1963, Tatsumoto 1968, Puchalska 1967]. Since these first studies, stripe domains gained a lot of interest. Numerous studies concern the dependence of the remanent configuration on the material parameters, film thickness [Hubert 1998, Labrune 1994]. It is a well known fact that, the complexity of the domain and the wall configuration is strongly influenced by the competition between the magnetocrystalline anisotropy and the shape anisotropy, quantified by the so-called *quality factor*,  $Q = \frac{2K_{anis}}{\mu_0 M_s^2}$ . Based on the value of  $Q$  one can

identify three situations, depicted in Figure II.11. If the perpendicular magnetocrystalline anisotropy is dominant,  $Q \gg 1$ , the walls separating the up and down domains are very thin. For  $Q \ll 1$  the shape anisotropy forces the magnetization to lay in-plane. For  $Q \approx 1$ , a structure of compromise is stabilized. The latter structure includes, in the central part, domain walls of Bloch type, and near the surfaces, large closure domains. The stripe period, pattern and domain size can be determined based on the material parameters.

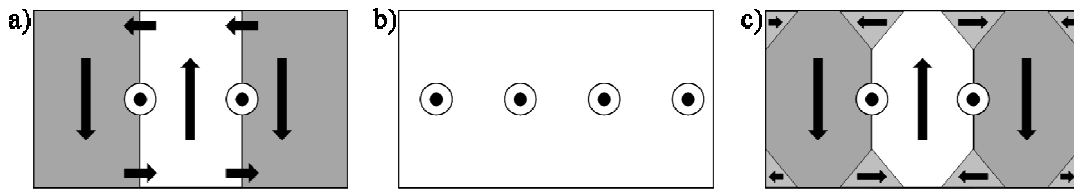


Figure II.11: Domain structure for different values of  $Q$ : a)  $Q \gg 1$ , b)  $Q \ll 1$  and c)  $Q \approx 1$ .

From an experimental point of view, the interest for such materials arises due to the large number of domain walls and the easy manipulation of the equilibrium period and domain orientation. Numerically, these systems are also very attractive due to two symmetry properties: the invariance of the system along the stripes' direction and the periodicity along the  $Ox$  direction (Figure II.12). The first feature makes possible their study using 2D simulation tools, whereas the periodicity allows to reduce the geometry from a very large (infinite) system to a finite-sized 2D geometry, for example a rectangle having the thickness of the thin film and the length equal to its equilibrium period. In the following we will test the FE approach based on the weak form WF1 on such a system. The material parameters used to obtain the following results are given in Table II.2.

Table II.2: Material parameters.

$A_{ex}$ (J/m)	$\mu_0 M_S$ (T)	$K_{anis}$ (J/m <sup>3</sup> )	$l_{ex}$ (nm)	$l_B$ (nm)	$Q$
$2 \cdot 10^{-11}$	1	$5 \cdot 10^5$	7.08	6.32	1.25

Choosing  $Q=1.25$ , the system belongs to the latter category (Figure II.11 c) and therefore the wall structure is quite complex: Bloch in the center of the film with two small flux closure domains near the upper and lower surface. The equilibrium period of the system was determined to be around 200 nm, and therefore the model system consists of a rectangle having this length and the height 40 nm. A schematic representation of the model system is given in Figure II.12:

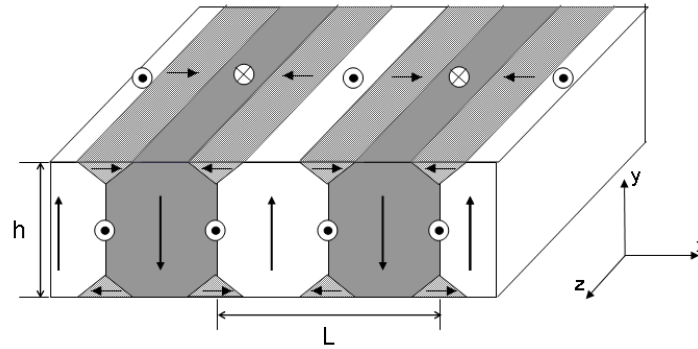


Figure II.12: Schematic representation of the stripe structure in a thin film.

To check whether the WF1 results for this first test case were correct or not, they were compared with those obtained using the GL\_FFT software, presented in chapter II.1. The mathematical background of the two implementations is completely different, this being reflected even in the model systems used. As input for the FD software, the geometry consists only of the magnetic system, thus a rectangle of 200nm x 40 nm. The FE model system is more complex because the treatment of the magnetostatic problem requires regularity at infinity. The truncation method was implemented to cope with this issue; hence two 200nm x 300 nm large vacuum regions were attached to the magnetic region, on its upper and lower side (Figure II.13).

The FD discretization consists of squares of constant size, while the FE mesh consists of irregular triangles. The choice of the mesh size is sustained by the rule of thumb



derived in the chapter I.3, where the LLG equation was discussed (see equations (I.46)). In the two implementations the same mesh size of 2.5 nm was used, as this value seemed to be optimal, in terms of computation time and accuracy. Testing smaller mesh sizes, for example  $\delta=1$  nm, showed that the results are not significantly improved, whereas the computation time is very much increased.

An example of the model systems and the discretization is shown in Figure II.13. In the FE model, beyond the magnetic system, a couple of vacuum regions must also be discretized. The mesh in the vacuum region is not subject to any restriction, because the variable defined here,  $\Phi$ , varies smoothly [Brown 1963]. Nevertheless, a maximal size of 20 nm was imposed. Despite this large mesh size, the presence of these “extra” regions is not at all advantageous, increasing very much the computation time.

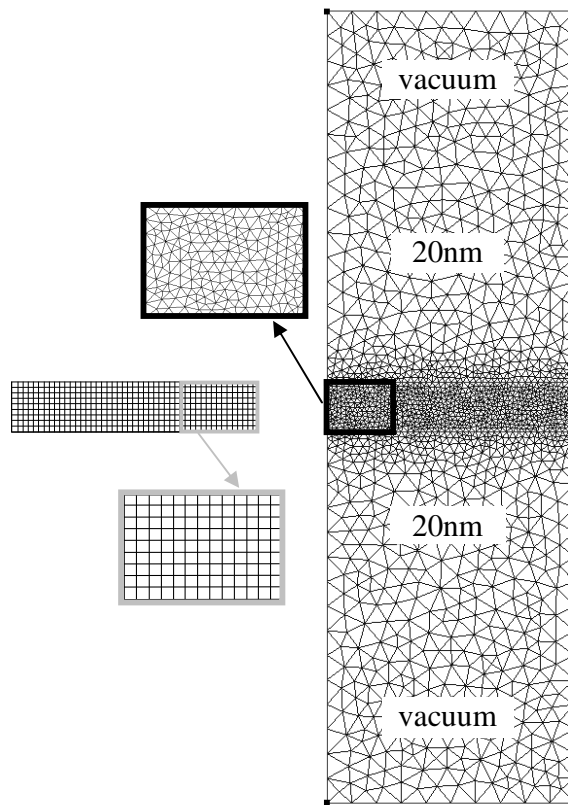


*Figure II.13: On the left side the FD model system and on the right side the FE model system.*

Concerning the boundary conditions:

- in the FE approach the Brown condition (I.36) is naturally included in the weak form.
- to conserve the periodic character of the magnetic system, on the left and right side periodic boundary conditions were implemented for both approaches.

As input, besides the material parameters, an initial magnetization distribution is also given, chosen so to satisfy the constraint on the magnetization amplitude. For this test case, the configuration is a perfectly sinusoidal one, given by the following equations and depicted in Figure II.14:

$$m_x = 0, \quad m_y = \cos\left(2\pi \frac{x}{L}\right), \quad m_z = \left|\sin\left(2\pi \frac{x}{L}\right)\right| \quad (\text{II.78})$$

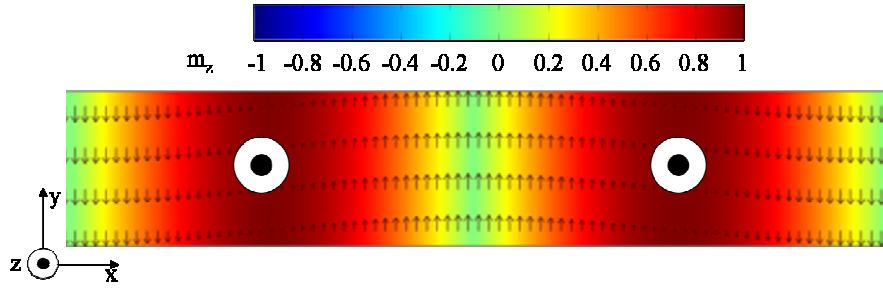


Figure II.14: Initial magnetization distribution. The arrows represent  $m_x$  and  $m_y$  and the color code stands for the  $z$  component.

### Static computation

First, a static simulation, where the damping parameter is set to 1, has been carried out. An initial comparison between the equilibrium states obtained with the two approaches is therefore possible. The equilibrium states are shown in Figure II.15. The magnetization lies mainly in the Oxy plane, except for two vortex-like walls separated by a distance of  $L/2$  ( $\approx 100$  nm). A basic qualitative analysis reveals a very good agreement between the two configurations. The wall structure seems to be the same: a central Bloch part pointing outwards and small flux closure domains oriented along the  $\pm O_x$  direction are formed near the surface.

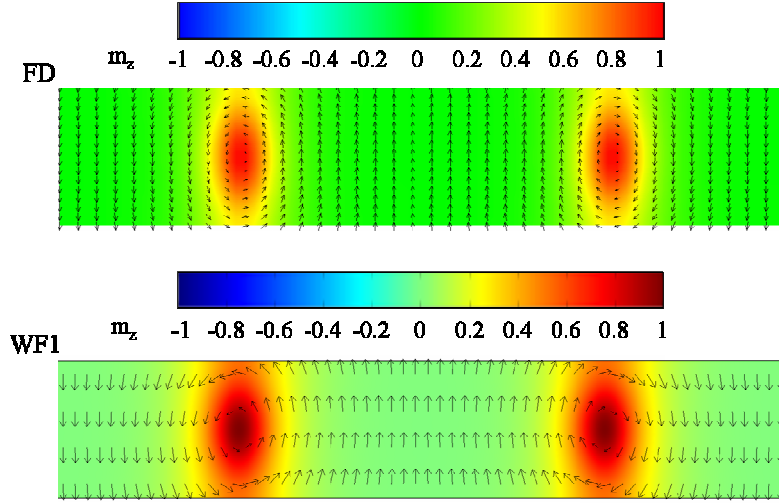


Figure II.15: Equilibrium magnetization distribution obtained with the FD and the WF1 approaches. The same colour code is used as previously.

Beyond this simple visual comparison, by sampling the WF1 results on a regular grid corresponding to the one used by the FD method, the angle between the magnetizations could be determined. This quantity is depicted in Figure II.16.

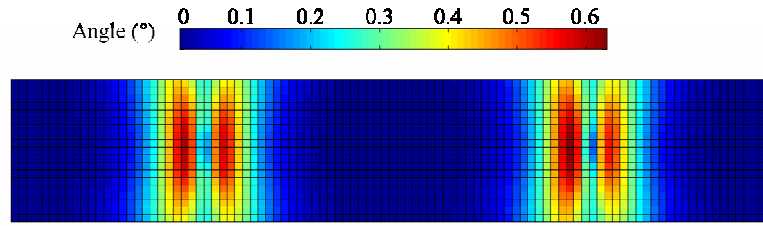


Figure II.16: The angle between the equilibrium magnetizations.

This analysis revealed that, the main discrepancies are localized in the vicinity of the vortices, where the maximal value of the angle was found to be around  $0.6^\circ$ .

Until now we looked only to the equilibrium magnetization distribution. Even though, a good match between the FD and WF1 configurations is very important, it is not enough to guarantee the correctness of the FE approach. A very important indicator is the relaxation process itself. Eventual flaws of the integration scheme could surface in the evolution of the total energy or of the magnetization components. The progress of these two quantities versus time process is depicted in Figure II.17:

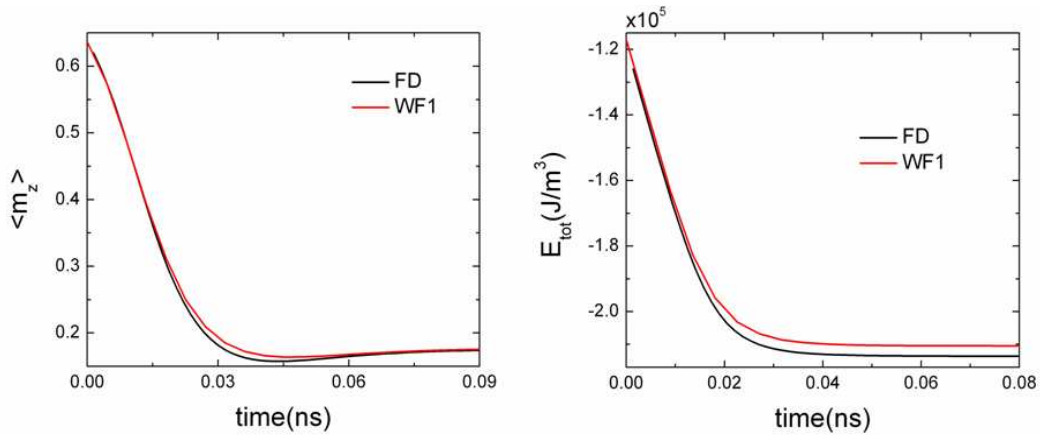


Figure II.17: Time evolution of the  $m_z$  magnetization component and of the average value of the total energy density.

The evolutions seem to match almost perfectly. In the WF1 approach, the magnetization component evolves a little differently than in the FD approach, but as expected from the comparison of the equilibrium states, the final values are almost identical. The comparison of the total energy densities predicts a small energy difference at equilibrium. To retrieve the source of this energy gap, the evolution of the separate energy terms (Figure II.18), exchange, magnetocrystalline anisotropy and demagnetizing is checked. The largest discrepancies occur in the exchange term. From the equilibrium values, listed in Table II.3, the same conclusion can be drawn. The large difference in the exchange energy was predicted already by the comparison of the equilibrium configurations, where the most important variations laid in the region of the walls (Figure II.16), that is, in the region where the exchange is the most perturbed.

Overall, the existing differences are acceptable, if one bears in mind that the technique of evaluating the energy terms are entirely different: FD uses local estimations of the magnetization vector and the effective field, whereas in FE the energy expression is applied to the magnetization field interpolated on each element.

Table II.3: Equilibrium values of  $\langle m_z \rangle$  and the energy densities.

Method	$\langle m_z \rangle$	$E_{\text{tot}} (\text{J/m}^3) \cdot 10^5$	$E_{\text{ex}} (\text{J/m}^3) \cdot 10^4$	$E_{\text{anis}} (\text{J/m}^3) \cdot 10^5$	$E_{\text{dem}} (\text{J/m}^3) \cdot 10^5$
FD	0.1742	-2.1358	6.2365	-4.1812	1.4216
WF1	0.1757	-2.1045	6.4789	-4.1697	1.4172
Error	0.9%	1.5%	3.9%	0.3%	0.3%

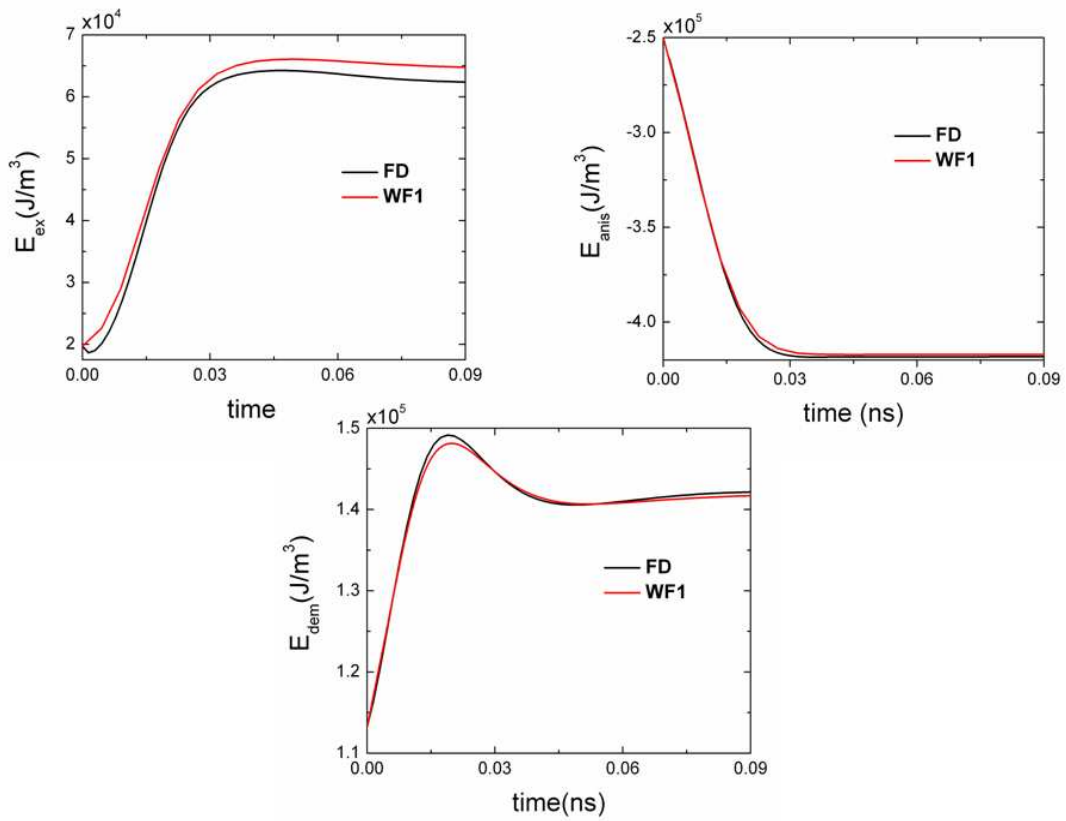


Figure II.18: The exchange, magnetocrystalline anisotropy and dipolar energy densities as a function of time.

### Dynamic computation

In real stripe domain materials the damping parameter is around 0.1-0.01. Passing to such values changes the relaxation process completely. First of all, the evolution towards equilibrium takes more time, as the velocity of energy loss is proportional to the damping parameter. Second of all, the magnetization will have an oscillatory behavior, and the duration of the oscillations increases with the diminution of  $\alpha$ . The behavior of the magnetic system for several  $\alpha$  values is shown in Figure II.19.

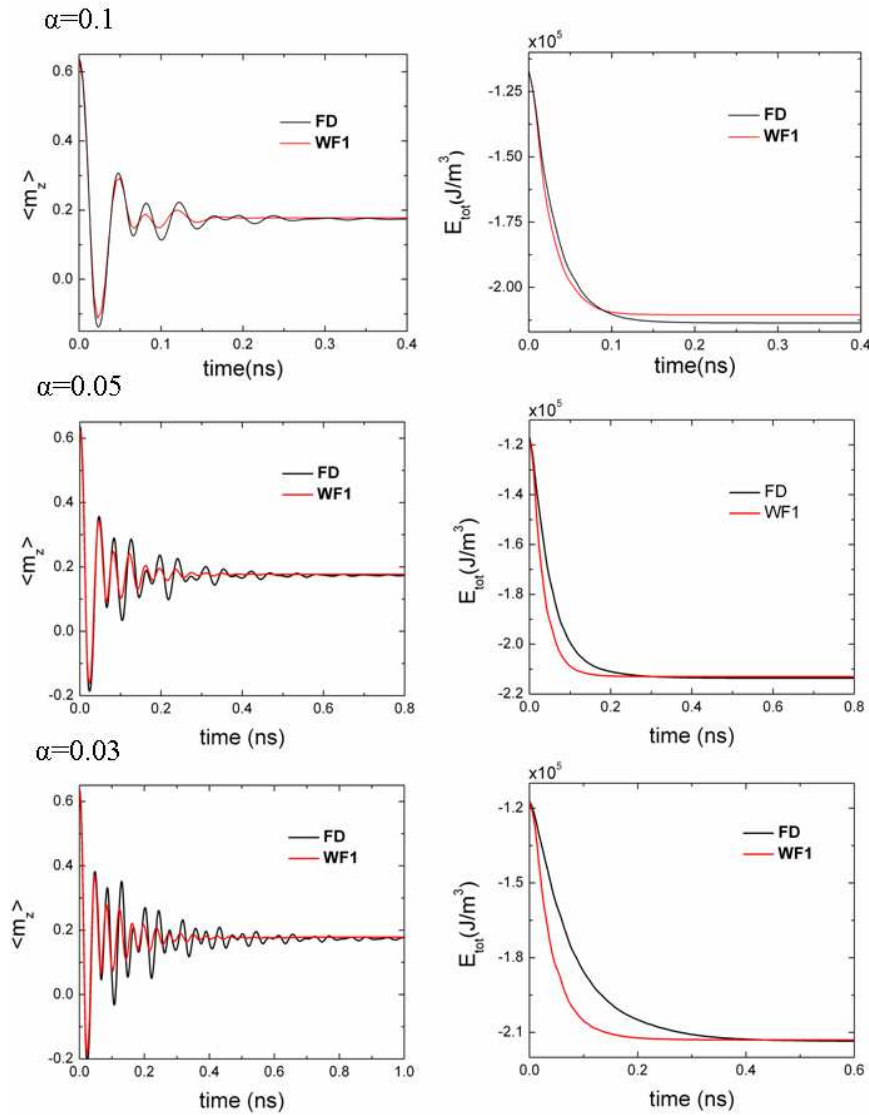


Figure II.19: Details of the relaxation process for  $\alpha$  of 0.1, 0.05 and 0.03.

As the value of the damping parameter decreases, the oscillatory behavior of the magnetization is accentuated. Figure II.19 shows only the evolution  $\langle m_z \rangle$ . For the other components,  $\langle m_x \rangle$  and  $\langle m_y \rangle$ , a similar behavior is observed. An important conclusion can be drawn by analyzing these curves: there is a relative agreement between the FD and WF1 results for the first 2-3 oscillations, but then the results issued by the FE approach seem to be more damped than the FD evolution. Apparently the WF1-based implementation overestimates the relaxation term. This same behavior is observable in the total energy versus time curves. For large values of  $\alpha$  (1 and 0.1), there is a small gap between the equilibrium values, even though the path described during relaxation is very similar. For realistic, and therefore small values, like 0.05 or 0.03, the equilibrium state is reached sooner in the FE simulation than in the FD calculation (at 0.23 ns instead of 0.37 ns for  $\alpha=0.05$  and 0.3 ns instead of 0.53 ns for  $\alpha=0.03$ ).

#### *II.2.3.2. Exchange coupled magnetic moments in an infinite prism with square cross-section*

It is necessary to determine the source of this over damped motion. Even though not the only one, but probably the main cause of the over damping lays in the complexity of the weak form. It is very important to keep in mind that, the FE method is based on the interpolation of the unknown and of the test function. When it comes to interpolation errors, the exchange term is the most exposed, as it contains two interpolated quantities: the magnetization and its space derivative. To weight the influence of the exchange term, a second, mathematical, 2D test case was considered, consisting of an infinite prism with a square cross-section of 2nm×2nm, in which the magnetic moments are coupled only through exchange ( $A_{ex}=1$  a.u.).

The initial magnetization configuration consists of a sinusoidal distribution. At equilibrium, as only the exchange interaction is present, all the magnetic moments are aligned. The initial and equilibrium configurations are depicted in Figure II.20

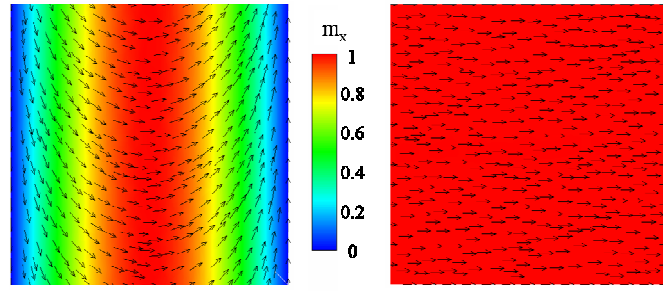


Figure II.20: Initial and equilibrium state distributions for an infinite prism with a square cross section of  $2\text{nm} \times 2\text{nm}$ .

The value of the damping parameter was taken to be 0.02. The dynamics calculated with WF1 was again compared with that obtained by the FD approach (Figure II.21). The mesh size was of 0.125 nm, resulting, for the FE approach in around 1000 elements and 250 elements for the FD discretization.

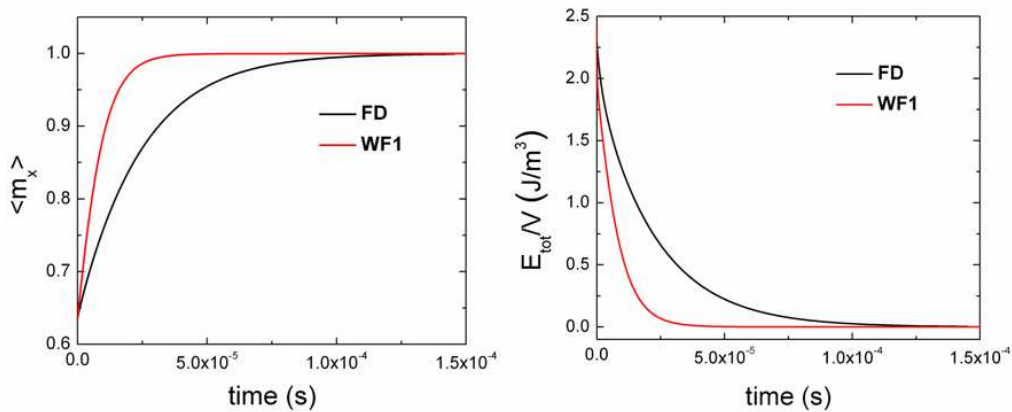


Figure II.21: Evolution of the average value of the  $\langle m_x \rangle$  magnetization component and the total energy density as a function of time.

The comparison shows that, although the equilibrium states are the same, the paths followed by the magnetization in the relaxation process are very different, with WF1 the energy decreases faster than with the FD approach. This observation is a clear indicator of the importance of the exchange term, making the hypothesis of over damped motion due to the interpolation errors a very plausible one.



In conclusion, a classical finite element weak form of the Landau-Lifshitz-Gilbert equations was developed and implemented to deal with 2D micromagnetic systems. This scheme was benchmarked against the more usual approach of finite differences. A good agreement was found for the results in the highly damped regime ( $\alpha=1$ ,  $\alpha=0.1$ ). For smaller values of the damping parameter the dynamics calculated by the finite element approach is altered by a numerical over-damping. Three sources of this overestimation of the relaxation term are conceivable:

1. the integration scheme,
2. the constraint on the magnetization
3. the interpolation errors.

To be able to describe correctly the magnetization dynamics, an improved weak form is needed, one derived so that, the above mentioned error sources are either eliminated, or, at least reduced as much as possible. If feasible, the exchange term should be simplified to reduce interpolation errors, and the constraints on  $\mathbf{v}$  should be eliminated. Moreover, one has to prove that the time integrator gives a physically correct velocity of energy dissipation, impossible to show for the present case.

#### II.2.4. *The finite element approach – WF2*

It is clear, from the results showed for the classical weak formulation WF1, that in order to get a correct description of the dynamics of a magnetic system, an improved FE formulation has to be found. The conditions that this new formulation should meet are: a simplified exchange, no constraints on  $\mathbf{v}$  and a time integrator that describes a dissipation scheme. In 2006 Alouges [Alouges 2006, Alouges 2008] proved the feasibility of writing such a weak form and a corresponding integration scheme.

In the weak form WF1 the unknown  $\mathbf{v}$  belonged to the tangent space of the magnetization  $\mathbf{m}$ , whereas the test functions were classical  $\mathbb{R}^3$  vectors, without any restriction on the orientation. Whether this is an important factor or not, it is difficult to determine, as a weak formulation should be valid for any continuous test function. Nevertheless, selecting test functions belonging to the tangential space of  $\mathbf{m}$  could have a benefic effect. Based on this, Alouges developed an original weak formulation for the LLG equations, but taking into account only the exchange term. Noting  $\mathbf{w}'$ , the vector function such that  $(\mathbf{m}, \mathbf{w}', \mathbf{w})$  form a direct trihedron, one can replace in WF1, the test function  $\mathbf{w}$  by  $\mathbf{m} \times \mathbf{w}'$ , knowing that  $\mathbf{m} \cdot \mathbf{w}' = 0$ . Here we present a weak form for the LLG equations derived on the basis of Alouges's work, including all the field terms.

By replacing in (II.46)  $\mathbf{w}$  by  $\mathbf{m} \times \mathbf{w}'$ , the following weak form, noted hereafter WF2, is obtained:

$$\int_{V_m} \alpha \mathbf{w}' \cdot \mathbf{v} dV + \int_{V_m} \mathbf{w}' \cdot (\mathbf{m} \times \mathbf{v}) dV = \int_{V_m} \mu_0 \gamma \mathbf{w}' \cdot \mathbf{H} dV \quad (\text{II.79})$$

The exchange term becomes:

$$\int_{V_m} \mathbf{w}' \cdot \Delta \mathbf{m} dV = \int_{V_m} \nabla (\mathbf{w}' \cdot \nabla \mathbf{m}) dV - \int_{V_m} \nabla \mathbf{w}' \cdot \nabla \mathbf{m} dV = - \int_{V_m} \nabla \mathbf{w}' \cdot \nabla \mathbf{m} dV \quad (\text{II.80})$$

the weak form transforming into:

$$\int_{V_m} \alpha \mathbf{w}' \cdot \mathbf{v} dV + \int_{V_m} \mathbf{w}' \cdot (\mathbf{m} \times \mathbf{v}) dV = - \int_{V_m} \frac{2A_{ex}\gamma}{M_S} \nabla \mathbf{w}' \cdot \nabla \mathbf{m} dV + \int_{V_m} \mu_0 \gamma \mathbf{w}' \cdot \mathbf{H} dV \quad (\text{II.81})$$

where the solution space is  $\{\mathbf{v} \in H^1(V_m)^3: \mathbf{m} \cdot \mathbf{v} = 0\}$  and the test functions are vectors chosen from  $\{\mathbf{w}' \in H^1(V_m)^3: \mathbf{m} \cdot \mathbf{w}' = 0\}$ .

Analyzing WF2, one can easily notice several advantages:

1. The first one is that, the constraints, either that on the magnetization, or the one imposed on  $\mathbf{v}$  in WF1, were eliminated. Thus the process of solving WF2 is straightforward in comparison with solving WF1, where several steps had to be covered before arriving to the final solution.
2. The second advantage lies in the simplicity of the exchange term. As seen earlier, in the case of the WF1 formulation, this term was very sensitive to interpolation errors. Using WF2, one is less exposed to this kind of numerical artifacts, as the exchange term in WF2 contains only  $\nabla \mathbf{m}$ . These advantages make us believe that this weak form is better adapted for dynamic computations than the first one.

To retrieve the magnetization, one proceeds exactly like in the previous case, the vector  $\mathbf{m}^{n+1}$  is reconstructed using  $\mathbf{m}^{n+1} = \mathbf{m}^n + \delta t \mathbf{v}$  and must be normalized at each mesh node.

Three sources of over-damped dynamics were identified in WF1. Using WF2 two of them - the exchange term and the constraints - were eliminated. The last one, related to the integration scheme, will be treated in the following.

The same classical  $\theta$ -scheme is used as before. The magnetization in the exchange term is expressed as  $\mathbf{m}^n + \theta \delta t \mathbf{v}$ , modifying the weak formulation (II.81) as follows:

$$\begin{aligned} \alpha \int_{V_m} \mathbf{w}' \cdot \mathbf{v} dV + \int_{V_m} \mathbf{w}' \cdot (\mathbf{m}^n \times \mathbf{v}) dV + \theta \delta t \int_{V_m} \gamma \frac{2A_{ex}}{M_S} \nabla \mathbf{w}' \cdot \nabla \mathbf{v} dV = \\ - \int_{V_m} \gamma \frac{2A_{ex}}{M_S} \nabla \mathbf{w}' \cdot \nabla \mathbf{m}^n dV + \int_{V_m} \gamma \mu_0 \mathbf{w}' \cdot \mathbf{H}_r \{\mathbf{m}^n\} dV \end{aligned} \quad (\text{II.82})$$

with  $0 \leq \theta \leq 1$ . In particular, for  $\theta=0$  one retrieves an explicit scheme, for  $\theta=1/2$  a Crank-Nicholson-like scheme, and finally  $\theta=1$  represents an implicit integration scheme.

### II.2.4.1. $\theta$ integration scheme for the exchange term

The relaxation process of magnetic systems is assured if the total energy difference,  $\delta E$ , between two consecutive time steps:

$$\delta E = E(\mathbf{m}^{n+1}) - E(\mathbf{m}^n) = E(\mathbf{m}^n + \delta t \mathbf{v}) - E(\mathbf{m}^n) \quad (\text{II.83})$$

is always negative. From a numerical point of view, the behavior of  $\delta E$  can give information about the accuracy and the correctness of the integration scheme, help determining eventual constraints on the time step and finding the most convenient value for the  $\theta$  parameter.  $E$  refers to the total energy, the sum of the exchange, magnetocrystalline, demagnetizing and applied field terms. For sake of simplicity, in a first time only the exchange term is taken into account, both for the weak form and for the energy. The necessary stability conditions will be determined for a first order integration scheme. Next, the same procedure is applied but to all the terms in the weak form. Finally, the requirements for a second order integration scheme are determined.

Before proceeding to the treatment of the exchange energy density, an important remark about the calculation of  $E(\mathbf{m}^{n+1})$  has to be made. Prior to the calculation of this term, the magnetization  $\mathbf{m}^{n+1}$  has to be normalized. Therefore, when calculating the

expression of  $E(\mathbf{m}^{n+1})$ ,  $\mathbf{m}^{n+1}$  stands for  $\frac{\mathbf{m}^n + \mathbf{v} \delta t}{|\mathbf{m}^n + \mathbf{v} \delta t|}$ , or written under a simpler form:

$$\mathbf{m}^{n+1} = \mathbf{m}^n + \mathbf{v} \delta t - \frac{1}{2} \mathbf{m}^n v^2 \delta t^2 \quad (\text{II.84})$$

Taking these into account when writing down the exchange energy

$$E_{ex}(\mathbf{m}) = \int_{V_m} A_{ex} (\nabla \mathbf{m})^2 dV \text{ for } \mathbf{m}^{n+1} \text{ one obtains:}$$

$$\begin{aligned}
E_{ex}(\mathbf{m}^{n+1}) &= \int_{V_m} A_{ex} \left[ \nabla \left( \mathbf{m}^n + \mathbf{v} \delta t - \frac{1}{2} \mathbf{m}^n v^2 \delta t^2 \right) \right]^2 dV \\
&= \int_{V_m} A_{ex} (\nabla \mathbf{m}^n)^2 dV + \delta t \int_{V_m} 2A_{ex} \nabla \mathbf{v} \cdot \nabla \mathbf{m}^n dV + \delta t^2 \int_{V_m} A_{ex} \left[ (\nabla \mathbf{v})^2 - v^2 (\nabla \mathbf{m}^n)^2 \right] dV \\
&= E_{ex}(\mathbf{m}^n) + \delta t \int_{V_m} 2A_{ex} \nabla \mathbf{v} \cdot \nabla \mathbf{m}^n dV + \delta t^2 \int_{V_m} A_{ex} \left[ (\nabla \mathbf{v})^2 - v^2 (\nabla \mathbf{m}^n)^2 \right] dV
\end{aligned} \tag{II.85}$$

In the energy expression above the terms in  $\delta t^3$  and higher were neglected. The exchange energy difference  $\delta E_{ex}$  between two consecutive time steps  $n$  and  $n+1$  is then:

$$\delta E_{ex} = \delta t \int_{V_m} 2A_{ex} \nabla \mathbf{v} \cdot \nabla \mathbf{m}^n dV + \delta t^2 \int_{V_m} A_{ex} \left[ (\nabla \mathbf{v})^2 - v^2 (\nabla \mathbf{m}^n)^2 \right] dV \tag{II.86}$$

Several contributions arise:

- one combines  $\mathbf{v}$  and the magnetization  $\mathbf{m}^n$
- one containing only  $\mathbf{v}$
- one using only  $\mathbf{m}^n$ .

To eliminate the first contribution, the weak formulation (II.82) is written only for the exchange field:

$$\int_{V_m} \alpha \mathbf{w}' \cdot \left( \mathbf{v} + (\mathbf{m}^n \times \mathbf{v}) \right) dV + \theta \delta t \int_{V_m} \gamma \frac{2A_{ex}}{M_S} \nabla \mathbf{w}' \cdot \nabla \mathbf{v} dV = - \int_{V_m} \gamma \frac{2A_{ex}}{M_S} \nabla \mathbf{w}' \cdot \nabla \mathbf{m}^n dV \tag{II.87}$$

In (II.87), the substitution of  $\mathbf{w}'$  by  $\mathbf{v}$ , is a mathematically valid operation, as these two vectors belong to the same subspace. The weak form (II.87) reduces then to:

$$\int_{V_m} \alpha v^2 dV + \theta \delta t \int_{V_m} \gamma \frac{2A_{ex}}{M_S} (\nabla \mathbf{v})^2 dV = - \int_{V_m} \gamma \frac{2A_{ex}}{M_S} \nabla \mathbf{v} \cdot \nabla \mathbf{m}^n dV \tag{II.88}$$

and the first term of  $\delta E_{ex}$  is obtained. (II.86) becomes:

$$\delta E_{ex} = -\delta t \int_{V_m} \alpha \frac{M_S}{\gamma} \mathbf{v}^2 dV - \left( \theta - \frac{1}{2} \right) \delta t^2 \int_{V_m} 2A_{ex} (\nabla \mathbf{v})^2 dV - \delta t^2 \int_{V_m} A_{ex} v^2 (\nabla \mathbf{m}^n)^2 dV \tag{II.89}$$

It is readily seen that, by choosing  $\theta \in [1/2, 1]$  the system's energy is guaranteed to decrease in time. The integration scheme obtained above is of first order. The accuracy of the integration scheme can be improved tuning the value of the  $\theta$  parameter. For example, to

obtain a more precise scheme the value of  $\theta$  is set exactly to  $1/2$ . Doing so, the second term on the right-hand-side of (II.89) is eliminated:

$$\delta E_{ex} = -\delta t \int_{V_m} \alpha \frac{M_s}{\gamma} \mathbf{v}^2 dV - \delta t^2 \int_{V_m} A_{ex} v^2 (\nabla \mathbf{m}^n)^2 dV \quad (\text{II.90})$$

Taking  $\theta$  to be  $1/2$  is equivalent with the substitution of  $\mathbf{m}^*$  with  $\mathbf{m}^{n+1/2} \mathbf{v} \delta t$ . This scheme seems to be close to a second order one, however it remains still of first order, because a  $\delta t^2$  term it is still present in the variation of the energy.

#### II.2.4.2. First order integration scheme including all the field terms

Introducing in the weak formulation for the exchange the rest of the field terms, (keeping however, the  $\theta$  formalism only for the exchange field), new stability conditions will be deduced for the integration scheme. To determine the requirements for having a correct dissipation process for all the energy terms, the above described procedure is followed.

##### *Magnetocrystalline anisotropy term*

To determine the expression of the anisotropy energy at time  $n+1$ , in  $E_{anis}(\mathbf{m}) = -\int_{V_m} K_{anis} ((\mathbf{m} \cdot \mathbf{u}_K)^2) dV$ ,  $\mathbf{m}$  is replaced again by (II.84). Then  $E_{anis}(\mathbf{m}^{n+1})$  becomes:

$$\begin{aligned} E_{anis}(\mathbf{m}^{n+1}) = E_{anis}(\mathbf{m}^n) &- \delta t \int_{V_m} 2K_{anis} (\mathbf{m}^n \cdot \mathbf{u}_K) (\mathbf{v} \cdot \mathbf{u}_K) dV \\ &- \delta t^2 \int_{V_m} K_{anis} (\mathbf{v} \cdot \mathbf{u}_K)^2 dV + \delta t^2 \int_{V_m} K_{anis} v^2 (\mathbf{m}^n \cdot \mathbf{u}_K)^2 dV \end{aligned} \quad (\text{II.91})$$

### The applied field energy term

The energy term arises when a magnetic field acts upon the system. This energy term is given by  $E_{app}(\mathbf{m}) = - \int_{V_m} \mu_0 M_s (\mathbf{m} \cdot \mathbf{H}_{app}) dV$ . Writing this term for  $\mathbf{m}^{n+1}$  the following relationship is obtained:

$$E_{app}(\mathbf{m}^{n+1}) = E_{app}(\mathbf{m}^n) - \delta t \int_{V_m} \mu_0 M_s (\mathbf{v} \cdot \mathbf{H}_{app}) dV + \frac{1}{2} \delta t^2 \int_{V_m} \mu_0 M_s v^2 (\mathbf{m}^n \cdot \mathbf{H}_{app}) dV \quad (\text{II.92})$$

### Demagnetizing energy

To be able to follow a similar path in the treatment of the demagnetizing energy, it is more convenient to first write the demagnetizing field under a different form. As  $\mathbf{H}_{dem}$  depends linearly on  $\mathbf{m}$ , one can write it as  $-M_s L \mathbf{m}$ , where  $L$  is a symmetric ( $L^t = L$ ) and positive  $\int \mathbf{v} \cdot L(\mathbf{v}) \geq 0$  operator. The demagnetizing energy density takes then the form

$E_{dem}(\mathbf{m}) = \frac{1}{2} \int_{V_m} \mu_0 M_s^2 \mathbf{m} \cdot L(\mathbf{m}) dV$ . Replacing  $\mathbf{m}$  by the normalized  $\mathbf{m}^{n+1}$  one obtains:

$$\begin{aligned} E_{dem}(\mathbf{m}^{n+1}) &= E_{dem}(\mathbf{m}^n) + \frac{1}{2} \delta t \int_{V_m} \mu_0 M_s^2 (\mathbf{v} \cdot L(\mathbf{m}^n) + \mathbf{m}^n \cdot L(\mathbf{v})) dV \\ &\quad + \frac{1}{2} \delta t^2 \int_{V_m} \mu_0 M_s^2 \mathbf{v} \cdot L(\mathbf{v}) dV - \frac{1}{2} \delta t^2 \int_{V_m} \mu_0 M_s^2 v^2 \mathbf{m}^n \cdot L(\mathbf{m}^n) dV \end{aligned} \quad (\text{II.93})$$

If  $L$  is a symmetric operator, then:

$$\mathbf{m}^n \cdot L(\mathbf{v}) + \mathbf{v} \cdot L(\mathbf{m}^n) = \mathbf{v} \cdot L^t(\mathbf{m}^n) + \mathbf{v} \cdot L(\mathbf{m}^n) = 2 \mathbf{v} \cdot L(\mathbf{m}^n) \quad (\text{II.94})$$

and (II.93) becomes:

$$\begin{aligned} E_{dem}(\mathbf{m}^{n+1}) &= E_{dem}(\mathbf{m}^n) + \delta t \int_{V_m} \mu_0 M_s^2 \mathbf{v} \cdot L(\mathbf{m}^n) dV \\ &\quad + \frac{1}{2} \delta t^2 \int_{V_m} \mu_0 M_s^2 \mathbf{v} \cdot L(\mathbf{v}) dV - \frac{1}{2} \delta t^2 \int_{V_m} \mu_0 M_s^2 v^2 \mathbf{m}^n \cdot L(\mathbf{m}^n) dV \end{aligned} \quad (\text{II.95})$$

In the energy expressions above the terms in  $\delta t^3$  and higher were neglected. The next step is to assemble all the energy contributions (including the exchange):

$$\begin{aligned}
\delta E = & \delta t \int_{V_m} 2A_{ex} \nabla \mathbf{v} \cdot \nabla \mathbf{m}^n dV + \delta t^2 \int_{V_m} A_{ex} (\nabla \mathbf{v})^2 dV - \delta t^2 \int_{V_m} A_{ex} v^2 (\nabla \mathbf{m}^n)^2 dV \\
& - \delta t \int_{V_m} 2K_{anis} (\mathbf{m}^n \cdot \mathbf{u}_K) (\mathbf{v} \cdot \mathbf{u}_K) dV - \delta t^2 \int_{V_m} K_{anis} \left[ (\mathbf{v} \cdot \mathbf{u}_K)^2 + v^2 (\mathbf{m}^n \cdot \mathbf{u}_K)^2 \right] dV \\
& + \delta t \int_{V_m} \mu_0 M_S^2 \mathbf{v} \cdot L(\mathbf{m}^n) dV + \frac{1}{2} \delta t^2 \int_{V_m} \mu_0 M_S^2 \left[ \mathbf{v} \cdot L(\mathbf{v}) - v^2 \mathbf{m}^n \cdot L(\mathbf{m}^n) \right] dV \\
& + \delta t \int_{V_m} \mu_0 M_S (\mathbf{v} \cdot \mathbf{H}_{app}) dV + \frac{1}{2} \delta t^2 \int_{V_m} \mu_0 M_S v^2 (\mathbf{m}^n \cdot \mathbf{H}_{app}) dV
\end{aligned} \tag{II.96}$$

Like in the simplified case of the exchange term, again three contributions are identified: terms combining the magnetization at time  $n$  and  $\mathbf{v}$ , contributions based only on  $\mathbf{v}$  and eventually those containing only  $\mathbf{m}^n$ . The combined term can be eliminated if one transforms the weak form (II.81) by substituting the test function  $\mathbf{w}'$  by  $\mathbf{v}$ :

$$\begin{aligned}
& \int_{V_m} \gamma \frac{2A_{ex}}{M_S} \nabla \mathbf{v} \cdot \nabla \mathbf{m}^n dV - \int_{V_m} \gamma \mu_0 \mathbf{v} \cdot \left( H_{anis} (\mathbf{m}^n \cdot \mathbf{u}_K) \mathbf{u}_K - M_S L(\mathbf{m}^n) + \mathbf{H}_{app} \right) dV \\
& = -\alpha \int_{V_m} v^2 dV - \theta \delta t \int_{V_m} \gamma \frac{2A_{ex}}{M_S} (\nabla \mathbf{v})^2 dV
\end{aligned} \tag{II.97}$$

with  $H_{anis} = \frac{2K_{anis}}{\mu_0 M_S}$ . Introducing this in (II.96), a simpler form of  $\delta E$  is obtained:

$$\begin{aligned}
\delta E = & -\delta t \int_{V_m} \alpha \frac{M_S}{\gamma} v^2 dV \\
& - \delta t^2 \left( \theta - \frac{1}{2} \right) \int_{V_m} A_{ex} (\nabla \mathbf{v})^2 dV - \delta t^2 \int_{V_m} A_{ex} v^2 (\nabla \mathbf{m}^n)^2 dV \\
& - \delta t^2 \int_{V_m} K_{anis} (\mathbf{v} \cdot \mathbf{u}_K)^2 dV + \delta t^2 \int_{V_m} K_{anis} v^2 (\mathbf{m}^n \cdot \mathbf{u}_K)^2 dV \\
& + \frac{1}{2} \delta t^2 \int_{V_m} \mu_0 M_S^2 \mathbf{v} \cdot L(\mathbf{v}) dV - \frac{1}{2} \delta t^2 \int_{V_m} \mu_0 M_S^2 v^2 \mathbf{m}^n \cdot L(\mathbf{m}^n) dV \\
& + \frac{1}{2} \delta t^2 \int_{V_m} \mu_0 M_S v^2 (\mathbf{m}^n \cdot \mathbf{H}_{app}) dV
\end{aligned} \tag{II.98}$$

Knowing that  $\int_{V_m} A_{ex} v^2 (\nabla \mathbf{m}^n)^2 dV$  and  $\int_{V_m} \mu_0 M_S^2 v^2 \mathbf{m}^n \cdot L(\mathbf{m}^n) dV$  are both positive quantities, an upper limit for  $\delta E$  is established:



$$\begin{aligned}
\delta E \leq & -\delta t \int_{V_m} \alpha \frac{M_s}{\gamma} v^2 dV - \delta t^2 \left( \theta - \frac{1}{2} \right) \int_{V_m} A_{ex} (\nabla \mathbf{v})^2 dV \\
& - \delta t^2 \int_{V_m} K_{anis} (\mathbf{v} \cdot \mathbf{u}_K)^2 dV + \frac{1}{2} \delta t^2 \int_{V_m} \mu_0 M_s^2 \mathbf{v} \cdot L(\mathbf{v}) dV \\
& + \frac{1}{2} \delta t^2 \int_{V_m} \mu_0 M_s v^2 (\mathbf{m}^n \cdot \mathbf{H}_{app}) dV
\end{aligned} \tag{II.99}$$

From (II.99) a first order integration scheme is easily established. Such a scheme should meet the following requirements:

- $\theta \in [1/2, 1]$  to assure a dissipative behavior of the exchange term

$$\begin{aligned}
\text{➤ } \delta t < & \frac{\int_{V_m} \alpha \frac{M_s}{\gamma} v^2 dV}{-\int_{V_m} K_{anis} (\mathbf{v} \cdot \mathbf{u}_K)^2 dV + \frac{1}{2} \int_{V_m} \mu_0 M_s^2 \mathbf{v} \cdot L(\mathbf{v}) dV + \frac{1}{2} \delta t^2 \int_{V_m} \mu_0 M_s v^2 (\mathbf{m}^n \cdot \mathbf{H}_{app}) dV} \quad \text{for} \\
& \text{stability.}
\end{aligned}$$

The condition on the time step plays a very important role. The demagnetizing contribution is the most problematic, as it necessitates the evaluation of this field not based on the magnetization, but based on  $\mathbf{v}$ . This problematic condition can be removed if a fully second order integration scheme is used.

#### II.2.4.3. Second order integration scheme for the exchange field

The steps to follow when deriving a second order integration scheme are demonstrated again only on the exchange term. A second order integration scheme supposes the extra term in  $\delta t^2$  to be removed from (II.90). Jaisson [Jaisson] proposed to do this modifying the weak formulation as follows:

1. the  $\theta$  parameter is set to 1/2
2. a term that depends on the exchange energy density is included in (II.87), resulting in a new weak form that looks like:

$$\int_{V_m} \alpha \mathbf{w}' \cdot (\mathbf{v} + (\bar{\mathbf{m}} \times \mathbf{v})) dV + \int_{V_m} \gamma \frac{2A_{ex}}{M_s} \nabla \mathbf{w}' \cdot \nabla \bar{\mathbf{m}} dV = \delta t \int_{V_m} \gamma \frac{A_{ex}}{M_s} (\nabla \mathbf{m}^n)^2 \mathbf{w}' \cdot \mathbf{v} dV \tag{II.100}$$

Here  $\bar{\mathbf{m}}$  stands for  $\mathbf{m}^{n+1/2}\mathbf{v}\delta t$ . It is easily seen that, using this weak form to evaluate the terms combining  $\mathbf{v}$  and  $\mathbf{m}^n$ , the variation of the exchange energy between two consecutive time steps agrees with the physical energy loss:

$$\delta E_{ex} = -\delta t \int_{V_m} \alpha \frac{M_s}{\gamma} v^2 dV \quad (\text{II.101})$$

After exemplifying the procedure of deriving a second order scheme for the exchange term we pass now to the next step: determining the terms to be added in the weak form in order to have such an integration scheme for all the field terms.

#### II.2.4.4. Second order integration scheme for all the field terms

In a first time, the explicit field expressions are introduced in the weak form and  $\mathbf{w}'$  is substituted with  $\mathbf{v}$ :

$$\int_{V_m} \alpha v^2 dV = \int_{V_m} \gamma \frac{2A_{ex}}{M_s} \nabla \mathbf{v} \cdot \nabla \mathbf{m} dV - \int_{V_m} \mu_0 \gamma \mathbf{v} \cdot \left( H_{anis} (\mathbf{m} \cdot \mathbf{u}_K) \mathbf{u}_K - M_s \hat{L} \mathbf{m} + \mathbf{H}_{app} \right) dV \quad (\text{II.102})$$

$\mathbf{m}$  is then replaced with  $\mathbf{m}^{n+1/2} \mathbf{v} \delta t$ :

$$\begin{aligned} \int_{V_m} \alpha v^2 dV &= \int_{V_m} \gamma \frac{2A_{ex}}{M_s} \nabla \mathbf{v} \cdot \nabla \mathbf{m}^n dV + \frac{1}{2} \delta t \int_{V_m} \gamma \frac{2A_{ex}}{M_s} (\nabla \mathbf{v})^2 dV \\ &\quad - \int_{V_m} \mu_0 \gamma H_{anis} (\mathbf{v} \cdot \mathbf{u}_K) (\mathbf{m}^n \cdot \mathbf{u}_K) dV - \frac{1}{2} \delta t \int_{V_m} \mu_0 \gamma H_{anis} (\mathbf{v} \cdot \mathbf{u}_K)^2 dV \\ &\quad + \int_{V_m} \mu_0 \gamma M_s \mathbf{v} \cdot \hat{L} \mathbf{m}^n dV + \frac{1}{2} \delta t \int_{V_m} \mu_0 \gamma M_s \mathbf{v} \cdot \hat{L} \mathbf{v} dV \\ &\quad - \int_{V_m} \mu_0 \gamma M_s \mathbf{v} \cdot \mathbf{H}_{app} dV \end{aligned} \quad (\text{II.103})$$

Comparing with  $\delta E$  as given in (II.96), one sees that the  $\delta t^2$ -terms combining  $\mathbf{v}$  and  $\mathbf{m}^n$  and those containing only  $\mathbf{v}$  disappear indeed. However, the terms in  $\mathbf{m}^n$  remain. For that reason, in the weak formulation some supplementary terms are introduced. Noting

$\bar{\mathbf{m}} = \mathbf{m}^n + \frac{1}{2} \delta t \mathbf{v}$  the appropriate weak formulation is:

$$\begin{aligned}
& \alpha \int_{V_m} \mathbf{w} \cdot (\mathbf{v} + \bar{\mathbf{m}} \times \mathbf{v}) dV + \int_{V_m} \gamma \frac{2A_{ex}}{M_s} \nabla \mathbf{w} \cdot \nabla \bar{\mathbf{m}} - \int_{V_m} \mu_0 \mathbf{w} \cdot \left( H_{anis} (\bar{\mathbf{m}} \cdot \mathbf{u}_K) \mathbf{u}_K - M_s \hat{L} \bar{\mathbf{m}} + \mathbf{H}_{app} \right) dV = \\
& = \frac{1}{2} \delta t \int_{V_m} \mathbf{w} \cdot \mathbf{v} \left( \frac{2A}{M_s} \gamma (\nabla \mathbf{m}^n)^2 - H_{anis} (\mathbf{m}^n \cdot \mathbf{u}_K)^2 + \mu_0 M_s \mathbf{m}^n \cdot \hat{L}(\mathbf{m}^n) - \mu_0 (\mathbf{m}^n \cdot \mathbf{H}_{app}) \right) dV \\
& \quad \quad \quad (II.104)
\end{aligned}$$

for which  $\delta E = -\delta t \int_{V_m} \alpha \frac{M_s}{\gamma} \mathbf{v}^2 dV + \vartheta(\delta t^3)$ . The terms on the right-hand-side correspond

in fact to the total energy density in the case of uniaxial magnetocrystalline anisotropy.

For the moment, in the WF2 implementation, only the first order scheme with all the terms is included. The implementation of the second order scheme is left for future work, as the demagnetizing term raises some serious issues.

The WF2 implementation was carried out using the C++ language. The solving process comports the same steps as those presented in the flowchart for the WF1 implementation (Figure II.9). However a few particularities appear: when solving the demagnetizing problem first a preconditionner is used (ILU from the GMM++ library). The GMRES solver (from the GMM++ library) is then employed for determining  $\mathbf{H}_{dem}$ . For the micromagnetic part the use of a preconditionner was not necessary, the solution being sought using the same GMRES solver [GMM++ site]

In the next part, the WF2 implementation will be tested, first on the two model systems used to benchmark the WF1 approach. Then other stripe domain structures, with more or less complex geometries, will be analyzed, both by WF2-based static and dynamic simulations.

## II.2.5. Applications WF2

### II.2.5.1. *Infinite prism*

To check the performance of the WF1 approach two test cases were chosen. The importance of calculating a correct exchange term has been revealed by the simple geometry consisting of a square-sectioned infinite prism  $2\text{nm} \times 2\text{nm}$ , with only the exchange interaction acting upon the magnetic moments. For this simple test case already, an unphysically over-damped motion was calculated with WF1. Figure II.22 shows a comparison between the results obtained applying the WF2 and the FD approach to the LLG equation. The WF1 results are also reminded here.

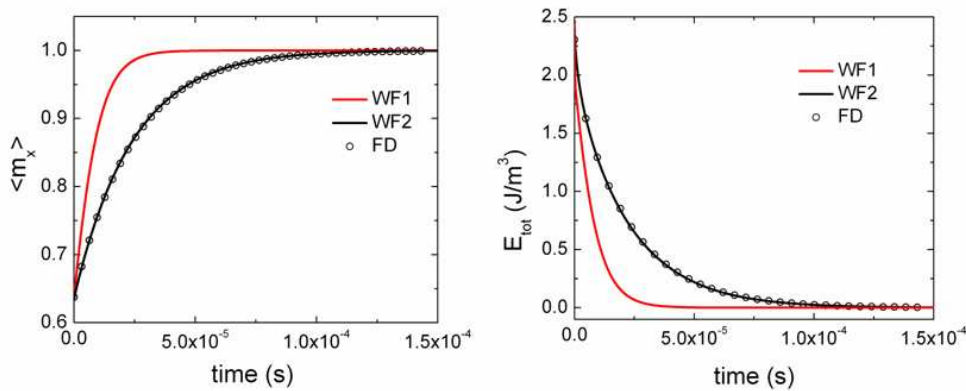


Figure II.22: Time evolution of the  $\langle m_x \rangle$  magnetization component and the total energy density for a damping parameter  $\alpha=0.02$ .

The simulations were carried out using the same mesh size, the approximate number of mesh elements in the FE approaches reaching 1000, while for the FD case their number rises up to 250. Figure II.22 shows clearly that, for this simple test case, the WF2 and FD results are in a very good agreement. The equilibrium state values are very close: 1 was the value obtained for  $m_x$  at equilibrium, with all three approaches, whereas for the energy density the final value is basically 0 ( $\approx 10^{-4}$  for FD and  $\approx 10^{-5}$  for WF1 and WF2). Both for the  $\langle m_x \rangle$  magnetization component and the energy density, the WF2 and FD curves are perfectly superposed, and consequently, equally distanced from the over-damped WF1 curve. Therefore, one can presume that WF2 is a better candidate for micromagnetic

simulations that WF1. Nevertheless, before jumping to conclusions, the results of the second test case will also be examined.

### II.2.5.2. Stripe domains structure

For the second test case, the stripe domains, to make sure that the WF1 issued over-damped motion is not reproduced, the relaxation process for several small values of the damping parameter was investigated in detail. The results for these dynamic computations (the damping parameter equal to 0.05 and 0.03) are presented in Figure II.23.

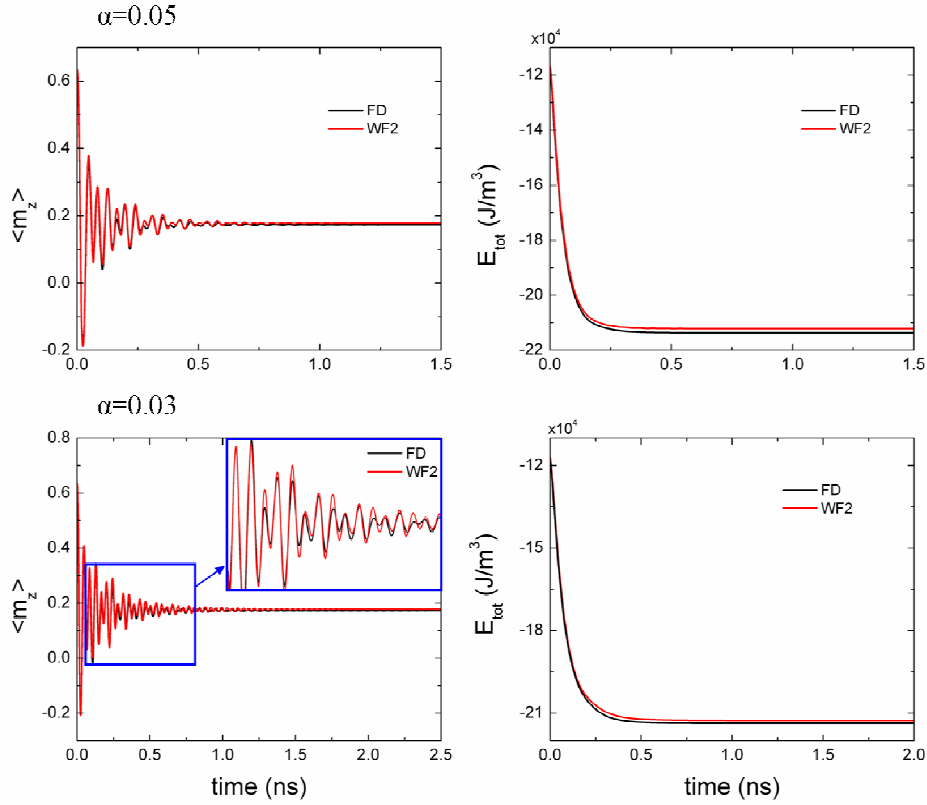


Figure II.23: Evolution of the  $\langle m_z \rangle$  magnetization distribution and the average total energy density versus time for  $\alpha=0.05$  and  $\alpha=0.03$ .

The comparison is very satisfying as WF2 follows appropriately the dynamics given by the FD approach, for all given values of the damping parameter. Even though, from time to time small differences appear in the  $\langle m_z \rangle$  versus time curves, the characteristic times are the correct ones and the equilibrium states match. The time evolution of the total energy is

consistent with a dissipation process towards equilibrium. The evolutions of the separate energy terms (depicted in Figure II.24) present a similar good agreement:

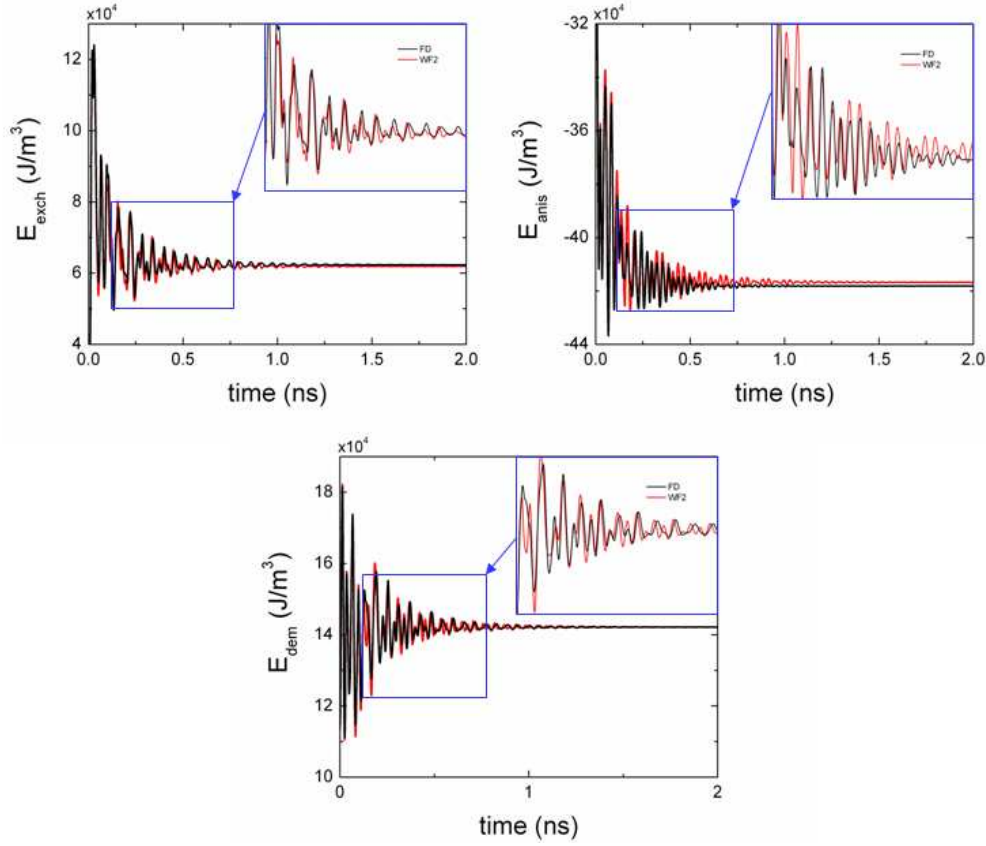


Figure II.24: The exchange, magnetocrystalline anisotropy and demagnetizing energy densities versus time. The value of the damping parameter is 0.03.

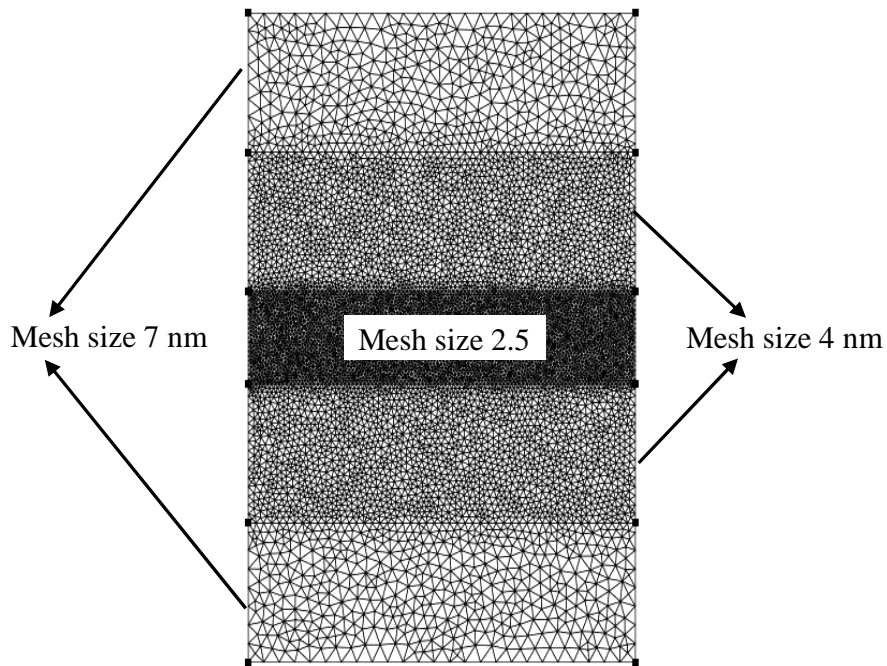
The values of the average  $m_z$  magnetization value and the energy densities at equilibrium, together with the relative difference are listed in Table II.4:

Table II.4: Equilibrium values of  $\langle m_z \rangle$  and the energy densities.

	$\langle m_z \rangle$	$E_{\text{tot}} (\text{J/m}^3) \cdot 10^5$	$E_{\text{ex}} (\text{J/m}^3) \cdot 10^4$	$E_{\text{anis}} (\text{J/m}^3) \cdot 10^5$	$E_{\text{dem}} (\text{J/m}^3) \cdot 10^5$
FD	0.1742	-2.1358	6.2365	-4.1812	1.4216
WF2	0.1771	-2.1258	6.1941	-4.1672	1.4219
Error	1.6%	0.5%	0.7%	0.3%	0.02%

For the WF2 approach, when determining the demagnetizing field, both methods dealing with the condition at infinity on the magnetic scalar potential (the truncation

method and the method based on space transformations) were implemented. The model system used for the truncation method is the same as in Figure II.13, whereas the model system used for the geometrical transformations (described in the paragraph II.2.1.1) is presented in Figure II.25. This consists of the magnetic system and four smaller regions, with a dimension of  $200\text{nm} \times 60\text{ nm}$ , attached two - to the upper side and two - to the lower side of the magnetic system. The mesh size in the magnetic system was  $2.5\text{ nm}$ , whereas in the vacuum regions that are the closest to the magnetic system the mesh size was  $4\text{ nm}$  and in the exterior vacuum regions the size of the elements goes as high as  $7.5\text{ nm}$ .



*Figure II.25: FE model system and mesh used when handling the regularity condition of the scalar potential at infinity with space transformations.*

The WF2 results shown in Figure II.23 and Figure II.24 were obtained using spatial transformations. We showed only these, as it seems that the results are little dependent on the method used for handling the boundary condition at infinity. Figure II.26 shows the evolution of several elements (magnetization components and total energy density) obtained applying the two different methods for the demagnetizing field:

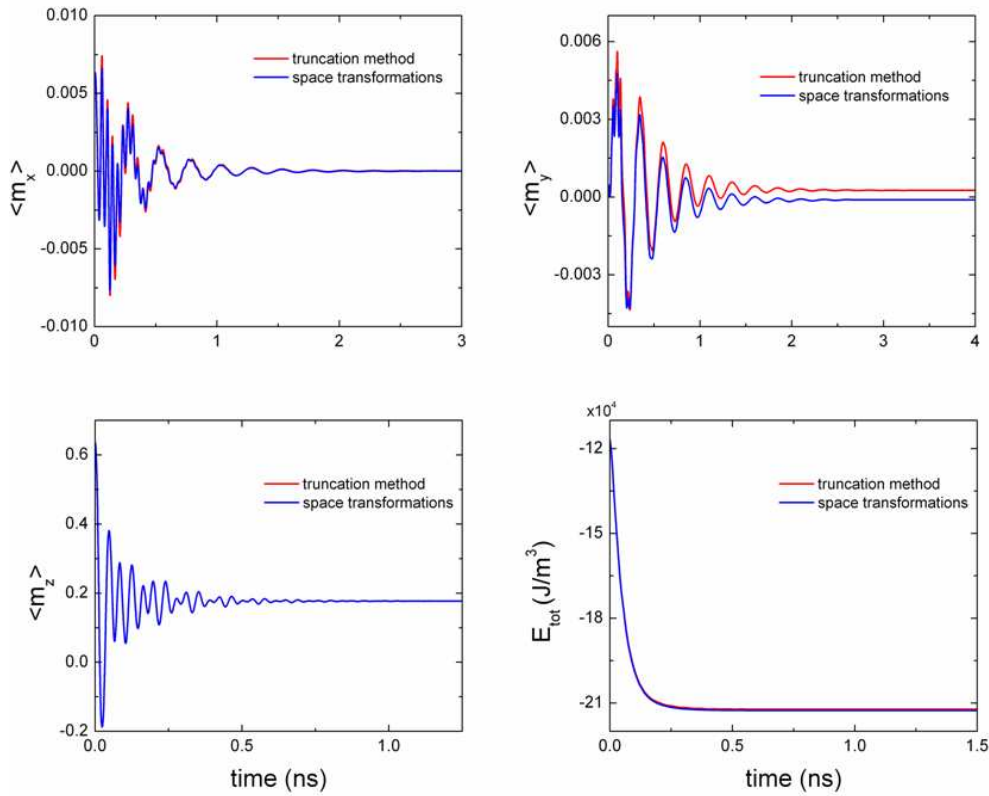


Figure II.26: Comparison of the results obtained using the truncation method, and respectively space transformations for handling the cancellation of  $\Phi$  at infinity. The value of the damping parameter was set to 0.05.

For the  $\langle m_x \rangle$  and the  $\langle m_z \rangle$  magnetization components the differences are almost inexistent. The same is true for the total energy density. For the  $\langle m_y \rangle$  contribution, due mostly to the magnetization in the domains, a gap between the two methods is found, but this is of the order of  $10^{-4}$ .

Besides the comparison of averaged values, magnetization distributions taken at specified times were also examined. Several configurations are presented in Figure II.27. On the left-hand side are the FD configurations, whereas on the right-hand side - the WF2 results are shown. A simple qualitative observation reveals the same good agreement as the one seen before from the relaxation process. The presented configurations were obtained for a damping parameter equal to 0.03 and they show the very important changes that the magnetic system goes through during the relaxation process (see for example the third configuration, where the vortex core extends only over a couple of mesh elements).



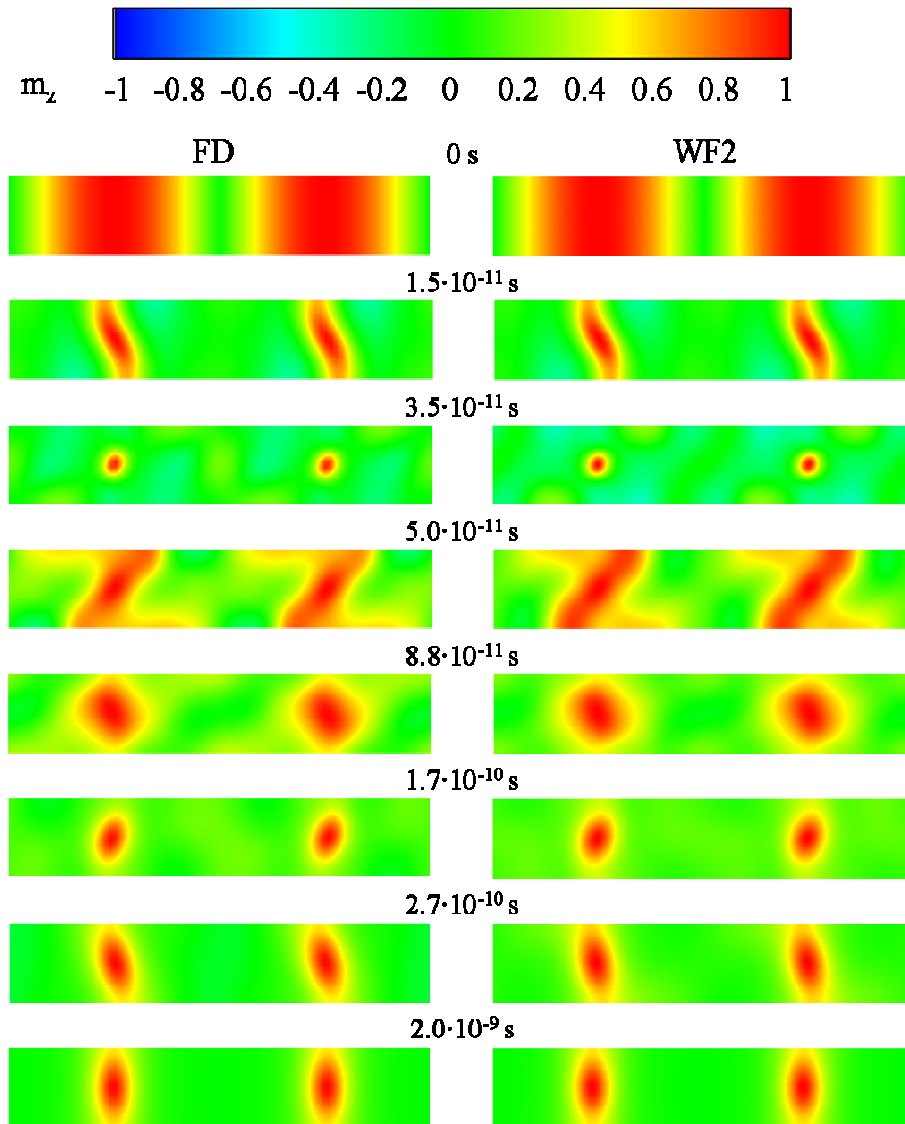


Figure II.27: Magnetization distributions taken at specified time steps. The color scale corresponds to the  $m_z$  magnetization component.

Sampling the WF2 results on the grid corresponding to the FD method, the angle between the equilibrium magnetizations was evaluated, shown in Figure II.28

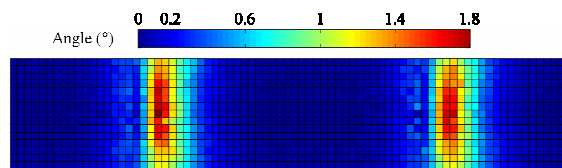


Figure II.28: The angle between the FD and the WF2 magnetization vectors.

This angle varies between  $0.03^\circ$  and  $1.8^\circ$ . The most important differences are in the regions where the domain walls are placed, understandable if one takes into account the significant changes affecting all the energy terms in these regions.

The conclusion of this study, based on the comparison of the evolution of averaged values and the comparison of magnetic configurations taken at certain time steps, is that, the stripe domain structure characterized by the material parameters given in Table II.2 is accurately described by the FE approach based on the weak formulation WF2.

### *II.2.5.3. Stripe domains structure with moderate magnetocrystalline anisotropy*

The good results obtained for the first two test cases encouraged us to apply the WF2 approach to a second stripe domain configuration, characterized by the material parameters presented in Table II.5. They correspond, in fact, to a FePd material with the equilibrium period of 110 nm [Gehanno 1997, Hubert 1998, Ebels 1999, Vukadinovic 2000].

*Table II.5: Material parameters*

$A_{ex}$ (J/m)	$\mu_0 M_S$ (T)	$K_{anis}$ (J/m <sup>3</sup> )	$l_{ex}$ (nm)	$l_B$ (nm)	$Q$
$0.7 \cdot 10^{-11}$	1.31	$2.4 \cdot 10^5$	3.2	5.4	0.35

The same initial magnetization distribution is used as before. The equilibrium configuration, depicted in Figure II.29, differs significantly from the previous stripe domain system. The vortices are rather circular, not elongated, allowing the flux closure domains to occupy a large surface. This appears because of the moderate value of the out-of-plane anisotropy and it is imposed by the important magnetostatic interactions.

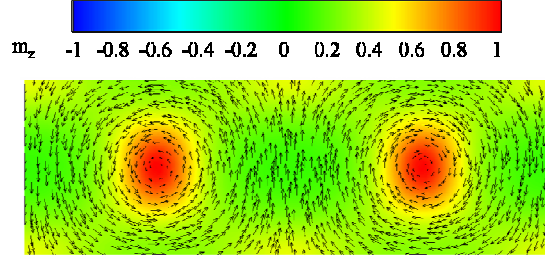


Figure II.29: Equilibrium configuration for a stripe domain system characterized by the material parameters listed in Table II.5. The color surface represents the  $m_z$  component, whereas the arrows correspond to  $m_x$  and  $m_y$ .

Since the damping parameter for this system is known,  $\alpha=0.02$ , we are interested, primarily, in verifying if for this  $\alpha$  the dynamics calculated with the FD and WF2 approaches corresponds. The evolution of  $\langle m_z \rangle$  and of the total energy density is represented in Figure II.30, indicating a very good agreement.

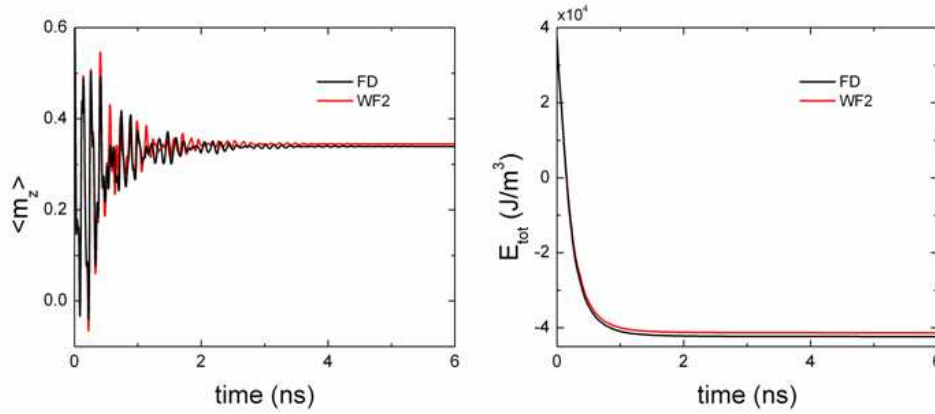


Figure II.30: The evolution of  $\langle m_z \rangle$  and of the total energy density versus time for  $\alpha=0.02$ .

For the magnetization component, the oscillations seen in the FD curve are reproduced in a great part by the WF2 approach. Obviously, differences are expected to appear because of the entirely dissimilar anatomy of the two methods. Still the equilibrium states are very close, the energy gap between the FD and the WF2 state being around 2%. The evolution of the exchange, anisotropy and demagnetizing energy densities, presented in Figure II.31, sustain the same conclusion of a good description of this stripe domain structure.

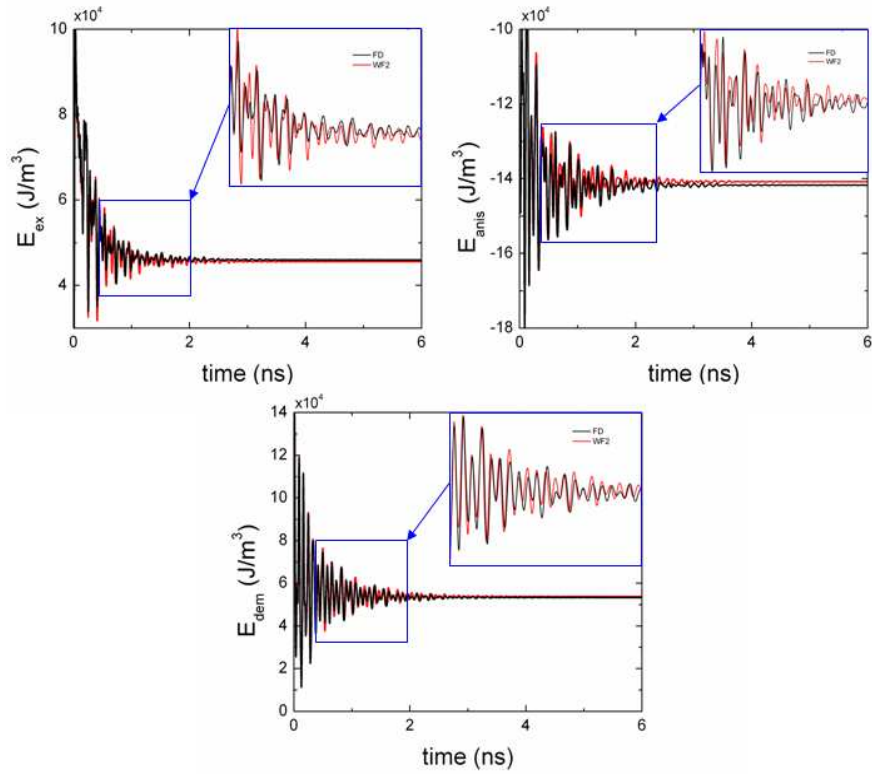


Figure II.31: Relaxation of the separate energy terms for a damping parameter of 0.02.

The equilibrium state values and the relative difference between them are given in Table II.6.

Table II.6: Equilibrium state values.

	$\langle m_z \rangle$	$E_{\text{tot}} (\text{J/m}^3) \cdot 10^4$	$E_{\text{ex}} (\text{J/m}^3) \cdot 10^4$	$E_{\text{anis}} (\text{J/m}^3) \cdot 10^4$	$E_{\text{dem}} (\text{J/m}^3) \cdot 10^4$
FD	0.33975	-4.2303	4.6022	-14.1681	5.3355
WF2	0.34506	-4.1320	4.5612	-14.0776	5.3843
Error	1.6%	2.3%	0.9%	0.6%	0.9%

Evaluating averaged quantities revealed a good accord between the FD and WF2 approaches. Still, the equilibrium states have to be compared. Based on the same procedure as before, the WF2 was sampled on a grid corresponding to the FD mesh. Figure II.32 represents the angle formed by the FD and WF2 magnetization vectors determined in each mesh node:

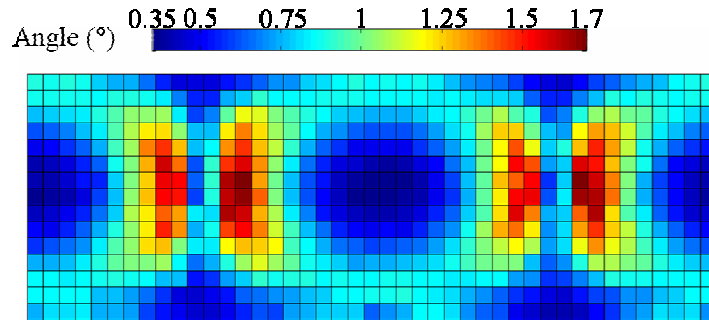


Figure II.32: Angle between the FD magnetization vector and the WF2 magnetization sampled on a grid corresponding to the FD space discretization.

The maximal angle is of  $1.7^\circ$ , situated again in the vortices' neighborhood. Small differences (up to  $1^\circ$ ) are also observable in the region surrounding the magnetic domains. In the domains and the quite large flux-closure domains the orientation of the magnetization is uniform over a relatively large area, whereas in the walls and around the domains the magnetization is turning, and therefore small differences are acceptable.

One can conclude that, based on the comparison of the relaxation process and also of equilibrium configurations, the agreement between the two results is very good and therefore the WF2 description of this second stripe domain structure is accurate.

#### II.2.5.4. Constricted stripe domains

Until now, our FE approach based on the weak form WF2 was tested only on simple rectangular geometries. We apply it now to a constricted system, as such magnetic systems are very common in experiments, and therefore their study is of large interest.

The main advantage of the FE method is that it imposes no restrictions on the geometry to be simulated. In principle, the FD discretization can more difficultly reproduce surface roughness, as the round boundaries are subject to the *staircase approximation* [García-Cervera 2003].

The test case chosen consists of a thin film with periodic constrictions. The constrictions are quite large and smooth, so that the geometry is still rather far from the rough samples occurring in experiments. The model systems (for the FE case only the

magnetic system is represented), after discretization are shown in the Figure II.33. It is clear that the curved boundaries are much better described using a finite element mesh.

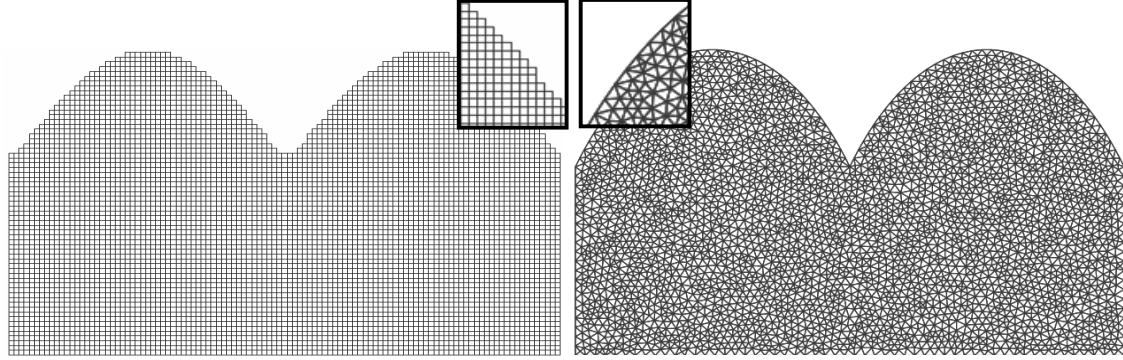


*Figure II.33: FD and FE meshing of a constricted thin film. A zoom on the surface shows how the constriction is reproduced by the mesh.*

The geometrical characteristics of the system are: length 110 nm, full thickness 65 nm and thickness at the base of the constriction 40 nm. The material parameters considered for this system are the same as before (Table II.5). The starting magnetization configuration is the same as the one considered for the regular geometry.

A comparison between the two relaxation processes obtained by FD and WF2 calculations is shown in Figure II.34 for a damping parameter equal to 0.02. The  $\langle m_z \rangle$  magnetization component is represented, together with the total energy density and also the separate energy terms. There are certain discrepancies between the evolutions, related, most likely, to the different geometrical description of the system. The results presented above were obtained using an FD mesh size of 1 nm, while for the WF2 implementation the mesh consisted of elements of 2.2 nm (the micromagnetic rule of thumb imposes a space step smaller than 3 nm). Increasing the FD space step to 2.2 nm results in a dramatic decrease of the concordance between the results. The mismatch is important especially in the demagnetizing energy, where the relative difference becomes two times larger than the value obtained for the finer mesh.

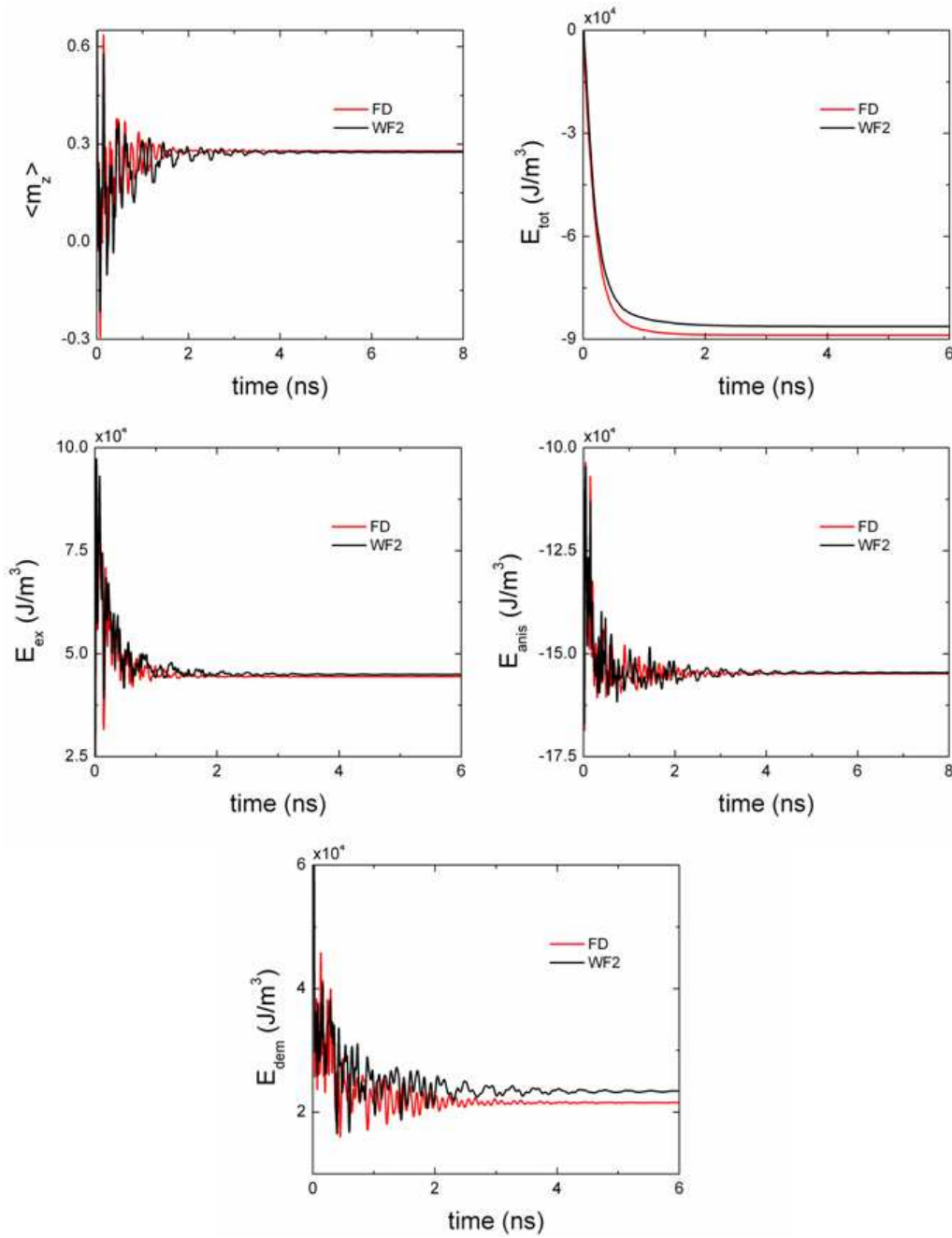


Figure II.34: The evolution of the  $m_z$  magnetization component and the energy densities for the constricted thin film. The damping parameter is set 0.02.

The equilibrium state values are listed in Table II.7 (the relative difference marked in *italic*). The big discrepancy in the demagnetizing energy is a clear indicator of the negative influence of the staircase approximation induced by the regular discretization used in the FD method. It is known that, the most ravaging effects appear for the

demagnetizing and exchange terms [García-Cervera 2003]. Therefore, while for the previous test cases, the FD result was always taken as reference, for this constricted geometry the WF2 approach should be considered the correct one.

Table II.7: Equilibrium state values.

	$\langle m_z \rangle$	$E_{\text{tot}}$ (J/m <sup>3</sup> )·10 <sup>4</sup>	$E_{\text{ex}}$ (J/m <sup>3</sup> )·10 <sup>4</sup>	$E_{\text{anis}}$ (J/m <sup>3</sup> )·10 <sup>5</sup>	$E_{\text{dem}}$ (J/m <sup>3</sup> )·10 <sup>4</sup>
FD	0.2692	-8.3446	4.5152	-1.5448	2.5887
WF2	0.2726	-8.5949	4.5648	-1.5471	2.7906
mesh size 1nm	1.3%	3%	1.1%	0.15%	7.8%
WF2	0.2795	-8.8777	4.5829	-1.5479	3.0210
mesh size 2.2nm	3.8%	6.4%	1.5%	0.2%	16.7%

Concerning the equilibrium states, given in Figure II.35, it is a quite surprising situation:

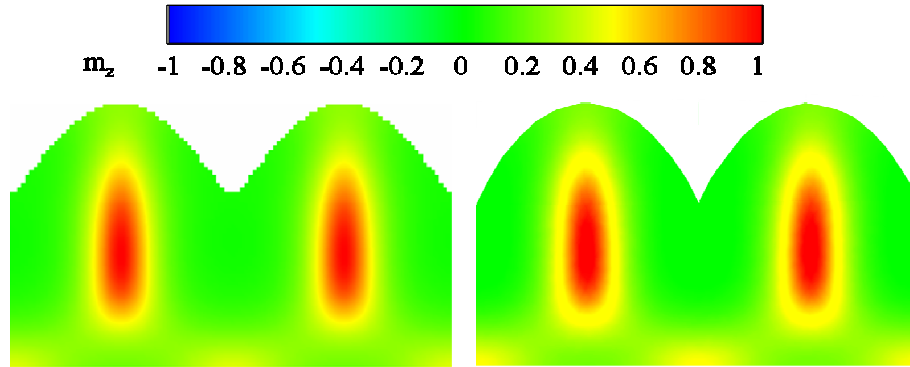


Figure II.35: Equilibrium state: on the left the FD configuration and on the right the WF2 result.

One would have expected the domain walls to translate during relaxation, placing themselves in the constricted region. Normally, this would minimize the wall surface, and consequently the wall energy. In the present case, however, such a positioning, instead of reducing the total energy of the magnetic system, it would increase it, because of the important magnetostatic effects that would appear on the system's surface. Comparing the FD and the WF2 equilibrium states, they are quite similar. Small differences appear in the



vortices, as they seem to be slightly wider in the FD configuration. Also in the regions where the domains are situated, close to the lower un-constricted boundary, the yellow parts are less enhanced in the FD state than in the FE equilibrium configuration.

Proceeding to the sampling the WF2 results on the grid corresponding to the FD discretization, a more quantitative comparison is possible. The values of the angle formed by the magnetization vectors are shown in the Figure II.36.

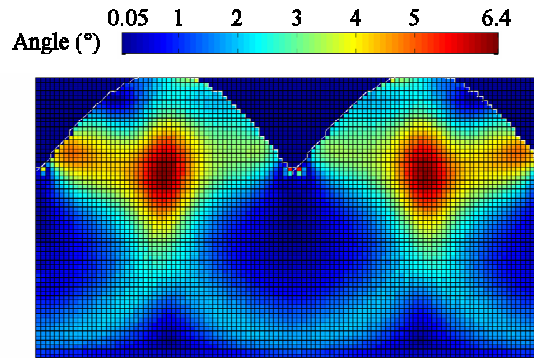


Figure II.36: The angle formed by the two equilibrium magnetization vectors.

The comparison concords with the qualitative observations based on the simple “naked eye” analysis of the equilibrium states. It shows that the main discrepancies are localized at the surface of the constricted region and in the zone neighboring the vortices’. The angle goes up to  $6.4^\circ$ . Like in the previous cases, this is due to the strong perturbation of the exchange interaction, as the magnetization varies rapidly in the region where the walls are placed, and also to the demagnetizing term playing a very important role in this system ( $J_S=1.3\text{T}$ ).

#### II.2.5.5. Numerical ferromagnetic resonance

Continuing to test the WF2 approach, this last part concerns further studies of the magnetization dynamics in FePd materials. The effect of small perturbations will be studied. From such data interesting information can be extracted about the value of the damping parameter. In the following, we will check if the WF2 properly reproduces previous experimental and numerical findings [Vukadinovic 2000a, Vukadinovic 2000b, Vukadinovic 2001, Ebels 2001] on a simple FePd thin film. Then, the same type of

simulations is carried out on the thin film with periodical constrictions. These results are presented in the last part of this paragraph.

Nowadays two experimental techniques are used to determine  $\alpha$ , either based on the broadening of the linewidth in ferromagnetic resonance (FMR) experiments or measuring the domain-wall mobility [Malozemoff 1979, Bokov 1998]. It is worth noting that the values determined with these two methods are usually different, [Dourlat 2008] being difficult to name which of the two methods is the correct one. In the following paragraph the principle of the FMR technique is presented together with the numerical approaches treating this topic.

The FMR technique is a very powerful tool for investigating magnetization dynamics in thin films. In FMR experiments a non-equilibrium magnetization state is induced by applying a small external field. This excitation induces the precession of the magnetic moments around their equilibrium states, as long as the local torque is not nil. As due to energy dissipation, the system would finally regain its initial equilibrium state, to maintain the precession, periodically energy has to be pumped into the system. Using an external excitation whose frequency coincides with the system's eigenfrequency, a resonance process can be observed.

Non-uniformly magnetized system, like the case of the stripe domain structure presented before, are very interesting, as being the assembly of magnetic domains and complex walls structures, the local field inside the sample is highly non-uniform. Consequently, the domain walls have different resonance frequencies than the magnetic domains. By means of FMR measurements one can access these "localized" frequencies and the oscillation modes, exciting different regions by applying differently oriented magnetic fields. Once the resonance spectrum extracted from the FMR data, the interpretation of each separate resonance peak is sought in analytical models [Kittel 1948, Ramesh 1988] or, when these fail, by means of numerical simulation.

Once the equilibrium state of the magnetic system determined, numerically the ferromagnetic resonance experiments can be reproduced in two ways.

*Method 1:* Calculating the dynamic susceptibility  $\chi$ , obtained from the linearized LLG equations [Vukadinovic 2001]. This first technique uses a small alternating magnetic field  $\delta \mathbf{h}_{\text{ext}}$ . The outcome of this excitation is a small variation of the magnetization  $\delta \mathbf{m}$ . To determine the susceptibility, one replaces  $\mathbf{m}(\mathbf{r}, t)$  and  $\mathbf{H}(\mathbf{r}, t)$  in the LLG equation by  $\mathbf{m}_{\text{eq}}(\mathbf{r}) + \delta \mathbf{m}(\mathbf{r}, t)$ , and respectively by  $\mathbf{H}_{\text{eq}}(\mathbf{r}) + \delta \mathbf{h}_{\text{ext}}(t) + \mathbf{H}_{\text{eff}}(\delta \mathbf{m})$ . Here  $\mathbf{m}_{\text{eq}}$  and  $\mathbf{H}_{\text{eq}}$  are the equilibrium magnetization distribution and the corresponding effective field. Considering a harmonic time dependence for  $\delta \mathbf{h}_{\text{ext}}$  and  $\delta \mathbf{m}$ , and  $|\delta \mathbf{h}_{\text{ext}}| \ll |\mathbf{H}_{\text{eq}}|$ ,  $|\mathbf{H}_{\text{eff}}(\delta \mathbf{m})| \ll |\mathbf{H}_{\text{eq}}|$  and  $|\delta \mathbf{m}| \ll |\mathbf{m}|$  the following linear system is obtained:

$$\left( -\frac{i\omega}{|\gamma|} I + D_2 - D_1 D_H \right) \delta \mathbf{m} = D_1 \delta \mathbf{h}_{\text{ext}} \quad (\text{II.105})$$

with  $I$  the unit matrix. Considering a vector  $\mathbf{v}$ , the matrices  $D_1$ ,  $D_2$  and  $D_H$  are defined as:

$$\begin{aligned} D_1 \mathbf{v} &= \mathbf{m}_{\text{eq}} \times \mathbf{v} \\ D_2 \mathbf{v} &= \left( \mathbf{H}_{\text{eq}} + \frac{i\alpha\omega}{|\gamma|} \mathbf{m}_{\text{eq}} \right) \times \mathbf{v} \\ D_H \mathbf{v} &= \mathbf{H}_{\text{eff}}(\mathbf{v}) \end{aligned} \quad (\text{II.106})$$

Solving the (II.105), the susceptibility  $\chi$  in every mesh node can be calculated from:

$$\chi = \frac{1}{N} \sum_{i=1}^N \frac{\delta \mathbf{m}_i \cdot \delta \mathbf{h}_i}{|\delta \mathbf{h}_i|^2} \quad (\text{II.107})$$

The implementation of the first method in a finite element framework requires a weak form to be established for the modified dynamic equation and then solved as presented in previous chapters.

*Method 2:* Applying a small rotation to all the magnetic moments is equivalent to the effect of a magnetic field. The magnetization is then left to relax until a stable state is reached. Applying the Fourier transform to the magnetization versus time curve, the resonance frequencies are calculated. This second method presents the advantage that it does not require any further development of the WF2-based simulation tool, as only simple equilibrium state computations have to be carried out. Obviously the damping parameter for the first step - the calculation of the equilibrium state - can be set as high as needed,

while in the second part, the susceptibility spectrum is determined carrying out simulations with an appropriate value for the damping parameter.

This second approach will be applied to the FePd thin film. This type of magnetic systems was previously explored by experimental means, the resonance modes being calculated using the FD-based approach described in paragraph II.1 [Vukadinovic 2001a, Vukadinovic 2001, Toussaint 2002]. The WF2 results will be therefore compared with these data.

### *Simple FePd thin film*

Starting with an equilibrium configuration (corresponding to the last magnetization distribution in Figure II.27), we proceeded to a small rotation of the magnetization with respect to the Oy axis (along the direction of the magnetic domains). After the relaxation towards equilibrium (with  $\alpha=0.02$ ) has come to an end, the Fourier transform of the dynamic response of the  $\langle m_y \rangle$  magnetization is computed. The real and imaginary parts of the magnetization's response, issued both by the FD and the WF2 approaches, are represented below in Figure II.37. From this figure, one might conclude that there is a very good agreement between the FD and the WF2 responses. Analyzing the resonance spectrum, four resonances are observed. The FD and WF2 frequencies are given in Table II.8.

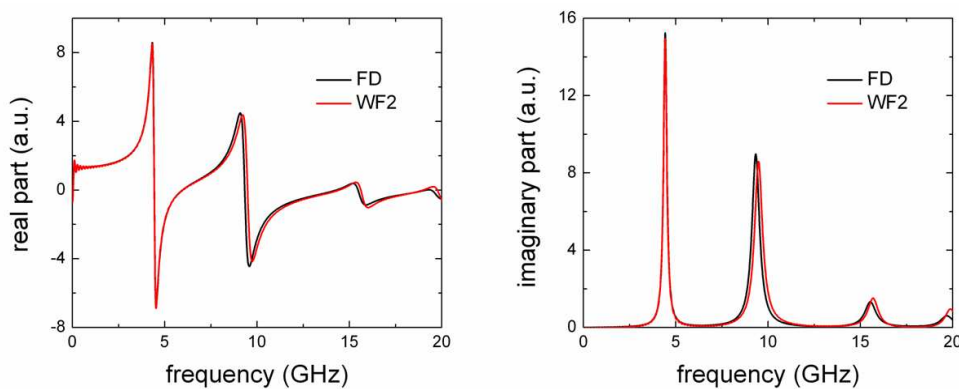


*Figure II.37: The real and imaginary parts of the Fourier transform obtained from the response of the magnetization to a small excitation.*

Small differences can be observed, for example in the amplitude of the last three peaks, which are also a little bit shifted towards higher frequencies with respect to the FD

peaks. The relative differences between the resonance frequencies are also given in Table II.8 (the values marked in *italic*).

*Table II.8: The resonance frequencies for a thin film of FePd when the field is applied along the Oy axis*

Method	$f_1$ (GHz)	$f_2$ (GHz)	$f_3$ (GHz)	$f_4$ (GHz)
FD	4.42	9.33	15.53	19.68
WF2	4.42	9.47	15.68	19.86
<i>Error</i>		<i>1.5%</i>	<i>1%</i>	<i>1%</i>

To be able to tell what element of the magnetic structure (the domains or parts of the walls) resonates at which frequency, the resonance modes were also calculated. The most intensive modes, corresponding to the first three frequencies, obtained by the FD and the WF2 approach, are shown in Figure II.38. They seem to correspond perfectly.

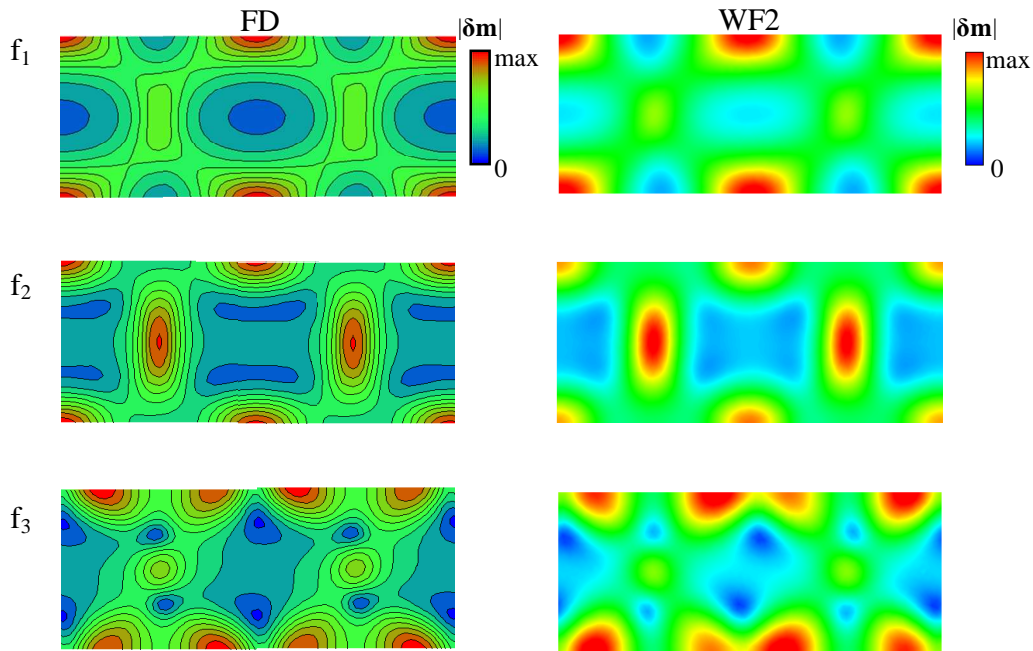


*Figure II.38: Resonance modes of a FePd thin film of thickness 40 nm and equilibrium period of 110 nm.*

The origin of these oscillation modes was determined previously [Vukadinovic 2001]. The first one appears to be a demagnetizing one, as the oscillation amplitude is the most important in the surface of the domains (maximum value marked in *italic*, minimum

in blue). The cores of the Bloch walls seem to contribute also, but to a lesser extent. For the second resonance, energy is pumped both in the domains' surfaces and in the Bloch walls. Therefore, the area covered by red regions increases. Moreover, in this mode the highly resonating regions are clearly delimited by the magnetic domains, which are not influenced by the external field, as they are oriented along its direction. In comparison with the first two modes, the third one is similar to spin wave mode. It is almost exclusively a surface mode, as important resonance is observed at the surfaces of the domains.

Both the FD resonance spectrum and the vibration modes are reproduced by the WF2 approach accurately. We can conclude then, that this first system is well described by this FE approach. This good agreement was however predictable, as the rectangular geometry is known to be well described by both numerical techniques. To gain further information about the performance of the FD and the WF2 methods, it is interesting to explore a more complex geometry, for example the constricted thin film, presented in paragraph II.2.5.4.

#### *Constricted FePd Thin film*

The same principle was used to carry out a ferromagnetic resonance simulation on this system: knowing the equilibrium state, the magnetization is rotated with respect to the Oy axis. Applying the Fourier transform to the evolution of the  $m_y$  magnetization component, the resonance frequencies given in Table II.9 are obtained:

*Table II.9: The resonance frequencies for a constricted thin film of FePd when the field is applied along the Oy axis*

Method	$f_1$ (GHz)	$f_2$ (GHz)	$f_3$ (GHz)	$f_4$ (GHz)	$f_5$ (GHz)
FD	4.56	7.19	9.52	11.95	19.94
WF2	4.62	7.1	9.59	12.29	20.31
<i>Error</i>	<i>1.3%</i>	<i>1.2%</i>	<i>0.7%</i>	<i>2.8%</i>	<i>1.8%</i>

The resonance spectrum is presented in Figure II.39. At a first glance the FD and the WF2 spectra look almost identical. Although the material parameters used in this simulation were the same as the ones used for the simple, rectangular FePd stripe, the geometry leaves

its mark on the resonance spectrum. From the data listed in Table II.9 it is clear that some differences occur between the FD and WF2 results, as the last resonance peaks are shifted towards high frequencies. Still the discrepancy remains quite small.

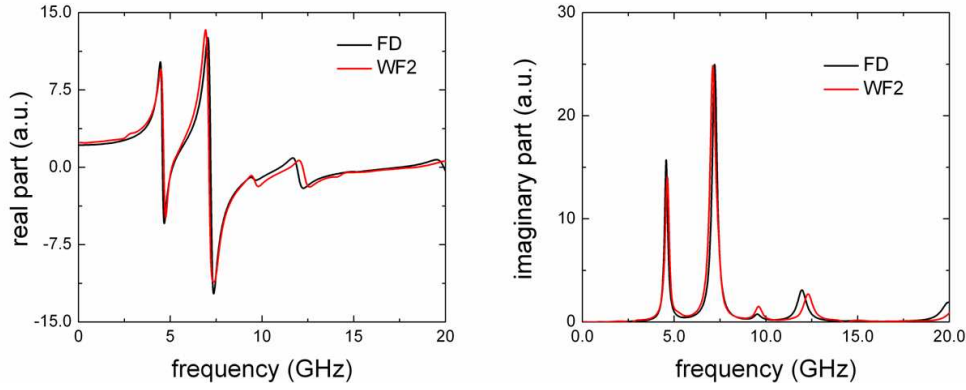


Figure II.39: The real and imaginary parts of the Fourier transform obtained for the constricted stripe domains.

The modes corresponding to the  $f_1$ ,  $f_2$  and  $f_4$  frequencies are shown in Figure II.40.

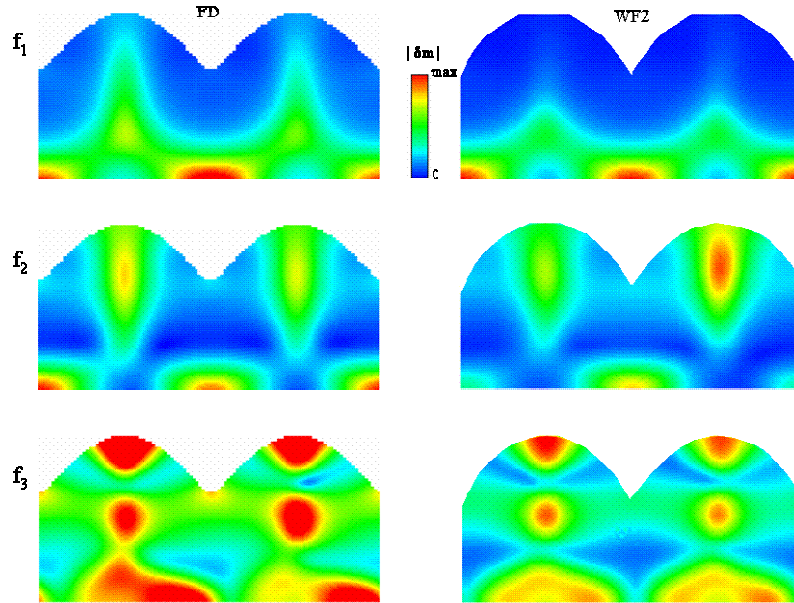


Figure II.40: Resonance modes for the frequencies  $f_1$ ,  $f_2$  and  $f_4$ .

As for the simple stripe, the first mode seems to be a surface mode. The vibration is localized in most part at the lower, not curved surface of the magnetic domains and to a lesser extent in the domain walls, or to be more specific in their core. Even though, the modes are similar, the differences between the FD and the WF2 results become

perceptible. Looking to the WF2 and FD configurations, the maximum of  $|\delta \mathbf{m}|$  is localized in the same zone, but the green areas are far more extended in the FD case than in the WF2 image. For the second mode the situation is even more alarming. Here, even to establish a clear localization of the vibrations becomes difficult. On one hand, the FD mode is quite symmetric, with the oscillations localized on the surfaces and in the regions where the walls are situated. On the other hand, the WF2 configuration is somehow asymmetric, with the surface of the central domain and the right Bloch wall being more influenced by the excitation than the other similar parts of the magnetic configuration. Therefore it is not clear if this mode is characteristic to all the vortices and the domain surfaces, or is a “coupled” vibration of a vortex core and an adjacent surface. The third mode is a coupled oscillation of the vortex cores and the surfaces. Small differences occur, but over all there is a good agreement between the two approaches is obtained. Bearing in mind that for this system the equilibrium states determined with the two approaches comported differences (see for example Table II.7 or Figure II.36), it is than understandable for the resonance phenomenon to show such small differences.

The present results demonstrate that the WF2 approach can provide a relatively good description of the magnetization dynamics in the limit of small oscillations. Nevertheless, an explanation for the difference in the second resonance mode has to be found. Also the study has to be completed, by determining all the resonance modes, including those excited by fields along the  $Ox$  and the  $Oz$  directions.



In conclusion, our first attempt (named WF1) to develop a weak form for the LLG equation does not provide a correct description of the magnetization dynamics in the limit of small damping parameters ( $\alpha < 0.1$ ). The second approach, WF2, based on the weak form proposed by Alouges, characterized by the use of test functions that belong to the tangential space to  $\mathbf{m}$ , seems to be more successful in the description of magnetization dynamics in 2D micromagnetic systems.

This second scheme was successfully benchmarked against the more usual approach of finite differences. Several test cases were taken into account: an infinite prism with square cross-section where the magnetic moments were coupled only through the exchange interaction. Next a couple of stripe domain systems were studied, both with strong and moderate magnetocrystalline anisotropy. The magnetization dynamics produced by the finite difference method, considered as a reference, is reproduced for both cases with great accuracy by the WF2-based finite element approach.

In the last part, the results for a constricted stripe domain were presented. For the rectangular stripes the differences were visible mostly for the exchange term. For this complex-shaped test case, the discrepancies are the most visible for the demagnetizing term. The reason is that the curved boundaries reveal the less efficient character of the regular discretization employed by the finite difference method.

The last part of the chapter concerned reproducing some dynamical results, but situated now in the limit of small perturbations. Ferromagnetic resonance spectra were calculated, together with the vibration modes, for a simple and a constricted thin film of FePd. The results were compared with experimental and (finite differences) numerical findings and a very good agreement was found.

All these seem to indicate that the WF2 weak formulation is well adapted for study of magnetization dynamics in 2D micromagnetic systems.

## References

- [**Albuquerque 2001**] G. Albuquerque, J. Miltat, A. Thiaville, “Self-consistency based control scheme for magnetization dynamics”, *J. Appl. Phys.* 89, 6791 (2001).
- [**Alouges 2006**] F. Alouges, P. Jaisson, “Convergence of a finite element discretization for the Landau-Lifshitz equations in micromagnetism”, *Math. Models Methods Appl. Sci.* 16, 299 (2006).
- [**Alouges 2008**] F. Alouges, “A new finite element scheme for Landau-Lifshitz equations”, *Discrete and Continuous Dynamical Systems S* 1, 187 (2008)
- [**d’Aquino 2005**] M. d’Aquino, C. Serpico, G. Miano, “Geometrical integration of Landau–Lifshitz–Gilbert equation based on the mid-point rule”, *J. Comp. Phys.* 209, 730 (2005).
- [**Bagnérés 1991**] A. Bagnérés-Viallax, P. Bara, J. B. Albertini, “2D and 3D calculations of micromagnetic wall structures using finite elements”, *IEEE Trans. Magn.* 27, 3819 (1991).
- [**Bartels 2005**] S. Bartels, “Stability and convergence of finite-element approximation schemes for harmonic maps”, *SIAM J. Numer. Anal.* 43, 220 (2005).
- [**Berger 1978**] L. Berger, “Low-field magnetoresistance and domain drag in ferromagnets”, *J. Appl. Phys.* 49, 2156 (1978).
- [**Berkov 1993**] D. V. Berkov, K. Ramstock, A. Hubert, “Solving micromagnetic problems-towards on optimal numerical”, *Phys. Stat. Sol. a* 137, 297 (1993).
- [**Bettes 1988**] P. Bettes, “Finite elements modeling of exterior electromagnetic problems”, *IEEE Trans. Magn.* 24, 238 (1988).
- [**Bokov 1998**] V. A. Bokov, V. V. Volkov, N. L. Petrichenko, “Relation between relaxation losses in domain-wall motion and ferromagnetic resonance in garnet films”, *Phys. Solid State* 40, 1377 (1998).
- [**Bottauscio 2008**] O. Bottauscio, M. Chiampi, A. Manzini, “An edge element approach for dynamic micromagnetic modeling”, *J. Appl. Phys.* 103, 07D911 (2008).
- [**Braess 2001**] D. Braess, “Finite elements”, 2<sup>nd</sup> ed., Cambridge University Press, Cambridge, 2001.

- [**Brunotte 1991**] X. Brunotte, “Modélisation de l’infini et prise en compte de régions magnétiques minces- Application a la modélisation des aimantations de navires”, PhD Dissertation, Institut National Polytechnique de Grenoble, 1991.
- [**Buda 2001**] L. D. Buda, “Développement d’un code de calcul micromagnétique 2D et 3D: applications a des systèmes réels de types films, plots et fils”, PhD Dissertation, Université Louis Pasteur de Strasbourg, 2001.
- [**Cabrera 1974**] G. G. Cabrera, L. M. Falicov, “Theory of the residual resistivity of Bloch walls I. Paramagnetic Effects”, Phys. Status Solidi (b) 61, 539 (1974).
- [**Chen 1997**] Q. Chen, A. Konrad, “A review of finite element open boundary techniques for static and quasi-static electromagnetic field problems”, IEEE Trans. Magn. 33, 663 (1997).
- [**Comsol site**] <http://www.comsol.com/>
- [**Courant 1943**] R. Courant, “Variational methods for the solution of problems of equilibrium and vibrations”, Bull. Amer. Math. Soc. 49, 1 (1943).
- [**Dourlat 2008**] A. Dourlat, V. Jeudy, A. Lemaître, C. Gourdon, “Field-driven domain-wall dynamics in GaMnAs films with perpendicular anisotropy”, arXiv:0808.0119v1 (2008).
- [**Ebels 1999**] U. Ebels, P. E. Wigen, K. Ounadjela, “Probing domain wall structures in Co(0001) thin films using ferromagnetic resonance”, Europhys. Lett. 46, 94 (1999).
- [**Emson 1988**] C. R. Emson, “Methods for the solution of open-boundary electromagnetic-field problems”, IEE Proc. 135, 151 (1988).
- [**Ferré 1995**] R. Ferré Gimenez, thèse Université Joseph Fourier, Grenoble (1995).
- [**FFTW site**] <http://www.fftw.org>
- [**Fidler 2000**] J. Fidler, T. Schrefl, “Micromagnetic modeling - the current state of the art”, J. Phys. D: Appl. Phys. 33, R135 (2000).
- [**Fredkin 1987**] D. R. Fredkin, T. R. Koehler, “Numerical micromagnetics by the finite element method”, IEEE Trans. Magn. 23, 3385 (1987).
- [**Fredkin 1988**] D. R. Fredkin, T. R. Koehler, “Numerical micromagnetics of small particles”, IEEE Trans. Magn. 24, 2362 (1988).
- [**Fredkin 1990**] D. R. Fredkin, T. R. Koehler, “Hybrid method for computing demagnetizing fields”, IEEE Trans. Magn. 26, 415 (1990).

- [**García-Cervera 2003**] C. J. García-Cervera, Z. Gimbutas, E. Weinan, “Accurate numerical methods for micromagnetics simulations with general geometries”, *J. Comput. Phys.* 184, 37 (2003).
- [**Gehanno 1997**] V. Gehanno, Y. Samson, A. Marty, B. Gilles, A. Chamberod, “Magnetic susceptibility and magnetic domain configuration as a function of the layer thickness in epitaxial FePd(001) thin films ordered in the  $L1_0$  structure”, *J. Magn. Magn. Mat.* 172, 26 (1997).
- [**GMM++ site**] <http://home.gna.org/getfem>
- [**Gregg 1996**] J. F. Gregg, W. Allen, K. Ounadjela, M. Viret, M. Hehn, S. M. Thompson, J. M. D. Coey, “Giant magnetoresistive effects in a single element magnetic thin film”, *Phys. Rev. Lett.* 77, 1580 (1996).
- [**Hertel 2002**] R. Hertel, H. Kronmüller, “Finite element calculations on the single-domain limit of a ferromagnetic cube - a solution to  $\mu$ MAG Standard Problem No. 3”, *J. Magn. Magn. Mat.* 238, 185 (2002).
- [**Hertel 2004**] R. Hertel, W. Wulfhekel, J. Kirschner, “Domain-wall induced phase shifts in spin waves”, *Phys. Rev. Lett.* 93, 257202 (2004)
- [**Hubert 1998**] A. Hubert, R. Schafer, “Magnetic domains”, Springer, New York, 1998.
- [**Imhoff 1990a**] J. F. Imhoff, G. Meunier, J. C. Sabonnadiere, “Finite element modeling of open boundary problems”, *IEEE Trans. Magn.* 26, 588 (1990).
- [**Imhoff 1990b**] J. F. Imhoff, G. Meunier, X. Brunotte, J. C. Sabonnadiere, “An original solution for unbounded electromagnetic 2D and 3D problems throughout the finite element method”, *IEEE Trans. Magn.* 26, 2196 (1990).
- [**Jaisson**] Private communication .
- [**Kevorkian 1998**] B. M. Kevorkian, “Contribution à la modélisation du retournement d’aimantation. Application a des systèmes magnétiques nanostructurés ou de dimensions réduites”, Ph.D. dissertation, Université Joseph Fourier, Grenoble, 1998.
- [**Kittel 1948**] C. Kittel, “On the theory of ferromagnetic resonance absorption”, *Phys. Rev.* 73, 155 (1948).
- [**Koehler 1997**] T. R. Koehler, “Hybrid FEM-BEM method for fast micromagnetic calculations”, *Physica B* 233, 302 (1997).

- [**Labrune 1994**] M. Labrune, J. Miltat, “Strong stripes as a paradigm of quasi-topological hysteresis”, *J. Appl. Phys.* 75, 2156 (1994).
- [**Lewis 2003**] D. Lewis, N. Nigam, “Geometric integration on spheres and some interesting applications”, *J. Comp. Appl. Math.* 151, 141 (2003).
- [**Lopez-Diaz 1999**] L. Lopez-Diaz, J. Eicke, E. Della Torre, “A comparison of micromagnetic solvers”, *IEEE Trans. Magn.* 35, 1207 (1999).
- [**Lucquin 1995**] B. Lucquin, O. Pironneau, “Introduction au calcul scientifique”, Masson, Paris, 1995.
- [**Malozemoff 1979**] A. P. Malozemoff, J. C. Slonczewski, “Magnetic domain walls in bubble materials”, Academic Press, New York, 1979.
- [**Mansuripur 1988**] M. Mansuripur, R. Giles, “Demagnetizing field computation for dynamic simulation of the magnetization reversal process”, *IEEE Trans. Magn.* 24, 2326 (1988).
- [**Mish 2000**] K. D. Mish, L.R. Herrmann, L. Haws, *Finite Elements Course: “Finite elements procedures in applied mechanics”*, 2000.
- [**Muller 1961**] M. W. Muller, “Distribution of the magnetization in a ferromagnet”, *Phys. Rev.* 122, 1485 (1961).
- [**Nakatani 1989**] Y. Nakatani, Y. Uesaka, N. Hayashi, “Direct solution of the Landau-Lifshitz-Gilbert equation for micromagnetics”, *J. Appl. Phys.* 28, 2485 (1989).
- [**OOMMF site**] <http://math.nist.gov/oommf/>
- [**Puchalska 1967**] I. B. Puchalska, R. P. Ferrier, “High-voltage electron microscope observation of stripe domains in Permalloy films evaporated at oblique incidence”, *Thin Solid Films* 1, 437 (1968).
- [**Ramesh 1988**] M. Ramesh, P. E. Wigen, “Ferromagnetodynamics of paroled stripe domains-domain walls system”, *J. Magn. Magn. Mat* 74, 123 (1988).
- [**Schabes 1988**] M. E. Schabes, H. N. Bertram, “Magnetization processes in ferromagnetic cubes”, *J. Appl. Phys.* 64, 1347 (1988).
- [**Scheinfein 1991**] M. R. Scheinfein, J. Unguris, J. Blue, K. Coakley, D. Pierce, R. Celotta, P. J. Ryan, “Micromagnetics of domain walls at surfaces”, *Phys. Rev. B* 43, 3395 (1991).
- [**Scholz 1999**] W. Scholz, “Micromagnetic simulation of thermally activated switching in fine particles”, PhD Dissertation, Technischen Universität Wien, 1999.

- [Schrefl 1999] T. Schrefl, “Finite elements in numerical micromagnetics”, *J. Magn. Magn. Mat.* 207, 45 (1999).
- [Spain 1963] R. J. Spain, “Dense-banded domain structure in “rotatable anisotropy” Permalloy films”, *Appl. Phys. Lett.* 3, 208 (1963).
- [Süss 2002] D. Süss, “Micromagnetic simulations of antiferro- and ferromagnetic structures for magnetic recording”, PhD Dissertation, Technischen Universität Wien, 2002.
- [Tatsumoto 1968] E. Tatsumoto, K. Hara, T. Hashimoto, “A new type of stripe domains”, *Japan J. Appl. Phys.* 7, 176 (1968).
- [Toussaint 2002] J. C. Toussaint, A. Marty, N. Vukadinovic, J. Ben Youssef, M. Labrune, “A new technique for ferromagnetic resonance calculations”, *Comp. Mat. Sci.* 24, 175 (2002).
- [Vermolen 2008] F. Vermolen, “Introduction into finite elements”, <http://ta.twi.tudelft.nl/users/vermolen/wi3098/wi3098.pdf>
- [Vukadinovic 2000a] N. Vukadinovic, H. Le Gall, J. Ben Youssef, V. Gehanno, A. Marty, Y. Samson, B. Gilles, “Magnetization dynamics and relaxation in epitaxial FePd thin films with a stripe domain structure”, *Eur. Phys. J. B* 13, 445 (2000).
- [Vukadinovic 2000b] N. Vukadinovic, O. Vacus, M. Labrune, O. Acher, D. Pain, “Magnetic excitations in a weak-stripe-domain structure: A 2D dynamic micromagnetic approach”, *Phys. Rev. Lett.* 85, 2817 (2000).
- [Vukadinovic 2001] N. Vukadinovic, M. Labrune, J. Ben Youssef, A. Marty, J. C. Toussaint, H. Le Gall, “Ferromagnetic resonance spectra in a weak stripe domain structure”, *Phys. Rev. B* 65, 054403 (2001).
- [Weiss 1907] P. Weiss, “L’hypothèse du champ moléculaire et la propriété ferromagnétique”, *J. Phys.* 6, 401 (1907).
- [Yang 1996] B. Yang, D. R. Fredkin, “Dynamical micromagnetics of a ferromagnetic particle: Numerical studies”, *J. Appl. Phys.* 79, 5755 (1996).
- [Yang 1998] B. Yang, D. R. Fredkin, “Dynamical micromagnetics by the finite element method”, *IEEE Trans. Magn.* 34, 3842 (1998).
- [Zhu 1989] J.-G. Zhu, H. N. Bertram, “Reversal mechanisms and domain structures in thin-film recording media”, *J. Appl. Phys.* 66, 1291 (1989).



### III. Domain wall motion

The identity card of the electron is known from long time: an electric charge of  $1.60 \cdot 10^{-19}$  C, a mass of approximately  $9.11 \cdot 10^{-31}$  kg and spin 1/2. The electron as a charge carrier has been exploited for a long time by classical electronics in numerous applications. Recently, scientists turned their attention to another property of the electron, namely its spin, and a new topic is emerging called *spintronics* [Prinz 1998, Wolf 2001, Chappert 2008]. Spintronic applications concern information technology, promising advantages of low power dissipation, nonvolatility and high integration density. The giant magnetoresistance [Tsymbal 2001] and the tunneling magnetoresistance [Tsymbal 2002] are already used in hard disk read heads, the next in line being the magnetic random access memories [Tehrani 2003, MRAM site]. Related to these, lately, new approaches for switching such magnetic nanostructures are sought. The conventional method employs an external magnetic field. Since the first demonstration of current-induced switching [Myers 1999, Katine 2000] through the spin transfer effect, this alternate procedure has attracted a lot of interest. The use of an electric current instead of a magnetic field has the advantage that it simplifies the design of spintronic devices, as the circuits that generate the magnetic field required for the switching are eliminated. Moreover using electric current the problem of selectivity is eliminated, as one is able to address localized memory cells, without influencing the neighbors.

Domain wall (DW) displacement comes into play as it offers new ways of manipulating information. DW motion is achieved either by magnetic field or spin-polarized current. For example, Allwood et al. [Allwood 2002] confirmed the possibility of performing logical NOT operations using DWs that move under the effect of an external magnetic field applied parallel to a 200nm×5nm Permalloy nanowire. Grolier et al.



[Grollier 2001] showed that it is possible to switch a spin valve by moving a DW across the structure using a spin-polarized current.

DW motion has been studied both by theoretical and experimental means. From theoretical point of view, the details of field-driven displacement are all very well known. On the other hand, the effect of a spin-polarized current, although predicted almost in the same period as the studies on field-induced motion, is still a controversial subject. One thing to bear in mind is that in most part of the theoretical/numerical studies ideal systems are treated. The predictions are truthful, especially as far as the mechanism of DW motion is concerned, comparison with experimental data resulting in a good qualitative agreement. Although several possibilities were foreseen that could help to approach real systems (spatial variation of materials parameters, surface roughness, geometrical constrictions, intrinsic pinning), however, up to now, it is not clear which are the predominant mechanisms and how exactly should one take into account these.

From experimental point of view, the trend in this topic is dictated by the possible applications and consequently, changes quite rapidly. While in the beginning, field-induced motion was explored, the first proof of the applicability of current-induced wall motion in logic devices made everybody turn their attention in this direction. This is why, the number of publications on field-driven DW displacement is small in comparison with the studies on spin torque and DWs. The large diversity of results on current-driven motion (many of them contradictory) testifies once again about the difficulties and the need of a better understanding of the spin torque effect in DWs.

There is also a trend related to the materials used to fabricate the samples. The most extensively studied systems, for the moment, are the ones consisting of Permalloy ( $\text{Ni}_{80}\text{Fe}_{20}$ ). This material presents advantages as: low anisotropy and magnetization, high Curie temperature. The numerous experimental papers indicate that the critical current for starting DW motion in such systems goes up to  $10^{12} \text{ A/m}^2$  ( $10^8 \text{ A/cm}^2$ ), which is not very appealing from the viewpoint of applications. Due to the dominant shape anisotropy, the magnetization inside the sample lies in-plane, while the walls have a complex three-dimensional structure, being either transverse or vortex, depending on the geometrical characteristics of the system considered [McMichael 1997, Nakatani 2005]. As the DWs

are wide ( $\approx 100$  nm), when it comes to pinning they are not very sensitive. Therefore these systems cannot serve for distinguishing between the possible causes of the high threshold current, information that is absolutely necessary for a better theoretical/numerical treatment of this topic. On the other hand, recent results have been reported on magnetic semiconductors [Yamanouchi 2006] and also systems with strong out-of-plane magnetocrystalline anisotropy [Ravelosona 2005, Ravelosona 2006, Tanigawa 2008]. The interest in out-of-plane magnetized systems is due to the smaller threshold current required for DW propagation than the one found for the in-plane geometry. The DWs in CoPt multilayers [Ravelosona 2005] extend over 10-15 nm and can be considered almost ideal 1D Bloch walls. This has both advantages and disadvantages. The simple structure and the narrowness of the walls make them adequate model systems for studying the effect of pinning, intrinsic defects or internal magnetic DW stiffness. On the contrary, the high sensibility to pinning gives to the wall displacement process a highly random character.

In the following part, the existent theoretical and experimental results will be shortly presented as well as the numerical results found in the literature. Next the micromagnetic simulation tool developed to study DW motion is described briefly. The chapter closes with the numerical results obtained for the case of a system with strong out-of-plane magnetocrystalline anisotropy.

### III.1. State of the art

#### III.1.1. Theory

##### III.1.1.1. Theory of field-driven domain wall motion

Consider a Bloch wall, defined by the polar angles  $\theta$  and  $\varphi$ , as shown in Figure III.1. Its dynamics is described by the classical LLG equation.

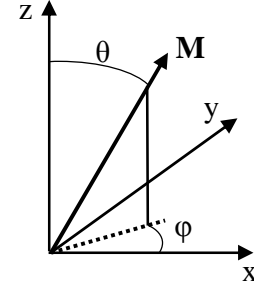


Figure III.1: The angles  $\theta$  and  $\varphi$  used to characterize the wall.

Walker was the foremost to investigate the dynamics of such magnetic entities, deriving the first analytical solution for the motion of a Bloch wall in a uniaxial bulk material [Schryer 1974]

under the influence of an applied field  $H_{\text{app}}$ . He predicted the existence of two motion regimes:

- a) the steady motion regime, extending up to a critical field value (Walker field)
- b) the precessional regime, corresponding to high field values.

The accuracy of this relatively basic approach has been confirmed experimentally [Beach 2005]. Slonczewski and Malozemoff [Malozemoff 1979] generalized this 1D model, reasoning in terms of two generalized coordinates: the position of the DW centre  $q$  and the azimuth angle of the wall  $\psi$  ( $\psi=\varphi$ ). A pair of differential equations is then set up:

$$\begin{cases} \frac{\partial q}{\partial t} = \gamma M_s \sin(2\psi) + \alpha \Delta_0 \frac{\partial \psi}{\partial t} \\ \frac{\partial \psi}{\partial t} = \gamma H_{\text{app}} - \alpha \frac{1}{\Delta_0} \frac{\partial q}{\partial t} \end{cases} \quad (\text{III.1})$$

where  $\Delta_0 = (A_{\text{ex}}/K_{\text{anis}})^{1/2}$ . These two equations have very simple physical interpretations. The first one, called *torque equation of wall motion*, indicates that in order to have a non-zero wall velocity a torque must be acting upon the DW. The second equation represents the *pressure equation of the wall motion*. The pressure on the DW arises from any field that lowers the energy of one domain with respect to the energy of the opposite one. This

second equation describes the in-plane precession of the magnetization inside the wall, the precession frequency is  $\omega = \gamma H_{\text{net}}$ , where  $H_{\text{net}}$  is the effective field along the Oz direction. These equations are more general than the ones deduced by Walker, as they are convenient for the description of complex wall structures, even small deformations of a DW can be considered. These results were determined based on the assumption that only four fundamental interactions are present in the magnetic system: exchange, magnetocrystalline anisotropy, demagnetizing and Zeeman. Considering additional terms the torque on the wall can be enhanced.

Döring studied the DW dynamics by introducing the wall mass concept [Döring 1948]. Thiele [Thiele 1973, Thiele 1974] rewrote the dynamic LLG equation under a generalized form, so that the dynamics of various micromagnetic entities can be easily calculated. He defined static and dynamic forces that must equilibrate each other. The dynamic contribution is made up from two parts: a gyrotropic component generating a force perpendicular to the velocity of the wall, and the dissipation dyadic, responsible for the relaxation of the system.

In most of the theoretical paper simple Bloch walls were considered. Recently, Thiaville et al. and Porter et al. published papers where they treat systems with in-plane magnetization, where the magnetic domains are separated by transverse DWs. In both cases, the analytical results are supported by micromagnetic simulations. The group of Thiaville carried out calculations for nanowires of small diameter (a few exchange lengths), showing that the DW dynamics in such systems is close to the one predicted by Walker for 1D Bloch walls [Thiaville 2002]. Porter et al. [Porter 2004] went further, deriving the dependence of the driving demagnetizing field on the film thickness and width.

### *III.1.1.2. Theory of domain wall motion under spin-polarized current*

The process of field and current-induced DW motion was first studied in the 1970's. Although the field-driven wall motion revealed most of its secrets, the effect of spin-polarized current on DWs still raises a lot of questions. It is a commonly accepted

idea that, current-induced wall motion is due to the transfer of spin angular momentum, associated with the current flow through a magnetic body.

Berger predicted in the 1970's that, a spin-polarized current should apply a torque to a magnetic DW. In his papers [Berger 1973, Berger 1974, Berger 1978, Berger 1984, Berger 1992], he gave a meticulous description of his vision on this phenomenon, including, in addition, the first experimental observations of DW displacement [Freitas 1988, Hung 1988].

According to Berger, two types of interactions can occur if a current is injected in a sub-micron-sized magnetic system. The first is the hydromagnetic drag [Berger 1973, Berger 1974]. Considering a thin film, the current lines are displaced towards one side of the sample due to the Hall effect. This interaction is dominant only for film thicknesses larger than 100 nm. The second manner in which the current can interact with the DW is through the *s-d exchange interaction* [Berger 1984, Berger 1992]. Berger derived the force on the wall, proportional to the carrier drift velocity, the wall velocity and the wall mobility. Furthermore he calculated the torque exerted by a spin-polarized current, resulting in the canting of the wall magnetization towards the hard axis.

More recently, there is a tendency to describe the spin transfer effect by inclusion of new terms in the LLG equation. Slonczewski [Slonczewski 1996] was the first who derived such a spin torque term for a 3 layer geometry (two magnetic layer separated by a non-magnetic spacer). In his approach the magnetization is considered to be uniform in the two ferromagnetic layers, and thus is not adapted for the case of DWs. The dynamics of the magnetization is supposed to be slow compared to that of the conduction electrons. Based on this assumption, the hypothesis of *adiabaticity* states that, the spin of the conduction electrons follows the direction of the local magnetic moment, transferring completely their angular momentum to the latter one. Several torque terms were proposed [Bazalyi 1998, Li 2004, Thiaville 2004] founded on this assumption. However, it was rapidly proven, using micromagnetic simulations, that a completely adiabatic approximation does not give a correct description of the wall displacement. It appears that using this approach the wall motion can not be sustained solely by a current. Somehow the influence of the mistracking

of the electrons must be included in theoretical models. In the LLG equation two new torque terms are therefore added: an adiabatic and a non-adiabatic one.

In a very short period, less than a year, four groups presented formulations of the adiabatic and the non-adiabatic torques:

1. Tatara and Kohno [Tatara 2004] separated the effect of a current in two contributions. There is a contribution due to the reflection of the conduction electrons (linear momentum transfer), giving rise to a force on the wall. A second contribution, the *spin torque*, appears when angular momentum is transferred from the conduction electrons to the magnetic electrons. The authors pointed out the fact that, depending on the wall width, there is a threshold current for DW motion even in the absence of pinning due to sample roughness. For thick walls, where the adiabatic approximation is valid, the pinning does not affect the motion, an intrinsic critical drive current arising due to the hard-axis magnetocrystalline anisotropy ( $K_{\perp}$ ). For narrow walls, the wall displacement is controlled by momentum transfer, the threshold current being related to the wall resistivity.
2. Viret et al. [Waintal 2004, Vanhaverbeke 2007] presented in their approach the Larmor precession of the spin of the conduction electrons around an effective local magnetization. The torque on the DW, depending on the conduction electrons spins' relative direction, can be nil or at its maximum. Like the previous papers, two contributions were identified: one (adiabatic) that deforms the wall, and a second one that applies a pressure on the wall, pushing it in the direction of the current.
3. Starting with the s-d Hamiltonian,  $H_{sd} = -J_{ex} \mathbf{s} \cdot \mathbf{S}$ , where  $\mathbf{s}$  and  $\mathbf{S}$  are the dimensionless spins of conduction and localized electrons, and  $J_{ex}$  is the exchange integral coupling them, Zhang and Li [Zhang 2004] derived a dynamic equation containing four terms. Two of them arise from the time variation of the magnetization and two other, proportional to the current density, originate from the variation in space of the magnetization. The terms defining the spin transfer effect are weighted by two coefficients  $b_j$

and  $c_J$  related to the current, the magnetization and a parameter  $\xi$  defined as the ratio between the *exchange time*,  $\tau_{ex}=\hbar/SJ_{ex}$ , and the *spin-flip lifetime*,  $\tau_{sf}$ . Both parameters  $b_J$  and  $c_J$  have the units of velocity. The predominant term is the adiabatic one ( $c_J/b_J=0.01$ ). They demonstrated, on the simple example of a Néel wall, the role of each of these spin torque terms. The adiabatic term causes the wall distortion, being relevant only in the initial motion. The terminal velocity of the DW is closely related to the non-adiabatic term.

4. Almost in the same time with the publication of Zhang, Thiaville et al. [Thiaville 2005] introduced a phenomenological non-adiabatic term in the LLG equation. Their approach is presented in detail later on, as our micromagnetic simulation tool is based on this form of the LLG equation.

### *III.1.2. Experiments*

#### *III.1.2.1. Field induced motion*

A quick overview of the experimental studies reveals a great variety of results. DW motion under applied field was a topic of great interest. The most significant part of the measurements has been carried out on thin films, with the purpose of studying the magnetoresistance effect and depinning phenomena. Also, using ferromagnetic resonance experiments, material parameters like the damping parameter were determined.

In the nanowire geometry field-induced DW dynamics was extensively studied. One of the parameters widely used when talking about DW displacement is the wall mobility, defined as the rate of change of wall velocity with the field. A few of the most important findings in such systems are presented in the following.

In 1999, Ono [Ono 1999] measured velocities, in nanowires made of NiFe/Cu/NiFe trilayers using the GMR effect (at temperatures between 100K and 160K). They found relatively low wall mobilities.

In 2003 Atkinson et al [Atkinson 2003] used a MOKE magnetometer to determine whether the switching of a nanowire, made this time of a single layer of NiFe, by means of DW displacement was successful or not. The measurements were carried out at room temperature. In this case values for the wall mobility were several times larger than those found by the Japanese group.

In 2005 the group of Beach et al. [Beach 2005] was the first to identify, experimentally, the two motions regimes predicted by Walker. Single layer Permalloy nanowires were measured using a MOKE magnetometer. DW displacement was induced by applying field pulses. The experimental findings were in a good qualitative agreement with Walker's analytical predictions.

The above presented results refer all to in-plane magnetized wires. Depending on the relative positioning of the occurring pinning forces and the force arising from external sources (like an applied field or current), the behavior of the DW can be placed either in a



*creep*, and thus pinning dominated regime, or in a *flow* regime, where the DW moves almost freely, without feeling the obstacles set by disorder. The materials characterized by narrow DWs (CoPt for example) are very interesting from this point of view. If the DW is only a few nanometers wide, the pinning forces acting upon it are very strong, the creep behavior being the leading one at low fields. On the contrary the Permalloy materials presenting wide DWs, the creep motion is less visible.

In 2007 by Metaxas et al. [Metaxas 2007] studied very thin films (0.5-0.8 nm) of Pt/Co/Pt characterized by strong perpendicular magnetocrystalline anisotropy. Their conclusions were founded on wall displacements over large distances (larger than 10  $\mu\text{m}$ ), and consisted in identifying experimentally the creep and flow regimes and in determining the DW mobility. This value served as a base for calculating the value of the damping parameter, that was found to be consistent with values determined via other measurement techniques.

### *III.1.2.2. Current driven domain wall motion*

Since the first experimental evidence of current-driven DW motion, presented almost 30 years ago by Berger [Freitas 1985, Hung 1988], researches have been trying to gain deeper insight in the anatomy of this phenomenon in various ways. The materials are the same as the ones used for field-driven motion: single or multilayer structures of NiFe and different systems with out-of-plane magnetization.

The various measurement methods (AMR, GMR, MFM, MOKE), the multiple geometries that were tested (simple wire connected to nucleation pads with different shapes, ring, U shaped, L shaped, constrictions) all indicate the difficulty of drawing a clear conclusion about how the two spin torque terms intervene in the displacement of a DW. It is still not clear how one can discriminate between the different factors that could assist or counter the DW motion: spin torque, Joule heating, pinning and depinning mechanisms, current generated Oersted field.

Although, the interest in systems with out-of-plane orientation of the magnetization grows, up to now the most extensively studied material is still the Permalloy. Due to the

wideness of the walls in this material the adiabatic approximation should be valid [Tatara 2004, Thiaville 2005]. Following the tendency imposed by theory, in the early experiments, the signature of this first spin torque term was sought. The group of Kläui [Rothman 2001, Kläui 2001, Kläui 2002] made (anisotropic) magnetoresistance measurements on Permalloy rings. This geometry has the advantage that it makes easier the manipulation of a single head-to-head (or tail-to-tail) domain. Using dc currents, with the density going up to  $7 \cdot 10^{11} \text{ A/m}^2$  (and later current pulses of  $20 \mu\text{s}$  and similar values for the current densities), they observed that, the magnetic field required to displace a DW can be tuned by changing the direction of the dc current. Similar experiments were presented by Vernier et al. [Vernier 2004]. They showed that is possible to move a DW only with an electric current, using a MOKE magnetometer to measure the magnetization in a “U” shaped wire. An interesting detail was that, they were able to estimate the pressure on the wall per unit current density, finding values close to those determined by Berger. Another testimony about the role of the spin transfer came from Tsoi et al. [Tsoi 2004]. They carried out both AMR and MFM measurements on CoFe nanowires, moving a transverse DW between two constrictions. The current threshold to depin the DW was found to be in agreement with values given previously [Gan 2000].

The first velocity values were produced by Yamaguchi et al. [Yamaguchi 2004] using an L-shaped  $\text{Ni}_{81}\text{Fe}_{19}$  wire. To detect wall motion, an MFM was employed. Current pulses of different lengths were used to move the DWs. It has been determined that the distance over which the DW is propagated increases linearly with the pulse duration, indicating a constant wall velocity of  $\approx 3 \text{ m/s}$ . The wall velocity was measured as a function of the intensity of the current pulse, showing an increase when the current intensity is amplified. The critical current required for initiating motion is  $6.7 \cdot 10^{11} \text{ A/m}^2$ .

Trying to explain the above described experimental findings including a single spin torque term in the LLG equation, numerical simulations were carried out by Thiaville and the group of Kläui. The latter group found a relatively good agreement when simulating motion of transverse walls, however, for vortex walls, a factor of 3 was found between experiment and calculation. Thiaville et al. found threshold currents an order of magnitude higher than the experimental ones. These inconsistencies appear as the adiabatic term is equivalent to a hard-axis field, and consequently can not sustain the motion, only if the

current density exceeds a certain value, that is higher than the intrinsic depinning threshold current. Adding the non-adiabatic term, a certain current is still required to free the wall from the local pinning sites, but then the DW motion occurs normally. Numerical studies [Thiaville 2005] predict that, similarly to field-driven motion, two motion regimes exist: a regime, where the velocity varies linearly with the current, and a second regime, where the wall structure goes through essential changes and where the wall velocity is characterized by an oscillatory motion. In 2005, the group of Kläui provided experimental evidence of the transformation of a transverse wall into a vortex wall [Kläui 2005]. Later on the group of Hayashi et al. [Hayashi 2007] was able to demonstrate that the chirality of the transverse DWs changes periodically.

From the results presented above, we may conclude that the numerical simulations provide a relatively good qualitative description of the current-driven DW motion. However, there is still an important discrepancy between the theoretically predicted velocity values and those retrieved from experimental data. To determine its origin, one should be able to verify the existence of the two motion regimes. This implies applying high current densities, quite difficult to achieve experimentally because the effect of the Joule heating becomes non-negligible and, almost surely, the samples are destroyed. Instead of looking directly to the dependence of the velocity on the injected current, a more successful alternative is to study the modifications that occur when both the force from a magnetic field and a spin-polarized current are put together to move DWs. Several such experiments were done, resulting again in a large variety of conclusions. As demonstrated by the group of Parkin, this technique can be employed to retrieve information about the non-adiabatic spin transfer parameter [Thomas 2006, Hayashi 2007]. Adding short current pulses to the effect of a magnetic field, the velocities are profoundly influenced; however, the value of the Walker field does not seem to be sensible to such an exterior factors. The conclusion that can be drawn from these experimental observations is that, the value of the *non-adiabatic spin transfer parameter*  $\beta$  is close to the value of the Gilbert damping parameter. Similar results were found by Beach et al. [Beach 2006, Beach 2008]. Moreover, they found a strange dependence of the wall velocity on the injected current, which can be decomposed into a linear and a quadratic component. The exact cause of such an unconventional behavior is still under debate. Kläui et al. [Heyne 2008] deduced,

based on the displacement of a vortex core under current, that  $\beta$  and  $\alpha$  are different. Nevertheless, they were not able to quantify the relation between the two parameters.

A less exploited process, that could shed some light on the spin torque, is the depinning process. Using nanosecond-long current pulses [Thomas 2006], it was shown that DWs can exit local confining potentials at smaller current densities than those seen when dc current is used. The probability of depinning was found to vary with the pulse length. The issue of pinning was considered also in perpendicular-to-the-plane magnetized systems. Ravelosona et al. [Ravelosona 2005] showed that the spin transfer efficiency is rather high in spin valve structures consisting of (Co/Pt)/Cu/(CoPt) layers. Here, the DWs can be approximated by 1D Bloch walls. Based on extraordinary Hall effect measurements, they were able to conclude that the  $\approx 10$  nm wide Bloch walls can be moved with current densities smaller than  $10^{11}$  A/m<sup>2</sup>, despite the large pinning field.

A last result that should be mentioned is the small current density required for DW motion reported in magnetic semiconductors. Close to the ferromagnetic transition temperature (90K), Yamanouchi et al. [Yamanouchi 2006] measured a record current density of  $10^9$  A/m<sup>2</sup> in GaMnAs wires. The small value is explained by the low  $M_S$ . To continue with the results on GaMnAs systems, recently [Dourlat 2008], both the steady and precessional flow regimes were observed, in layers with a perpendicular easy axis. The value of the damping parameter was calculated from the DW displacement measurements (based on magneto-optical imaging and a magnetic field pulse technique) and was found to be 30 times larger than the one deduced from ferromagnetic resonance.

The results presented above underline clearly that, as far as the interaction between a spin-polarized current and a DW is concerned, in spite of the impressive quantity of experimental findings, the number of unknowns is still very large. The theoretical approaches give a relatively correct description of the behaviors presented above, although the agreement is unfortunately more qualitative, than quantitative. Details concerning the value and the origin of the  $\beta$  parameter are still required. The effect of Joule heating has to be further explored, together with the Oersted field, for the moment neglected in most cases.

### *III.2. Numerical approaches*

#### *III.2.1. State of the art*

The effect of spin-polarized currents on DWs was analyzed firstly from a theoretical point of view, followed by experimental evidence supporting or not the view of theoreticians. Besides the pure theoretical approach, another possibility of investigating this matter is by means of numerical simulations. The micromagnetic theory, described in chapter I, stands at the base of such numerical implementations.

Field induced motion is relatively easy to handle, as this process is described by the classical LLG equation (paragraph I.3). The first numerical studies on DW motion were carried out by Walker [Schryer 1974]. He developed a 1D model that describes the evolution of a Bloch wall in a bulk system, supporting the theoretical predictions by results issued by numerical simulations. Later H. N. Bertram [Yuan 1991] looked to the evolution under an easy/hard axis field of an asymmetric Bloch wall in Permalloy films. Two motion regimes were identified. For small field values, applied along the easy axis, a uniform wall structure is conserved during translation at constant velocity. At high fields however, the wall velocity develops an oscillatory behavior, as predicted by the 1D model of Walker. In this oscillatory motion regime, depending on the thickness of the Permalloy film several modifications of the wall structure are foreseeable. For thin films (500 Å), the precessional motion is accompanied by a periodical change from vortex to asymmetric Néel wall and then again to vortex, but with an opposed chirality. For thicker films (for example 2000 Å) instead of Bloch-Néel transitions, the initial vortex wall breaks up into three vortices with different chiralities. The explanation is that, in thick films it is energetically favorable to accommodate a certain number of vortices, whereas in thinner films both vortex and Néel walls are foreseeable as they are energetically equivalent. Applying fields along the in-plane hard axis, an irreversible hysteretic behavior was observed, characterized by two different transition fields, one from Bloch to Néel and a second one for the opposite case, from Néel to Bloch. Both fields increase with film thickness. The conclusion of this study was that the Walker's 1D model is not accurate enough for the description of such systems. The

discrepancies arise mainly because of complexity of the wall structure is not entirely taken into account in the 1D model, and such an approach takes no notice of the influence of the finite thickness of the film on demagnetizing interactions.

Thiaville [Thiaville 2002] reduced furthermore the system's dimension, looking to the behavior of nanowires with diameters smaller than 50 nm. The magnetization lies in-plane and head-to-head DWs are expected. He found that, a relatively correct description of such systems can be obtained adapting Walker's model developed for Bloch walls. He included a second degree (uniaxial) transverse anisotropy  $K$  (besides  $K_{anis}$ ), the adapted Walker field being then  $H_c = \alpha K/M_S$ .

Until now, only ideal geometries were considered. In such wires, two motion regimes are defined: the viscous and the turbulent one. In the turbulent regime the wall velocity oscillates between positive and negative values, following the modifications that appear in the wall structure. During motion, because of the asymmetric wall shape (the wall looks like a V), an antivortex appears in the corner of the V. It crosses the wire width, during this time the wall velocity decreases as the energy supplied by the field is absorbed by this transverse motion. Once the antivortex expelled, a new V-shaped wall becomes visible and the velocity increases. In the continuation of this study, the influence of surface roughness was explored [Nakatani 2003]. As the Permalloy material considered in these studies is polycrystalline, the edge roughness was generated based on the grain size. Numerical simulations revealed that, in such systems the wall moves faster as, the occurrence of the antivortex is prevented by the edge imperfections. The antivortex nucleation is replaced by spin wave emission and, the energy that would have been invested in translating this wall across the wire width is now spent in displacing the wall. Therefore the wall velocity does not drop, but motion goes on at a maximal speed. However, the amplitude of the edge fluctuations plays a very important role. In order to have this enhanced-velocity behavior, the size of the roughness should be larger than the exchange length. For smaller values, the ideal behavior is retrieved, while if the surface is too rough, the DW can be pinned.

It is well known that in field-driven motion the demagnetizing field of the wall plays a key role. D. G. Porter and M. J. Donahue [Porter 2004] carried out micromagnetic

simulations to see how geometrical features influence this central parameter. The dependence of this field on the simulated geometry was considered through the demagnetizing factors, calculated for the region where the wall is placed. The Walker field is defined now as  $H_c = \alpha \max_{\theta} \{H_D\}$ , where  $\alpha$  is the Gilbert damping parameter,  $\theta$  is the out-of-plane tilt angle due to the torque from the applied field and  $H_D$  is the component of the demagnetizing field perpendicular to the magnetization in the wall.

Recent numerical studies [Fukami 2008] on perpendicularly magnetized systems indicate that, the critical current for precessional motion in perpendicular anisotropy strips is much smaller than that of strips with in-plane anisotropy. This current density was found to decrease when the thickness of the wire is reduced. Moreover, simulations of the depinning from a small notch showed that, the depinning current of perpendicular systems is quite small, in comparison with the value found for the in-plane geometry. On the contrary, the magnetic field required to release the wall from the same notch was higher in the perpendicular material.

These are the most significant results reported on field-driven DW motion. When experimental evidence of the effect of spin-polarized current on DWs started to appear, first, complex theoretical approaches were developed, based on the pioneering work of Berger. However soon enough it was clear that numerical studies are required to fully understand this phenomenon. Based on Slonczewski's idea of including a spin torque term in the LLG equation, approach that he developed for spin-valve structures, several forms of spin torque terms were added to the dynamic equation. Most of these were presented in the paragraph III.1.1.2, covering the existing theoretical approaches.

The biggest part of the numerical studies is due to Thiaville and his group. The results we will present in the following chapters were obtained using a micromagnetic simulation tool that employs the form of the LLG equation proposed by Thiaville et al. in [Thiaville 2005]. Therefore their approach will be presented in detail in the following paragraph.

### *III.2.2. Domain wall dynamics under spin-polarized current as proposed by Thiaville et al.*

Based on the first hypotheses, as in most of the cases, Thiaville and collaborators included [Thiaville 2004], in the first time, only the adiabatic torque term in the LLG equation. The adiabatic term was derived from a Lagrangian form of the dynamic equations, combining the micromagnetic energy density and a dissipation function. Field-driven and current-assisted motion was then simulated both in ideal and rough Permalloy wires. The conclusion of this study was that no DW motion can be observed in the absence of a magnetic field, which is contrary to the experimental findings. Therefore, either the adiabatic torque has to be written under another form or, a second spin torque term must be attached to the LLG. Simulations carried out including a phenomenological non-adiabatic spin torque term provided better agreement with experiments. They proposed the following form for the LLG equation including the effect of a spin-polarized current:

$$\frac{\partial \mathbf{m}}{\partial t} = -\mu_0 \gamma (\mathbf{m} \times \mathbf{H}_{\text{eff}}) + \alpha \left( \mathbf{m} \times \frac{\partial \mathbf{m}}{\partial t} \right) - (\mathbf{u} \cdot \nabla) \mathbf{m} + \beta \mathbf{m} \times [(\mathbf{u} \cdot \nabla) \mathbf{m}] \quad (\text{III.2})$$

On the right side, one identifies firstly the well-known precession term describing the rotation of the magnetization around the effective field  $\mathbf{H}_{\text{eff}}$ , and secondly the cross product that counts for Gilbert damping, leading to a parallel alignment of  $\mathbf{m}$  and  $\mathbf{H}_{\text{eff}}$ . The third term describes the adiabatic contribution of the spin torque, whereas the last term stands for the non-adiabatic torque. This term, weighted by the non-adiabatic spin transfer parameter  $\beta$ , accounts for the conduction electrons' mistracking when passing through the wall. The value of this  $\beta$  coefficient depends on how one defines the adiabatic limit. Several possibilities were presented before. In the approach of Tatara [Tatara 2004] the characteristic length is the Fermi wavelength. Zhang [Zhang 2004] relates the  $\beta$  factor to the exchange and spin-flip time, while in the models described in papers by Viret et al. [Vanhaverbeke 2007, Waintal 2004], the characteristic length in the Larmor wavelength. Despite the large variety of definitions, all the signs indicate that the value of  $\beta$  is smaller than 1, close to the value of the damping parameter. Finally, in (III.2) the vector  $\mathbf{u}$  has the unit of a velocity and is parallel to the direction of electron flow:



$$\mathbf{u} = \mathbf{J}_{\text{app}} \frac{g \mu_B P}{2 e M_S} \begin{pmatrix} 1 & 0 & 0 \end{pmatrix} \quad (\text{III.3})$$

Here  $g=2$  is the free electron's Landé factor,  $\mu_B$  is the Bohr magneton,  $\mathbf{J}_{\text{app}}$  is the current density,  $P$  is the current polarization rate ( $0 \leq P \leq 1$ ) and  $e$  is the electron charge.

All the results that will be presented in the following paragraph were obtained solving numerically the equation (III.2), implemented in the micromagnetic software that we called WALL\_ST (the details of the numerical implementation will be presented later on). However, before passing to the study of systems with out-of-plane orientation of the magnetization, the accuracy and performance of our implementation had to be tested. As the interest in such systems is recent, and therefore no test cases were available, our micromagnetic simulation tool was benchmarked against the results provided by Thiaville et al. for an ideal Permalloy nanowire [Thiaville 2005]. In the following we present shortly the results obtained by Thiaville et al. superposed, if available, with our own results.

The simulations concern a defect-free nanowire of NiFe with the material parameters listed in Table III.1:

*Table III.1: Material parameters used for the simulations concerning the NiFe nanowire:*

$M_S$ (kA/m)	$A_{\text{ex}}$ (J/m)	$K_{\text{anis}}$ (J/m <sup>3</sup> )	$\alpha$
800	$10^{-11}$	0	0.02

The computation region consists of a rectangular prism of 2000nm×120nm×5nm. The numerical discretization consists of elements of 4nm×4nm×5nm.

The first step was to find the equilibrium wall structure, in the absence of magnetic field or spin-polarized current. An isolated transverse wall is obtained, showed in Figure III.2. All the magnetization configurations presented in the following were obtained using the WALL\_ST software.

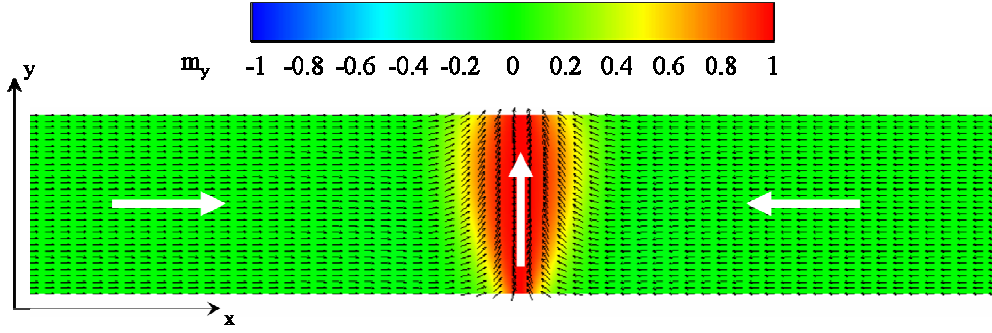


Figure III.2: Equilibrium magnetization distribution in a Permalloy wire. The head-to-head domains are separated by a V-shaped transverse DW. The size of the system is of  $2000\text{nm} \times 120\text{nm} \times 5\text{ nm}$ .

Then several simulations were carried out for several current values taking  $\beta=0$  and  $\beta=0.01$ . The results found by Thiaville et al. are reproduced in the Figure III.3:

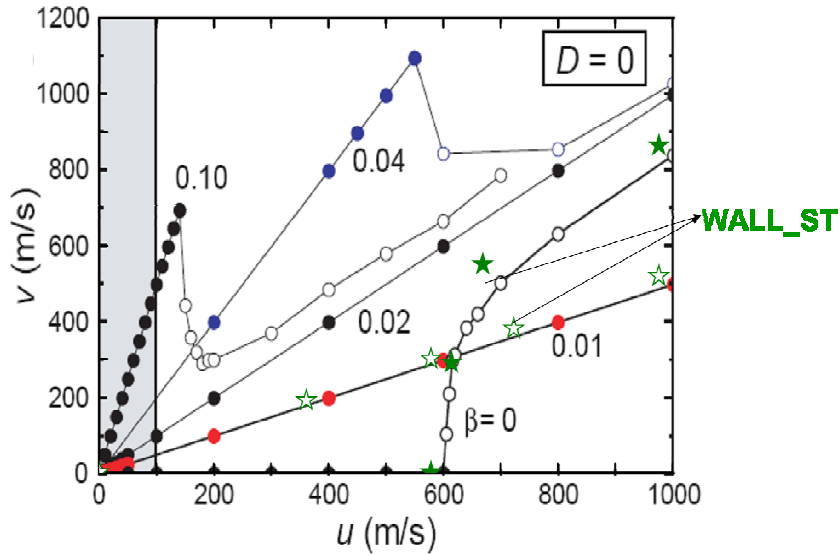


Figure III.3: Evolution of the wall velocity versus the injected current. To test the WALL\_ST simulation tool we carried out simulations for two values of the  $\beta$  parameter: 0 (plotted in red line) and 0.01 (the green curve) [Thiaville 2005].

The filled and empty green stars depict the velocity values obtained with WALL\_ST. It is readily seen that our approach reproduces accurately the results obtained by Thiaville, and one can therefore foresee its further use.

*1D motion equations*

Taking a closer look to the numerical results shown in Figure III.3, a behavior similar to the one seen for field-driven motion is observed. Two motion regimes are identified: a steady regime going up to a critical current density, and, then at high current densities, a precessional regime. This similarity can be easily understood transposing the LLG equation in the framework proposed by Slonczewski (see equation (III.1)). Using  $\psi$ , the wall angle, and  $q$ , the coordinate of the wall centre, the equation (III.2) transforms into:

$$\begin{cases} \frac{\partial q}{\partial t} = \gamma H_k \sin \psi \cos \psi + \frac{u}{\Delta} + \alpha \Delta \frac{\partial \psi}{\partial t} \\ \frac{\partial \psi}{\partial t} = \beta \frac{u}{\Delta} - \frac{\alpha}{\Delta} \frac{\partial q}{\partial t} \end{cases} \quad (\text{III.4})$$

Here  $K$  is a transverse anisotropy,  $H_k$  standing for  $2K/(\mu_0 M_s)$ , and

$$\Delta(\psi) = \sqrt{\frac{A_{ex}}{K_{anis} + K \sin(2\psi)}}. \text{ The terms arising from the current intervene as in-plane field}$$

terms  $u/(\gamma\Delta)$ , the non-adiabatic term being preceded by  $\beta$ . Comparing these equations with the ones describing the wall evolution under field (see equation (III.1)), it is clear that, an applied field and injected current have completely different influence on a DW. An applied field induces an in-plane rotation of the magnetization, the “pressure” being provided by the resulting demagnetizing field. In field-driven motion the displacement direction was imposed by the direction of  $\mathbf{H}_{dem}$  (resulting, in the precessional regime, in a back and forth shift of the wall). In the case on the current-induced motion, there is, again, a demagnetizing field arising from the non-adiabatic contribution ( $\beta u/\Delta$ ). However, it is not the sole drive force acting on the wall, as the most important part of the force from the current (the adiabatic one) is invested, directly, in changing  $q$ . As  $u/\Delta$  has a constant direction, and is, presumably, stronger the  $\mathbf{H}_{dem}$ , the wall moves always in the same direction, that is - the direction of the electron flow.

The critical value of  $u$ , for which a steady solution is valid, is:

$$|u_c| = \frac{\gamma H_k}{2} \Delta \frac{\pi}{4} \frac{\alpha}{|\beta - \alpha|} \quad (\text{III.5})$$

The wall velocity is connected to the quantities characterizing the spin-polarized current,  $u$ ,  $\beta$  and to the Gilbert damping parameter via the relationships:

$$v_{steady} = \frac{\beta}{\alpha} u \quad (\text{III.6})$$

$$\langle v_{osc} \rangle = \frac{1+\alpha\beta}{1+\alpha^2} u \quad (\text{III.7})$$

The numerical results revealed another interesting feature of current-induced DW motion, namely the very important role played by the  $\beta$  parameter. Depending on its value, in a velocity-versus-current density diagram, one of the motion regimes mentioned above might be present or not. Three possible scenarios are foreseeable:

1. In the case when  $\beta \neq \alpha$  and  $\beta \neq 0$ , both a steady and a precessional regime can be identified. In the steady motion, the misalignment between the conduction electrons and the wall results in a non-zero  $\phi$  angle. In the first moments of the motion the wall velocity increases. Then, the wall translates steadily with a tilted structure and constant velocity. For values above  $J_c$ , the wall has a precessional motion. Here, the torque from the current dominates the demagnetizing and damping ones. During motion, on the narrower end of the transverse wall an antivortex makes its appearance. As the wall moves forward, the antivortex traverses the wire width, being expelled on the edge - opposite to the one where it entered the wire. The configurations presented in Figure III.4 exemplify this behavior. The antivortex appears periodically. During the change in the wall structure, the wall velocity oscillates between a (positive) minimum and maximum, its average value being different from 0.
2. If  $\beta = \alpha$  a new kind of motion is discerned. The critical current limiting the steady motion is infinite, the wall moving with a velocity equal to the velocity-like quantity  $u$ . The spins in the wall do not tilt, because the non-adiabatic term compensates perfectly the damping term resulting a pure translation regime.
3. For  $\beta = 0$  a threshold current density  $J_c$  is required for sustained DW motion. If  $J_{app} < J_c$  the magnetization in the DW tilts towards the hard axis, but instead of accelerating it slows down. As only the adiabatic torque acts on the wall, the

motion is blocked and the wall velocity going to zero. For  $J_{\text{app}} > J_c$  the precessional motion described for the previous case is seen.

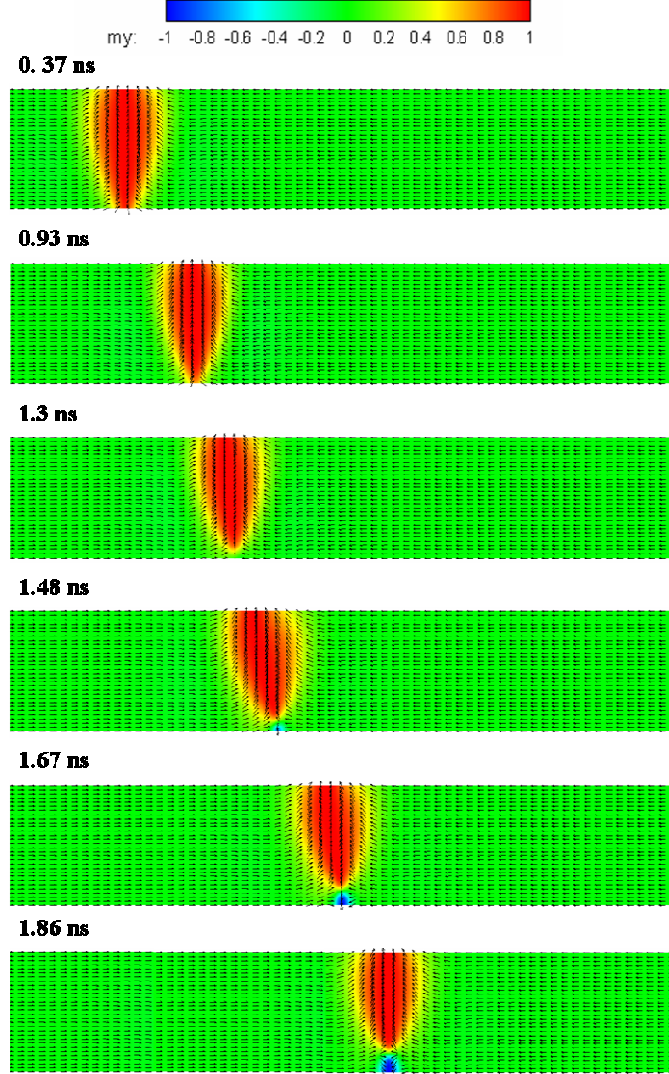


*Figure III.4: Several configurations taken during DW displacement, showing the modifications that occur in the wall structure. In the fourth image the antivortex makes its first appearance in the lower part of the wire. The last configurations present how the antivortex grows and evolves towards the upper part of the wire*

Whereas field-induced DW motion has revealed all of its interesting features, looking at the various possibilities that occur depending on the  $\beta$  value and its positioning relatively to the value of the damping parameter, one realizes that, certain details are still needed for a complete understanding of current-induced DW motion. The exact origin and value of the non-adiabatic spin transfer parameter are still to be determined. Also it would

be interesting to determine the possibilities of enhancing the effect of the spin torque on a DW.

The observations presented above are valid for ideal systems. Very important influences in real systems have for example pinning of the DWs and thermal effects. The sources of pinning are various: surface roughness, variations of the material parameters ( $K_{anis}$  for example). Also different type of constrictions can be considered. Joule heating due to the high current densities can eventually help depinning, but these effects have not been studied in detail for the moment.

### *III.2.3. The WALL\_ST micromagnetic tool*

The micromagnetic simulation tool is based on the finite difference approximation. WALL\_ST is derived from the code GL\_FFT, whose main features were presented in paragraph II.1. Here we will mention a few adaptations that had to be made, in order to take into account the effect of the current and assure a correct description of the studied magnetic systems.

A complete overview of field and current-induced motion implies a profound understanding of the role of each intervening factor. Besides the external factors (the applied field and the injected current), it is important to identify the internal elements that must be taken into account. One of these is the demagnetizing field of the wall. To get some information about the behavior of this contribution, known to be dependent on the shape and size of the magnetic system, simulations were carried out on three types of geometries: bulk, thin film and wire with rectangular cross section. The hypothesis of uniform magnetization along the Oy and Oz direction is considered for the bulk system and along Oy for the film. It is clear then that certain special “effects” have to be used in order to cope with the infiniteness of the model system, as one can not simulate infinity. To treat the infinite length, a common feature of all the three cases, the geometry is decomposed in several parts as depicted in Figure III.5:

- The “real” computation region is made of a rectangular prism of finite length. The magnetization is fixed on the left and right surfaces.
- Two semi-infinite regions, connected to the left and right side of the computation region. In these regions the magnetization is uniform, and has the direction imposed by the magnetization of the cells on the lateral sides of the computation region. The field generated by the magnetization in these regions is calculated analytically. Thus the demagnetizing field  $\mathbf{H}_{\text{dem}}$  includes the stray field radiated by these two semi-infinite regions and the stray field radiated from the computation region itself.

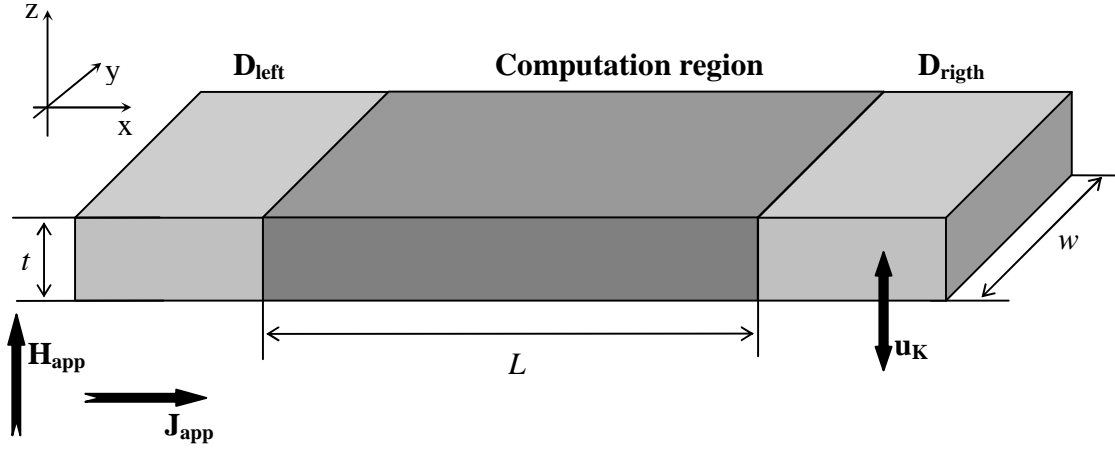


Figure III.5: Definition of the computation region (colored in blue). While its length is fixed ( $L=512\text{nm}$ ), its width  $w$  and thickness  $t$  might be varied. On the lateral surfaces, where the computation region meets the semi-infinite  $D_{\text{left}}$  and  $D_{\text{right}}$  regions, the magnetization is fixed. Periodic boundary conditions can be applied on the front and back, respectively upper and lower surface.

In the case of the thin film and the bulk systems, infiniteness along other directions than  $Ox$  has to be taken into account. This requirement is assured by the use of periodic boundary conditions, on both the  $Oy$  and the  $Oz$  direction for the bulk and only on the  $Oy$  direction for the film.

The computation region is split up in  $N_x \times N_y \times N_z$  discretization cells. The initial wall position corresponds to  $N_x/2$ . During the simulation, the wall is left to travel along the  $Ox$  direction. Due to the finite size of the computation region, precautions have to be taken, as the moving wall might approach too closely the lateral surfaces, where the magnetization is fixed, and thus its dynamics could be altered. In order to prevent this, a scheme was implemented that maintains the DW in a region where one can be sure that no parasite effects occur. The wall position is constantly monitored (the methods for determining this parameter are described later on). If its value is smaller than  $N_x/4$  or bigger than  $3N_x/4$  the wall is translated so that its center is placed at  $N_x/4$ . The distance of  $N_x/2$  on which the wall is allowed to move, was determined based on observations of the magnetization distribution inside the wall. The wall occupies a certain volume, over which the transverse magnetization components smoothly attenuate, to become finally zero in the domains' region. By placing the wall such that, its center is at a distance of  $N_x/4$  from the lateral



borders of the computation region, one can be sure that these fixed-magnetization surfaces will not influence the wall dynamics. It is important to note that the criterion of  $N_x/4$  might be valid only for the present case. For a different wall structure, magnetization configuration, or sample size the optimal value has to be re-evaluated.

*Discretization:* The length of the computation region is fixed (512 nm), independently on the type of the geometry (bulk, film or wire). On the other directions, the size is varied based on which kind of system is simulated: bulk, film or wire. Generally speaking, in numerical micromagnetism the size of the discretization elements is subject to certain constraints. Namely the lateral size of the elements must be smaller than the minimum of the exchange and Bloch lengths, which in the present case sets a limit of 8 nm. As the length of the computation region is constant, here this restriction on the space step is respected,  $\delta_x$  being set to 4 nm in all the following simulations, resulting in 128 mesh elements. However, taking into account the specificity of the simulated geometries, together with the width and height,  $\delta_y$  and  $\delta_z$  have to be also adapted. In the following the geometrical features and the numerical parameters chosen for each of the three geometries are presented.

- a) *Bulk system:* To have a realistic approximation of the bulk, the magnetization is supposed to be invariant along the width and the height of the computation region. In addition to the periodic boundary conditions imposed along the concerned directions, Oy and respectively Oz, a single discretization element was considered along these directions. Therefore the mesh consists of  $128 \times 1 \times 1$  cells, the size of a cell being  $4\text{nm} \times 10\mu\text{m} \times 10\mu\text{m}$ .
- b) *Thin film:* The thin film is considered to be infinitely wide. To respect this hypothesis, the same method was used as for the bulk: periodic boundary conditions are imposed along Oy and the width of the mesh element is very large. The thickness of the film (and also the wire) is quite reduced, 11 nm, very close to the characteristic lengths. As far as the space step  $\delta_z$  is concerned, a study was carried out to see whether using a sole mesh element ( $N_z=1$ ), a result accurate enough is obtained. Two sets of results are presented in Figure III.6. The first

image shows the evolution of the  $\langle m_x \rangle$  magnetization component while the second one represents the wall position as a function of time. The results, obtained using one or four mesh cells along the Oz direction, are in a very good agreement, the differences being unnoticeable.

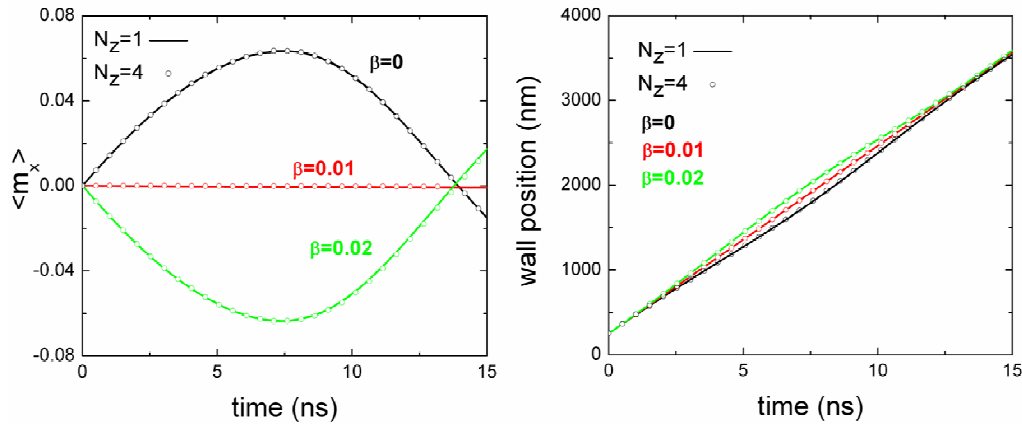


Figure III.6: The average  $m_x$  magnetization component and the wall position as a function of time for one, respectively four mesh elements along the Oz direction.

In Figure III.7 several configurations taken at different time steps are compared.

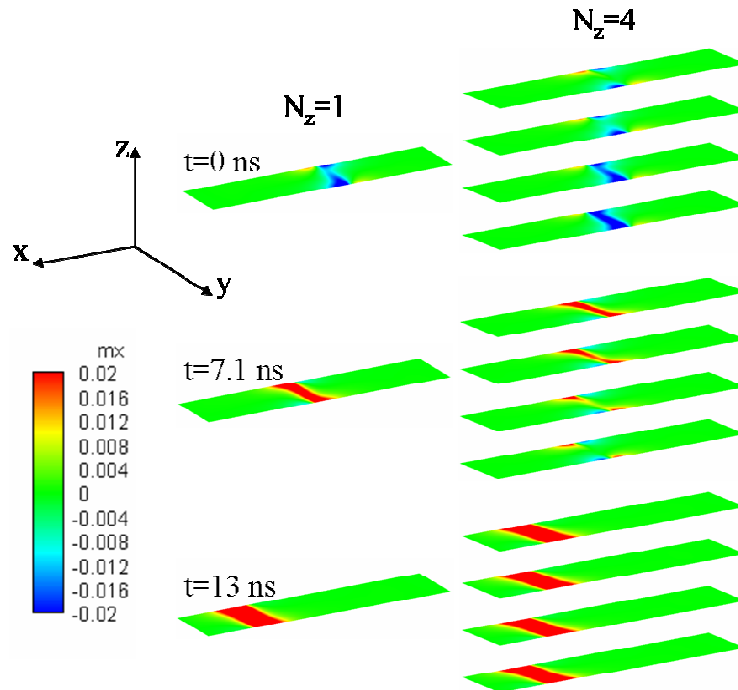


Figure III.7: Comparison between magnetization configurations obtained using  $N_z=1$  or  $N_z=4$ . Considering the values of the  $m_x$  magnetization component, the differences are negligible.

The configurations on the left-hand-side were obtained using a single mesh cell along Oz, whereas the groups of four layers on the right-hand side, correspond to the situation when  $N_z=4$ . Each one of the colored surfaces represents the  $m_x$  magnetization in one of the four mesh layers along Oz. Only the  $m_x$  component is represented, as if differences occur in the magnetization distribution along the film thickness, for this quantity they are the most visible. Looking at the  $m_x$  values it is clear that the discrepancy is insignificant. One can therefore conclude that using  $N_z=1$  the description of the thin film (and the wire) is accurate enough. The space discretization is then based on  $128 \times 1 \times 1$  cells, each of them occupying a volume of  $4\text{nm} \times 10\mu\text{m} \times 11\text{nm}$ .

- c) *Nanowire*: The mesh size along the Ox direction is set to 4 nm. Along the Oz direction it has been shown that setting a mesh size of 11nm, the system is appropriately described. Along the remaining axis, corresponding to the wire width, several possibilities were explored. Taking into account the rule of thumb limiting the mesh size, a mesh size of 4, respectively 8 nm, was tested (resulting in  $N_x=30$  and  $N_x=15$  elements). However, assuming an invariant magnetization along Oy, one is allowed to use a single mesh element along the wire width (with the volume  $4\text{nm} \times 120\text{nm} \times 11\text{nm}$ ) and quasi-1D simulations can be carried out. Although essentially the accuracy of such calculations is questionable, still it can provide a general idea about how the system behaves within reasonable computation time.

*Determining the wall center*: Several ways of determining the wall center were tested: one can either calculate the wall's center of mass or look to the value of the  $m_z$  magnetization component. Both approaches were tested showing very small, almost irrelevant differences between the results.

*Integration scheme*: Concerning the integration scheme used for solving the LLG equation, a predictor-corrector Heun scheme was implemented. The time scale of the magnetization dynamics imposes a very small time step, of the order of 1fs.

*Initial magnetization distribution:* In order to determine the effect of a magnetic field or a spin-polarized current one has to find, firstly, the equilibrium state of the magnetic system without any of these external factors. The equilibrium state is calculated based on the LLG equations, using the material parameters characteristic to the magnetic system. However, as the dynamics it is not the point of interest in this first part, the damping parameter is set to 1. Once the equilibrium state is found, the obtained magnetization distribution is set as initial configuration for the field/current-driven DW motion simulations. For these, the real value of the damping parameter is employed.

*Field/current distribution:* There are several possibilities to initiate DW motion. Besides continuous field/current, the external excitations can take the form of pulses with different duration and shape. Also, one can choose either a uniform field/current distribution or, if required spatially varying distributions can be considered. The choice of generating non-uniform distribution for the material parameters:  $A_{ex}$ ,  $M_S$  and  $K_{anis}$ , was also implemented. Even more, besides the simplest geometry of a rectangular prism, constrictions with different shape and size can be created. These various possibilities are all generated before starting the simulation using simple subroutines of the WALL\_ST simulation tool.

*Output:* The results contain an evolution file, where the values of the magnetization components, the energy terms and the total energy, the wall position and velocity at consecutive time steps are recorded. Moreover, one can chose to export magnetization configurations at certain time steps.

Knowing these, in the next part the results obtained for out-of-plane magnetized systems will be presented. This chapter is organized as follows: first the results obtained for the bulk system are presented, both for field and current-driven motion. Then, the influence of the geometry on the critical values and on the mechanisms of DW displacement was studied, by reducing the system firstly, to a thin film, and then to a nanowire. Ending the simulations on ideal systems, in the last part of this chapter several kind of pinning possibilities were considered.

### III.3. Results

#### III.3.1. Bulk system

The bulk system represents the second test case, after the Permalloy wires. The first test case proved that our implementation can reproduce accurately the results obtained previously for in-plane magnetized systems by the group of Thiaville [Thiaville 2005]. However, for the moment, this conclusion is valid only for systems with such a magnetization orientation, and the validation of the WALL\_ST simulation tool for perpendicular domain configuration is still required.

As the topic of perpendicularly magnetized systems is relatively new, the amount of numerical results concerning such systems is very small and therefore the only possibility we had to verify the performance of the WALL\_ST solver was to look at analytical solutions [Schryer 1974]. Even though this benchmarking step seems trivial, it is absolutely necessary. The eventual good agreement with Walker's analytical predictions for field-driven motion assures the correctness of the future findings.

The study of bulk system has a second role also; it serves as a reference for the results obtained for systems with reduced dimension, like the thin film and the wire, where the magnetostatic effects are modified with respect to what occurs in the bulk.

For all the simulations reported below the material parameters [Rodmacq 2006] used are listed in Table III.2.

*Table III.2: Material parameters:*

$M_S$ (kA/m)	$A_{ex}$ (J/m)	$K_{anis}$ (J/m <sup>3</sup> )	$\alpha$	P
254.54 ( $\mu_0 M_S = 0.32$ T)	$10^{-11}$	127270 ( $H_{anis} = 1$ T)	0.01	1

Besides the spontaneous magnetization, the exchange stiffness constant, the magnetocrystalline anisotropy constant and the damping parameter  $\alpha$ , the current

polarization is also included. For the non-adiabatic spin transfer parameter several values were considered.

In a spherical coordinate system [Hubert 1998] the DW can be defined as the region where the angle  $\theta$  varies between  $0^\circ$  ( $D_{\text{left}}$ ) and  $180^\circ$  ( $D_{\text{right}}$ ) (Figure III.5).  $\varphi$  is the angle of the wall with the plane ( $yOz$ ): if  $\varphi$  is zero the wall is of Bloch type and when  $\varphi=90^\circ$  the wall is of Néel type (Figure III.1).

### *III.3.1.1. Domain wall motion under applied field in a bulk system*

In an infinite magnetic system, divided in two domains separated by a Bloch wall, an external field, applied along the domains' direction will tend to extend the domain that is oriented along its direction at the expense of the anti-parallel domain. The growth is in fact achieved via displacement of the wall separating the two domains. If the wall is defined by the angles  $\theta$  and  $\varphi$  (the latter one being 0 in the initial state, Figure III.1), then, looking only to the central spin, the wall displacement can be viewed as happening whenever a change (rotation) in  $\theta_{\text{centre}}$  occurs.

Under the influence of the field, the magnetization in the wall tries to align itself parallel with the field, describing a damped precessional motion. Depending on the strength of the external field several scenarios are possible:

1. If the field is small, the torque arising from it is not strong enough to orient the magnetization, its sole effect being a tilting away from the original direction, the angle  $\varphi$  attaining a certain value different from zero. Results obtained by our numerical approach sustain this. As shown in Figure III.8 the “equilibrium” value of the  $\varphi$  increases with the applied field. It is important to note that the change in  $\varphi$  engages modification in the wall width. However these are less significant, as the maximal change, for  $\varphi=45^\circ$  represents less than 10%.

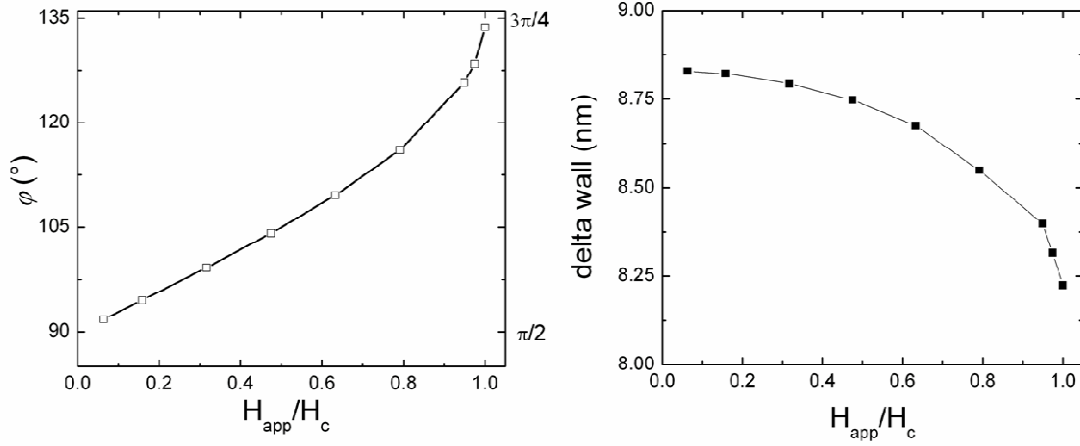


Figure III.8: The behavior of the angle  $\varphi$  and the DW width as a function of field for the bulk system in the steady motion regime.

The pure Bloch wall is magnetic charge free, but any change in  $\varphi$  (supposed constant throughout the wall) gives rise to magnetic charges, and therefore to an in-plane demagnetizing field  $\mathbf{H}_{dem}$ , perpendicular to the wall. The fields and torques occurring are shown schematically in Figure III.9.  $\mathbf{H}_{dem}$  adds up to the damping that tends to align the magnetization with the applied field and, provides the torque necessary to produce a change in  $\theta$ , and therefore to push the wall forward.

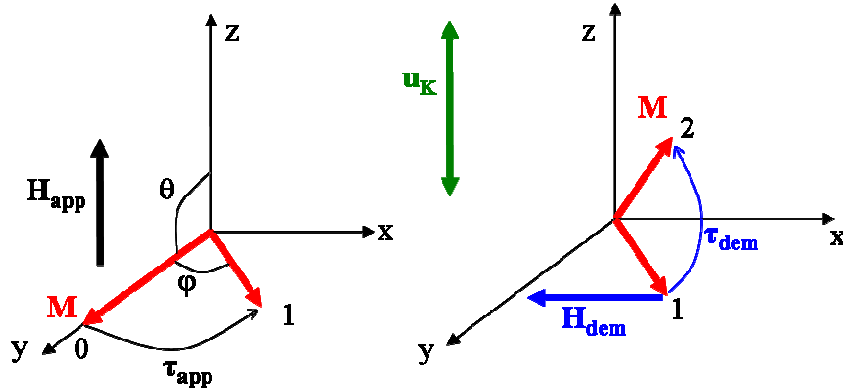


Figure III.9: The fields and torques responsible for the movement of a DW. The applied field rotates the magnetization  $\mathbf{M}$  from position 0 to 1. Then the torque from the demagnetizing field rotates  $\mathbf{M}$  towards the  $Oz$  axis, from position 1 to 2.

The displacement occurs as follows: simultaneously with the increase of  $\varphi$  due to the applied torque, the wall velocity also increases, as shown in Figure III.10.

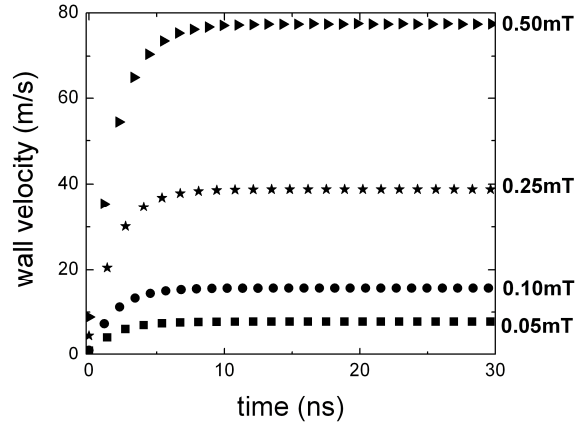


Figure III.10: The variation of the wall velocity versus time for several values of the applied field. The evolution comport two parts: first the wall accelerates up to a final velocity, and then the motion occurs steadily.

The magnetization tilts until equilibrium between the applied and the damping torques is reached (the first nanoseconds on the curves given in Figure III.10). Once the rotation ceases, the wall moves on steadily, having an intermediate Bloch-Néel structure. The wall velocity depends on the strength of the driving force - that is - the demagnetizing field. As this field is limited, reaching its peak when  $\varphi=45^\circ$ , the wall velocity is also bounded by a maximal value given by:

$$v_{steady} = \frac{\gamma_0 \Delta}{\alpha} H_{app} \quad (III.8)$$

The critical field value under which this steady behavior occurs was defined by Walker as:

$$H_c = \frac{\alpha M_s}{2} \quad (III.9)$$

For values higher than the one issued by (III.9), the external field drives the in-plane wall magnetization to angles larger than  $\varphi=45^\circ$ . Torque equilibrium is not possible in this case, and the in-plane magnetization does not stop precessing around the z-component of the effective field. Instead, it covers periodically the interval  $[0, 360^\circ]$ , taking the wall through Bloch and Néel configurations. The evolution of the  $\theta$  and  $\varphi$  angles during a cycle of Bloch-Néel transitions is shown in Figure III.11:



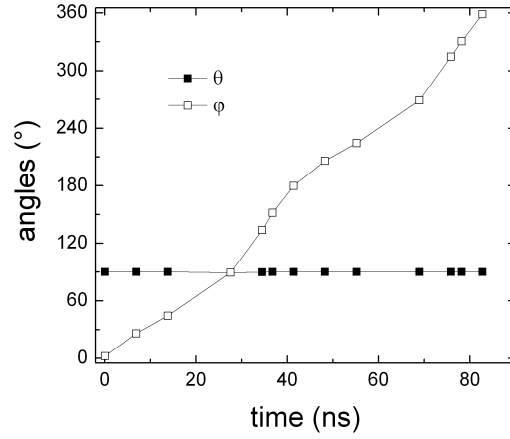


Figure III.11: The angles  $\varphi$  and  $\theta$  during a complete cycle of Bloch-Néel transformations.

As the driving field is generated by the magnetic charges, the provided torque is affected by the structural modifications of the wall, changing direction every time when  $\varphi$  is equal to a multiple of  $90^\circ$ . This can be recognized in the behavior of the wall position and the wall velocity, depicted in Figure III.12. The wall moves back-and-forth, while the wall velocity attains both positive and negative values. The maximal, respectively minimal values that the velocity can attain are  $v_{max}=v_c$ , respectively  $v_{min}=-v_c$ , where  $v_c$  is the velocity attained for  $H_{app}=H_c$ :

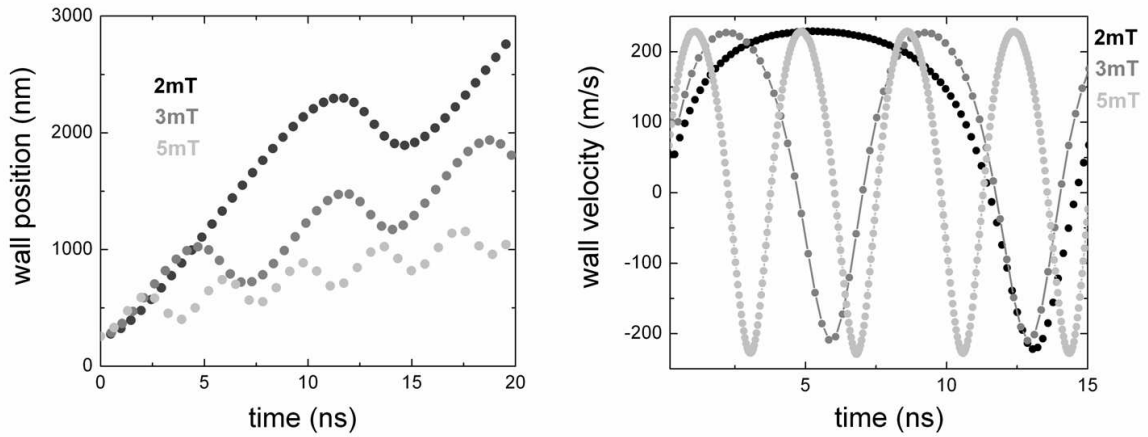


Figure III.12: Wall position and velocity for values of  $H_{app}$  higher than  $H_c$ .

The velocity is zero when the wall is either pure Bloch or pure Néel type. When transiting between the two structure types, the velocity evolves either towards a maximum/minimum value. Higher the applied field, higher the oscillation frequency of  $\varphi$ . The oscillation period of the angle  $\varphi$  was determined to be twice the oscillation period of the wall velocity.

Walker predicted the existence of two linear-velocity motion regimes. The first extends until  $H_{app}=H_c$ , followed by a transient regime, where wall motion occurs by precession, the DW going through periodical changes (Bloch to Néel and vice-versa). In this transition regime, although it is known that the average velocity has a decreasing tendency, no relationship between this quantity and the applied field could be derived. Nevertheless, at fields much larger than  $H_c$ , the average velocity increases again. The net effect of the demagnetizing field on the displacement of the wall is zero. The damping torque is the one that - trying to align the magnetization with the applied field - sets the wall in motion. The average velocity tends towards the asymptotic limit:

$$\langle v_{osc} \rangle = \gamma_0 \Delta \frac{\alpha}{1+\alpha^2} H_{app} \quad (III.10)$$

The two motion regimes for the bulk system are represented in Figure III.13.

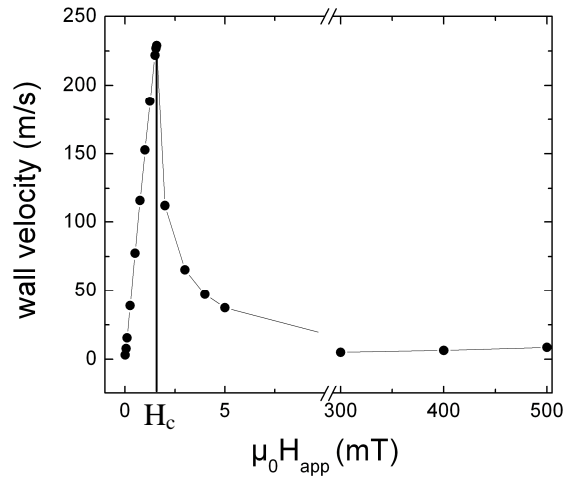


*Figure III.13: Two motion regimes identified by Walker: the steady and the precessional regime. In both these regimes the wall velocity, respectively its average value, increases linearly with the applied field. A transition region, where the average velocity decreases, separates the two linear motion regimes.*

The value of the critical field determined by simulation was compared to the one calculated using (III.9). The two values are very close:  $H_{simulation}=1.58\text{mT}$ , whereas,  $H_{analytic}=1.6\text{mT}$ . Furthermore, the simulations reproduced accurately the details concerning the in-plane angle  $\phi$  and the wall velocity of DW motion given in [Schryer 1974]. An important conclusion can be drawn from the above presented results. Based on the good agreement with the analytical results provided by Walker's model, the WALL\_ST simulation tool

seems to be well adapted for the study of field or current-induced DW motion in materials with perpendicular magnetization orientation.

### *III.3.1.2. Domain wall motion under spin-polarized current in a bulk system*

Similarly with the case of field-induced DW displacement, two motion regimes are defined: a steady and a precessional regime, delimited by a critical current  $J_c$  [Mougin 2007]:

$$J_c = \frac{e M_s^2}{g \mu_B P} \gamma_0 \Delta \frac{\alpha}{|\beta - \alpha|} \quad (\text{III.11})$$

The steady motion regime covers the interval of  $J_{\text{app}} \in [0, J_c]$ . It is followed by a transition region, exactly like in field-induced motion, and then by the precessional regime, at high current densities. The wall velocity is connected to the quantities characterizing the spin-polarized current,  $u$  and  $\beta$  and to the damping parameter  $\alpha$ , via the relationships (III.6) and (III.7). The difference between field and current-induced motion is that, whereas in the first case, the direction of the wall motion changes with respect to the direction of the demagnetizing field, if wall displacement is due to spin-polarized current, the DW follows always the direction of the electron flow.

In the paragraph presenting the results on the Permalloy nanowire, it was shown that the value of the  $\beta$  parameter determined the presence or absence of one of the above mentioned regimes in a velocity-versus-current diagram. This is true for the present system also. As shown in Figure III.14 three different kind of curves are present. If  $\beta=0$  for  $J_{\text{app}} < J_c$  the wall velocity is zero. When the precessional regime is reached the average velocity increases linearly with the current.

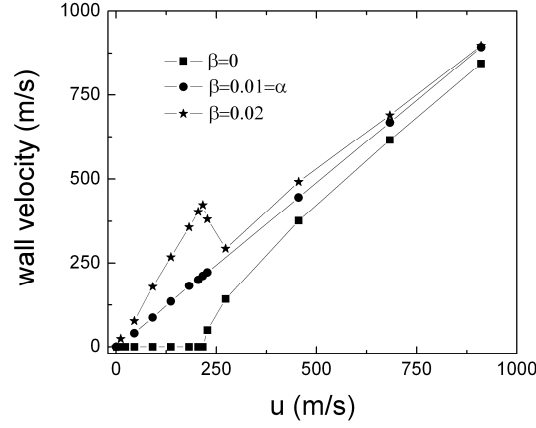


Figure III.14: Summary of the behavior of a Bloch wall's velocity in current driven DW motion, showing clearly the important role played by the non-adiabatic parameter  $\beta$ .

If  $\beta=\alpha$  the wall moves always steadily, as the critical current density for Walker breakdown is infinite. The pure Bloch wall (see in Figure III.15 that the angle  $\varphi$  remains constant during motion independently on the current value) translates with a velocity equal to  $u$ .

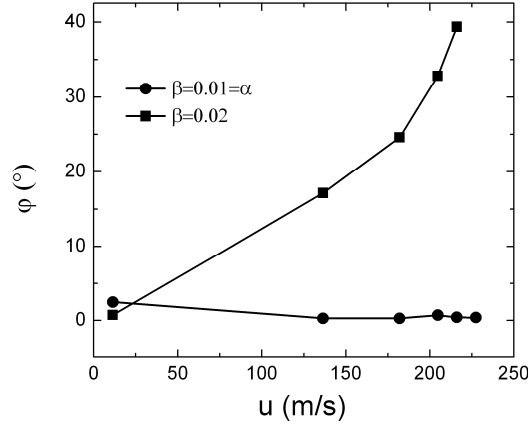


Figure III.15: The variation of the angle  $\varphi$  as a function of  $u$  and the value of the  $\beta$  parameter. While for  $\beta=0.02$  a field-like behavior is observed, if  $\beta=\alpha$ , the wall remains pure Bloch during the whole duration of the motion.

For  $\beta \neq 0$  and  $\beta \neq \alpha$ , both the steady and oscillatory regimes are present. The behavior is similar with the field-driven one, with a terminal velocity (in the steady regime) and, respectively, an average velocity (in the precessional regime) that increases linearly with the current.

Although analytical solutions for the bulk were given only for field-driven motion, the experimental observations and the numerous theoretical/numerical predictions prove that the above described behavior is correct.

This first part of the results had a pure pedagogical purpose. The good agreement found for this second test case shows that our micromagnetic simulation tool reproduces the analytical results for out-of-plane magnetized systems accurately. Therefore the treatment of systems with reduced geometries (thin film and the nanowire) is, for the moment at least justified, and as it will be shown later, also accurate.

Comparing the motion of such a 1D Bloch wall with the displacement of transverse walls, one remarks that the two processes are quite similar. Obviously, the wall velocity values and the critical breakdown field/current are different, but the wall motion mechanism apparently respects the same rules. The steady motion extends to a threshold field/current value, above which the changes in the wall magnetization impose the cyclical modification of the wall structure, and consequently, periodic variations of the wall velocity. For in-plane materials the wall structure oscillates between a transverse and an antivortex structure, while in the second case, it cycles between Bloch and Néel type walls. The direction of motion either changes, following the demagnetizing field - in the case of field-driven motion, or stays constant when the wall motion is due to a spin-polarized current. These conclusions are valid for the bulk system. In experiments, however, mostly systems with reduced dimension are used, e.g. thin films or wires with different cross sections. The question that arises now is how the reduction of the geometry's dimension influences the process of DW motion.

### III.3.2. *Size effects*

#### III.3.2.1. *Size effects in the framework of quasi-1D simulations*

Modifying the lateral size means changing the ratio between the geometric features. While the exchange and magnetocrystalline anisotropy terms are insensible to such factors, a strong influence on the wall's demagnetizing field is expected. The most natural way to look at this problem is by making use of the demagnetizing factors of the wall.

Two systems with reduced dimension were considered: a thin film with infinite length and width and a thickness of 11nm, and respectively an infinitely long nanowire with a width of 120nm and a thickness of 11nm.

In the first time, the hypothesis of a uniform magnetization along the Oy direction was taken into account. Based on this, a single mesh element along the geometry width was used. Therefore these simulations can be viewed as quasi-1D, where the local demagnetizing field is replaced by its value, averaged over the cell. The material parameters, inclusively the damping parameter  $\alpha$ , are those considered for the bulk material. Figure III.16 shows a comparison between the wall velocity versus applied field and versus injected current (for  $\beta=0.02$ ) for the three systems.

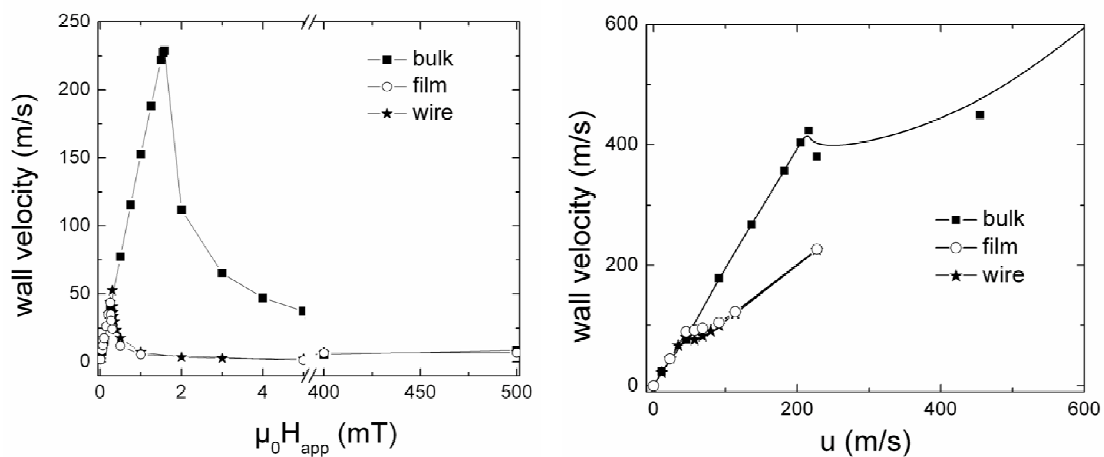


Figure III.16: Wall velocity versus applied field and injected current for the three systems: bulk, thin film and wire. The parameter  $\beta$  is 0.02.

It is clear that, modifying the geometry, leads to an essential decrease of the critical field/current. The values are assembled in Table III.3.

*Table III.3 Critical field and current density for the three studied systems*

System	$H_c(\text{mT})$	$J_c(\text{A/m}^2)$
Bulk	1.60	$95 \cdot 10^{10}$
Film	0.30	$22 \cdot 10^{10}$
Wire	0.25	$18 \cdot 10^{10}$

A detailed study revealed that the behavior of the angles  $\theta$  and  $\phi$  show the same features as those seen for the bulk. This indicates that, the displacement mechanism remains the same: slight tilting of the magnetic moments in the steady motion regimes and cyclical transformation between Bloch and Néel structures in the precessional regimes.

Working with the approximation of uniform magnetization along Oy placed us in the framework of analytical approaches coping with the dependence of the critical field/current on the geometry. Several papers addressed already this topic for the case of in-plane magnetization [Thiaville 2002, Porter 2004]. Mougín et al [Mougín 2007] considered also the case of out-of-plane magnetized systems, giving formulas for the “reduced” critical field/current. They take into account the size effect through the demagnetizing factors:

$$\begin{aligned}
 H_c &= \frac{\alpha M_s}{2} |N_{xx} - N_{yy}| \\
 J_c &= \frac{\alpha e M_s^2}{g \mu_B P} \frac{\gamma \Delta}{|\beta - \alpha|} |N_{xx} - N_{yy}|
 \end{aligned}
 \tag{III.12}$$

We compared the results obtained by simulation with values calculated with the expressions above. In order to determine the demagnetizing factors, the DW was approximated either by a uniformly magnetized ellipsoid [Osborn 1945] or rectangular prism [Aharoni 1998]. The dimensions used to approximate with corresponding geometric bodies are: the length is equal to the DW width (9.97 nm for the film and 9.92 nm for the wire), the width equal to infinity for the thin film and 120nm for the wire, and height of 11nm.

Independently on the method used to calculate the demagnetizing factors, a very important discrepancy is found between the analytical and the numerical values. The simulated values are more than 2.5 times smaller than those predicted by eq.(III.12). For example, for the nanowire  $H_c$  obtained by simulation is 0.25 mT, while from the analytical formula one obtains  $H_c=0.75$  mT. The same discrepancy occurs for the critical current density:  $J_{\text{simulation}}=19 \cdot 10^{10} \text{ A/m}^2$ , while  $J_{\text{analytic}}=58 \cdot 10^{10} \text{ A/m}^2$ . However, we observed that by taking the length of the geometrical object to be  $\pi \cdot \Delta$  instead of  $\Delta$ , as in the approach proposed in [Porter 2004], the agreement between the results is improved, the values obtained for the nanowire are  $H_c=0.27$  mT and  $J_c=21 \cdot 10^{10} \text{ A/m}^2$ . The relative difference for these new values is around 10%, and thus acceptable.

Even though, tuning the DW width results seemingly in better agreement between analytical and numerical solutions, this method remains an artificial one. Based on results provided by real 3D micromagnetic simulations, it will be shown, that the hypothesis of uniformly magnetization along the wire width is not appropriate and results in an erronated estimation of the critical field/current.

### *III.3.2.2. Size effects revisited: framework of 3D simulations*

3D micromagnetic simulations were carried out for the nanowire. The 3D character is assured by the use of a large number of discretization elements along the wire width. This will help better capturing the eventual variations of the magnetization along this direction. Several space discretizations were tested:  $128 \times 15 \times 1$  cells, each of them occupying the volume of  $4 \text{ nm} \times 8 \text{ nm} \times 11 \text{ nm}$ , and  $128 \times 30 \times 1$  cells of  $4 \text{ nm} \times 4 \text{ nm} \times 11 \text{ nm}$  each.

The purpose of this study was to see the influence of the discretization on the Walker field (or the equivalent current density) and the on the wall velocity. The results obtained are presented in the Figure III.17:



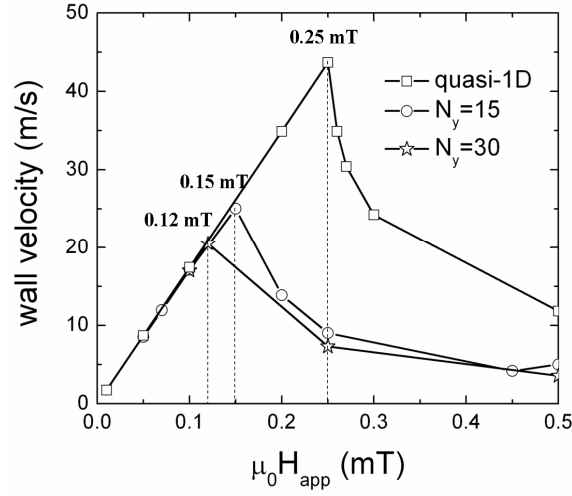


Figure III.17: Wall velocity versus applied field for several values of  $N_y$ .

From Figure III.17 it is clear that, there is a very important dependence of the critical field on the discretization along Oy. In fact, the value obtained for the critical field using the 1D approximation gives an upper bound. Using a mesh of  $128 \times 15 \times 1$  cells, the critical field decreases from 0.25 mT to approximately 0.13 mT, and for a mesh consisting of  $128 \times 30 \times 1$  cells the Walker breakdown occurs at a field of 0.12 mT. Here only two discretizations were considered, but one can be positive that a further refinement of the mesh would result in an even smaller critical field. Nevertheless, the two 3D values are relatively close, showing that we are approaching the “correct” value.

The reduction factor of 2, found between the 1D and the 3D Walker field, is retrieved also for value of the critical current density required for Walker breakdown in the current-driven motion. The computation time for the 3D simulations is very large, especially in the steady motion regime where the simulations had to be run during several weeks, in order to be sure that a steady state is reached. This is why, in this case only the discretization consisting of  $128 \times 30 \times 1$  cells was tested. The critical current for precessional motion decreases from  $20 \cdot 10^{10}$  A/m<sup>2</sup> to approximately  $7 \cdot 10^{10}$  A/m<sup>2</sup>.

One must determine the source of the discrepancy between the quasi-1D and the 3D results. The inaccuracy of the 1D approximation is related to the fact that the magnetization in the wall is not invariant along the Oy direction. Figure III.18 shows a magnetization distribution obtained using a space discretization of  $128 \times 30 \times 1$  cells,

together with the magnetization profile on the front, middle and back chain of mesh elements. After a simple “naked eye” analysis of the magnetization distribution one might be misled, as this reveals a rather uniform magnetization. Nevertheless, comparing the  $m_x$  value calculated in the center of the wall, on the borders and the central part, a variation of 33% was found, while for  $m_y$  the relative difference is only of 6%.

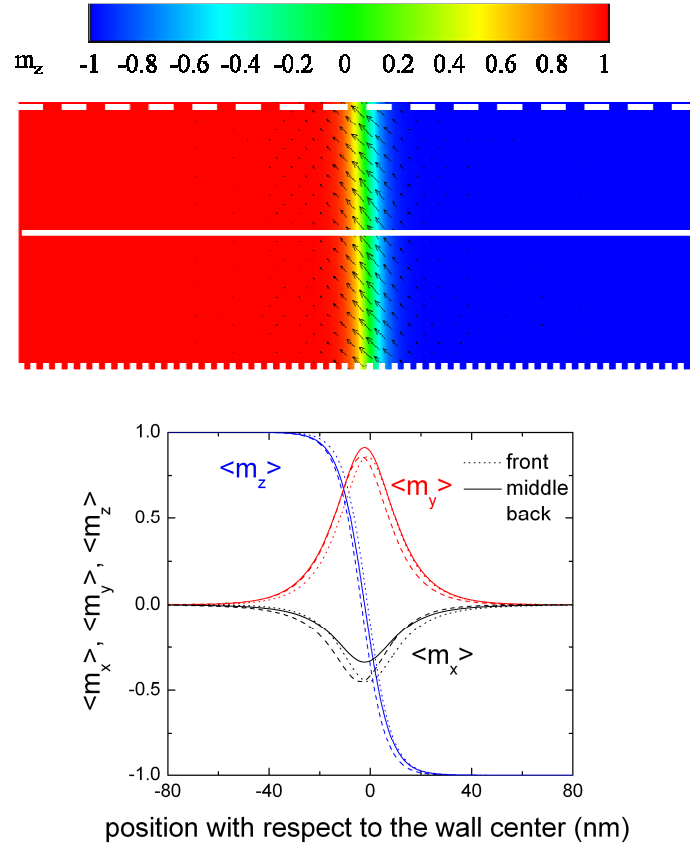


Figure III.18: The final magnetization configuration obtained for a discretization of  $128 \times 30 \times 1$  for a field of 0.1 mT together with the magnetization profile in the middle of the wire and on the front and back surfaces.

The presence of a certain number of mesh elements along the wire width was seen to reveal inhomogeneities in the magnetization distribution. The same effect is observed for the demagnetizing field of the wall, depicted in Figure III.19. Here only the values on the surfaces and the centre of the wire are represented.

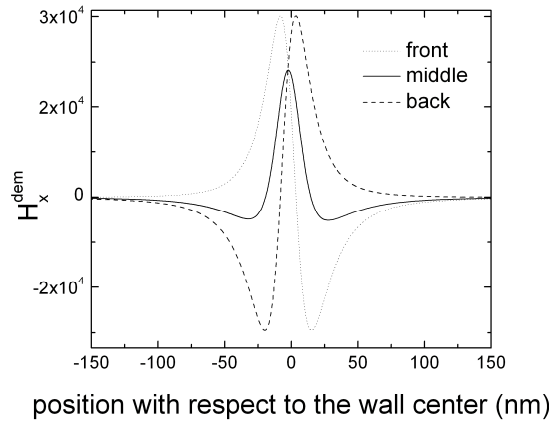


Figure III.19 The variation of the  $x$  component of the demagnetizing field inside the wall.

As more than a single cell along  $Oy$  is taken, when calculating the demagnetizing field, one has to take into account the existence of magnetic charges on the front/back surface that do not arise inside the sample volume. The effect of these charges is more than a simple change in the value of the field: the profile of the demagnetizing field is drastically modified (Figure III.19). On the surfaces  $\mathbf{H}_{\text{dem}}$  has an asymmetric behaviour. This asymmetry attenuates, as one moves towards the central part of the nano-wire.

The value of the demagnetizing field in the wall centre was found to be equal to the value found in the quasi-1D simulation. The values in the mesh elements situated close to the surface are modified. Consequently, the average value of the “effective” field responsible for pushing the DW will be different, and therefore the Walker field is as well modified. When approximating the DW by an ellipsoid or a rectangular prism, this demagnetizing field “distribution” is not detectable, and that is why the use of the demagnetizing factors is not accurate enough.

A very interesting remark concerns the wall velocity. One would have expected this quantity to be influenced also by the discretization. However, the values remain close to those issued by quasi-1D simulations. This is due to the fact that, the only change in the wall velocity comes from the DW width  $\Delta$ , and the magnetostatic effects alter only slightly this quantity. The wall width for the bulk, film and the wire (obtained by quasi-1D simulations) for several field values is shown below. The values of the wall width calculated from 3D simulations (not shown) are very close to those found by assuming a uniform magnetization along  $Oy$ .

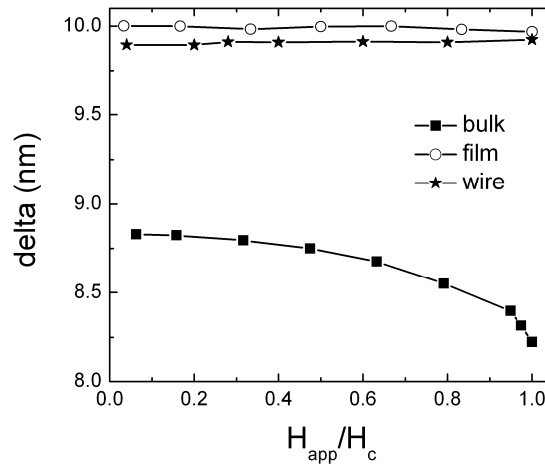


Figure III.20: Variation of the wall width as the geometry changes from bulk to nanowire.

In this first part, field/current-driven DW motion in *perfect* systems with perpendicular magnetocrystalline anisotropy was studied using micromagnetic simulations. The critical field and current for steady motion was determined for a bulk, thin film and a nanowire. For the first two systems, 1D micromagnetic simulations were carried out, whereas the latter was treated both by an 1D and 3D approach. The comparison of these results shows that, the finite size effect of the discretization along the wire width is rather important, as far as the value of the critical field/current density is concerned. In fact, a factor of 2 exists between the 1D and the 3D results. The discrepancy resides in the approximation of the DW by a uniformly magnetized system. The detailed analysis of magnetic configurations, issued by the 3D micromagnetic simulations, showed that the magnetization and the demagnetizing field can differ surprisingly much between the surfaces and the central part of the wire. Nevertheless, the importance of the 1D simulations is not to be neglected, as they have the advantage of a very short computation time and provide a good description of the mechanism of DW motion. For example, in Figure III.21 a comparison between the angles  $\theta$  and  $\varphi$  determined from the 1D and, respectively, the 3D results, for a complete cycle of Bloch-Néel transformations, is presented. Note that the 3D values represent the averaged values of the angles. The agreement is very satisfying.

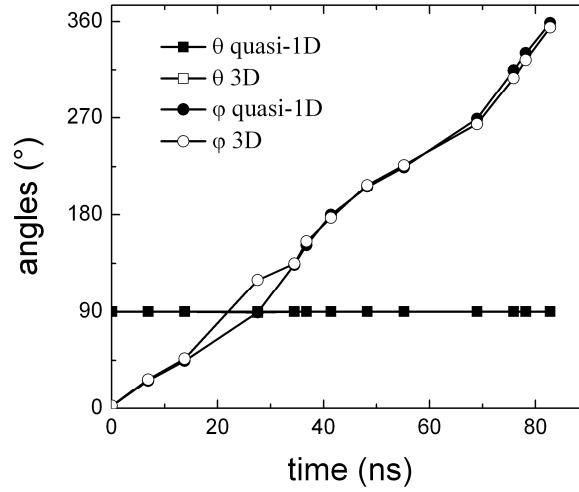


Figure III.21: The  $\theta$  and  $\phi$  angles during a complete cycle of Bloch-Néel transformations. The filled symbols are issued by quasi-1D simulations; while the empty ones correspond to the values obtained using 3D micromagnetic simulations.

The motivation for using 3D simulations becomes clear at high fields/currents. In Figure III.22 several configurations are shown. They represent the magnetization configuration in the magnetic system when an external field of 0.5 mT (the images on the left side) or 90 mT (the images on the right side) is applied. For the small field, the ends and the central part of the wall move in a somehow correlated way. For the field of 90 mT, the wall is similar to a deformed elastic object, with its ends acting in a different way than the central part. It is interesting to notice that although the wall center and its edges seem to be detached, the *local* wall position being different, on the surfaces, the position of the wall center is always the same. At some moments the wall center is in advance, other times the ends seem to pull the central part. All this can be explained based on the non-uniformity of the demagnetizing field.

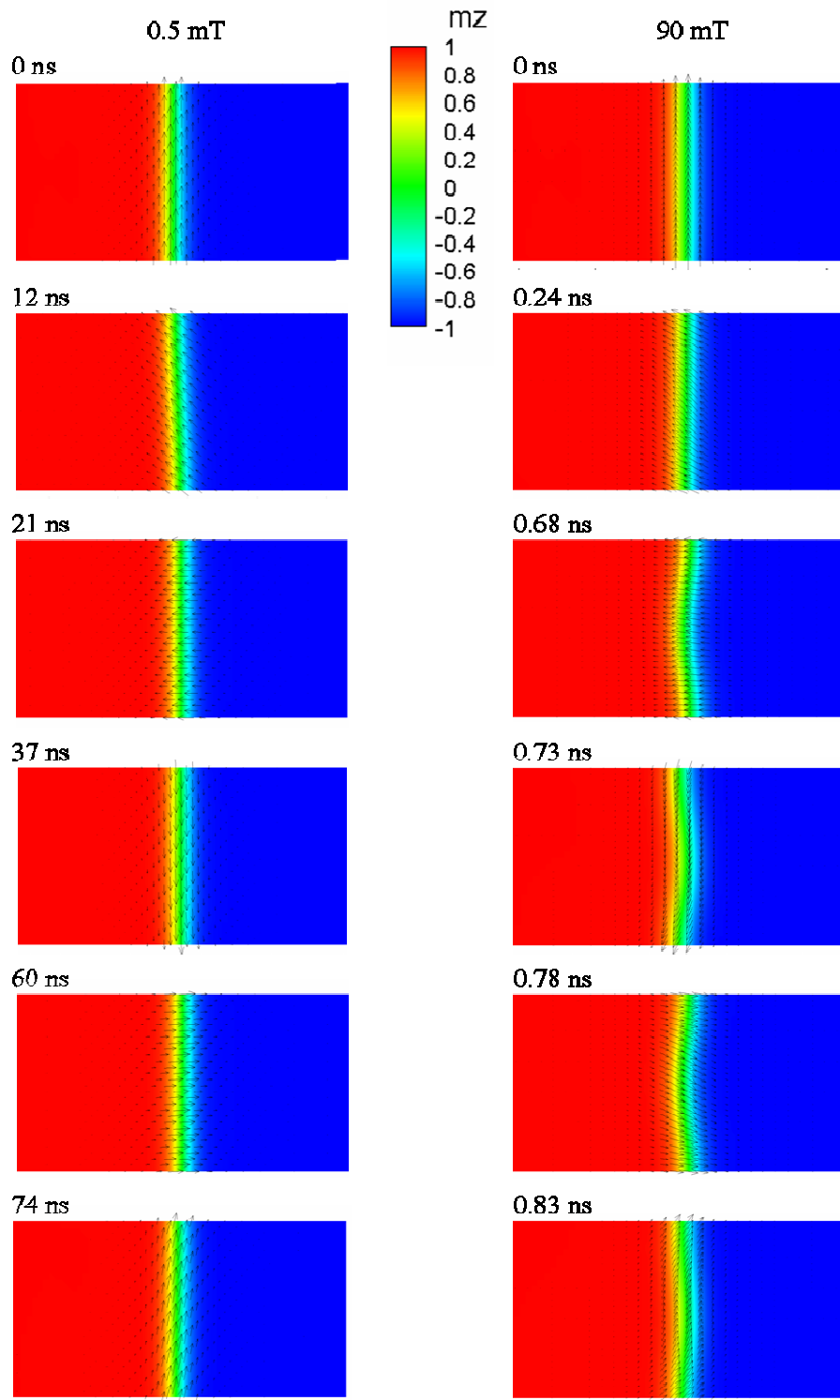


Figure III.22: configurations showing the passage from Bloch to Néel and vice versa for two field values. As  $H_{app}$  grows the non-uniformity of the magnetization inside the wall becomes more important.

### *III.3.3. The role of disorder in the displacement of Bloch walls*

DW motion is interesting from the point of view of applications. Memory devices based on this phenomenon were proposed [Parkin 2004]. To be able to draw conclusions about the feasibility and the operation mode of such devices, an exhaustive study of the phenomenon of DW motion must be carried out. Up to now the displacement of Bloch walls in ideal out-of-plane magnetized systems was analyzed in detail. We saw that one can propagate such walls either using a magnetic field or a spin-polarized current. The characteristics of the propagation process were determined for each case.

Real world devices do not incorporate such ideal nanowires, as in practice such a perfect quality of the samples is impossible to achieve. Several imperfections might occur. Some of them are intrinsic to the material, some of them are due to the manufacturing process and, there can be also provoked, artificial ones. In the first category one can include the spatial variations of the intrinsic material parameters, occurring due to the polycrystalline structure of the samples. For the case studied here, namely a nanowire characterized by strong out-of-plane magnetocrystalline anisotropy, it is interesting to see how the modulation of the anisotropy constant acts upon the DW propagation. The length scale of the modulation of  $K_{anis}$  is dictated by the grain size. The same length scale can characterize the surface roughness due to the patterning process.

The devices based on the displacement of a DW suppose that one is able to position the wall in certain stable location. To stabilize such a magnetic object, different kind of traps might be created: geometrical constrictions, local reduction of one of the material parameters (for example the orientation or the magnitude of the magnetocrystalline anisotropy), demagnetizing field traps, etc.

In the following, some insight will be gained on the influence of some of these factors. In the first time, the issue of spatially varying magnetocrystalline anisotropy is investigated. Results, obtained for an ideal (uniform  $K_{anis}$ ) CoPt-like nanowire, are compared to those obtained for wires in which the value of  $K_{anis}$  varies randomly. To get a somehow complete overview, several distributions of the anisotropy value have been considered. In the next step different kinds of pinning sites are introduced in the ideal

systems, in order to examine the depinning process. The issue of the influence of the  $\beta$  parameter in the depinning of the wall was also raised with this occasion. Results for both geometrical constrictions and anisotropy defects are shown.

### *III.3.3.1. Effect of anisotropy distribution*

In Permalloy nanowires it was shown that the surface roughness prevented the formation of antivortices. This resulted in a faster motion of the walls than in ideal wires. However, these “geometrical” defects might be only one possibility of generating pinning potentials. Besides surface roughness, the spatial variation of the material parameters must be also considered when talking about pinning. Even if the DW does not remain trapped due to this kind of defects, it can be heavily deformed, its motion taking place in a less “smooth” manner than for perfect wires. It is therefore interesting, and also necessary, to study DW motion occurring in systems in which such defects are present.

In out-of-plane magnetized systems, such an arrangement of the magnetization might appear due to two causes: either very small magnetization or strong perpendicular magnetocrystalline anisotropy. Here we consider the latter case. Comparing the in-plane and out-of-plane magnetized systems, it is clear that the former ones are affected by much weaker pinning fields. Bearing in mind the presence of a strong anisotropy, whereas in materials with in-plane magnetization the  $K_{anis}$  material parameter is very small or zero, the spatial variations of this material characteristic could be the explanation of the strength of the pinning potentials in out-of-plane systems.

Following this idea, in this first study, we carried out simulations to see the effect of an anisotropy distribution on the DW motion. The direction of the anisotropy field was kept constant but the value of the magnetocrystalline anisotropy constant  $K_{anis}$  was varied in each mesh cell. As experimentally the grain size in polycrystalline films was measured and it is known to be between 5-10 nm [Rodmacq 2006], taking anisotropy “cells” equal to the discretization cells seems to be an appropriate choice. Small values of the anisotropy will attract the wall, keeping it fix, whereas the regions with important anisotropy will be avoided by it.



To create a disorder in the system, random values of the anisotropy constant were generated, varying between  $[0.5, 1] \cdot K_{anis}$  - distribution D1- and  $[0.5, 1.5] \cdot K_{anis}$  - called D2, and then distributed in the mesh cells.  $K_{anis}$  is the value in the ideal wire. A distribution corresponding to the first category is shown in Figure III.23:

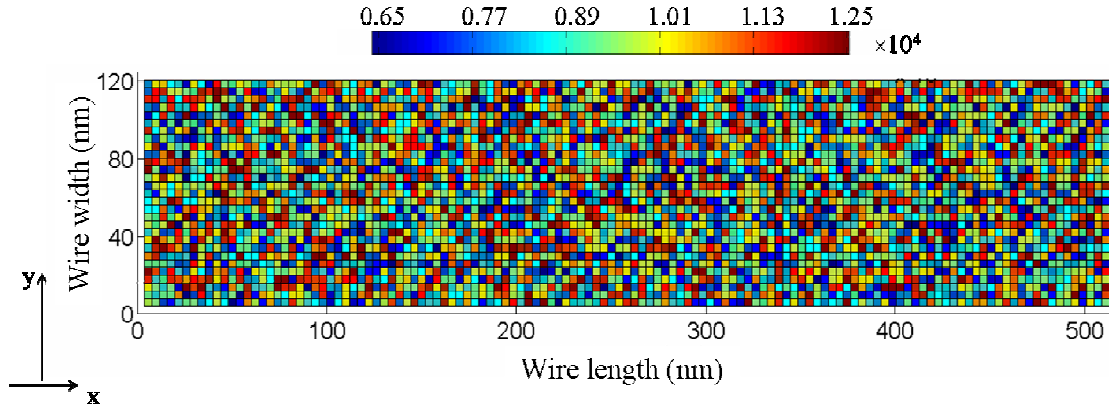


Figure III.23: Random anisotropy distribution of type D1.

Once these distributions generated, they are used as input of the WALL\_ST simulation tool. Three current densities have been considered:  $5 \cdot 10^{10}$ ,  $20 \cdot 10^{10}$  and  $50 \cdot 10^{10} \text{ A/m}^2$ . All these current values are above the current density corresponding to the Walker breakdown.

During displacement, the wall is translated whenever it approaches to closely the lateral surfaces of the computation region. Every time when such a translation occurs, the anisotropy distribution is regenerated, making sure that it is kept the same in the neighborhood of the wall. This way, the motion of the wall is happening in a wire with a truly random distribution of anisotropy values.

The wall is left to evolve during several tens of nanoseconds. The magnetization components and the wall position are all monitored throughout the motion duration. The curves obtained for the systems where disorder was introduced (traced in colored lines) are compared to the evolution obtained in the ideal wire, plotted in black. In Figure III.24 the results for  $J_{app} = 5 \cdot 10^{10} \text{ A/m}^2$  (on the left side) and  $J_{app} = 50 \cdot 10^{10} \text{ A/m}^2$  (on the right side) are shown.

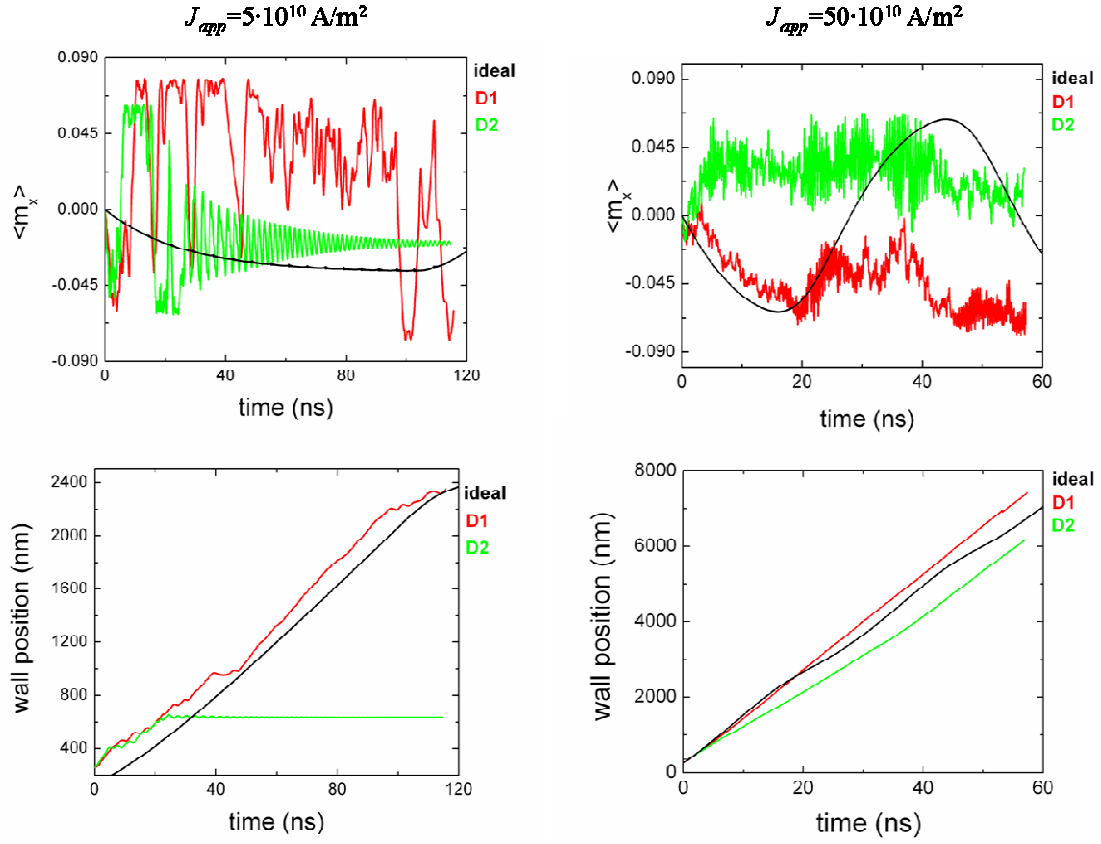


Figure III.24: The  $\langle m_x \rangle$  magnetization component and the wall position versus time for a current density of  $5 \cdot 10^{10} \text{ A/m}^2$  and  $50 \cdot 10^{10} \text{ A/m}^2$ .

The in-plane magnetization components give the Bloch or Néel character of the wall. As both current values are above the critical Walker breakdown current, the Bloch and Néel structures should be equally observed. Unfortunately, the presence of the random anisotropy distribution prevented the periodic appearance of Bloch/Néel configurations. Even more, for the smallest value of the current density, two kinds of behaviors were observed for the wall position. The wall can either move, more or less steadily (the red curve for  $J_{app} = 5 \cdot 10^{10} \text{ A/m}^2$ ), or it can reach a plateau, meaning that the wall remains trapped on some local pinning site. For the highest current density, however, the DW displacement seems to be less disturbed by the anisotropy distribution. For the intermediate current density of  $20 \cdot 10^{10} \text{ A/m}^2$  the behavior is similar with the one seen for  $50 \cdot 10^{10} \text{ A/m}^2$ .

Configurations taken at consecutive time steps (Figure III.25) reveal the cause of the oscillations in the in-plane magnetization components.

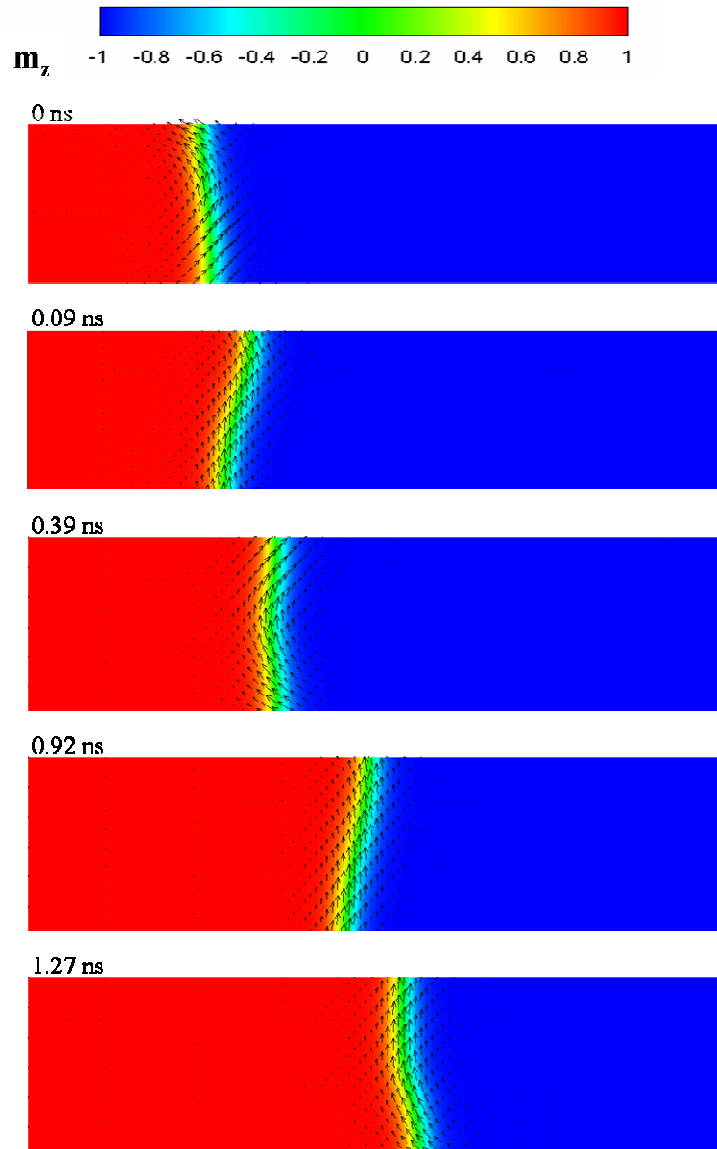


Figure III.25: Magnetization configuration taken at several time steps showing the deformations occurring as the wall moves through the wire with a random anisotropy distribution of type D1. The current density is of  $50 \cdot 10^{10} \text{ A/m}^2$  and  $\beta=0.02$ .

These images show that, at some moments the magnetization along the wire width is nearly aligned, like in the second and fourth configuration. Nevertheless, the wall is not straight but a little bit deformed. At other moments, (see configurations 1, 3 and 5) the orientation of the magnetization in the wall varies greatly between the edges and the central part. All these features explain the disorder observed in the evolution of  $\langle m_x \rangle$ .

Concerning the wall velocity, for the smallest current density, when the wall remains pinned, its final velocity tends towards 0. For the two other current densities the wall velocity varies as shown in Figure III.26:

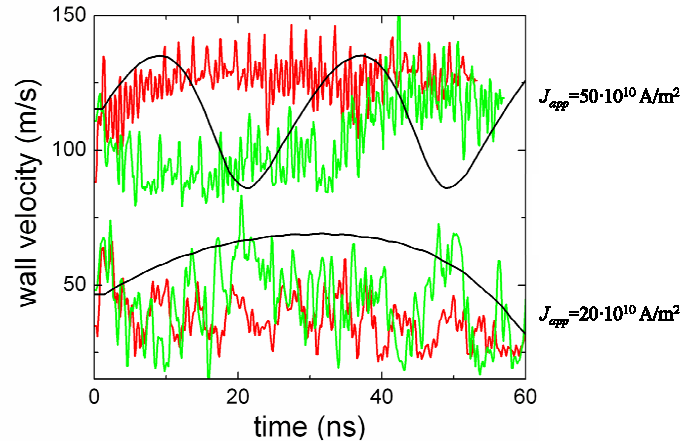


Figure III.26: The variation of the wall velocity versus time. Comparison between the evolution in an ideal wire (the black curve) and the wire in which disorder is introduced (red curve corresponds to a distribution of type D1, the green curve - to D2).

As foreseeable from the behavior of the  $\langle m_x \rangle$  magnetization component, the oscillatory behavior of the wall velocity observed in the ideal wire cannot be reproduced if an anisotropy distribution is considered. The average velocities in the wire with anisotropy distribution were also calculated and compared to the value obtained in the ideal wire. These values seem to be less affected by the disorder. For example, if  $J_{app} = 50 \cdot 10^{10} \text{ A/m}^2$ , the velocity in the ideal wire is 113 m/s, whereas using D1 or D2 a value of 126 m/s, respectively 103 m/s is obtained. The same is true for the smaller current of  $J_{app} = 20 \cdot 10^{10} \text{ A/m}^2$ , where the values are: for the ideal wire 51 m/s, with D1 37 m/s and with D2 45 m/s.

The results presented above demonstrate the important role that anisotropy defects can play in the displacement of a Bloch wall. As the wall propagates through the wire it meets several pinning sites. Depending on the current value, the wall can either be trapped, or continue its motion, the effect of the pinning sites being to distort the DW or locally perturb the magnetization orientation to a certain extent. On one hand, for small currents, it seems that the pinning force and the force from the current are comparable, as the probability of the DW being trapped can be quite important. The task of determining on what exactly the DW remains pinned is difficult. It is not clear whether the wall is strongly

attracted by clusters with reduced anisotropy, or strongly repulsed by those where the anisotropy is higher than the average. On the other hand, the current densities, which belong to the interval where precessional motion is expected, appear to be strong enough to move the wall with velocities close the ones measured in ideal wires. At this point it is worth noting that recent experimental results [Burrowes 2008], exploring field-induced depinning suggest the same kind of stochastic behavior for small values of the field.

### III.3.4. *Depinning from geometrical or anisotropy defects*

In DW-motion-based devices the walls are usually moved between two stable positions. To find the better manner in which the wall can be positioned in a specific location, several scenarios are foreseeable. We treat here only two possibilities: geometrical constrictions and pinning due to anisotropy defects - regions where the anisotropy is reduced with a certain ratio.

#### III.3.4.1. *Geometrical constrictions*

Four types of geometrical constrictions were tested, shown in Figure III.27:

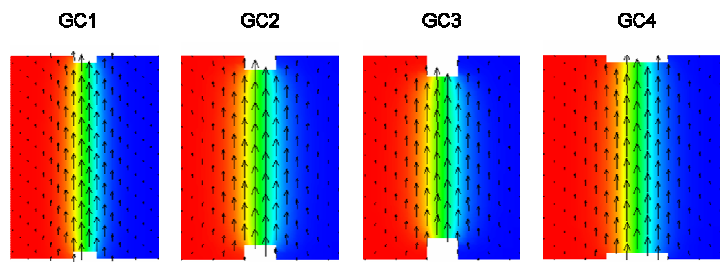


Figure III.27: The four types of geometrical constrictions.

The size of the constrictions is given in Table III.4:

Table III.4: Size of the geometrical constrictions

Name	Width (nm)	Depth (nm)	Thickness (nm)
GC1	8	4	11
GC2	8	8	11
GC3	8	12	11
GC4	20	4	11

In the beginning of the simulation, the wall was placed exactly in the centre of the constricted region. The aim of these simulations was to identify the current density required to expel the wall from the constriction.

Four values of the non-adiabatic spin transfer parameter were tested:  $\beta=0$ ,  $\beta=0.01=\alpha$ ,  $\beta=0.02$ , and finally a quite exotic value of  $\beta=1$ , chosen based on recent experimental results that demonstrate that such significant values of this parameter can be observed in special materials [Miron 2008]. The results obtained when the first constriction is used are presented in Figure III.28:

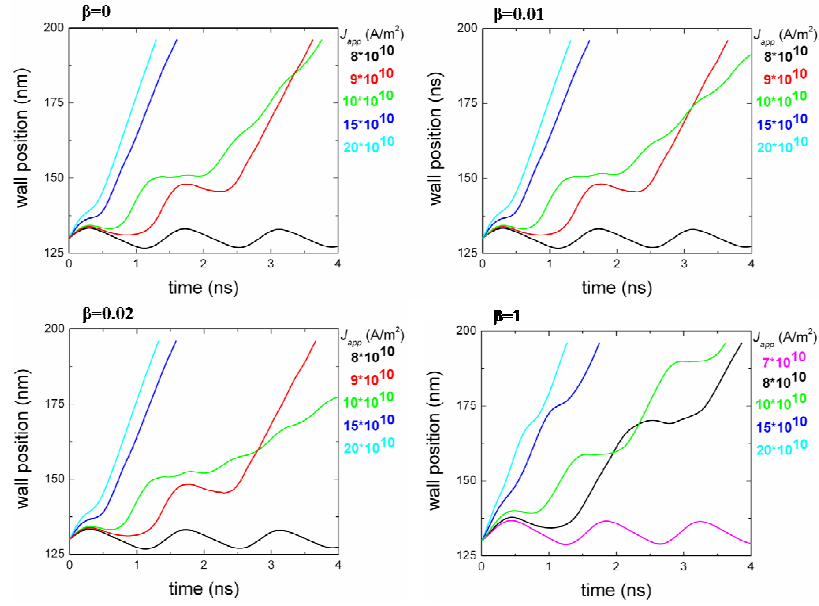


Figure III.28: The wall position versus current density, as a function of the value of  $\beta$ . For the first three values the behavior is almost identical. For  $\beta=1$  the depinning current decreases from  $9 \cdot 10^{10} A/m^2$  to  $8 \cdot 10^{10} A/m^2$ .

As predicted already in theoretical studies, two spin torques act upon a DW. The first spin torque term is known to be responsible for the DW distortion, its effect being visible in the beginning of the motion. The non-adiabatic torque term describes the influence of the mistracked electrons on the DW motion. This term is the one responsible for displacing of the DW, giving its terminal velocity. By comparing the above showed images, one observes that, apparently, the value of the non-adiabatic spin transfer parameter  $\beta$  has limited influence on the depinning process. Bearing in mind that the evolution of the wall is followed only throughout the first 4-5 ns of the motion this conclusion turns out to be quite normal, as we must be situated, most likely, in the interval in which the adiabatic term plays the dominant role, the non-adiabatic torque having a negligible influence.

A detailed analysis of the curves in Figure III.28 reveals that for the smallest values of  $\beta$  (0, 0.01 and 0.02), there is nearly no difference between the velocity versus-current-curves, the depinning current being around  $9 \cdot 10^{10} \text{ A/m}^2$ . If  $\beta=1$  the depinning occurs at a slightly smaller current value:  $8 \cdot 10^{10} \text{ A/m}^2$ . This decrease of around 10% shows that if the value of the  $\beta$  parameter approaches unity, the two torques have roles of equal importance in the depinning process.

For the other constrictions the behavior is similar, as shown in Figure III.29.

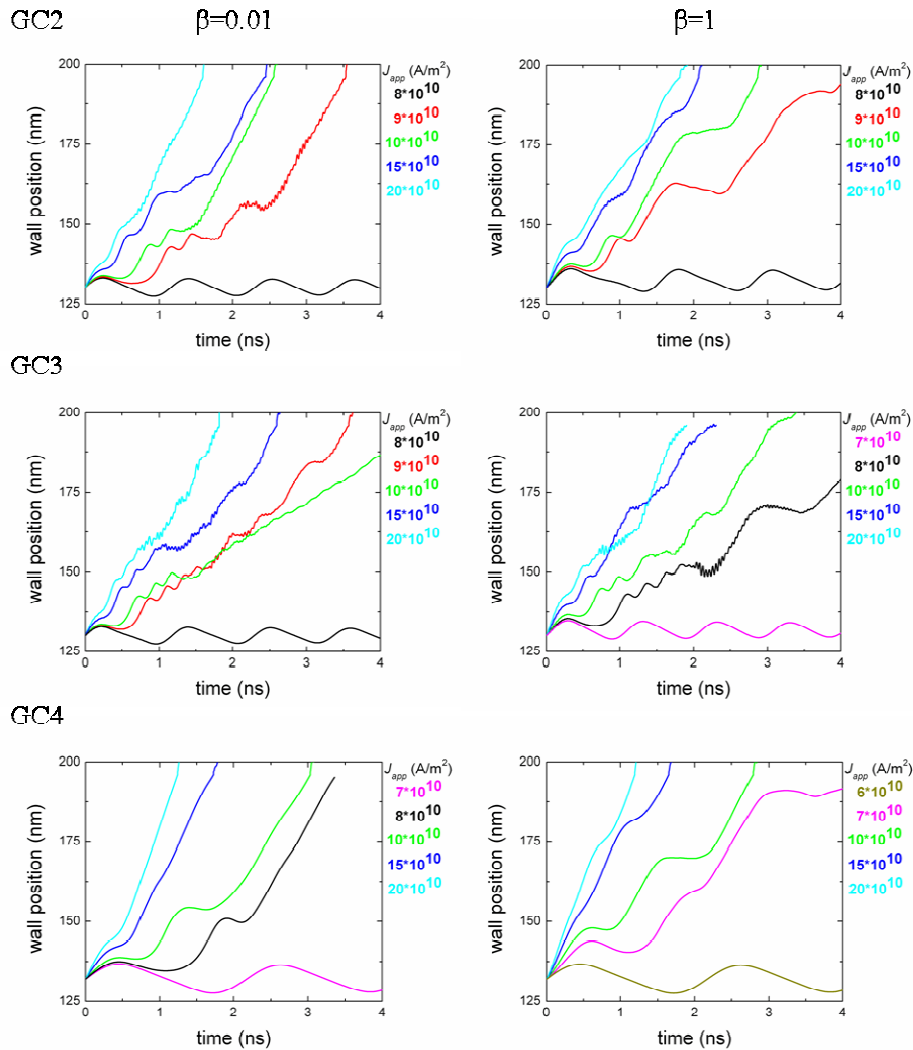


Figure III.29: the wall position versus time for the geometrical constrictions GC2, GC3 and GC4. The figures on the left side were obtained setting  $\beta=0.02$ , while on the right side the evolutions for  $\beta=1$  are shown.



Here only the  $\beta=0.02$  and the  $\beta=1$  curves are shown, the ones obtained for  $\beta=0$  and  $\beta=0.01$  being identical with the first one. Although the GC2 and GC3 constrictions are deeper than GC1, while the GC4 is wider having the same depth as GC1, the depinning current is not very affected by the variation of the constriction's size. For CG2, the depinning current is  $9 \cdot 10^{10} \text{ A/m}^2$  for all the  $\beta$  values. For the third case, GC3, the depinning current density varies between  $8 \cdot 10^{10} \text{ A/m}^2$  obtained if  $\beta=1$  and  $9 \cdot 10^{10} \text{ A/m}^2$  for the other  $\beta$  values. For the last constriction, as this is wide but not very deep, the depinning current goes down to  $6 \cdot 10^{10} \text{ A/m}^2$  for  $\beta=1$  and remains  $8 \cdot 10^{10} \text{ A/m}^2$  for small values of the non-adiabatic spin transfer parameter.

### *The depinning process*

Both Figure III.28 and Figure III.29 reveal that a certain threshold current is required to expel the Bloch wall from the constricted region. For currents smaller than this value, the wall remains in the constricted region and oscillates in this “stable” position, as shown in Figure III.30. The oscillation amplitude decreases in time, because of the damping. Overall, it takes 35-40 ns for the wall to completely stop moving.

The magnetization distributions shown in Figure III.30 were obtained for a current density of  $8 \cdot 10^{10} \text{ A/m}^2$  using the GC2 configuration, and they represent the two stable positions between which the wall oscillates. The second configuration is characterized by the tilt angle  $\psi$  that increases as the current becomes higher.

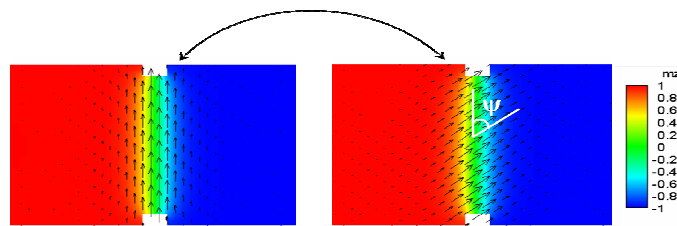


*Figure III.30: Configurations obtained using the second type of geometrical constriction. A current density of was used  $8 \cdot 10^{10} \text{ A/m}^2$  and  $\beta=0.02$ .*

Increasing the current density, the force from the current manages to tip the magnetization in the wall to  $90^\circ$  and depinning occurs. In the first time the wall bends and then one of the ends slowly detaches itself from the constricted region, pulling the rest out after itself. An example is given in Figure III.31.

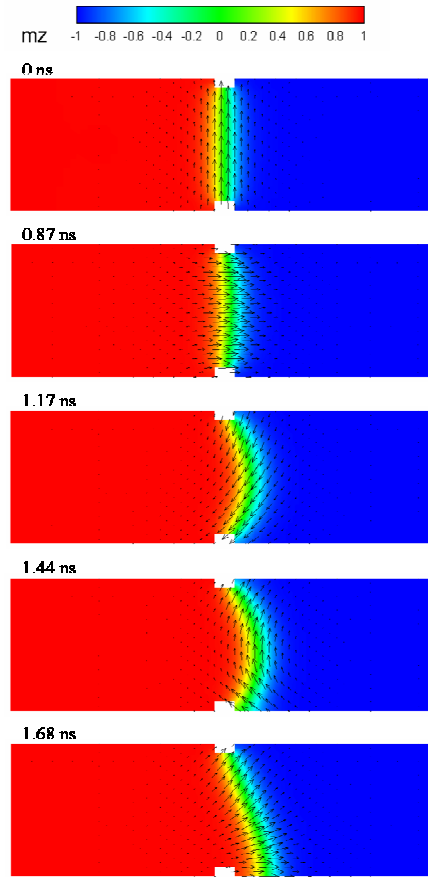


Figure III.31: The depinning process from a constriction of type GC2.

For the depinning current and current densities immediately above this value, the presence of the constriction is still visible during the motion period. In Figure III.28 for example, the curves with  $J_{\text{app}}=9 \cdot 10^{10} \text{ A/m}^2$  and  $J_{\text{app}}=10 \cdot 10^{10} \text{ A/m}^2$  (for  $\beta=0$ ,  $\beta=0.01$  and  $\beta=0.02$ ) and  $J_{\text{app}}=8 \cdot 10^{10} \text{ A/m}^2$  and  $J_{\text{app}}=9 \cdot 10^{10} \text{ A/m}^2$  (for  $\beta=1$ ) present important oscillations. At higher current densities, the evolution of the wall position takes up a smoother form, varying almost linearly in time. To explain this, one must take into account that, after leaving the constricted region, the wall is split up in three parts: the upper and lower ends and its center. The two ends move in a somehow decoupled manner, as there are moments when the upper end is ahead, and other times when the lower is the leading one, pulling after itself the rest of the wall. When the wall is the most distorted, the extremes of its two ends can be separated by a distance of around 30 nm. For higher current values however after leaving the constriction the wall moves less deformed, less disturbed by the constriction, the wall position varying almost linearly in time.

When working with geometrical constrictions, the current density is not uniform in the entire wire, namely in the constricted region - a proportional increase of the current is expected and taken into account in the simulations. This is why, a small sensitivity of the depinning current with respect to the size of the constriction was observed. It is also important to note that, such reduced-width regions represent “hot spots”, and the influence of a non-uniform temperature distribution is required to complete this study.

The above presented results show that it is possible to depin a Bloch wall with relatively small current densities. A decrease (of  $<10\%$ ) of the depinning current is obtained if  $\beta$  approaches unity. This decrease of the depinning current can be interpreted as: while for small values - it is the adiabatic torque only that frees the wall, for high values of  $\beta$  - it is both the spin torques that act on depinning the wall. A similar conclusion was drawn by He et al. [He 2005] after carrying out simulations for a nanowire with in-plane magnetization. They introduced a trapezoidal constriction and looked to the depinning of transverse DW.

#### *III.3.4.2. Crystalline defects*

Similarly with the four types of pinning sites generated by geometrical constrictions, four types of anisotropy defects (noted AD) were introduced in the nanowire and their effect is investigated in the following paragraph. The value of the magnetocrystalline anisotropy constant was reduced in a strip extending over the whole wire width. The characteristics of the four anisotropy defects are given in Table III.5:

*Table III.5: Value of the anisotropy constant  $K_{anis}$  and the size of the strip*

Defect	$K_{anis}$ value	Width (nm)
AD1	$K_{anis}/4$	8
AD2	$K_{anis}/2$	8
AD3	$3 \cdot K_{anis}/4$	8
AD4	$3 \cdot K_{anis}/4$ and $K_{anis}/2$	16

The anisotropy profiles corresponding to each type of crystalline constriction is given in Figure III.32:

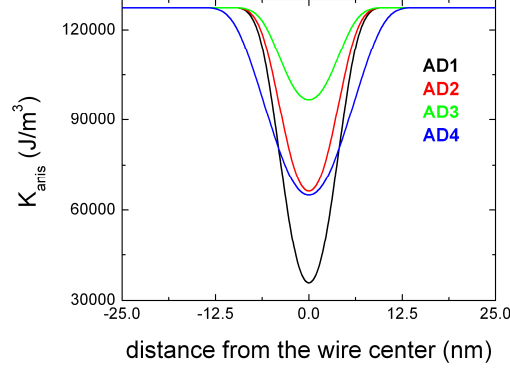


Figure III.32: Anisotropy defects introduced in the perfect wire. AD1, AD2 and AD3 have the same width, whereas AD4 is two times larger.

The purpose of this study was again to determine the current required to move the Bloch wall away from the low-anisotropy region. Simulations were carried out for three values of the non-adiabatic spin transfer parameter: 0, 0.01 and 1. The results obtained for the first anisotropy defect are shown in Figure III.33.

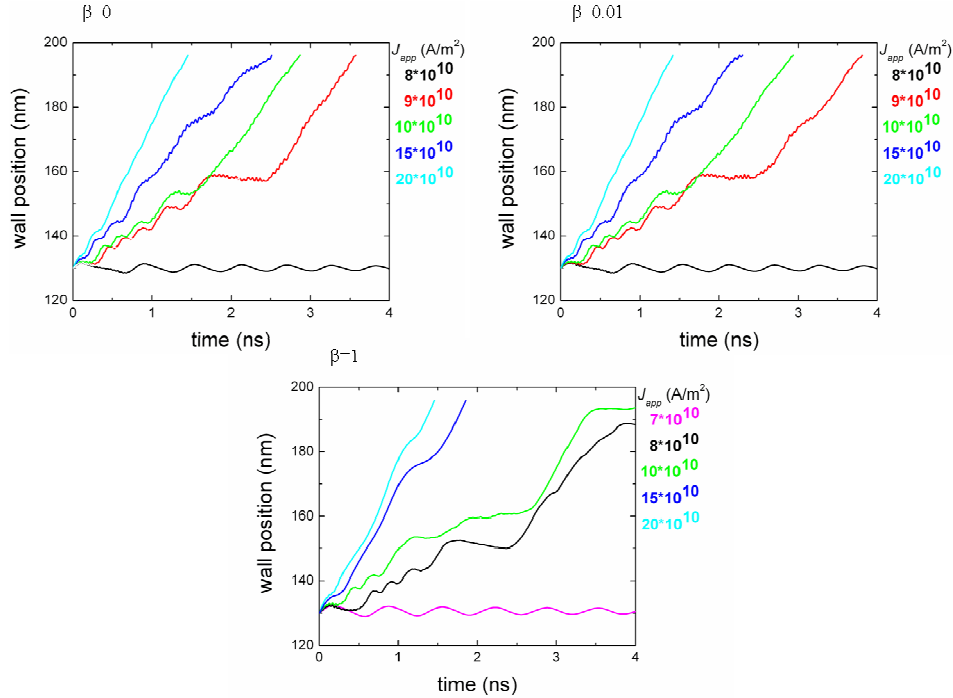


Figure III.33: The wall position versus current density, as a function of the value of  $\beta$ .

The curves are somehow similar to those seen when geometrical constrictions were used. The  $\beta=0$  and  $\beta=0.01$  are again for the most part equivalent, the depinning current being around  $9 \cdot 10^{10} \text{ A/m}^2$ . Using 1 for  $\beta$ , changes the behavior of the wall, the depinning current decreasing to  $8 \cdot 10^{10} \text{ A/m}^2$ . The data obtained for these scenarios are plotted in Figure III.34. Because of the equivalence of the  $\beta=0$  and  $\beta=0.01$  cases, only the results with  $\beta=0$  and  $\beta=1$  are given.

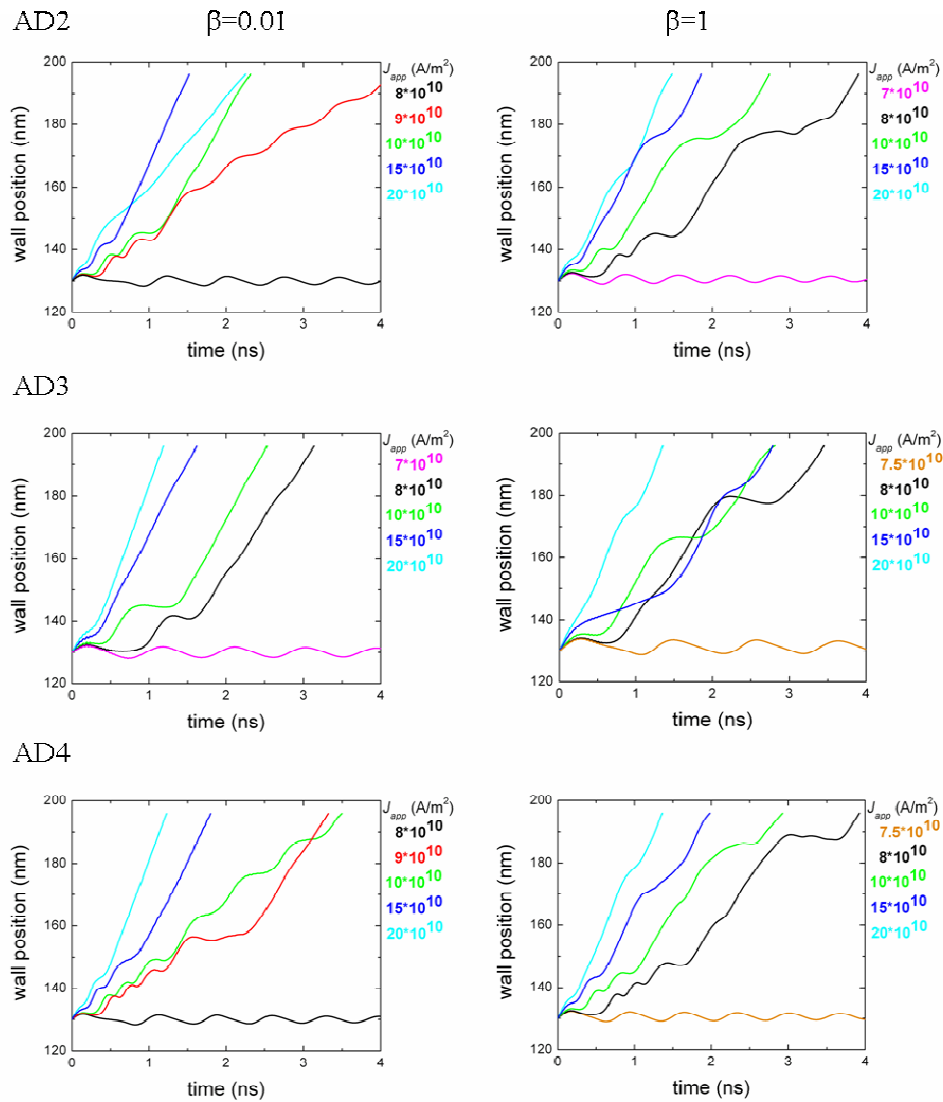


Figure III.34: The wall position versus time curves for the crystalline constrictions of type AD2, AD3 and AD4.

The value depinning current necessary for detaching the Bloch wall from the geometrical constrictions varied in the same range. Apparently, although by nature

completely different, the reaction of the wall to these two types of pinning sites is quite comparable. If pinned, the wall position describes periodic oscillations, with decreasing amplitude. At high current values, the wall is sensible to the presence of the low anisotropy region only until complete depinning occurs. Small distortions of the wall are observable, but as the current increases the wall starts to propagate more and more smoothly.

### *The depinning process*

Independently on the anisotropy defect used, for smaller current densities than the threshold depinning value, the DW oscillates between a pure and a tilted Bloch configuration. If the wall is pinned, everything happens exactly like with the geometrical constrictions (see Figure III.30). On the other hand, the depinning process takes a slightly different course than what was seen for the precedent case, as shown in Figure III.35:

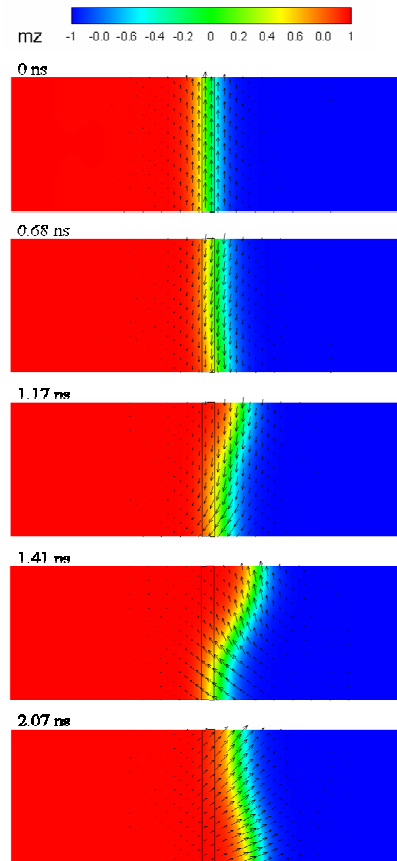


*Figure III.35: The depinning process from a constriction of type AD1. The black rectangle corresponds to the region where the value of  $K_{anis}$  is reduced.*

In geometrically pinned scenario, because of the two constrictions, the ends of the wall were somehow trapped in this region. Therefore, the current acted firstly on the free part of the DW - its center. The wall bend, taking up a semi-circular shape. The presence of a reduced-anisotropy region does not induce such a significant deformation of the wall. In fact, in the first part of the motion, when the wall, or a part of it, is still in the vicinity of the anisotropy defect, the magnetic moments in the wall move relatively coherently. As the magnetization in the wall makes a complete  $360^\circ$  turn, the force from the current succeeds in pushing a part of the wall out of the pinning site. Then one of the ends frees itself completely. After this partial freeing, the propagation of the wall is similar with the one seen in the presence of geometrical constrictions. In the next step, the remaining part of the wall is extracted from this region by the already liberated part. Once the wall is completely free, the ends alternatively take the leading role, pulling the rest of the wall after them.

It is worth noting that, in addition to examining the depinning process, the magnetostatic field acting on the wall was analyzed. Obviously, the inclusion of an anisotropy defect in the nanowire does not change the demagnetizing field distribution, as the geometry is the same as for the ideal wire. On the contrary, the geometrical constrictions modify the local value of the demagnetizing field. Depending on the constriction size,  $\mathbf{H}_{\text{dem}}$  on the surfaces is modified by 5% (for GC4) and up to 50% (GC3).

Before concluding this part, a remark concerning the values of  $\beta$  parameter, has to be made. It is known that if  $\beta$  is 0, motion occurs only above a certain critical current, even for perfect wires. The current densities used here are all above this critical value, that was determined to be smaller than  $7 \cdot 10^{10} \text{ A/m}^2$ . Therefore the use of  $\beta=0$  is justified.

The above presented results permit to draw several conclusions. First of all, assuming that  $\beta$  is around  $10^{-2}$ , using only current to depin and propagate the DW, the adiabatic torque plays the leading role in the depinning process. Testing the case when  $\beta=1$  showed that, now the spin torque terms work together to free the DW. Second of all, it seems from the data examined above, that small geometric constrictions or localized anisotropy defects can both act as pinning sites. The freeing of the wall from these locations happens in similar manners and also the current densities are contained in the same interval.

### III.3.5. Current pulses and Bloch wall displacement

In applications, continuous currents are rarely used for DW propagation, as these would heat and eventually, destroy the sample. The injection of current pulses of different shapes and amplitudes is more adapted for such purposes. Current pulses offer also a solution for the “hot spots” created by geometrical constrictions. Because of the variation of the sample size, the local current density in such regions can be much increased, leading to more important temperature effects. Trying to explore a little bit the possibilities, a study of the Bloch wall displacement under the effect of short (nanosecond and sub-nanosecond) pulses was carried out. The results are presented in the following.

First, the case of an ideal wire is considered. Figure III.36 shows the evolution of the wall position in time as a function of the pulse length, when  $J_{app}=10 \cdot 10^{10} \text{ A/m}^2$  and  $J_{app}=50 \cdot 10^{10} \text{ A/m}^2$ , with the pulse length varied from 0.5 ns to 1.2 ns:

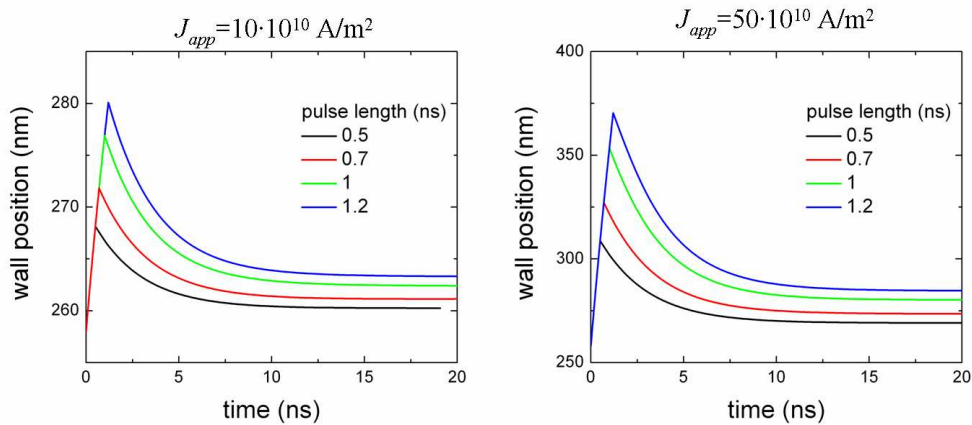


Figure III.36: The wall position versus time for two current values and several pulse lengths.

For both current values, the wall is displaced over a certain distance, distance that increases with the pulse length. The wall propagates in the direction of the electron flow as long as the current is present. When the external excitation is removed, the wall still continues to move, but in opposite direction, returning towards its original position. After the excitation energy is dissipated, the overall displacement of the wall is quite small, for the longest



pulse (1.2 ns) of  $10 \cdot 10^{10} \text{ A/m}^2$  the wall stops at a distance of 5 nm from its original position and, respectively 27 nm for a current of  $50 \cdot 10^{10} \text{ A/m}^2$ .

Taking a much larger current,  $J_{\text{app}} = 100 \cdot 10^{10} \text{ A/m}^2$ , one would expect a likewise behavior. As shown in Figure III.37, in this case depending on the pulse length the wall either returns or continues the initial motion. The propagation continues until damping halts the motion:

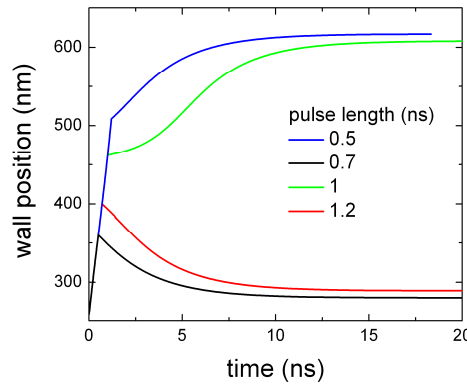


Figure III.37: The variation of the wall position for a current pulse of  $100 \cdot 10^{10} \text{ A/m}^2$  and several pulse lengths.

To understand this strange aspect, the spin torque terms must be revisited. The adiabatic torque has the role of tilting the magnetization in the DW. For the same current density, longer current pulses tilt the magnetization more. The tilt angle can be followed by monitoring the in-plane magnetization components. For example, the variation of the  $\langle m_x \rangle$  for  $J_{\text{app}} = 50 \cdot 10^{10} \text{ A/m}^2$  and  $J_{\text{app}} = 100 \cdot 10^{10} \text{ A/m}^2$ , for the pulse length set to 0.7 or 1.2 ns is shown in Figure III.38:

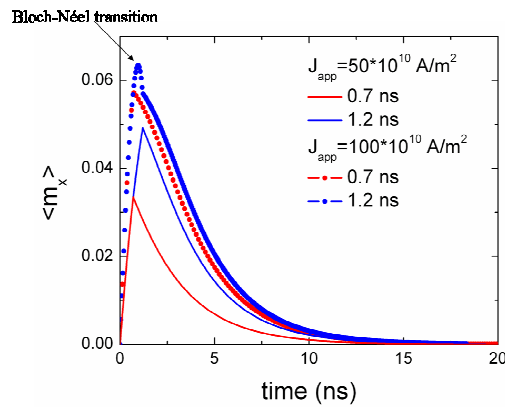


Figure III.38: The evolution of the  $\langle m_x \rangle$  magnetization component.

For two different current densities, if the pulse length is the same, the value of  $\langle m_x \rangle$  just before the current stops is different. In Figure III.38, for the smaller current, considering the cycle of Bloch-Néel transitions, the wall is still intermediate Bloch, with the initial chirality. For the current density of  $100 \cdot 10^{10} \text{ A/m}^2$ , the pulse of 1.2 ns (the same is true for a pulse length of 1 ns) tilts the magnetization so much, that the wall structure became Néel. Nevertheless, these observations still do not explain the forth or retrograde wall motion. Going further in the analysis of the wall propagation process, after the current is stopped, the only force acting upon the wall comes from its local demagnetizing field, arising due to the alteration of the pure (magnetic-charge-free) Bloch structure. Whereas the orientation of the demagnetizing field is imposed by the magnetization, the direction in which the wall will be displaced, after the current is eliminated, is given by both the orientation of  $\mathbf{H}_{\text{dem}}$  and the chirality of the wall. If the wall structure did not undergo a Bloch-Néel transition, both the chirality and the orientation of  $\mathbf{H}_{\text{dem}}$  remain constant, the wall being pushed by this force towards its initial position. If the pulse is longer, the tilt angle of the wall attains values beyond  $90^\circ$ , the chirality is therefore changed and so is the effect of the couple  $\mathbf{H}_{\text{dem}}$ -wall chirality. Consequently, the wall continues its forward motion, the magnetization turning until a Bloch structure is attained. At this moment as the torque on the wall is nil, the motion stops.

These preliminary results indicate that in order to have control over a Bloch wall using a current pulse, for the case of an ideal nanowire, two quantities have to be known. The first is the critical current for Walker breakdown. It is clear that for values lower than this critical current the wall returns towards its initial position, as the wall remains quasi-Bloch for such currents. For  $J_{\text{app}} > J_c$ , like the values given above, Bloch-Néel transitions are expected. To be able to precisely manipulate the DW it is necessary to know at which times do the Bloch-Néel transitions occur. In other words the oscillation frequency of the magnetization should be determined. Depending on the relative positioning of the pulse length with respect to this Bloch-Néel structure diagram, one would be able to tell in what direction is the wall moving after the current is stopped.

In the applications based on DW propagation, the purpose is to be able to move the wall between two stable positions. To obtain such sites, geometrical constrictions can be

created, with a certain periodicity. In the following, some results concerning DW propagation between two such constrictions, by means of current pulses, are given.

Earlier in this chapter, the depinning current required to expel the DW from geometrical constrictions with different sizes was determined. Based on this study, two constrictions of type GC1 (Table III.4) situated at a distance of 40nm, and respectively 80 nm, are introduced in the perfect wire. The wall position versus time is presented in Figure III.39 for these two scenarios.

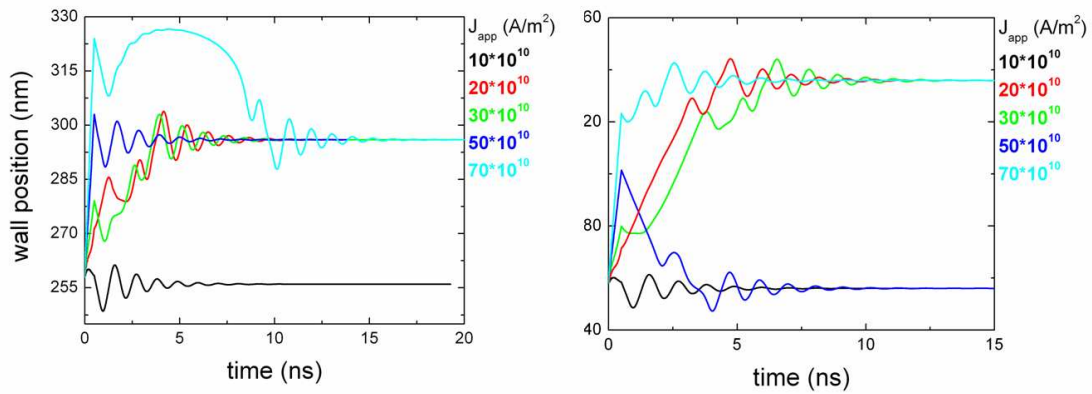


Figure III.39: The evolution of the wall position for two constrictions of type GC1 situated at a distance of 40nm (left) and 80 nm respectively (right).

For the first case the situation is simple. Apparently, a perfect combination of pulse length and distance between the constrictions was found, as after the wall is depinned, the DW remains stuck on the second constriction. On the other hand, for the second scenario, the DW can propagate and stay on the second constriction or return to its original position. While the current is present, somehow disregarding the presence of the constrictions the orientation of the magnetization remains relatively uniform. Therefore the explanation for forth or backward wall motion in the ideal wire, can be used also for this scenario.

The above described results show how important it is to know what basic physical phenomena stand behind current-induced displacement. The details of wall displacement, like the behavior in the linear velocity regimes or the oscillation period in the precessional motion, might seem trivial. Nevertheless, when current pulses are injected, they turned out to be very important factors.

Although this is not a complete study, and quantitative conclusions cannot be drawn from the data presented above, it has been demonstrated that is possible to displace a Bloch wall between two small geometrical constrictions by means of short current pulses.

## References

- [**Aharoni 1998**] A. Aharoni, “Demagnetizing factors for rectangular ferromagnetic prisms”, *J. Appl. Phys.* 83, 3432 (1998).
- [**Allwood 2002**] D. A. Allwood, G. Xiong, M. D. Cooke, C. C. Faulkner, D. Atkinson, N. Vernier, R. P. Cowburn, “Submicrometer ferromagnetic NOT gate and shift register”, *Science* 296, 2003 (2002).
- [**Atkinson 2003**] D. Atkinson, D. A. Allwood, G. Xiong, M. D. Cooke, C. C. Faulkner, R. P. Cowburn, “Magnetic domain-wall dynamics in a submicrometre ferromagnetic structure”, *Nat. Mater.* 2, 85 (2003).
- [**Bazalyi 1998**] Ya. B. Bazalyi, B. A. Jones, S. Zhang, “Modification of the Landau-Lifshitz equation in the presence of a spin-polarized current in colossal- and giant-magnetoresistive materials”, *Phys. Rev. B* 57, R3213 (1998).
- [**Beach 2005**] G. S. D. Beach, C. Nistor, C. Knutson, M. Tsoi, J. L. Erskine, “Dynamics of field-driven domain-wall propagation in ferromagnetic nanowires”, *Nat. Mater.* 4, 741 (2005).
- [**Beach 2006**] G. S. D. Beach, C. Knutson, C. Nistor, M. Tsoi, J. L. Erskine, “Nonlinear domain-wall velocity enhancement by spin-polarized electric current”, *Phys. Rev. Lett.* 97, 057203 (2006).
- [**Berger 1973**] L. Berger, “Dragging of domains by an electric-current in very pure, non-compensated, ferromagnetic metals”, *Phys. Lett. A* 46, 3 (1973).
- [**Berger 1974**] L. Berger, “Prediction of a domain-drag effect in uniaxial, noncompensated, ferromagnetic metals”, *J. Phys. Chem. Sol.* 35, 947 (1974).
- [**Berger 1978**] L. Berger, “Low-field magnetoresistance and domain wall drag in ferromagnets”, *J. Appl. Phys* 49, 2156 (1978).
- [**Berger 1984**] L. Berger, “Exchange interaction between ferromagnetic domain walls and electric current in very thin metallic films”, *J. Appl. Phys.* 55, 1954 (1984).
- [**Berger 1992**] L. Berger, “Motion of a magnetic domain wall traversed by fast-rising current pulses”, *J. Appl. Phys.* 71, 2721 (1992).

- [**Burrowes 2008**] Burrowes et al., to appear in Appl. Phys. Lett. (2008).
- [**Chappert 2007**] C. Chappert, A. Fert, F. Nguyen Van Dau, “The emergence of spin electronics in data storage”, Nat. Mat.6, 813 (2007).
- [**Döring 1948**] W. Döring, “Über die Trägheit der Wände zwischen Weisschen Bezirken”, Z. Naturforsch. 3a, 373 (1948).
- [**Dourlat 2008**] A. Dourlat, V. Jeudy, A. Lemaître, C. Gourdon, “Field-driven domain-wall dynamics in GaMnAs films with perpendicular anisotropy”, arXiv:0808.0119v1 (2008).
- [**Freitas 1985**] P. P. Freitas, L. Berger, “Observation of s–d exchange force between domain walls and electric current in very thin Permalloy films”, J. Appl. Phys. 57, 1266 (1985).
- [**Fukami 2008**] S. Fukami, T. Suzuki, N. Ohshima, K. Nagahara, N. Ishiwata, “Micromagnetic analysis of current driven domain wall motion in nanostrips with perpendicular magnetic anisotropy”, J. Appl. Phys. 103, 07E718 (2008).
- [**Gan 2000**] L. Gan, S. H. Chung, K. H. Aschenbach, M. Dreyer, R. D. Gomez, “Pulsed current-induced domain wall propagation in Permalloy patterns observed using magnetic force microscope”, IEEE Trans. Magn. 36, 3047 (2000).
- [**Grollier 2001**] J. Grollier, V. Cros, A. Hamzić, J. M. George, H Jaffrès, A. Fert, G. Faini, J. Ben Youssef, H. Legall, “Spin-polarized current-induced switching in Co/Cu/Co pillars”, Appl. Phys. Lett. 78, 3663 (2001).
- [**Hayashi 2007**] M. Hayashi, L. Thomas, C. Rettner, R. Moriya, S. S. P. Parkin, “Direct observation of the coherent precession of magnetic domain walls propagating along Permalloy nanowires”, Nat. Phys. 3, 21 (2007) .
- [**Heyne 2008**] L. Heyne, M. Kläui, D. Backes, T. A. Moore, S. Krzyk, U. Rüdiger, L. J. Heyderman, A. Fraile Rodríguez, F. Nolting, T. O. Montes, M. A. Niño, A. Locatelli, K. Kirsch, R. Mattheis, “Relationship between nonadiabacity and damping in Permalloy studied by current-induced spin structure transformations”, Phys. Rev. Lett. 100, 066603 (2008).
- [**Hubert 1998**] A. Hubert, R. Schafer, “Magnetic domains”, Springer, New York (1998).
- [**Hung 1988**] C. Y. Hung, L. Berger, “Exchange forces between domain wall and electric current in Permalloy films of variable thickness”, J. Appl. Phys. 63, 4276 (1988).

- [**Katine 2000**] J. A. Katine, F. J. Albert, R. A. Buhrman, E. B. Myers, D. C. Ralph, “Current-driven magnetization reversal and spin-wave excitations in Co/Cu/Co nanopillars”, *Phys. Rev. Lett.* 84, 3149 (2000).
- [**Kläui 2001**] M. Kläui, J. Rothman, L. Lopez-Diaz, C. A. F. Vaz, J. A. C. Bland, Z. Cui, “Vortex circulation control in mesoscopic ring magnets”, *Appl. Phys. Lett.* 78, 3268 (2001).
- [**Kläui 2002**] M. Kläui, C. A. F. Vaz, J. A. C. Bland, W. Wernsdorfer, G. Faini, E. Cambril, “Controlled magnetic switching in single narrow rings probed by magnetoresistance measurements”, *Appl. Phys. Lett.* 81, 108 (2002).
- [**Kläui 2005**] M. Kläui, P.-O. Jubert, R. Allenspach, A. Bischof, J. A. C. Bland, G. Faini, U. Rüdiger, C. A. F. Vaz, L. Vila, C. Vouille, “Direct observation of domain-wall configurations transformed by spin currents”, *Phys. Rev. Lett.* 95, 026601 (2005).F
- [**Li 2004**] Z. Li, S. Zhang, “Domain-wall dynamics and spin-wave excitations with spin-transfer torques”, *Phys. Rev. B* 70, 024417 (2004).
- [**Malozemoff 1979**] A. P. Malozemoff, J. C. Slonczewski, “Magnetic domain walls in bubble materials”, Academic Press, New York (1979).
- [**McMichael 1997**] R. D. McMichael, M. J. Donahue, “Head to head domain wall structures in thin magnetic strips”, *IEEE Trans. Magn.* 33, 4167 (1997).
- [**Metaxas 2007**] P. J. Metaxas, J. P. Jamet, A. Mougin, M. Cormier, J. Ferré, V. Baltz, B. Rodmacq, B. Dieny, R. L. Stamps, “Creep and flow regimes of magnetic domain-wall motion in ultrathin Pt/Co/Pt films with perpendicular anisotropy”, *Phys. Rev. Lett.* 99, 217208 (2007).
- [**Miron 2008**] I. M. Miron et al., submitted to *Phys. Rev. Lett.* (2008).
- [**Mougin 2007**] A. Mougin, M. Cormier, J. P. Adam, P. J. Metaxas, J. Ferré, “Domain wall mobility, stability and Walker breakdown in magnetic nanowires”, *Europhys. Lett.* 78, 57007 (2007).
- [**MRAM site**] <http://www.mram-info.com/>.
- [**Myers 1999**] E. B. Myers, D. C. Ralph, J. A. Katine, R. N. Louie, R. A. Buhrman, “Current-induced switching of domains in magnetic multilayer devices”, *Science* 285, 867 (1999).

- [**Nakatani 2003**] Y. Nakatani, A. Thiaville, J. Miltat, “Faster magnetic walls in rough wires”, *Nat. Mat.* 2, 521 (2003)
- [**Nakatani 2005**] Y. Nakatani, A. Thiaville, J. Miltat, “Head-to-head domain walls in soft nano-strips: a refined phase diagram”, *J. Magn. Magn. Mat.* 290/291, 750, 2005.
- [**Ono 1999**] T. Ono, H. Miyajima, K. Shigeto, K. Mibu, N. Hosoi, T. Shinjo, “Propagation of a magnetic domain wall in a submicrometer magnetic wire”, *Science* 284, 468 (1999).
- [**Osborn 1945**] J. A. Osborn, “Demagnetizing factors of the general ellipsoid”, *Phys. Rev.* 67, 351 (1945).
- [**Parkin 2004**] S. S. P. Parkin, U.S. Patent 6,834,005 (2004).
- [**Porter 2004**] D. G. Porter, M. J. Donahue, “Velocity of transverse domain wall motion along thin, narrow strips”, *J. Appl. Phys.* 95, 6729 (2004).
- [**Prinz 1998**] G. A. Prinz, “Magnetoelectronics”, *Science* 282, 1660 (1998).
- [**Ravelosona 2005**] D. Ravelosona, D. Lacour, J. A. Katine, B. D. Terris, C. Chappert, “Nanometer scale observation of high efficiency thermally assisted current-driven domain wall depinning”, *Phys. Rev. Lett.* 95, 117203 (2005).
- [**Ravelosona 2006**] D. Ravelosona, S. Mangin, Y. Lemaho, J. A. Katine, B. D. Terris, E. E. Fullerton, “Domain wall creation in nanostructures driven by a spin-polarized current”, *Phys. Rev. Lett.* 96, 186604 (2006).
- [**Rodmacq 2006**] B. Rodmacq, V. Baltz, B. Dieny, “Macroscopic probing of domain configurations in interacting bilayers with perpendicular magnetic anisotropy”, *Phys. Rev. B* 73 (2006) 092405.
- [**Rothman 2001**] J. Rothman, M. Kläui, L. Lopez-Diaz, C. A. F. Vaz, A. Bleloch, J. A. C. Bland, Z. Cui, R. Speaks, “Observation of a bi-domain state and nucleation free switching in mesoscopic ring magnets”, *Phys. Rev. Lett.* 86, 1098 (2001).
- [**Schryer 1974**] N. L. Schryer, L. R. Walker, “The motion of  $180^\circ$  domain walls in uniform dc magnetic fields”, *J. Appl. Phys.* 45 (1974) 5406.
- [**Slonczewski 1996**] J. C. Slonczewski, “Current-driven excitation of magnetic multilayers”, *J. Magn. Magn. Mat.*, 159, L1 (1996).



- [**Tanigawa 2008**] H. Tanigawa, K. Kondou, T. Koyama, K. Nakano, S. Kasai, N. Ohshima, S. Fukami, N. Ishiwata, T. Ono, “Current-driven domain wall motion in CoCrPt wires with perpendicular magnetic anisotropy”, *Appl. Phys. Express* 1, 011301 (2008).
- [**Tatara 2004**] G. Tatara, H. Kohno, “Theory of current-driven domain wall motion: spin transfer versus momentum transfer”, *Phys. Rev. Lett.* 92, 086601 (2004).
- [**Tehrani 2003**] S. Tehrani, J. M. Slaughter, M. Deherrera, B. N. Engel, N. D. Rizzo, J. Salter, M. Durlam, R. W. Dave, J. Janesky, B. Butcher, K. Smith, G. Grynkewich, “Magnetoresistive random access memory using magnetic tunnel junctions”, *Proc. IEEE* 91, 703 (2003).
- [**Thiaville 2002**] A. Thiaville, J. M. Garcia, J. Miltat, “Domain wall dynamics in nanowires”, *J. Magn. Magn. Mat.* 242/245, 1061 (2002).
- [**Thiaville 2004**] A. Thiaville, Y. Nakatani, J. Miltat, N. Vernier, “Domain wall motion by spin-polarized current: a micromagnetic study”, *J. Appl. Phys.* 65, 7049 (2004)
- [**Thiaville 2005**] A. Thiaville, Y. Nakatani, J. Miltat, Y. Suzuki, “Micromagnetic understanding of current-driven domain wall motion in patterned nanowires”, *Europhys. Lett.* 69, 990 (2005).
- [**Thiele 1973**] A. A. Thiele, “Steady-state motion of magnetic domains”, *Phys. Rev. Lett.* 30, 230 (1973).
- [**Thiele 1974**] A. A. Thiele, “Applications of the gyrocoupling vector and dissipation dyadic in the dynamics of magnetic domains”, *J. Appl. Phys.* 45, 377 (1974).
- [**Thomas 2006**] L. Thomas, M. Hayashi, X. Jiang, R. Moriya, C. Rettner, S. S. P. Parkin, “Oscillatory dependence of current-driven magnetic domain wall motion on current pulse length”, *Nature* 443, 197 (2006).
- [**Tsoi 2004**] M. Tsoi, R. E. Fontana, S. S. P. Parkin, “Magnetic domain wall motion triggered by an electric current”, *Appl. Phys. Lett.* 83, 2617 (2004).
- [**Tsymbal 2001**] E. Yu. Tsymbal, D. G. Pettifor, “Perspectives of giant magnetoresistance”, *Solid. State. Phys.* 56, 113 (2001).
- [**Tsymbal 2002**] E. Yu. Tsymbal, O. N. Mryasov, P. R. Le Clair, “Spin-dependent tunnelling in magnetic tunnel junctions”, *J. Phys.: Cond. Mat.* 15, R109 (2003).
- [**Vanhaverbeke 2007**] A. Vanhaverbeke, M. Viret, “Simple model of current-induced spin torque in domain walls”, *Phys. Rev. B* 75, 024411 (2007).

- [**Vernier 2004**] N. Vernier, D. A. Allwood, D. Atkinson, M. D. Cooke, R. P. Cowburn, “Domain wall propagation in magnetic nanowires by spin-polarized current injection”, *Europhys. Lett.* 65, 526 (2004).
- [**Waintal 2004**] X. Waintal, M. Viret, “Current-induced distortion of a magnetic domain wall”, *Europhys. Lett.* 65, 427 (2004).
- [**Wolf 2001**] S. A. Wolf, D. D. Awschalom, R. A. Buhrman, J. M. Daughton, S. von Molnár, M. L. Roukes, A. Y. Chtchelkanova, D. M. Treger, “Spintronics: A spin-based electronics vision for the future”, *Science* 294, 1488 (2001).
- [**Yamaguchi 2004**] A. Yamaguchi, T. Ono, S. Nasu, K. Miyake, K. Mibu, T. Shinjo, “Real-space observation of current-driven domain wall motion in submicron magnetic wires”, *Phys. Rev. Lett.* 92, 077205 (2004).
- [**Yamanouchi 2006**] M. Yamanouchi, D. Chiba, F. Matsukura, T. Dietl, H. Ohno, “Velocity of domain-wall motion induced by electrical current in the ferromagnetic semiconductor (Ga,Mn)As”, *Phys. Rev. Lett.* 96, 096601 (2006).
- [**Yuan 1991**] S. W. Yuan, H. N. Bertram, “Domain wall dynamic transitions in thin films”, *Phys. Rev. B* 44, 12395 (1991).
- [**Zhang 2004**] S. Zhang, Z. Li, “Roles of nonequilibrium conduction electrons on the magnetization dynamics of ferromagnets”, *Phys. Rev. Lett.* 93, 127204 (2004).

## Conclusions

The purpose of the work presented here is twofold.

The first task was to provide a simulation tool based on the finite element method, which would make possible the treatment of micromagnetic systems regardless of their shape. Two finite element formulations were tested. In a first time, the classical path in deriving a finite element formulation for the dynamic Landau-Lifshitz-Gilbert equation was followed. Two simple test cases were chosen: an infinite prism where the magnetic moments are coupled only through the exchange interaction, and a well-known magnetic structure, the so-called stripe domains, where all of the four most relevant interactions are included. The finite element results were compared with those obtained by a finite difference approach, previously developed in our group. Based on this comparison, it was shown that the magnetization dynamics is not accurately described by this classical finite element approach, as apparently it overestimates the damping term.

Making use of the geometrical interpretation of the constraint on the amplitude of the magnetization vector, that forces the magnetization to move on a sphere, a second integral formulation was derived and implemented. For all the test cases, both the static and the dynamic results provided by the finite difference software were accurately reproduced.

The interest in the finite element method arises mainly because it allows treating complex geometries. To obtain some information about the performances of this second finite element implementation, a stripe system with periodic constrictions was next considered. The curved surfaces are known to be less accurately described by the regular space discretization used by the finite difference, than by the irregular mesh used in the finite element method. Again the magnetization dynamics is correctly described by the second finite element formulation.

The previous test cases proved the high accuracy and performance of the finite element method. Therefore in the last part of the chapter concerning numerical

micromagnetism, a more physical result was presented. We studied magnetization dynamics in the limit of small perturbations, reproducing ferromagnetic resonance spectra and calculating the resonance modes on both a simple and a constricted FePd thin film. Comparing the finite elements results with previously found experimental and finite difference-based simulations a very good agreement was found for the simple structure. For the constricted geometry some small discrepancies are found, especially when looking at the resonance modes, but overall the results are satisfactory.

The second part of the manuscript concerns the study of magnetic domain wall displacement in systems with perpendicular magnetocrystalline anisotropy. We were mostly interested in current-driven wall propagation. Theoretical papers model the spin transfer by means of two new torque terms included in the Landau-Lifshitz-Gilbert equation. Therefore, further development of the finite difference implementation was required. After the obligatory benchmarking phase (against other numerical approaches and analytical treatments), carried out successfully, ideal systems were first studied. First a bulk system has been studied, as the value of the Walker field and of the critical current density can be calculated analytically. Next the dimension of the system was reduced to a thin film, and after that to a nano-wire. Consequently, the critical current/field values are decreasing, their reduction being related to the magnetostatic field within the wall. The mechanism of the domain wall motion does not seem to be affected by the geometry change. The importance of the space discretization used in the simulations was also addressed, namely we showed that it is difficult to evaluate the critical field/current exactly because of the finite size effects of the discretization. The micromagnetic simulations tend to prove that analytical models are not accurate enough in the estimation of the critical field/current.

In the last part of the chapter concerning domain wall displacement, several types of defects were introduced in the perfect nanowire, in order to explore their effect on magnetization dynamics. Firstly the amplitude of the magnetocrystalline anisotropy constant was varied randomly in the wire. It was shown that for small current densities the wall propagation is mostly dominated by the intrinsic pinning. At high current densities however the spin transfer torque overcomes the intrinsic pinning, the movement being governed by the spin transfer. Finally, the depinning current from geometrical and

crystalline defects was determined. This paragraph also shed some light on the depinning process, showing that for small values of the non-adiabatic spin transfer parameter the adiabatic torque is responsible for the depinning of the wall. Increasing  $\beta$ , the role played by the non-adiabatic torque becomes more important, the depinning current decreasing by a certain amount. In the last paragraph a preliminary study concerning domain wall displacement by injection of nanosecond-long current pulses is presented. The possibility of moving a domain wall between two geometrical constrictions by such short current pulses was demonstrated.